

**INVESTIGATION OF TITANIUM DIOXIDE
ALUMINIUM FLUORIDE AND VANADIUM OXIDE ON MULLITE DPFS
MICROSTRUCTURE AND TRAPPING MECHANISM.**



**A THESIS REPORT SUBMITTED IN PARTIAL FULFILLMENT
OF THE REQUIREMENTS FOR THE DEGREE OF
MASTER OF ENGINEERING IN AUTOMOTIVE ENGINEERING
INTERNATIONAL COLLEGE
KING MONGKUT'S INSTITUTE OF TECHNOLOGY LADKRABANG
ACADEMIC YEAR 2018
KMITL-2018-IC-M-004-011**

**INVESTIGATION OF TITANIUM DIOXIDE
ALUMINIUM FLUORIDE AND VANADIUM OXIDE ON MULLITE DPFS
MICROSTRUCTURE AND TRAPPING MECHANISM.**



**A THESIS REPORT SUBMITTED IN PARTIAL FULFILLMENT
OF THE REQUIREMENTS FOR THE DEGREE OF
MASTER OF ENGINEERING IN AUTOMOTIVE ENGINEERING
INTERNATIONAL COLLEGE
KING MONGKUT'S INSTITUTE OF TECHNOLOGY LADKRABANG
ACADEMIC YEAR 2018
KMITL-2018-IC-M-004-011**

This material is reserved for educational use only, not allowed for commercial use.
Forbidden to modify the content, and cite the document when use.



This material is reserved for educational use only, not allowed for commercial use.
Forbidden to modify the content, and cite the document when use.

THESIS TITLE Investigation of Titanium dioxide Aluminium fluoride and Vanadium oxide on Mullite DPFs Microstructure and Trapping mechanism.

STUDENT NAME Mr. Settavit Sirivarocha

STUDENT ID 59610027

DEGREE Master of Engineering

PROGRAMME Automotive Engineering

ADVISOR Asst.Prof.Dr. Preechar Karin

CO-ADVISOR Dr. Nuwong Chollacoop

CO-ADVISOR Prof.Dr. Katsunori Hanamura

ABSTRACT

The exhaust emissions from diesel combustion are the sources of particulate matter emitted to the atmosphere, which are components of air pollution that implicated in human health. At present, the diesel particulate filter (DPFs) can remove PM from the exhaust gas before emitted to the atmosphere. This research is investigating morphology and structure of acicular mullite to develop the fabrication process filter in order to study particulate matters trapping and oxidation mechanisms. This paper used two main substances to study the structure of DPFs; Aluminum oxide (Al_2O_3) and Silicon dioxide (SiO_2). These are mainly in the conventional DPFs. The variable substances are Titanium dioxide (TiO_2) Aluminium fluoride (AlF_3) and Vanadium oxide (V_2O_5), which added to investigate producing the acicular mullite DPFs structure. The mullite samples sintered at $1300\text{ }^\circ\text{C}$ with holding time of 1 h. Moreover, a constant amount of carbon black (CB) used to open the porosity of mullite DPFs. The images of mullite porous microstructure surface investigated using Scanning Electron Microscopy (SEM). In addition, the oxidation kinetics behavior of soot investigated by using isothermal Thermo-gravimetric analysis (TGA) method. The results of this paper provided useful information about impact of TiO_2 AlF_3 and V_2O_5 on mullite DPFs. Therefore, the results able used for the DPFs development of advanced academic and the practical in industry.

Keywords: Particulate Matters, Diesel Particulate filter, Acicular Porous Media, Sintered Mullite

ACKNOWLEDGEMENT

Without the contribution of many people, this thesis would not have been existed. It owes the existence to the supports and inspirations from many people.

To my thesis advisor Asst.Prof.Dr. Preechar Karin and co-advisor of International College at King Mongkut's Institute of Technology Ladkrabang, I would like to express my deepest gratitude for the encouragement and supervision through all obstacles and challenges since the beginning until the end of my study. Dr. Nuwong and Prof. Dr. Hanamura, thank you for being my great co-advisor.

I also want to express my gratitude to all lecturers for your support and guidance to me for the whole two years. In addition, I would like to thank all my friends who always be there to support and motivate me as always. Moreover, I also would love to express my gratitude to all respondents who contribute their information and time on this study. Moreover, I do believe the study could not been done without their input.

Finally, I must express my very greatest gratitude to my parents and all relatives for providing me with unfailing support and continuous motivation throughout my years of study. This accomplishment would not have been possible without them.

Settavit Sirivarocha

TABLE OF CONTENTS

Chapter	Page
ABSTRACT.....	I
ACKNOWLEDGEMENT.....	II
TABLE OF CONTENTS.....	III
LIST OF FIGURES.....	VI
CHAPTER 1 INTRODUCTION.....	1
1.1 Research Background.....	1
1.2 Objectives.....	5
1.3 Work Scope.....	5
CHAPTER 2 LITERATURE REVIEW.....	7
2.1 Internal Combustion Engine.....	7
2.2 Morphologies and Nanostructures of Particulate Matter.....	8
2.3 Particulate Matter Quantity.....	10
2.4 Single particle and Agglomerate particle.....	11
2.5 Nanostructures of Particulate matter.....	14
2.6 Oxidation kinetics.....	17
2.7 Diesel Particulate Filter.....	20
2.8 Diesel Particulate Trapping.....	23
CHAPTER 3 RESEARCH METHODOLOGY.....	29
3.1 Experimental conditions.....	29
3.2 Materials Fabrication Process.....	30
3.3 Scanning Electron Microscopy Image Analysis.....	35
3.4 Thermogravimetric analysis.....	39
3.5 Archimedes method for porosity.....	41

This material is reserved for educational use only, not allowed for commercial use.

Forbidden to modify the content, and cite the document when use.

3.6 Permeability equipment	44
CHAPTER 4 RESULTS AND DISCUSSIONS.....	47
4.1 Morphologies of Fabricated Porous Mullite	47
4.2 Images processing for pore size distribution	53
4.3 Porosity of Mullite.....	58
4.4 Pressure drop by permeability testing	60
4.5 Energy Dispersive X-ray Analyzer	61
4.6 SEM of carbon black trapping	65
4.7 Oxidation kinetics.....	69
CHAPTER 5 CONCLUSIONS AND RECOMMENDATIONS	73
REFERENCES.....	74
APPENDIX A : Publications	77
APPENDIX B : Data recorded of mullite.....	103
APPENDIX C : EDX Sheets	104
APPENDIX D : Drawings	115
APPENDIX E : Comment and questions from thesis defense.....	117
AUTHOR BIOGRAPHY	124

LIST OF TABLES

Table	Page
Table 3.1 Mullite Conditions.....	29
Table 3.2 Sintering Conditions.....	34
Table 4.1 Total amount of pore	56
Table 4.2 Porosity percentage of Mullite.....	56
Table 4.3 Display quantitative results with EDX.....	61
Table 4.4 Calculated activation energy.....	71



LIST OF FIGURES

Figure	Page
Figure 1.1 Energy consumption divided by sector.....	1
Figure 1.2 Industrialization and growing power demand	2
Figure 1.3 Diesel Engine.....	3
Figure 1.4 Soot or particulate matter emitted from Diesel Engine.....	3
Figure 1.5 Diesel Particulate Filter (DPF) in the exhaust gas and DPF structure.....	4
Figure 1.6 Acicular Mullite (ACM)	5
Figure 2.1 Efficiency of the ideal engine	8
Figure 2.2 Composition of particulate matter	9
Figure 2.3 Artist’s conception of diesel particulate matter.....	9
Figure 2.4 Quantity of PM using opacity smoke meter.....	11
Figure 2.5 TEM images of biodiesel engine’s ultrafine particles	12
Figure 2.6 TEM images of biodiesel engine’s nanoparticles	12
Figure 2.7 Size distributions of biodiesel and diesel	13
Figure 2.8 TEM Images of diesel and biodiesel and image processing	15
Figure 2.9 Platelet sizes distribution of diesel and biodiesel	16
Figure 2.10 Equation of Oxidation Kinetics	17
Figure 2.11 Chemical consistent by using PMs Mass conversion by TGA.....	18
Figure 2.12 PMs oxidation with pure oxygen and pure air.....	19
Figure 2.13 Diesel Particulate Filter system	20
Figure 2.14 Surface and cross sectional views of conventional DPF and DPMF.....	21
Figure 2.15 Optical surface views of trapping by conventional DPF and DPMF	22
Figure 2.16 Surface SEM image of Mullite	23
Figure 2.17 Movement mechanism of particle matter.....	24
Figure 2.18 PM of exhaust gas caught by various mechanisms.....	24

This material is reserved for educational use only, not allowed for commercial use.

Forbidden to modify the content, and cite the document when use.

Figure 2.19 The DPF pore diameter compare to particle size.....	25
Figure 2.20 Characteristics of the movement of soot particles	26
Figure 2.21 Characteristics of the movement of soot particles with different sizes...	27
Figure 2.22 Trapping characteristics of PM in DPF filters.....	28
Figure 3.1 Schematic diagram of mullite fabrication process.....	30
Figure 3.2a Grind and mix all substance	31
Figure 3.2b Filling binder PVA-1750	31
Figure 3.2c Move the mixture to the cylinder tool.....	31
Figure 3.2d Cylinder tool and press machine	32
Figure 3.2e Take mullite sample out from cylinder tool	32
Figure 3.2f Mullite sample diameter 25mm thickness 2mm.....	32
Figure 3.3a Mullite samples.....	33
Figure 3.3b Sintered mullite samples	33
Figure 3.4 Furnace machine	34
Figure 3.5 Scanning electron microscopy.....	35
Figure 3.6 The sample for SEM preparation and gold coating	36
Figure 3.7 Schematics of scanning electron microscopy operation	37
Figure 3.8a Raw SEM images.....	38
Figure 3.8b Two-color images	38
Figure 3.9 Schematics of thermogravimetric analysis operation	39
Figure 3.10a Mullite mixed with 50wt.% Carbon black	40
Figure 3.10b Mullite sample for TGA.....	40
Figure 3.11a Weight dry	41
Figure 3.11b Weight saturated	42
Figure 3.11c Weight immersed	42
Figure 3.12a The sample weight dry	43
Figure 3.12b The sample weight immersed.....	43

This material is reserved for educational use only, not allowed for commercial use.

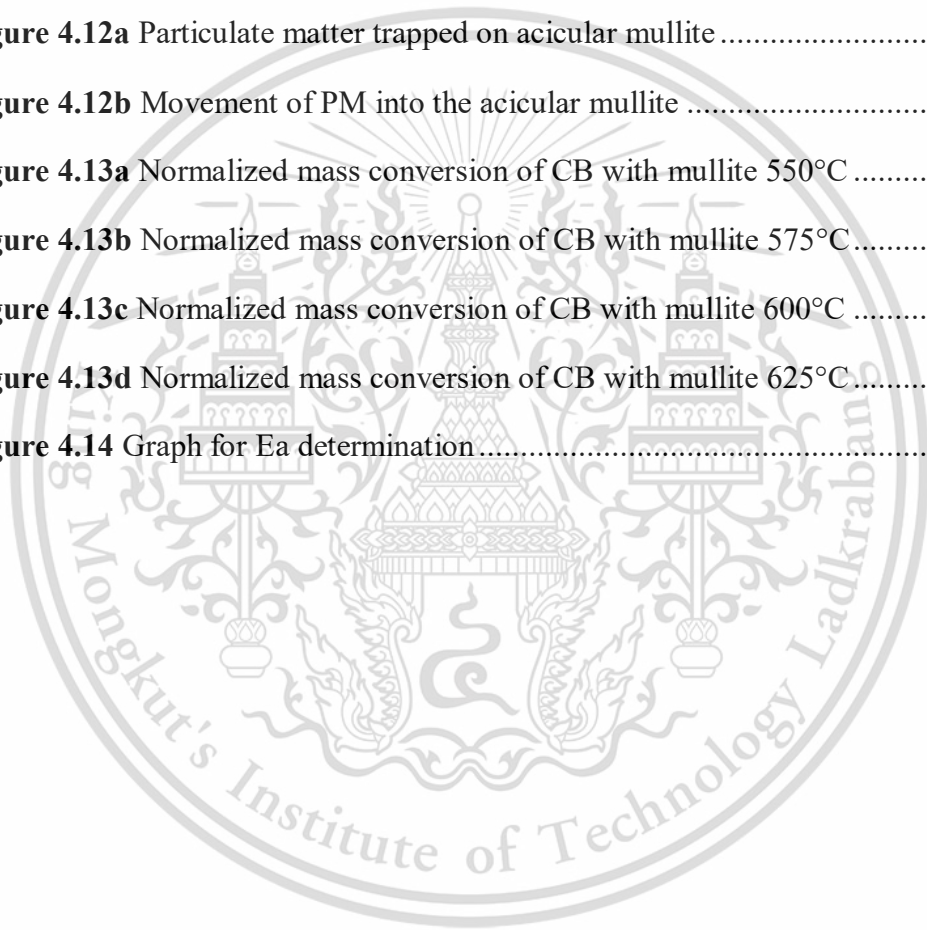
Forbidden to modify the content, and cite the document when use.

Figure 3.13 Permeability equipment.....	44
Figure 3.14 Airflow pipe.....	45
Figure 3.15 Difference pressure diagram.....	46
Figure 3.16 New coupling design.....	46
Figure 4.1a SEM images 300X of sintered Mullite.....	47
Figure 4.1b SEM images 300X of sintered Mullite + TiO ₂	48
Figure 4.1c SEM images 300X of sintered Mullite + TiO ₂ + AlF ₃	48
Figure 4.1d SEM images 300X of sintered Mullite + TiO ₂ + V ₂ O ₅	49
Figure 4.1e SEM images 300X of sintered Mullite + TiO ₂ + AlF ₃ + V ₂ O ₅	49
Figure 4.2a SEM images 1000X and 3000X of sintered Mullite.....	50
Figure 4.2b SEM images 1000X and 3000X of sintered Mullite + TiO ₂	51
Figure 4.2c SEM images 1000X and 3000X of sintered Mullite + TiO ₂ + AlF ₃	51
Figure 4.2d SEM images 1000X and 3000X of sintered Mullite + TiO ₂ + V ₂ O ₅	52
Figure 4.2e SEM images 1000X and 3000X of sintered Mullite + TiO ₂ + AlF ₃ + V ₂ O ₅	52
Figure 4.3a SEM and B&W images of sintered Mullite	53
Figure 4.3b SEM and B&W images of sintered Mullite + TiO ₂	54
Figure 4.3c SEM and B&W images of sintered Mullite + TiO ₂ + AlF ₃	54
Figure 4.3d SEM and B&W images of sintered Mullite + TiO ₂ + V ₂ O ₅	55
Figure 4.3e SEM and B&W images of sintered Mullite + TiO ₂ + AlF ₃ + V ₂ O ₅	55
Figure 4.4 Pore size distribution.....	56
Figure 4.5 Graph porosity compare with number of pore	59
Figure 4.6 Graph porosity compare with black area	59
Figure 4.7 Graph pressure drop.....	60
Figure 4.8a EDX of sintered Mullite	62
Figure 4.8b EDX of sintered Mullite with TiO ₂	62
Figure 4.8c EDX of sintered Mullite with TiO ₂ + AlF ₃	63

This material is reserved for educational use only, not allowed for commercial use.

Forbidden to modify the content, and cite the document when use.

Figure 4.8d EDX of sintered Mullite with $\text{TiO}_2 + \text{V}_2\text{O}_5$	63
Figure 4.8e EDX of sintered Mullite with $\text{TiO}_2 + \text{AlF}_3 + \text{V}_2\text{O}_5$	64
Figure 4.9 Carbon black trapping test.....	65
Figure 4.10a SEM of mullite with CB by mixing.....	66
Figure 4.10b SEM of acicular mullite with CB by mixing.....	66
Figure 4.11a SEM of mullite with CB by sprinkle	67
Figure 4.11b SEM of acicular mullite with CB by sprinkle	67
Figure 4.12a Particulate matter trapped on acicular mullite	68
Figure 4.12b Movement of PM into the acicular mullite	68
Figure 4.13a Normalized mass conversion of CB with mullite 550°C	69
Figure 4.13b Normalized mass conversion of CB with mullite 575°C	69
Figure 4.13c Normalized mass conversion of CB with mullite 600°C	70
Figure 4.13d Normalized mass conversion of CB with mullite 625°C	70
Figure 4.14 Graph for E_a determination.....	72



CHAPTER 1

INTRODUCTION

1.1 Research Background

At present, the major source of global energy comes from fossil fuels Oil is currently the most consumed form of fossil fuel for energy conversion. Therefore, this is the one of main pollutants problem in the world. Figure 1.1 Show energy consumption that divided by sector refers to Annual Energy Outlook 2009 (AEO 2009) they estimate the Energy Information looking in 2030. According to the chart of energy, not much is due to change And Oil still use around 34% and we consume in sector of transportation about 87%.

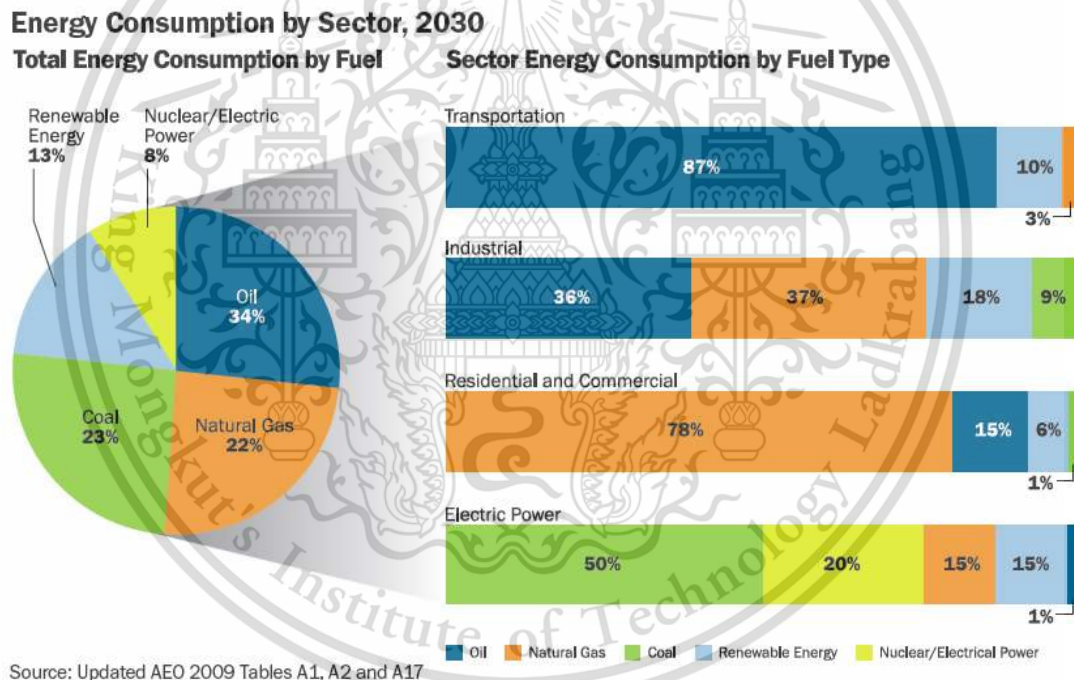


Figure 1.1 Energy consumption divided by sector [1]

For transport sector of figure 1.2 Industrialization and growing power demand in 2030. Transportation still being use and increasing in the future. So that demand for diesel engine is expect to continue to increasing in medium-upper car segments because thermal efficiency is more than 30%, when compare with other internal combustion engine at the same load. However, the transportation sector is one of the main sources contributing to emissions of air pollutants, when compared gasoline, emissions for diesel exhaust – mainly for oxides of nitrogen (NO_x) and particulate matter (PM) This material is reserved for educational use only, not allowed for commercial use.

Forbidden to modify the content, and cite the document when use.

emitted to the atmosphere, which is a component of the air pollution implicated in human cancer, heart and lung damage, and mental functioning. In 1 January 2012, the government of Thailand regulates to use the standard level 7 or Euro 4 to control the emission which release from diesel engine by the particulate matter must be not over 0.025 g/km and nitrogen oxide must be not over 0.25 g/km. However, the increasing numbers of vehicles in Bangkok has countered all the above efforts. Particulate matter levels in Bangkok still exceed the ambient air quality standards of Thailand. To further improve air quality in Bangkok and other parts of Thailand by reducing the emission of PM and nitrogen oxides, implementation of more stringent fuel quality and vehicle emission standards of Euro 5/6 are inevitable.

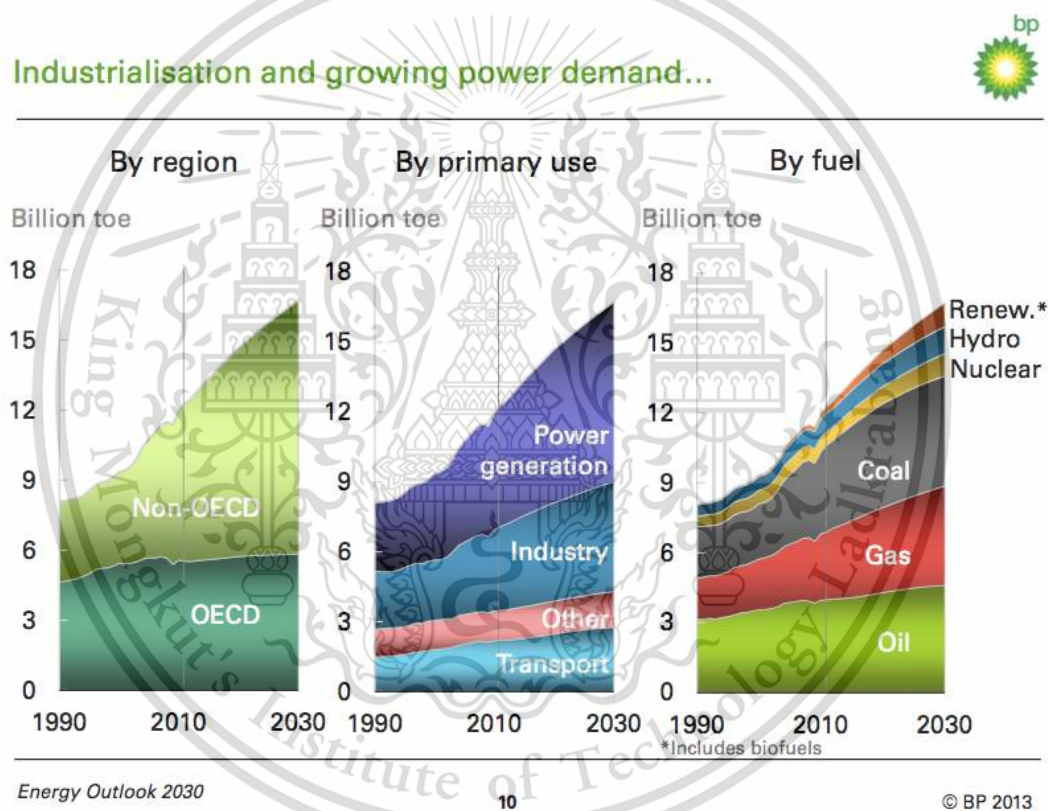


Figure 1.2 Industrialization and growing power demand [2]

Diesel engines in figure 1.3 are provide the highest thermal efficiency for internal combustion engines used in cars and Trucks when compared at the same load. However, diesel engines emit high levels of Particulate Matter (PM) particles and oxides of nitrogen (NOx) compared to gasoline engines of figure 1.4. These two types of pollution are a very bad effect on human politeness, whether it is cause of lung cancer and toxic environment Therefore, it is necessary to eliminate these two types of pollution. Particle pollution from diesel engines has a physical structure and very complex chemistry consisting of two parts: Solid Organic Fraction (SOL) is the main

component of carbon and metal ash (Metallic Ash). The second part is liquid (Soluble Organic Fraction; SOF) have main components are hydrocarbons from incomplete combustion

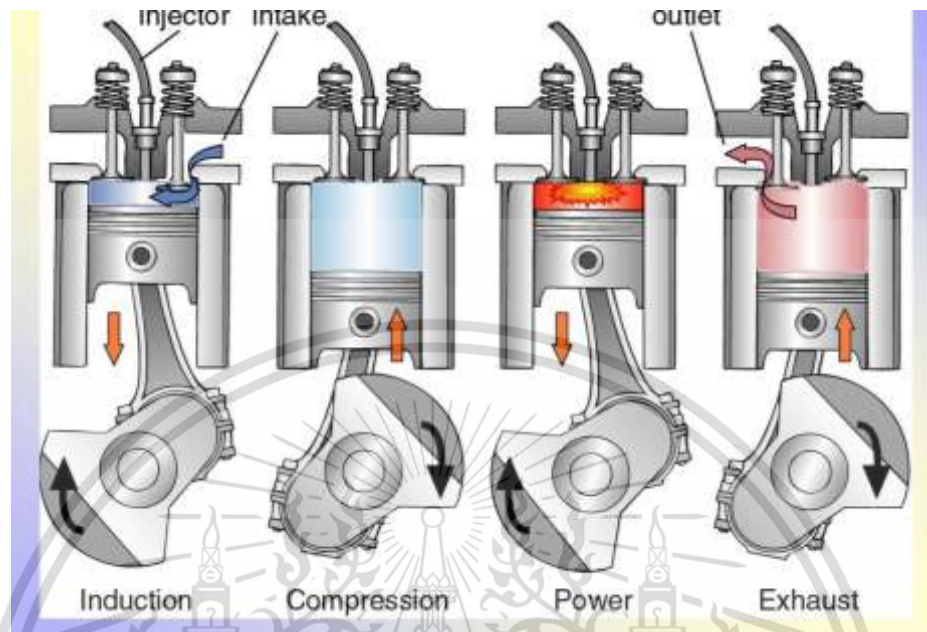


Figure 1.3 Diesel Engine [3]



Figure 1.4 Soot or particulate matter emitted from Diesel Engine [4]

The largest size of particle agglomeration and can be seen with the naked eye, which is in the range of 1-10 microns, sometimes called PM10 (size not more than 10 microns) and PM2.5 (not more than 2.5 microns), PM10 and PM2.5 can be seen in the general. Therefore, the after treatment technology is necessary to be used with diesel engines. This research deals with the development of equipment to eliminate particle pollution from engines. Nowadays diesel cars have Diesel Particulate Filter (DPF) in the exhaust

This material is reserved for educational use only, not allowed for commercial use.

Forbidden to modify the content, and cite the document when use.

gas to stop a soot passing into the atmosphere. Figure 1.5 shown the flow direction of particulate matter pass through into DPF. The structure of DPF consisting of many rectangular channels with alternate channels blocked at each end. The exhaust gas is forced to flow through the porous filter wall and PM were trapped in this stage and regeneration.

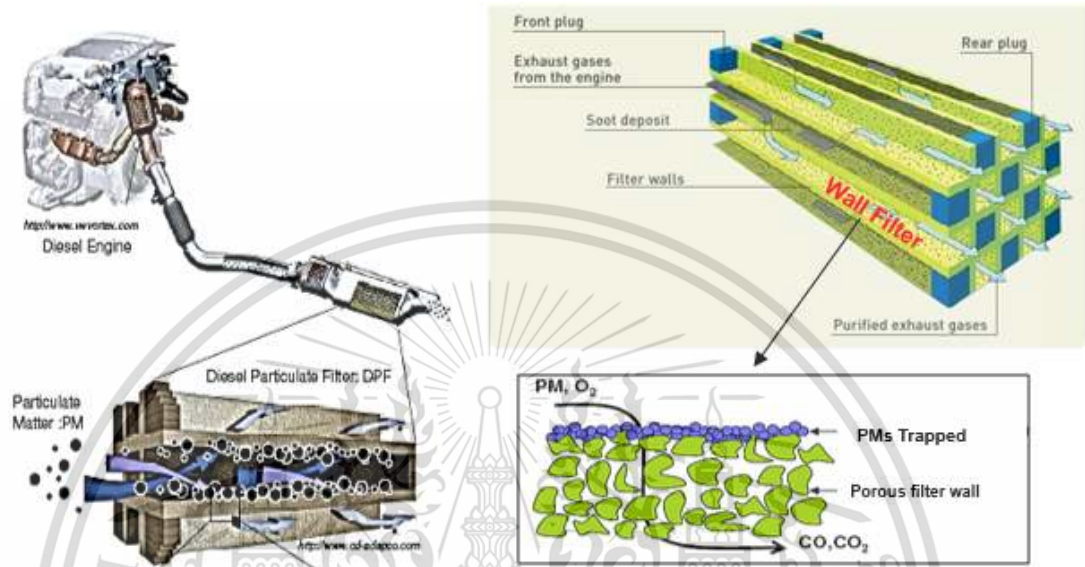


Figure 1.5 Diesel Particulate Filter (DPF) in the exhaust gas and DPF structure [5]

Normally, there are two materials for produce conventional DPFs in the markets Cordierite and SiC. However, In the future we need to find another option for new material to produce Diesel Particulate Filter (DPF) with improvement PM filtration efficiency. Therefore, the Mullite (Mullite DPFs) is one of new material to use for study a prototype particulate pollution filter and device manufacturing. The Mullite has two main components of Aluminium oxide (Al_2O_3) and Silicon dioxide (SiO_2) mixed with Titanium dioxide (TiO_2), Aluminium fluoride (AlF_3) and Vanadium oxide (V_2O_5). There is created with the technology currently available to be a guideline for advanced academic development and practical application in the industrial sector.

1.2 Objectives

- To fabrication and characterization acicular structure of mullite filter by using Titanium dioxide (TiO_2), Aluminium fluoride (AlF_3) and Vanadium oxide (V_2O_5)
- To characterization the impact of Titanium dioxide (TiO_2), Aluminium fluoride (AlF_3) and Vanadium oxide (V_2O_5) on soot oxidation kinetic

1.3 Work Scope

This research is investigating morphology and structure of acicular mullite (ACM) as Figure 1.6 to develop the fabrication process filter in order to study particulate matters trapping and oxidation mechanisms.

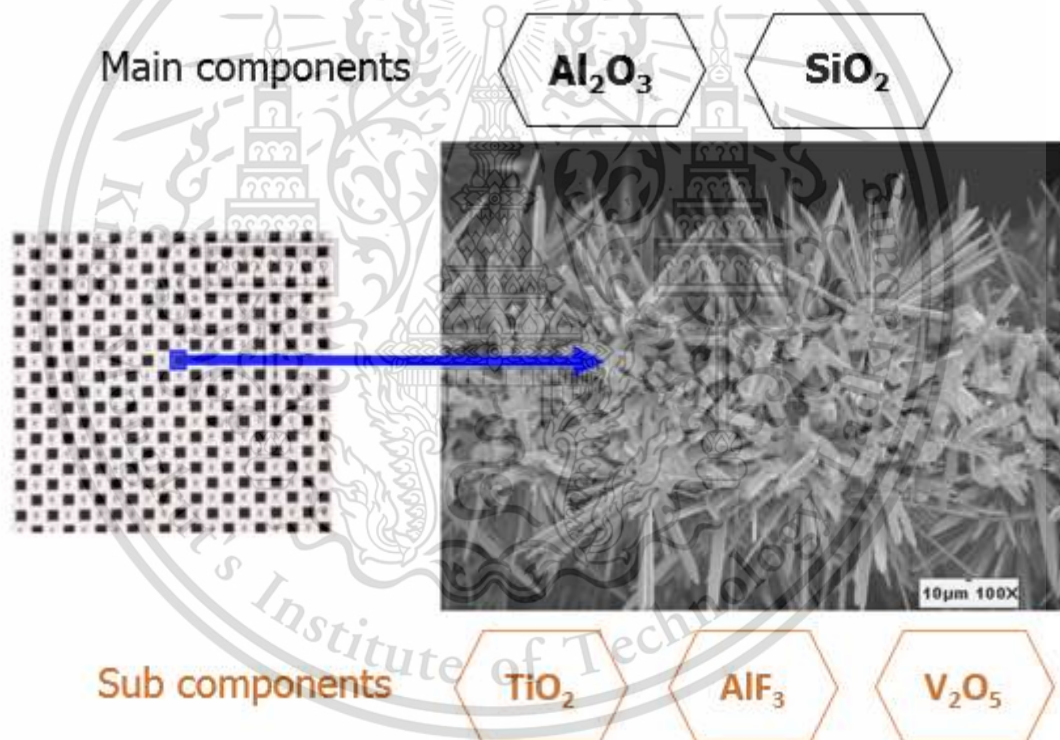


Figure 1.6 Acicular Mullite (ACM) [6]

Researches have been employed the ceramic mullite and concluded an advantages such as increased porosity and high mechanical strength with addition TiO_2 . The results showed that microstructure of mullite (ML) DPFs is improved by using 4wt.% AlF_3 and 3wt.% V_2O_5 contents at sintering temperature of 1300°C . The porosity is increased up to 50%. One of researched showed mullite sintered at 1000°C with 3 h holding time.

This material is reserved for educational use only, not allowed for commercial use.

Forbidden to modify the content, and cite the document when use.

This study reported that the mullite exhibited acicular mullite (ACM) with 0.06-0.3 μm in acicular diameter.

Previous research has shown that the mullite structures have high opened porosity and mechanical strength. However, the investigation on the morphologies, microstructures and mechanical properties of ACM have insufficient data. Further research is need to provide more evidence to support ACM design throughout the operation and trapping mechanism of DPFs.

The objective of this paper is to investigate the porosity and pore size distribution of mullite with TiO_2 , AlF_3 and V_2O_5 additions 10wt.% of each. Moreover, a constant amount of carbon black (CB N330) will use to open the porosity of mullite DPFs. Then using SEM and image processing and to develop the fabrication process of ACM in order to study DPFs structure and oxidation mechanisms. The samples of mullite are sinter at constant temperature of 1300°C with a holding time of 1 h. The image processing will do by using the Image J processing program. The compositional analysis of ACM structures will do by using SEM combined with an energy dispersive X-ray analyzer (EDX). The permeability will be evaluate by use airflow and difference pressure measurement.

In addition, Thermo-Gravimetric Analysis (TGA) have perform to study chemical kinetics of soot oxidation kinetics. The results will present in terms of morphologies of SEM and two-color image, porosity, pore size distribution, amount of pore percentage of mass conversion and rate of mass change of soot oxidation kinetics.

The results of this paper provided useful information about impact of Titanium dioxide (TiO_2), Aluminium fluoride (AlF_3) and Vanadium oxide (V_2O_5) on mullite DPFs. Therefore, the results should be useful for the DPFs development of advanced academic and the practical in industry.

CHAPTER 2

LITERATURE REVIEW

2.1 Internal Combustion Engine

Internal Combustion Engine (ICE) is a heat engine that acts to change the chemical energy contained in the fuel molecules into thermal energy by combustion, which is a chemical reaction between oxygen molecules obtained from the air and molecules of hydrocarbon compound used as fuel. The interaction between the two molecules of the above reactants will cause internal energy that is chemical energy in the form of heat. This chemical reaction is called Exothermic Reaction. The heat energy received during combustion chamber will cause molecular dynamics of the gas in the combustion chamber to increase. The force that the molecules of the gas carry on the combustion chamber wall, which is called the pressure in the combustion chamber, will be much higher.

The internal combustion engine can change the force that the gas molecules act on the mechanical energy of the combustion chamber wall using engineering mechanisms. Most of the current internal combustion engines are piston engines or Reciprocating Engines, which is to have a piston running outward and return in the cylinder within the combustion chamber. The surface of the piston acts as a force from the gas molecules. Therefore the movement of the piston, which is transformed into mechanical energy with the following mechanism to drive the motor

Diesel engines are engines that provide the highest thermal efficiency in internal combustion engines used in cars and trucks when comparing the same load as shown in Figure 2.1. However, diesel engines release particulate pollutants or Particulate Matter (PM) and oxides of nitrogen (NO_x) in high volumes compared to gasoline engines. These two types of pollutants have a very detrimental effect on human politeness, whether it is the cause of lung cancer and toxic environment. Therefore, it is necessary to eliminate these two types of pollution.

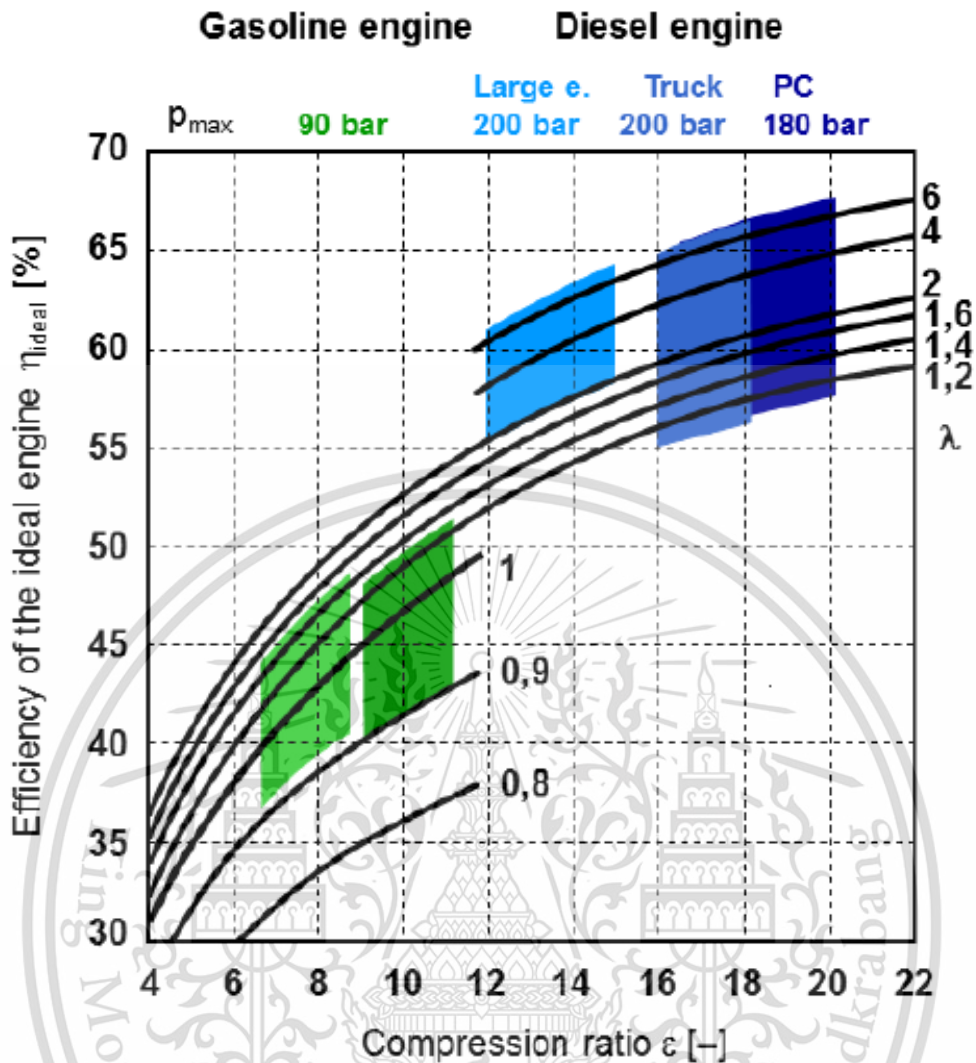


Figure 2.1 Efficiency of the ideal engine [7]

2.2 Morphologies and Nanostructures of Particulate Matter

Particulate matter contains microscopic solids or liquid droplets that are so small that they can be inhaled and cause serious health problems. The particle size is important as the particles smaller than 2.5 micrometers can reach lungs along with the inhaled air and cause health problems. The particles smaller than 2.5 micrometers constitute more than 90 percent mass of the total particulate matter in the diesel exhaust. Composition of particulate matter collected on a filter is schematically shown on Figure 2.2 various components adsorbed on the surface of spherical soot particles are shown.

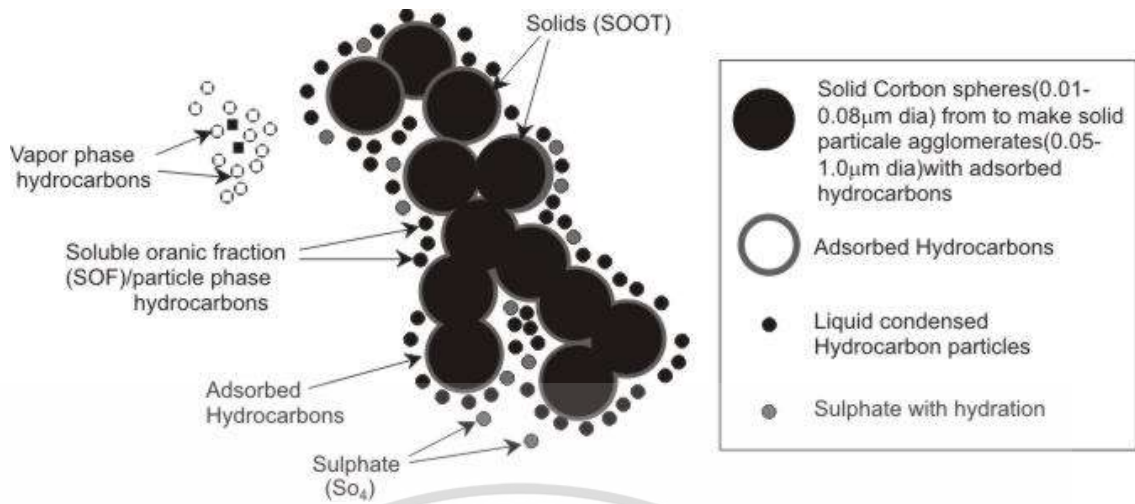


Figure 2.2 Composition of particulate matter [8]

Particulate emissions from diesel engine [9]

Figure 2.3 shows the diesel particulate matter consists of two types of particles: (a) fractal-like agglomerates of primary particles 15–30 nm in diameter, composed of carbon and traces of metallic ash, and coated with condensed heavier end organic compounds and sulfate; (b) nucleation particles composed of condensed hydrocarbons and sulfate. Structure of agglomerated particle contains a lot of soot in primary particle. The structure of the soot is composed of carbon platelet. Which we analyzed from images taken by the electron microscopy.

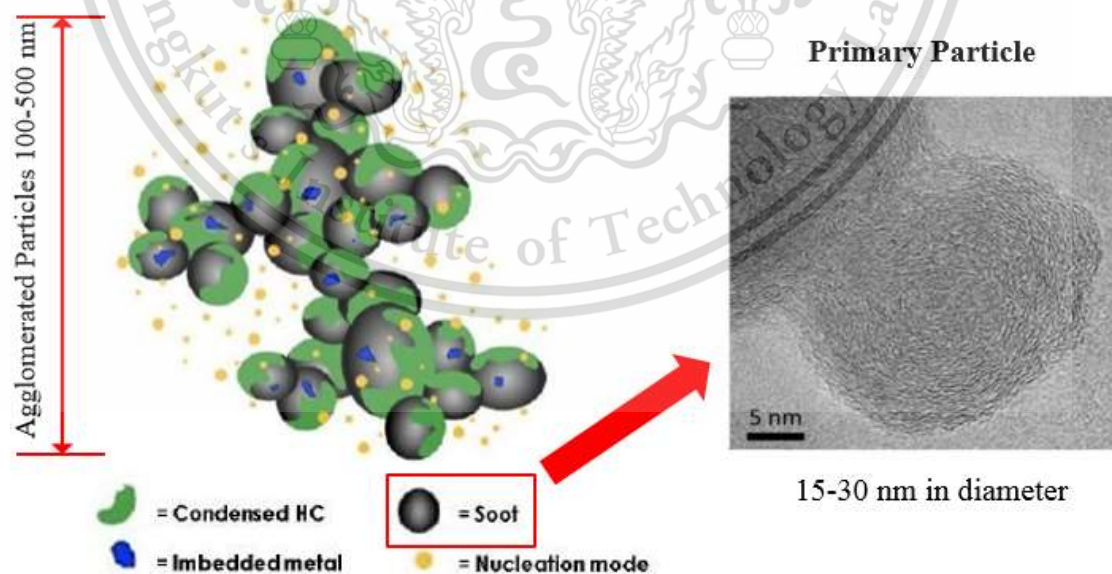


Figure 2.3 Artist's conception of diesel particulate matter [9]

This material is reserved for educational use only, not allowed for commercial use.

Forbidden to modify the content, and cite the document when use.

Particulate matter (PM) consists of microscopic solids or liquid droplets, which are so small size that can cause serious health problems. Particulate matter is the most important characteristics of diesel emissions, which is responsible for black smoke traditionally associated with diesel-powered vehicles. Diesel particulate matter emission is usually abbreviated as PM or DPM. Size of PM particles can classified into various types. Particles normally found in the atmosphere can be derived into four types; PM₁₀, fine particles, ultrafine particles and nanoparticles. The particle size is an important factor as considerable as PM smaller than 2.5 μm . The particles smaller than 2.5 μm constitute more than 90% by mass of the total PM in the diesel exhaust. Composition of PM collected on a filter. The various components adsorbed on the surface of spherical soot particles. From this reason, PM particles must remove before releasing to the environment. One of technique for removing PM is to develop the trapping mechanism process by enhancement of DPF filter.

2.3 Particulate Matter Quantity

Particulate Matter Quantity [10] Figure 2.4 shows measurement results of smoke intensity, which is an indirect method to estimate PM's quantity. The intensity is strongly dependent on the engine load. The more engine load, the greater smoke intensity due to more fuel supply for combustion. In this research, much amount of particle was used to determine the integrity of combustion process. The biodiesel produces less smoke than the diesel at almost all engine operating conditions because oxygenated fuel promote more complete combustion and better fuel-oxygen's reactivity.

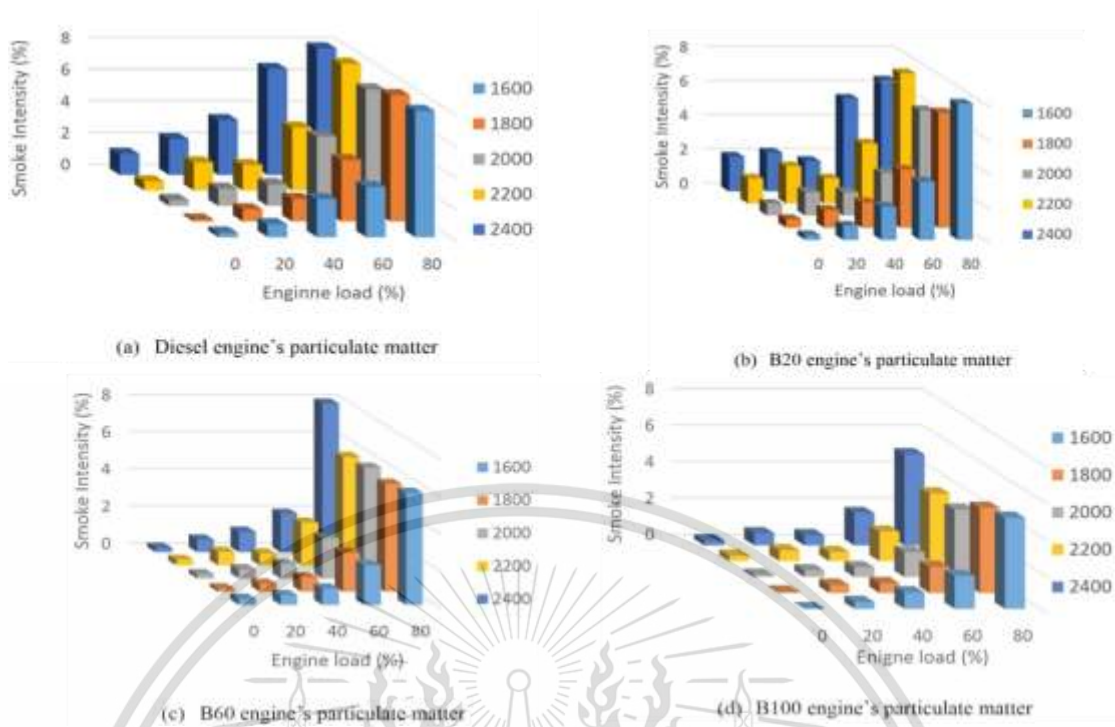


Figure 2.4 Quantity of PM using opacity smoke meter [10]

2.4 Single particle and Agglomerate particle

Single particle and Agglomerate particle [11]

Figure 2.5 show TEM images of biodiesel engine's agglomerate ultrafine particle and Figure 2.6 show primary nanoparticle in the condition 80% of engine load and 2400 rpm of engine speed. The agglomerate ultrafine particle and primary nanoparticle size were micron and submicron scale, respectively. Engine's agglomerate ultrafine particles consist of several uniform primary nanoparticles. Most of engine's primary nanoparticle diameter is smaller than 60 nm. The average agglomerate ultrafine particle sizes of both diesel and biodiesel engine's PMs are approximately 100-500 nm.

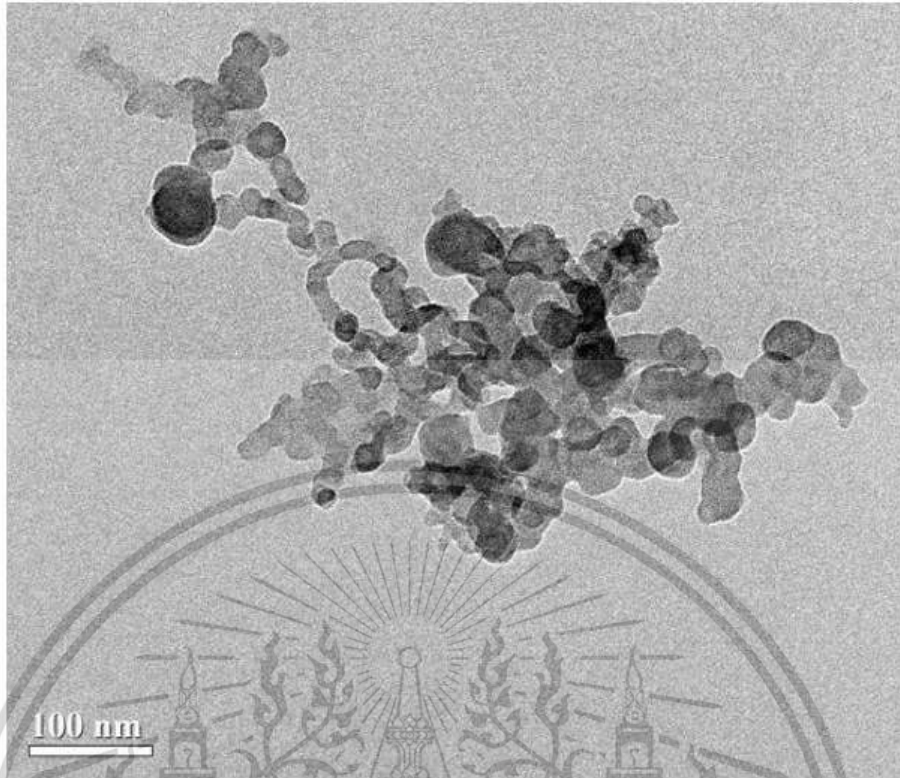


Figure 2.5 TEM images of biodiesel engine's ultrafine particles [11]

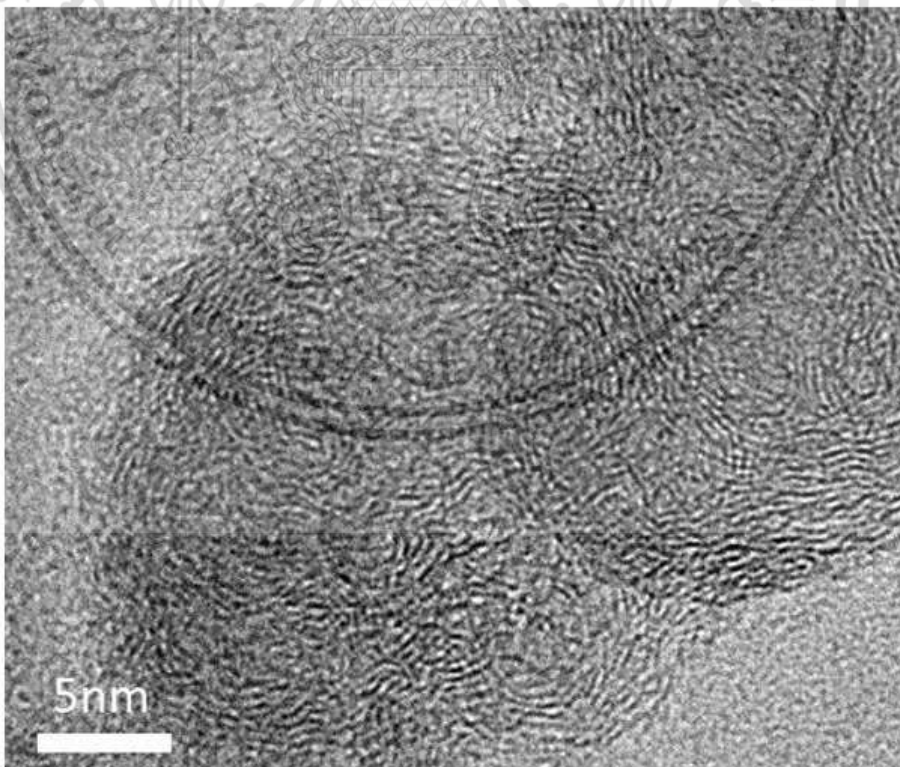
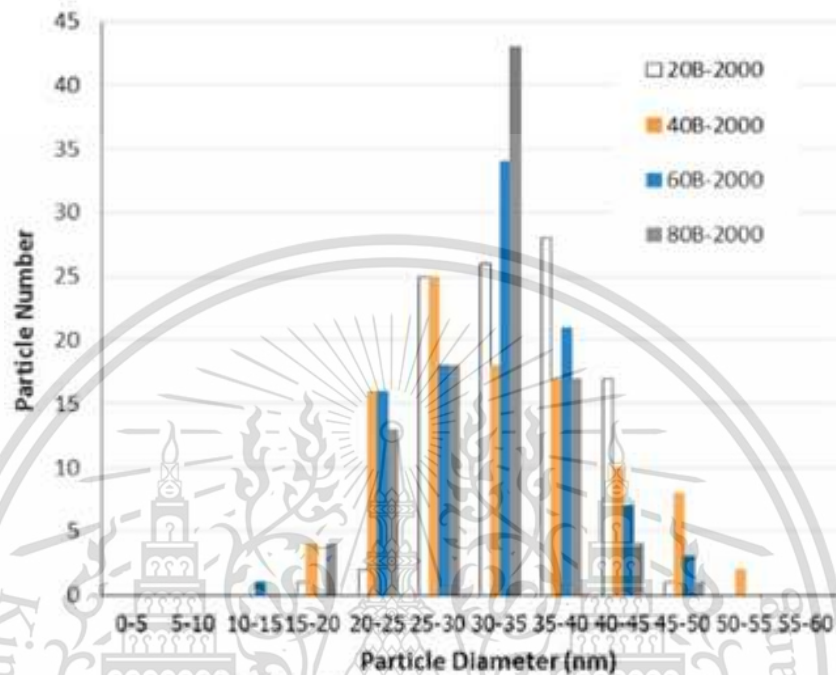
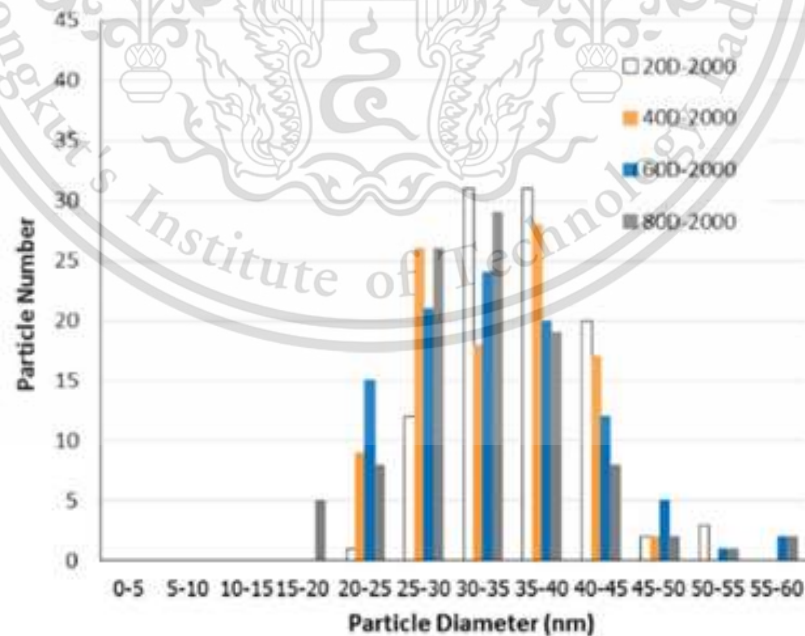


Figure 2.6 TEM images of biodiesel engine's nanoparticles [11]

Figures 2.7 show biodiesel and diesel engine's primary nanoparticle size distribution in the condition 20, 40, 60 and 80% of engine load 2000 rpm of engine speed, respectively. The primary nanoparticle diameters are in the range of 10-60 nm. It was clearly observed much amount of particle diameters are in the range of 30-40 nm.



(b) Biodiesel Engine 2000 rpm



(b) Diesel Engine 2000 rpm

Figure 2.7 Size distributions of biodiesel and diesel [11]

This material is reserved for educational use only, not allowed for commercial use.

Forbidden to modify the content, and cite the document when use.

Particle diameter size decreased when increasing engine speed for both of diesel and biodiesel's engine PMs. The exhaust gas temperature also gradually increased when increasing engine speed. It means PM oxidation rate inside combustion chamber increased when increasing engine speed (increasing temperature) due to lower heat loss on cylinder surface compare to lower engine speed. Similarly, particle diameter size decreased when increasing engine load for both of diesel and biodiesel's engine PMs. The exhaust gas temperature also gradually increased when increasing the engine load. It means PM oxidation rate inside combustion chamber increased when increasing engine load (increasing fuel injection quantity) resulting in higher combustion temperature compare to lower engine load. Moreover, the average diameter of biodiesel engine's PMs are significantly smaller than that of diesel engine's PMs because of bio oxygenate fuel.

2.5 Nanostructures of Particulate matter

Nanostructures of Particulate matter [12]

Figure 2.8 (a) shows TEM images of engine 80% load diesel and biodiesel single PMs. Single particles are nearly sphere shape even though surface are not so smooth. Carbon platelets in the surface of particle are not so close distance and look like not so strong contact with other platelets. TEM image shows the different structure of inner core zone and outer shell zone of PMs. The inner core diameters are approximately 5 to 10 nm.

Moreover, the structure of carbon platelet inside inner core zone shows short length and non-homogeneous platelets; whereas long length and homogeneous platelets could be clearly observe in outer shell zone. Single particle could be observe two to four inner core portions. In the first process of PM formation, agglomerated inner core portion might be accumulate to be a single primary particle. After that, surface of single primary particle growth up by carbon atom with time until approximately 100 nm of diameter depended on engine operation condition, which might be strongly effect on density of carbon atom per volume. In the last process, surface of PM is oxidized by oxygen molecule during combustion process. In addition, images show carbon platelet structures of connection zone between two single primary particles are also quite homogeneous platelet density compare to the inner core zone.

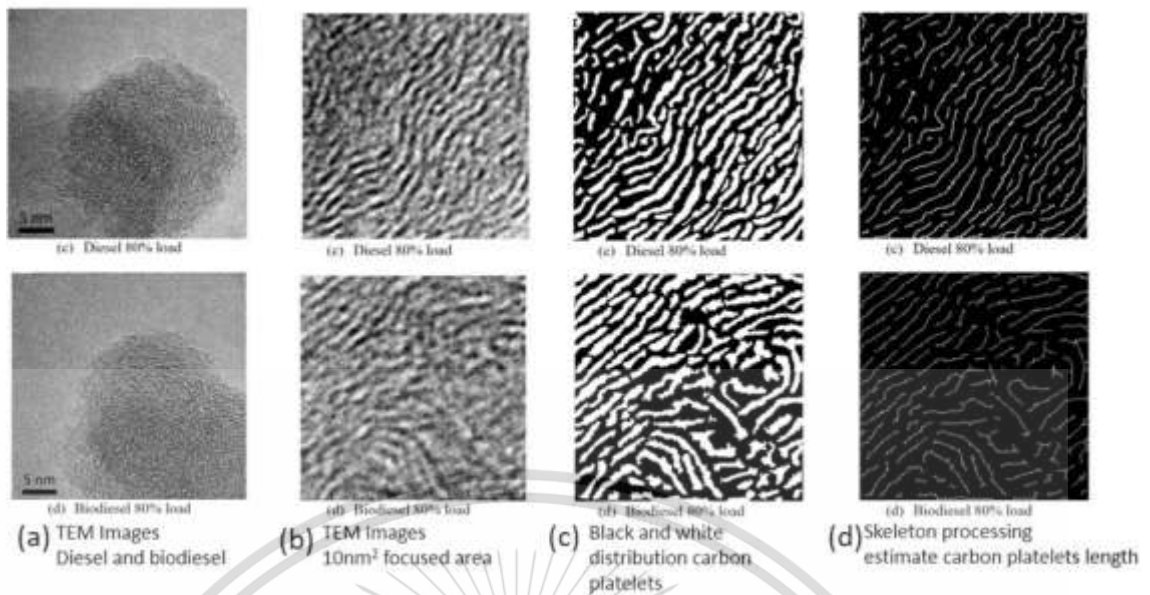


Figure 2.8 TEM Images of diesel and biodiesel and image processing [12]

PM is investigated for number of carbon atom include in the particle. TEM image is used for numerate platelet number that aggregate layered in the particle. Each of platelet is consisted properly by carbon atom from incomplete combustion product. Figures 2.8 (b) (c) and (d) are the images of original 10 nm² focused area, after post processing of two colors and after post processing of skeleton carbon platelet length estimation. The focused areas of all images are homogeneous platelet area in each outer shell zone. Original gray color could be successfully change to two colors images in the first step. The lengths of each platelet in each sample are quite different, whereas the distances of each platelet are also not too different. From the skeleton images, the carbon platelets inside the PM were measured by image processing program. The skeleton carbon platelets, which have 1 unit pixel width for each platelet, were measured for the white area in the image to be a carbon platelet length that shown in Figure 2.9

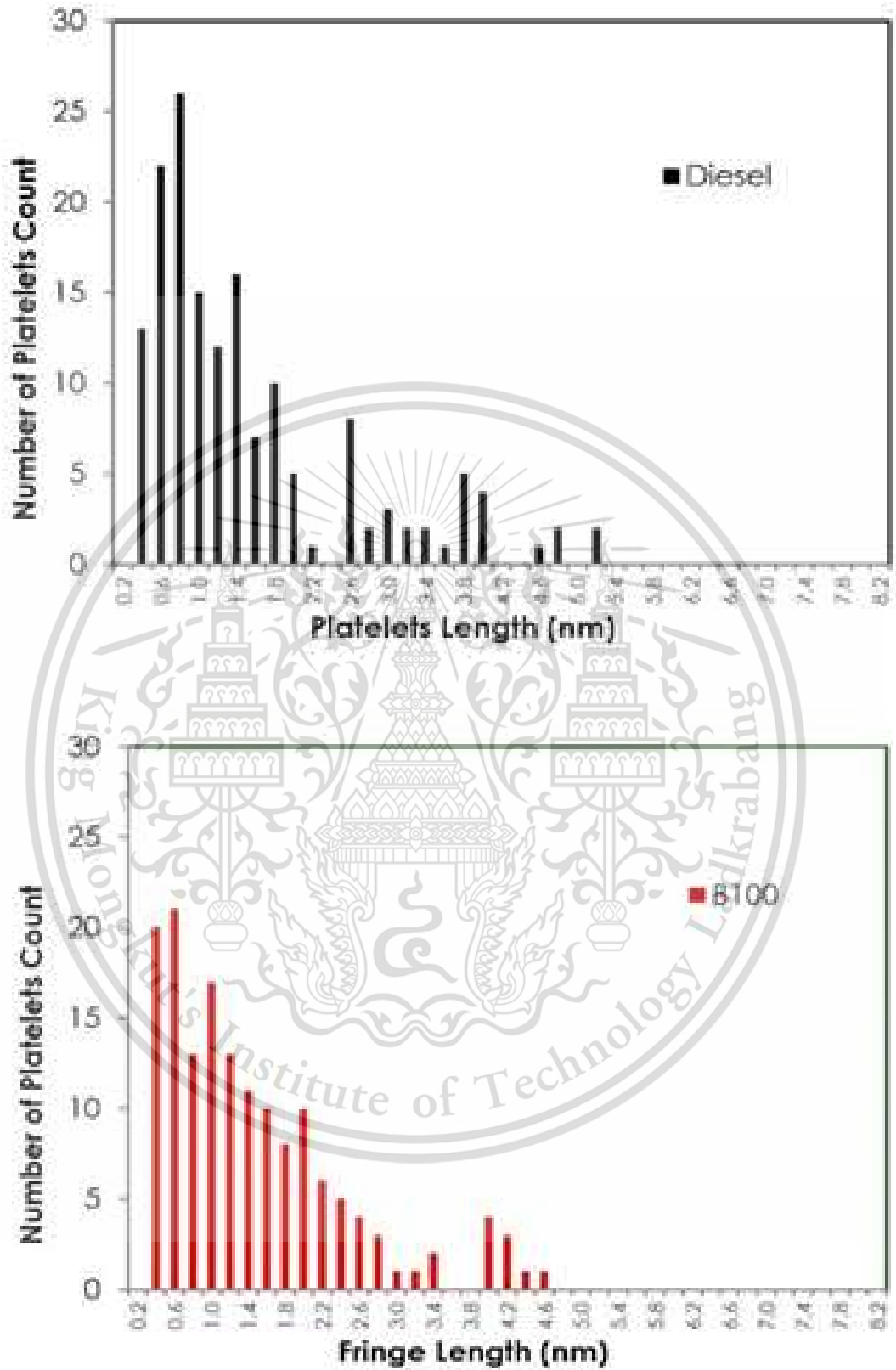


Figure 2.9 Platelet sizes distribution of diesel and biodiesel [12]

2.6 Oxidation kinetics

Oxidation kinetics [13]

The oxidation behavior of PMs has been investigated using thermogravimetric analysis (TGA) and temperature program oxidation (TPO) to evaluate reaction activity. The fit curve results of reaction order for both oxygen and carbon, and the activation energies, were defined and reported. The order in carbon is close to the order of 2/3 (0.67), making it applicable for the shrinking-core model. The order of reaction rate in oxygen is close to 1. The activation energy (E_a) of carbon oxidation is around 150170 kJ/mole. Chemical kinetics of PM oxidation is studied by using mass conversion behavior from TGA. As figure 2.0 the chemical reaction rate in equation (1) can be calculated from the TGA mass conversion curve based on the chemical kinetic in equation (2). Where PM is PM mass, t is time, n, m are the reaction order of PM and oxygen, respectively. The reaction order n is assumed to be 2/3 as shrinking core model because PM is like spherical shape. In order to calculate the apparent activation energy (E_a) of PM oxidation, the chemical reaction rate constant k at each temperature in equation (2) is expressed by equation (3). Where A is the frequency factor, E_a is the activation energy, R is the gas constant. Finally, the apparent activation energy can be calculated by equation (4) using the Arrhenius plot.



$$-\frac{d[PM]}{dt} = k[PM]^n [O_2]^m \quad (2)$$

$$k = A e^{-\frac{E_a}{RT}} \quad (3)$$

$$\ln \left[\frac{-1}{[PM]^n} \frac{d[PM]}{dt} \right] = -\frac{E_a}{RT} + (\ln A + m \ln [O_2]) \quad (4)$$

Figure 2.10 Equation of Oxidation Kinetics

Figure 2.11 shows the estimation results of chemical consistent inside diesel and biodiesel PM in each operation condition of the engine by TGA method. PM of the diesel engine is consisted approximately of 4% moisture, 68% unburned HC and 28% carbon of no-load condition while medium load condition has 6% moisture, 54% unburned HC and 40% carbon and high load condition has 4% moisture, 38% unburned

This material is reserved for educational use only, not allowed for commercial use.

Forbidden to modify the content, and cite the document when use.

HC and 58% carbon, as shown in Figure 2.11 (a). Figure 2.11 (b) shows the results of PMs emitted from the biodiesel engine. PM of biodiesel combustion is consisted approximately of 4% moisture, 83% unburned HC and 13% carbon of no-load condition while medium load condition has 9% moisture, 77% unburned HC and 14% carbon and high load condition has 4% moisture, 49% unburned HC and 47% carbon.

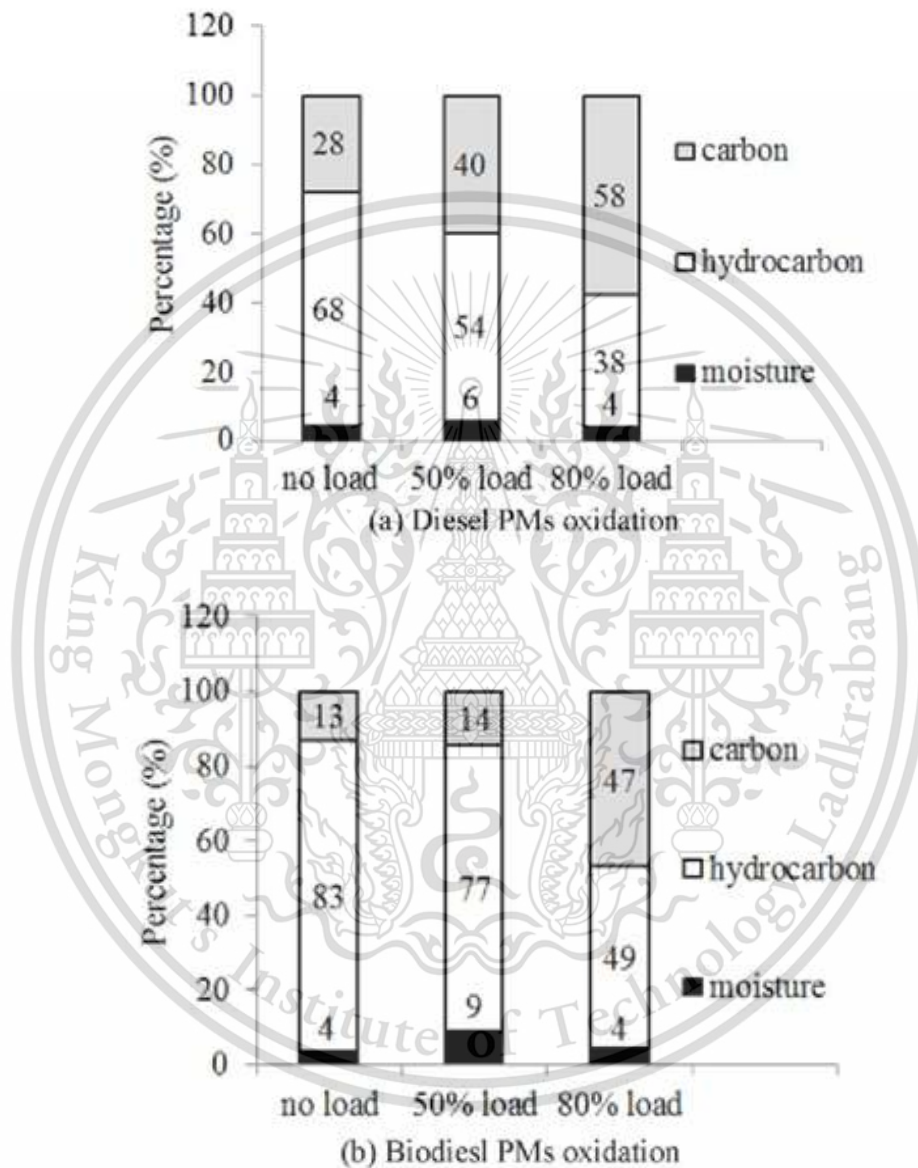


Figure 2.11 Chemical consistent by using PMs Mass conversion by TGA [13]

PM in the high load condition has lower unburned HC fraction than that of the lower load condition. It might be expected that the combustion temperature, the temperature of gas in high load condition is higher than from low load condition, are strongly impact to unburned HC fraction. Some of unburned HC might be oxidized with remain oxygen in high temperature inside the combustion chamber and exhaust gas in exhaust

This material is reserved for educational use only, not allowed for commercial use.

Forbidden to modify the content, and cite the document when use.

manifold. PM from biodiesel engine combustion has more unburned HC fraction than that of diesel engine combustion. According to that biodiesel fuel has lower heating value than that of diesel fuel. In the same load condition, biodiesel must be used more for fuel injection to combustion chamber in combustion duration. More of fuel remaining in combustion duration is burned to be more HC in PM.

Isothermal PMs Oxidation Kinetics of PMS [5]

The result of isothermal TGA at higher temperatures including 450, 500, 550 and 600°C is plotted at Figure 2.12 for oxygen and air, respectively. The conversion rate of all 80% engine load PM samples including diesel and biodiesel increases by increase of temperature. The conversion rate of biodiesel and diesel PMs is almost the same while after introduction of oxygen at desired temperature the PM sample from biodiesel shows a relatively faster conversion rate in comparison with the diesel. The main reason for all these behaviors is due to difference in composition of PM from diesel and biodiesel.

The PM from biodiesel consists of unburned oxygenated hydrocarbon (HC) in comparison with unburned non-oxygen hydrocarbon from diesel fossil fuel. As biofuels are oxygenated fuels, they may have more oxygen content in the PM, this can boost oxidation, and thus biodiesel shows faster oxidation rate in comparison with diesel. The increase in temperature is also responsible for increase in rate of conversion.

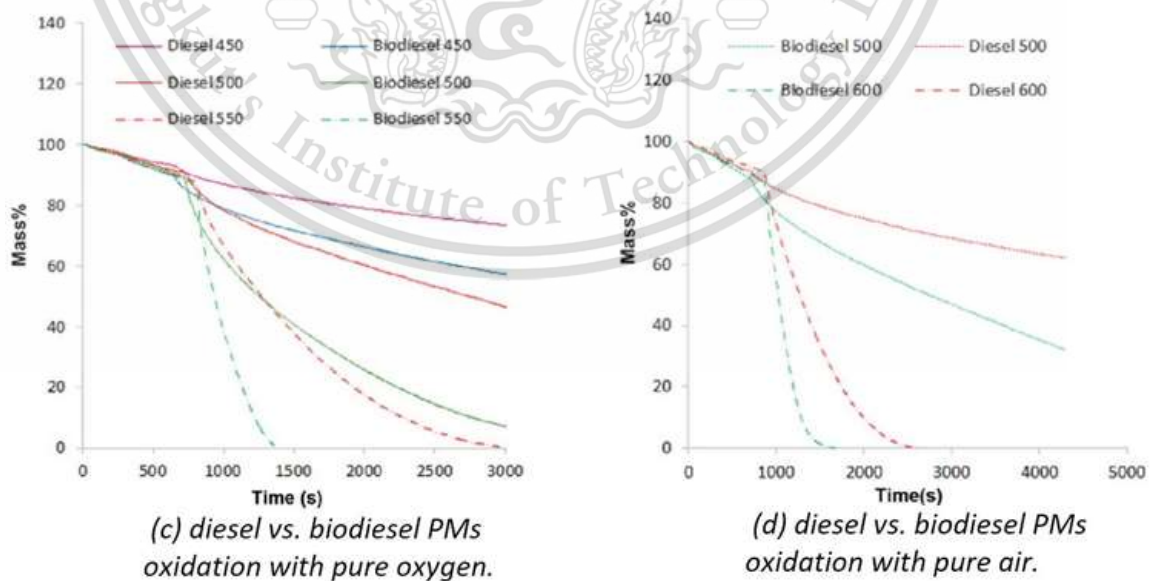


Figure 2.12 PMs oxidation with pure oxygen and pure air [13]

This material is reserved for educational use only, not allowed for commercial use.

Forbidden to modify the content, and cite the document when use.

2.7 Diesel Particulate Filter

Nowadays Figure 2.13 diesel cars have to be fitted with a Diesel Particulate Filter (DPF) in the exhaust to stop this soot passing into the atmosphere. The after-treatment technology is appropriate to use in particulate emission reduction. Diesel particulate filter is new technology for particulate matter removing application. Diesel particulate filter has two main types presently use. Full flow filter is high trapping efficiency, 90% removing by mass and 99% removing by number. Second, the partial flow filter collects some particulate matter out of engine while the residue is flow through to the air. The trapping efficiency of the partial flow is approximately 50%.

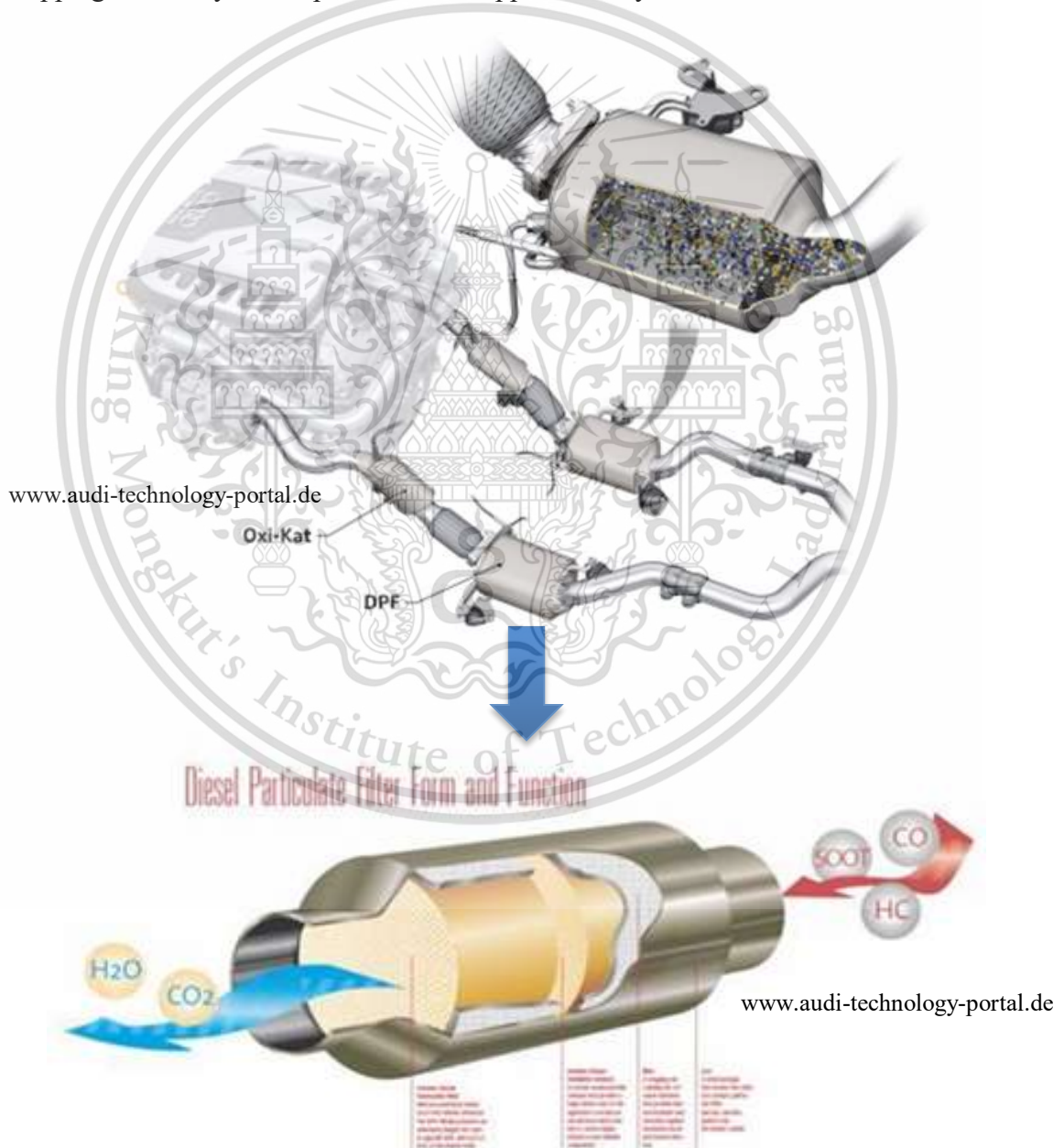


Figure 2.13 Diesel Particulate Filter system [14]

This material is reserved for educational use only, not allowed for commercial use.

Forbidden to modify the content, and cite the document when use.

Diesel Particulate Membrane Filter [15]

Through microscopic visualization experiments, a process generally known as depth filtration was shown to be caused by surface pores. Moreover, the existence of a soot cake layer was an important advantage for filtration performance because it could trap most of the particulates. We proposed an ideal diesel particulate filter (DPF), in which a silicon carbide (SiC) nanoparticle membrane (made from a mixture of 80 nm and 500 nm powders) instead of a soot cake was sintered on the DPF wall surface; this improved the filtration performance at the beginning of the trapping process and reduced energy consumption during the regeneration process. The proposed filter was called a diesel particulate membrane filter (DPMF).

Figures 2.14 (a) and (b) show the conventional DPF and a proposed DPMF, respectively. Three kinds of DPFs were tested. The conventional DPF is made of SiC micron particles, and it has a wall thickness of 300 μm and porosity of 42%. On the other hand, the DPMF has a membrane composed of SiC nanoparticles with mixed sizes of 80 and 500 nm, sintered on the conventional DPF at 1700 $^{\circ}\text{C}$. The membrane has a wall thickness of 20 μm and porosity of 60%. For the conventional catalyzed DPF (CDPF), a Pt/Pd catalyst was coated on the conventional DPF

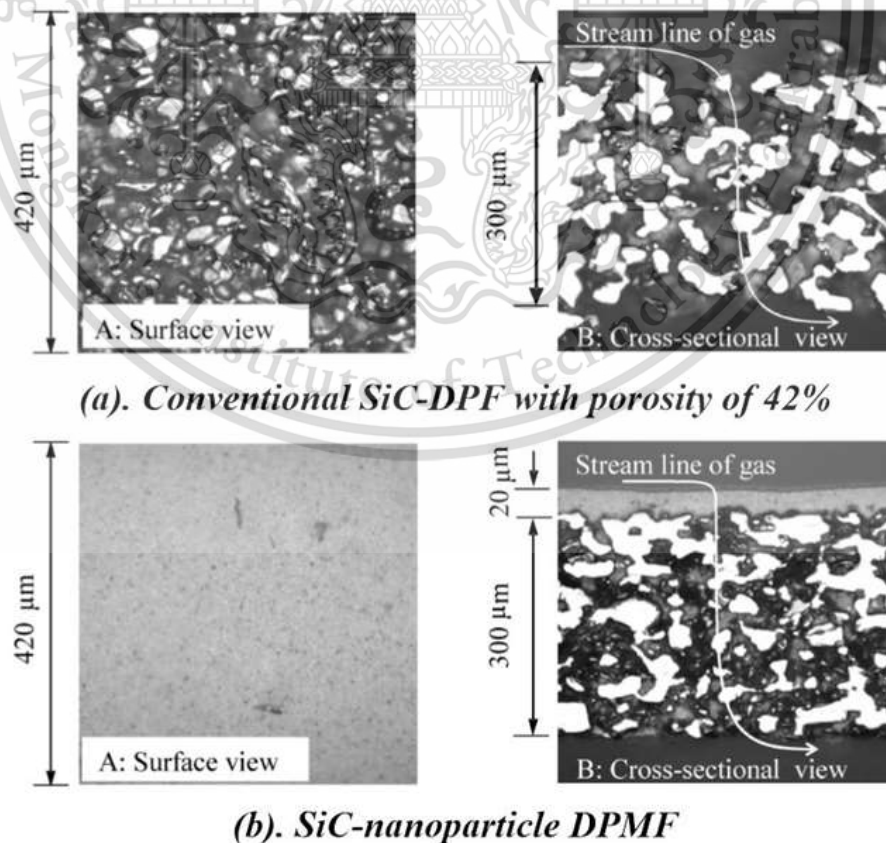


Figure 2.14 Surface and cross sectional views of conventional DPF and DPMF [15]

Figures 2.15 show time-sequenced surface views during particulate trapping using the conventional DPF (porosity of 42%), and DPMF, respectively. In the case of the DPMF, fine surface pores will trap the diesel particulates. The DPMF, the soot cake developed faster than in conventional DPFs with porosities of 42%, due to the very fine and very shallow surface pores. The particulates trapped inside the fine surface pores of the membrane and large surface pores of the conventional DPF decrease gradually with time along the contours of the pores.

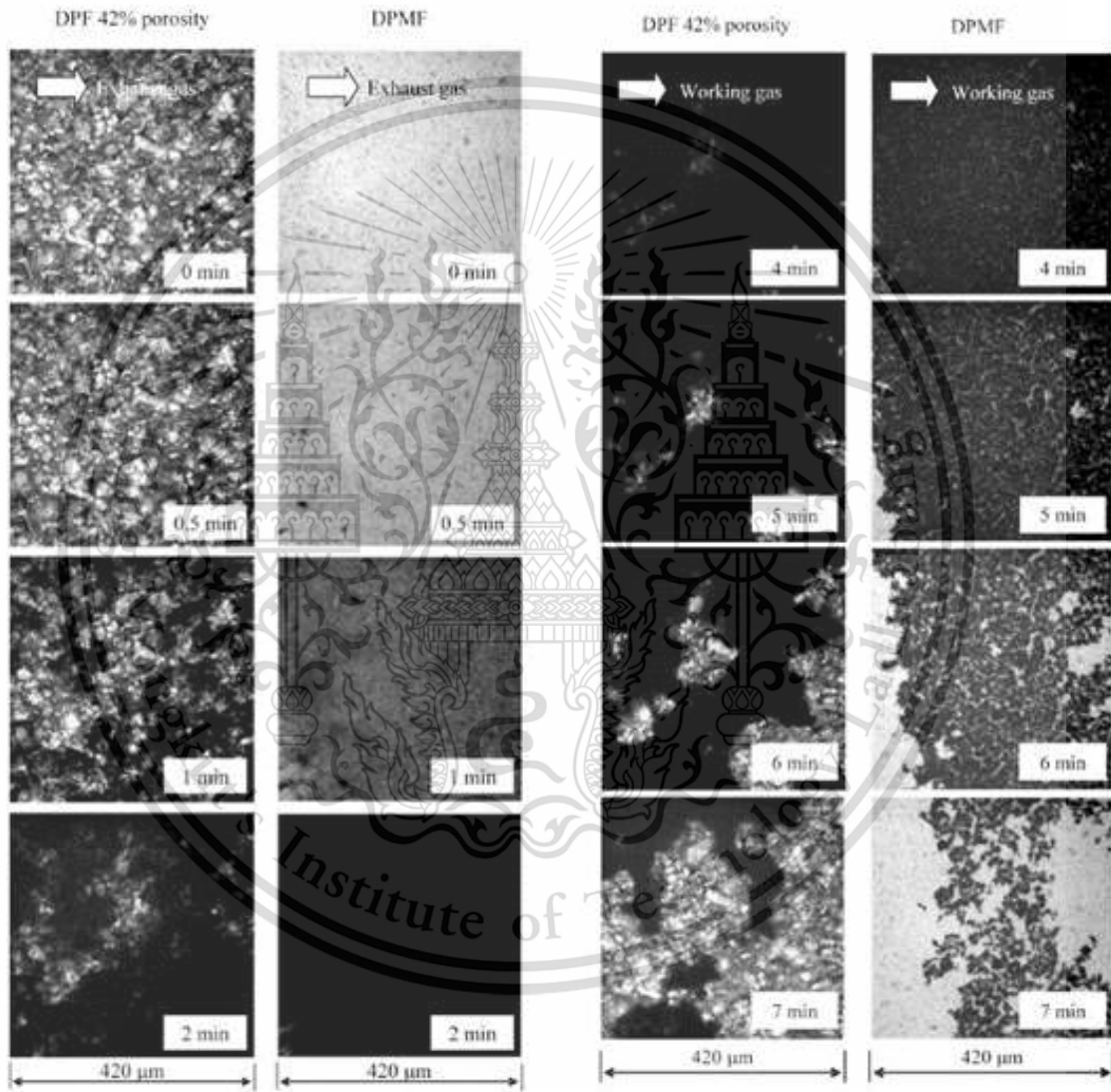


Figure 2.15 Optical surface views of trapping by conventional DPF and DPMF [15]

Recycling of waste fly ash for production of porous mullite ceramic membrane supports [16] this research studied about low-cost porous mullite ceramic membrane support that fabricated from recycling coal fly ash with addition of natural bauxite are AlF_3 and V_2O_5 . Because fly ash is generated during the combustion of raw coal in thermal-

This material is reserved for educational use only, not allowed for commercial use.

Forbidden to modify the content, and cite the document when use.

electric power plants, which cause of serious problem related to environmental pollution. And main components of fly ash are Al_2O_3 and SiO_2 , its quite suitable for fabrication of porous mullite membranes. The results show achieved addition 4% by weight of AlF_3 and 3% by weight of V_2O_5 . It can open porosity about 50% and have mechanical strength around 70 MPA at temperature 1300C that show in Figure 2.16

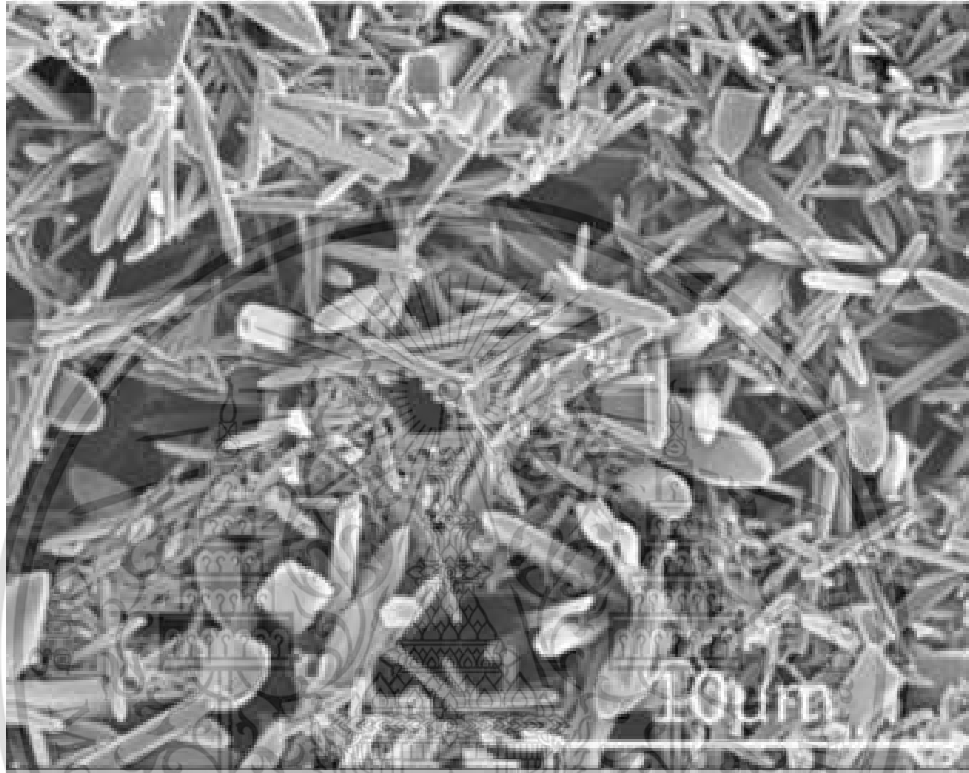


Figure 2.16 Surface SEM image of Mullite [16]

2.8 Diesel Particulate Trapping

Diesel particulate after-treatment technology that helps reduce emissions of diesel engine emissions is a Diesel Particulate Filter (DPF). DPF plays an important role in trapping particles and oxidation. These processes involve complex behavior of particle pollution and reaction phenomena. The engine particle trapping mechanism and the oxidation on the DPF wall surface were analyzed by real-time microscopy

Basic principles for filtering particulate matter movement mechanism is the particles caught and attached to the fibers. The filter material by the four major mechanisms is diffusion, impaction, interception and scalping. As shown in Figure 2.17 and Figure 2.18

This material is reserved for educational use only, not allowed for commercial use.

Forbidden to modify the content, and cite the document when use.

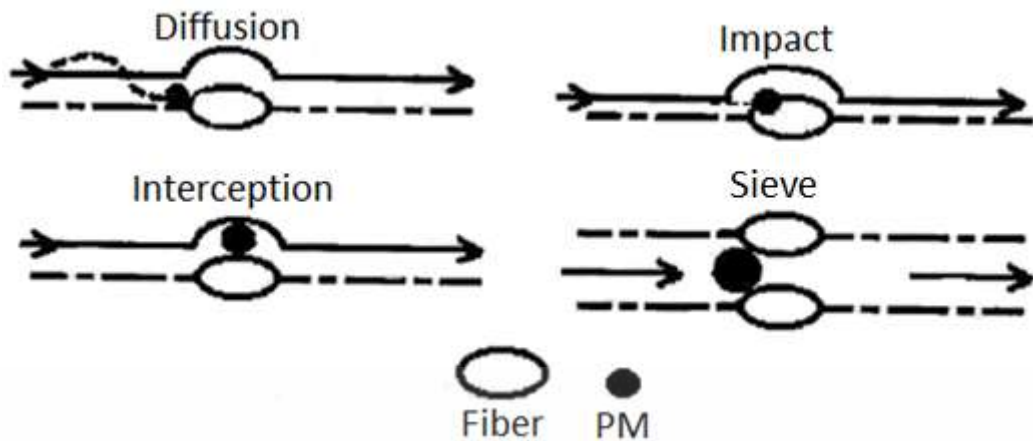


Figure 2.17 Movement mechanism of particle matter [17]

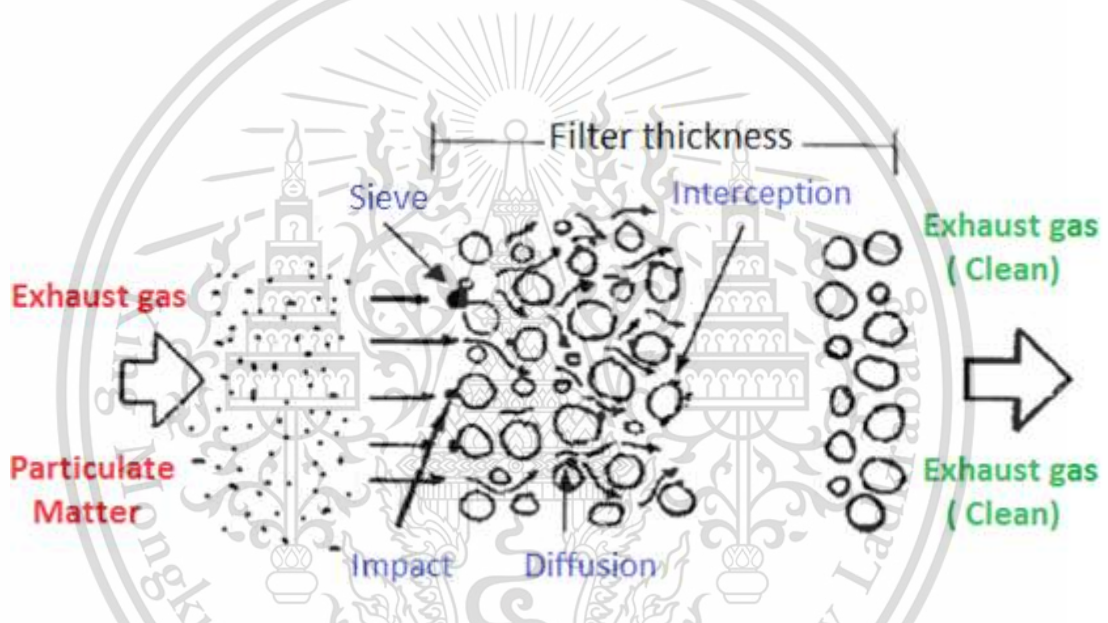


Figure 2.18 PM of exhaust gas caught by various mechanisms [17]

Diffusion

The diffusion of particles is a Brownian movement caused by collisions between particles, causing particles to move in an uncertain direction until colliding with the fibers of the filter. This Brownian movement has an increased rate when the particles are smaller. Therefore, the diffusion mechanism helps to eliminate small particles.

Impaction

The impact occurs when a particle cannot break through an obstacle causing the particles themselves to fall out of the air streamline. Therefore collided and buried with that obstacle because of the momentum of the particle. Most mechanisms occur with particles that are large and have high speeds.

This material is reserved for educational use only, not allowed for commercial use.

Forbidden to modify the content, and cite the document when use.

Interception

Interception is airflow when passing through the filter fibers. The current line of air will flow around the fibers. The Particles mixed with air may flow along the current line or may fall out of the current line adjacent to the fiber. Which depends on the distance between the stream and the fiber, if this distance is equal to the radius of the particle. The particles are attached to the fibers because of the Van Der Waals forces. The Van Der Waals forces is the gravitational attraction between molecules. Moreover, there are will increase when the distance between molecules is less.

Sieve

Sieve occurs when the particle is larger than the sieve hole, which cannot passed through. The speed of this particle can calculated from the distance that the particle penetrates into the sieve hole until the point stops. Because most particles have uneven shapes, therefore there is a conflict in the edge of the sieve. There are causing the hole of the sieve to be smaller, which makes it possible to capture smaller particles.

The factors affecting particulate matter filter trap of diesel engine particles such as particle density, density of filter trap, speed and pressure drop across the gas before entering the filter trap. Moreover, the size and physical characteristics of the filter trap. From previous studied, it was found that the soot particle size small group size nano-scale pollution, which is a very small size compared to the size of the pore on filter surface as shown in Figure 2.19

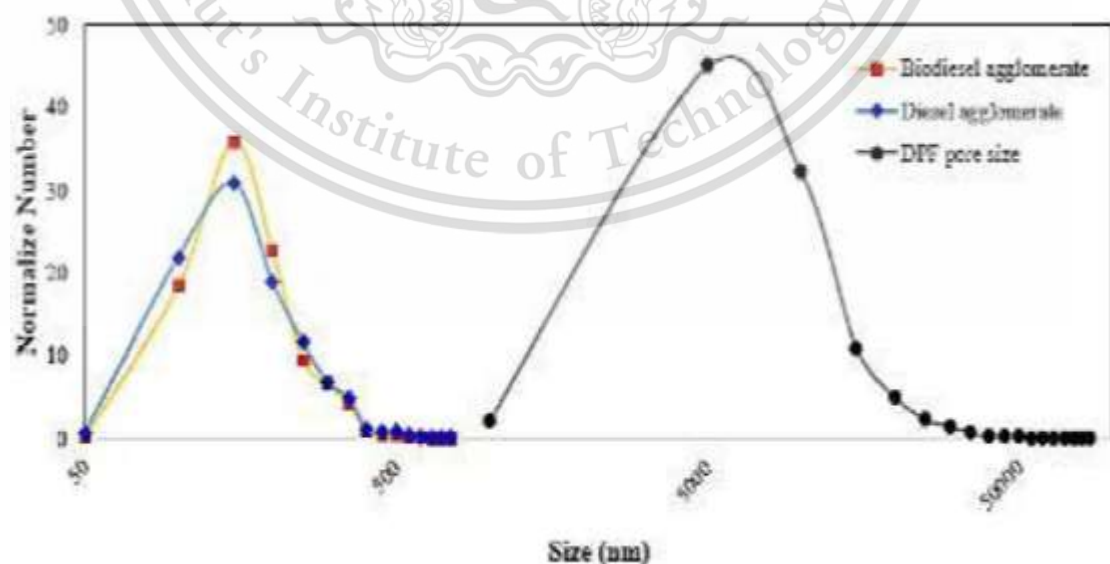


Figure 2.19 The DPF pore diameter compare to particle size [18]

This material is reserved for educational use only, not allowed for commercial use.

Forbidden to modify the content, and cite the document when use.

The particles small size will have a non-directional motion. It's can occur much more than large particles due to the small soot particles will be the molecules of the gas exhaust to cause able move in a more direction compared to the large soot particles. Therefore, the particles small size have large distance (r.m.s. displacement) due to increased particle movement as shown in Figure 2.21

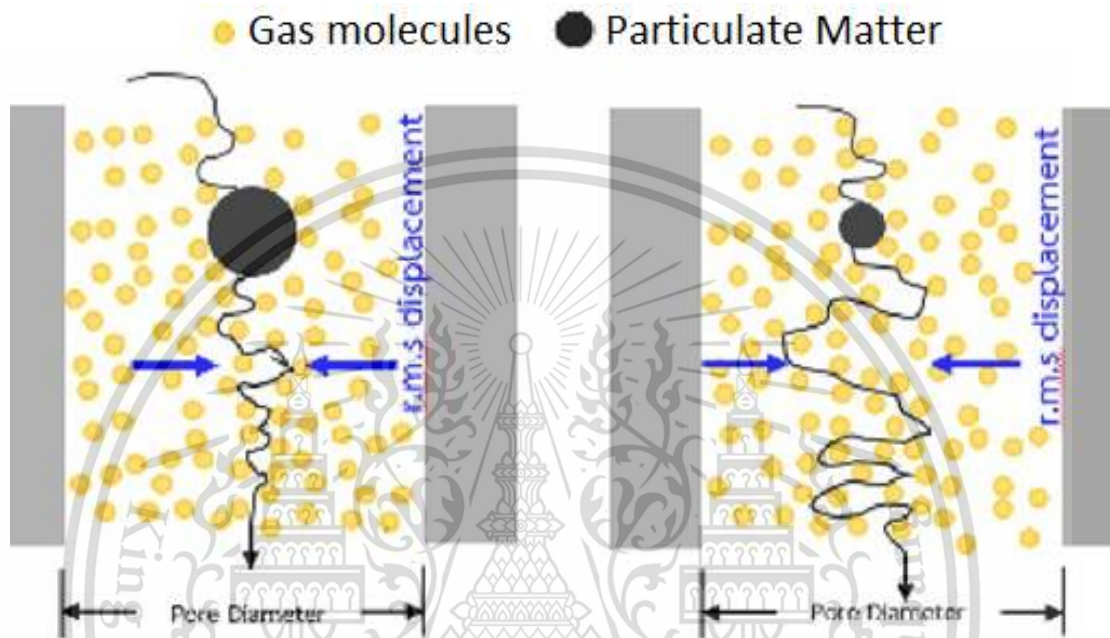


Figure 2.21 Characteristics of the movement of soot particles with different sizes [18]

According to the result of large distance will make the soot particles easier to move into the pore surface. Moreover, may have a chance of being trap if the F_D lower than F_D . Normally, the F_D force is lower than that of the F_C force will occur at the boundary layer of the flow. Causing the resistance to flow at the boundary layer (F_D boundary layer) is lower until the force from the electrostatic is greater and can overcome the flow resistance. Thus causing soot particles can attached to the surface in porous as shown in Figure 2.22



Figure 2.22 Trapping characteristics of PM in DPF filters [18]

Therefore, at the beginning of the process of particulate matter trapping. The large particles may pass through a certain amount of DPF porosity because there is less displacement in movement than small particles. Therefore, it is not easy to move into the surface of the porous surface and can be trapped by force from static electricity. However, in the case of small particles that can be intercepted since small particles have large displacement; there is a greater chance of moving to the surface of the pore and can be trapped by F_c force. However, over time, the large particles will be intercepted as well because the internal pore dimension of DPF is getting smaller and smaller. Which is the result of the small particles being trapped can be captured as shown in Figure 2.23

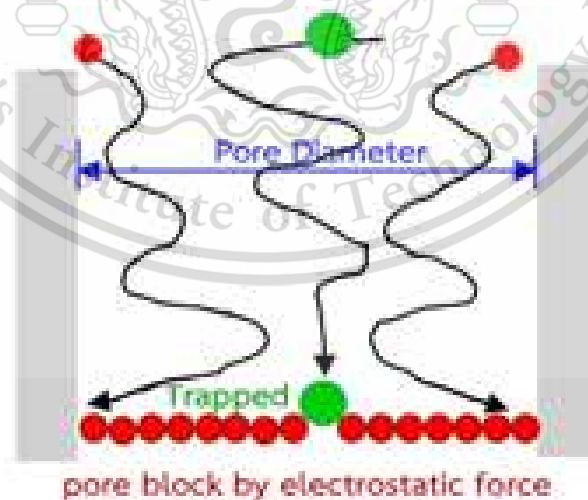


Figure 2.23 Trapping characteristics of PM in DPF filters over time [18]

CHAPTER 3

RESEARCH METHODOLOGY

3.1 Experimental conditions

In the experimental condition, this research implements 5 conditions:

- (1) Mullite (Al_2O_3 mixed with SiO_2)
- (2) Mullite mixed with TiO_2
- (3) Mullite mixed with TiO_2 and AlF_3
- (4) Mullite mixed with TiO_2 and V_2O_5
- (5) Mullite mixed with TiO_2 , AlF_3 and V_2O_5

as shown in Table 3.1 and The mullite sample has been prepared and burned at a constant temperature $1300\text{ }^\circ\text{C}$ and 1hour holding time. The structure of mullite is consists of 72wt.% Aluminum oxide (Al_2O_3) and 28wt.% Silicon dioxide (SiO_2). The Al_2O_3 and SiO_2 are main substances to prepare the chemical structure of mullite. The Titanium dioxide (TiO_2) Aluminium fluoride (AlF_3) and Vanadium oxide (V_2O_5) as additives were used to mix with mullite diesel particulate filter to prepare Acicular Mullite (ACM) structure as an additive, used to analyze porosity and pore size. Including the official features of the filter trap structure. Moreover, the TiO_2 , AlF_3 and V_2O_5 additions were applied at a constant amount of 10wt.%. This are precisely measure and evaluate for each step of mixing substance by digital weight scale. In addition, carbon black (CB) was also applied to mullite diesel particulate filter for open porosity in the same direction at constant amount of 35wt.%.

Samples	Main components	Sub components			Addition
	Mullite ($\text{Al}_2\text{O}_3 + \text{SiO}_2$)	TiO_2	AlF_3	V_2O_5	Carbon black N330
1	100wt.%	-	-	-	35wt.%
2	90wt.%	10wt.%	-	-	35wt.%
3	80wt.%	10wt.%	10wt.%	-	35wt.%
4	80wt.%	10wt.%	-	10wt.%	35wt.%
5	70wt.%	10wt.%	10wt.%	10wt.%	35wt.%

Table 3.1 Mullite conditions

3.2 Materials Fabrication Process

The fabrication process and characterization of the mullite structure have investigated in this research. The schematic diagram of mullite fabrication process is show in Figure 3.1. The mullite substances of TiO_2 , AlF_3 , V_2O_5 and CB are measure to ensure the chemical proportion with weight scale. The substances were ground and mixed all until homogeneous with 5wt.% organic binder PVA-1750 in the manually alumina mortar. The grinding and mixing time were around 10min per each sample. The hydraulic press machine at constant pressure of 500 psi was used to press the mixture into cylindrical pellet with approximately diameter of 25 mm, 2 mm in thickness by following experimental conditions. In this process of pressure substance to pellet, it should beware the sample broken every time because the sample still not have strength for fabricate all substance together and it is easy to crack from external force. Then, the cylindrical pellet is ready to sinter at constant heating rate $5\text{ }^\circ\text{C}/\text{min}$ by an electrically heated furnace. The mullite was kept at a constant temperature of $1300\text{ }^\circ\text{C}$ with holding time of 1 hour. Finally, measurement and record data of mullite sample.

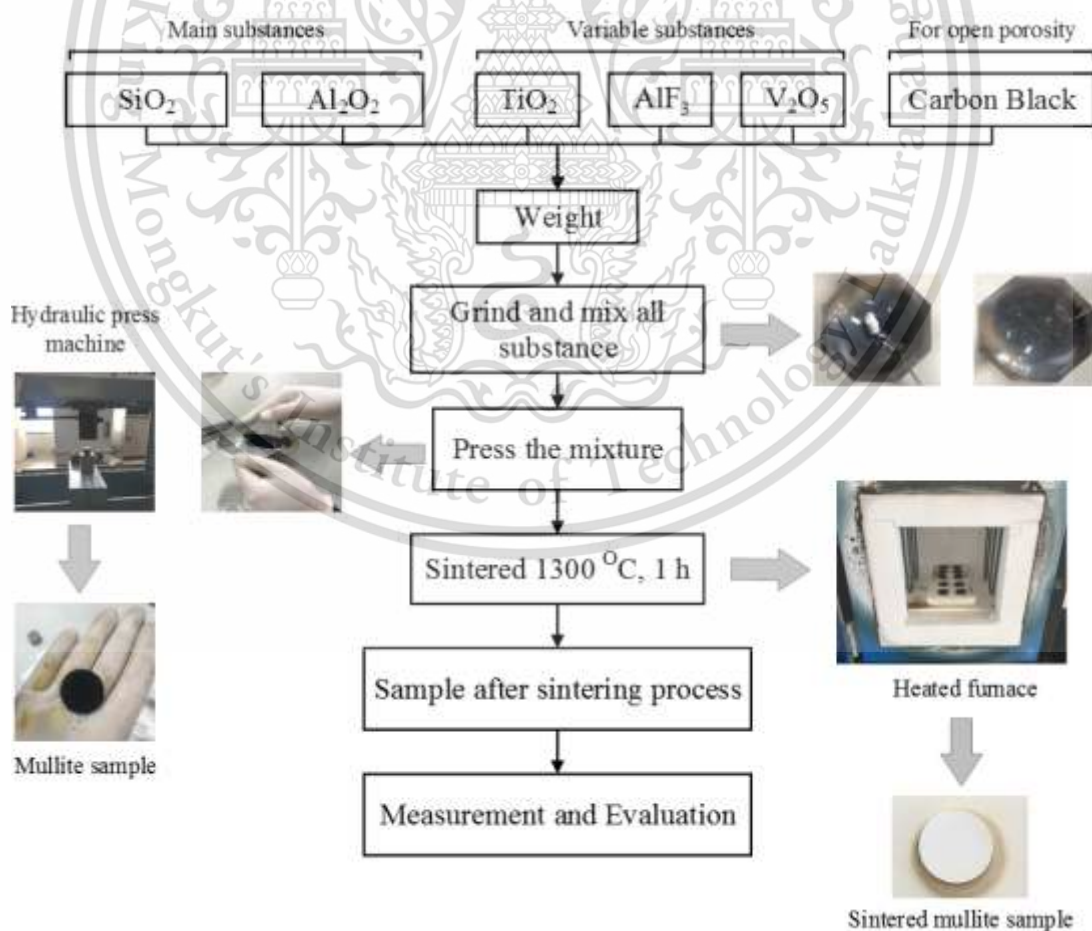


Figure 3.1 Schematic diagram of mullite fabrication process

This material is reserved for educational use only, not allowed for commercial use.

Forbidden to modify the content, and cite the document when use.

For the mullite sample making methodology. Firstly, mixing and grind all the substance together according to the calculated ratio figure 3.2a. Then, filled 5wt.% organic binder PVA-1750 for better combination and grind it all again until homogeneous as figure 3.2b. In this process use time around 10min per each sample. Then, move the mixing substance to the cylindrical tooling that for press substance to pellet figure 3.2c. The cylindrical tool can make pellet with approximately diameter of 25 mm, 2 mm in thickness by following experimental conditions.



Figure 3.2a Grind and mix all substance



Figure 3.2b Filling binder PVA-1750



Figure 3.2c Move the mixture to the cylinder tool

Secondly, the figure 3.2d show the cylindrical tool that have all mixing substance inside and pressing machine. The pressure force was setting at 500psi because if use higher force the sample might be crack after sintering. It to pellet by use this tooling for control

This material is reserved for educational use only, not allowed for commercial use.

Forbidden to modify the content, and cite the document when use.

shape and put it on pressing machine. Finally, after pressed by machine take sample out from tooling as figure 3.2e. The final sample have diameter of 25 mm, 1.9-2.0 mm in thickness as show in figure 3.2f

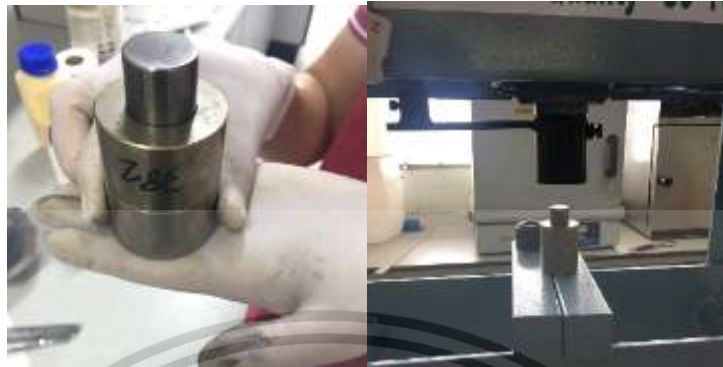


Figure 3.2d Cylinder tool and press machine



Figure 3.2e Take mullite sample out from cylinder tool

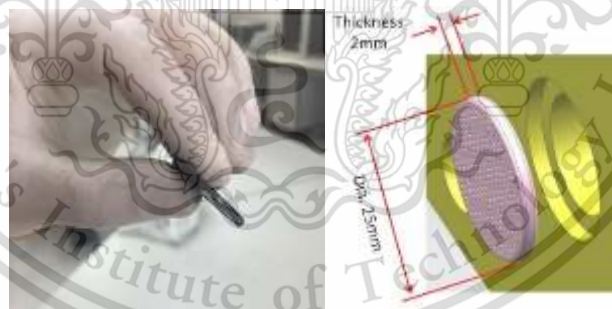


Figure 3.2f Mullite sample diameter 25mm thickness 2mm

Figure 3.3a show the mullite sample before sintering. All mullite sample are shown in black color because there are consisting of carbon black 35wt.%. However, after sintering the color of the sample has changed because the carbon powder was burned out if sintering temperature more than 1000°C. The colors of mullite sample number 1 are 100% pure mullite changed to white. The mullite sample number 2 are mullite consisting of TiO_2 and sample number 3 are mullite consisting of TiO_2 , AlF_3 changed to light brown color. However, the colors of sample number 4 and 5 are change to dark gray. There are might be effected from filling V_2O_5 as show in figure 3.3b

This material is reserved for educational use only, not allowed for commercial use.

Forbidden to modify the content, and cite the document when use.

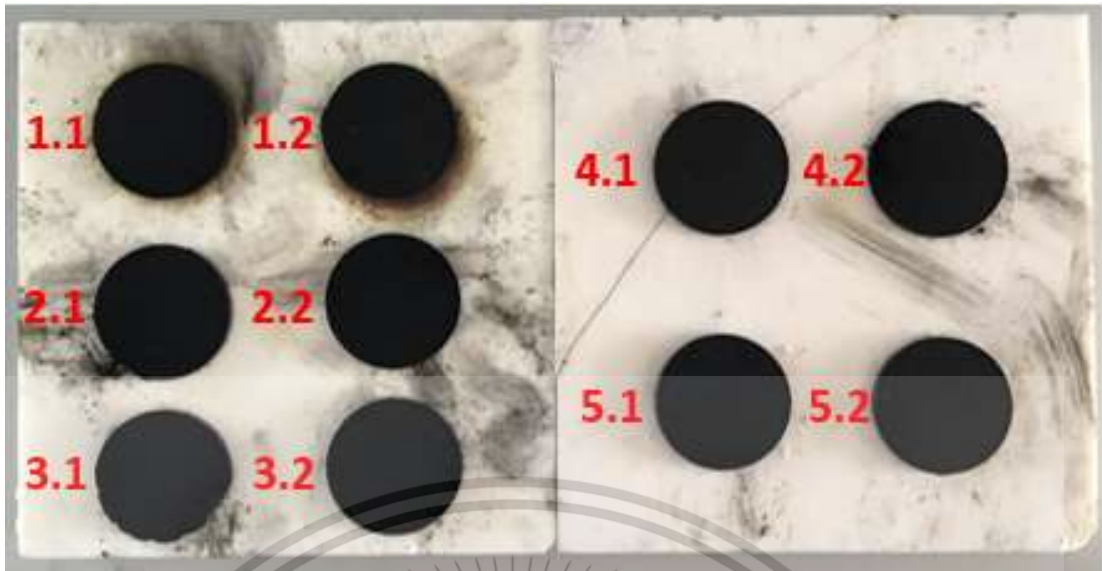


Figure 3.3a Mullite samples

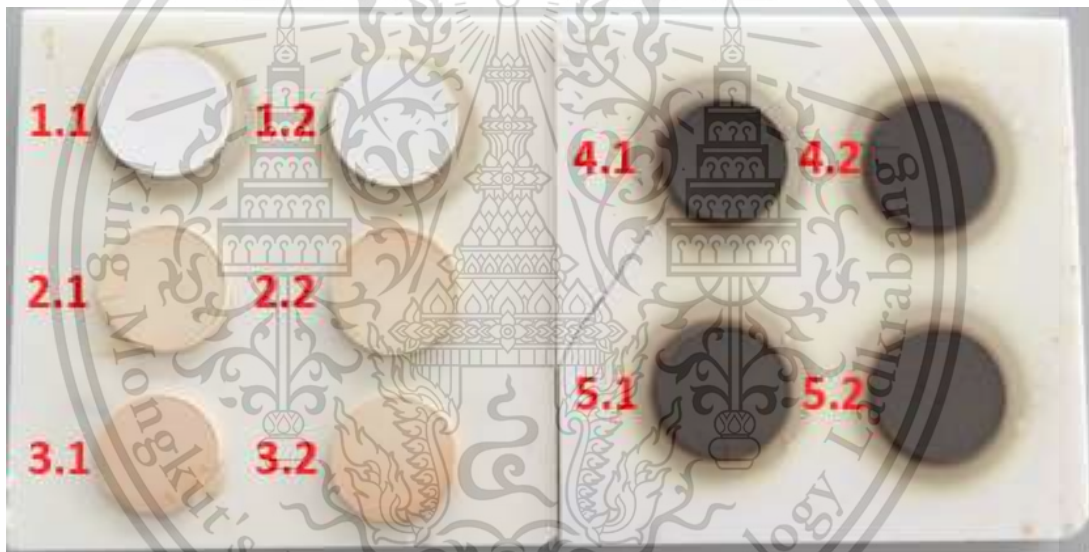


Figure 3.3b Sintered mullite samples

Table 3.1 show the sintering condition at temperature 1300 °C with holding time 1 hour. The sintering condition used rate of temperature at 5 °C/mins. Figure 3.4 show furnace machine that used to sinter the sample of mullite. Firstly, started from room temperature until 200 °C with holding time 34mins. Then, continue increasing of temperature to 500 °C with holding time 1hour. The mullite was kept at a constant temperature of 500 °C with holding time of 2 hour to eliminate the organic binder PVA-1750. Then, increasing temperature again to 1300 °C with holding time 1hour and kept at a constant temperature of 1300 °C with holding time of 1 hours. Finally, decreasing temperature from 1300 °C to 50 °C with holding time 4hours and 10mins.

This material is reserved for educational use only, not allowed for commercial use.

Forbidden to modify the content, and cite the document when use.

Sintering condition

Rate 5°C/mins

Step up

Room-200°C = 34mins

200-500°C = 1hour

Hold 500°C = 2hours

500-1300°C = 2hours

Hold 1300°C = 1hour

Step down

1300-50°C = 4hr10mins

Table 3.2 Sintering condition



Figure 3.4 Furnace machine

This material is reserved for educational use only, not allowed for commercial use.

Forbidden to modify the content, and cite the document when use.

3.3 Scanning Electron Microscopy Image Analysis

The Scanning Electron Microscopy (SEM, JSM-6400 model) is tungsten filament source, 3.5 nm resolution at 30 kV, magnification of 10-30000, SE and BE detector as figure 3.5, was used to observe the mullite and acicular mullite structure. The scanning electron microscope (SEM) uses a focused beam of high-energy electrons to generate a variety of signals at the surface of solid specimens. The signals that derive from electron-sample interactions reveal information about the sample including external morphology (texture), chemical composition, and crystalline structure and orientation of materials making up the sample as figure 3.6. In most applications, data are collected over a selected area of the surface of the sample, and a 2-dimensional image is generated that displays spatial variations in these properties. Areas ranging from approximately 1 cm to 5 microns in width can be imaged in a scanning mode using conventional SEM techniques.



Figure 3.5 Scanning electron microscopy

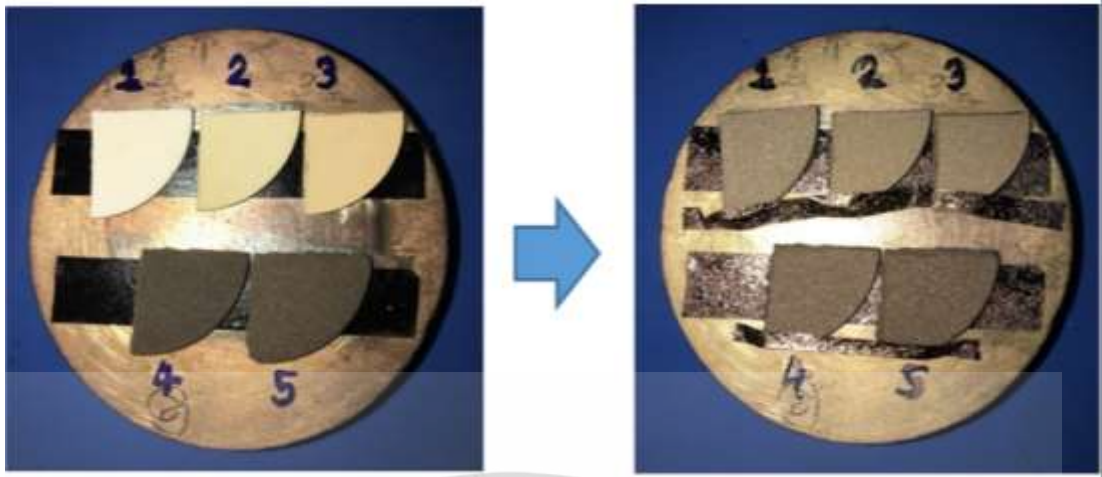


Figure 3.6 The sample for SEM preparation and gold coating

The main SEM components include: Source of electrons, Column down which electrons travel with electromagnetic lenses, Electron detector, Sample chamber and Computer and display to view the images as shown in Fig. 3.6. Electrons are produced at the top of the column accelerated down and passed through a combination of lenses and apertures to produce a focused beam of electrons, which hits the surface of the sample. The sample is mounted on a stage in the chamber area and, unless the microscope is designed to operate at low vacuums, both the column and the chamber are evacuated by a combination of pumps. The level of the vacuum will depend on the design of the microscope. Scan coils situated above the objective lens control the position of the electron beam on the sample. These coils allow the beam to be scanned over the surface of the sample. This beam scanning, as the name of the microscope suggests, enables information about a defined area on the sample to be collected. Because of the electron-sample interaction, a number of signals are produced. Then, appropriate detectors detect these signals.

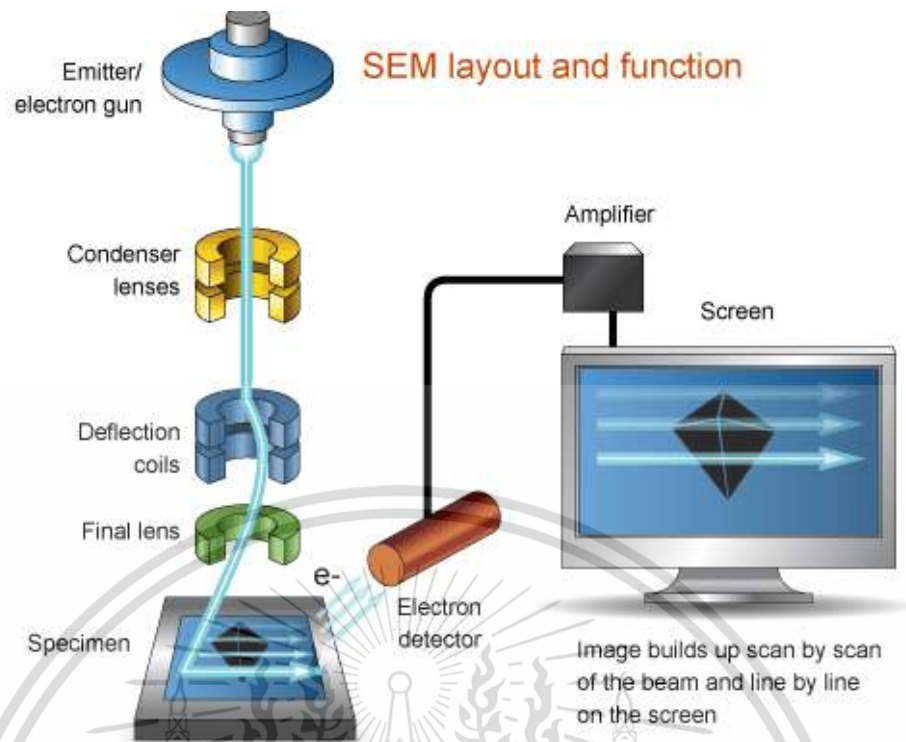


Figure 3.7 Schematics of scanning electron microscopy operation

Figure 3.8a show SEM images (1260 x 870 pixels, 300X) of mullite that used to analyze experimental data by image processing analysis using the Image J processing program. This SEM images shows the raw image of sintered mullite surface. The analytical image was used to measure quantitative data of the porosity and pore size distribution. The threshold of image is defined and setup 20-30% of background. The determination of porosity was evaluated as same as the determination of particle number by using SEM. In this paper, each point of black color is used to fine pore size as illustrated in Fig 3.8b.

The analytical data were presented in the term of morphologies of SEM images, porosity and pore size distribution. The porosity percentage is percentage of the black volume to total volume ratio based on Archimedes' principle of water substitution. In addition, using SEM applied the energy dispersive X-ray analyzer (EDX) technique to study and characterize the chemical composition of the mullite after sintered.

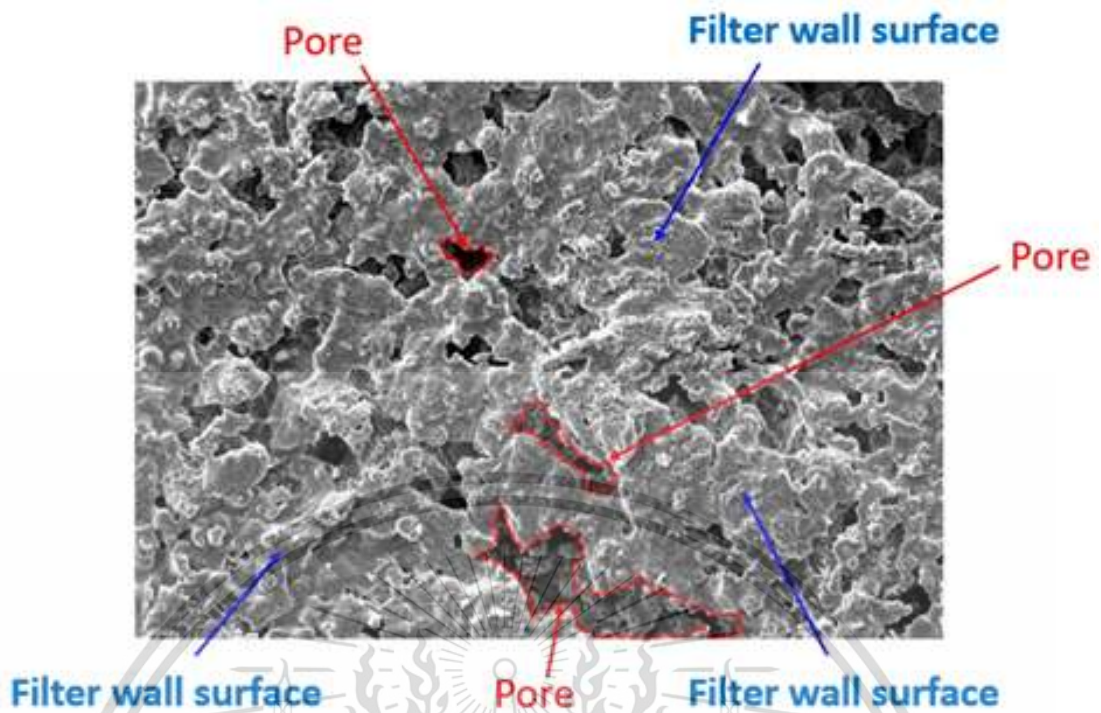


Figure 3.8a Raw SEM images

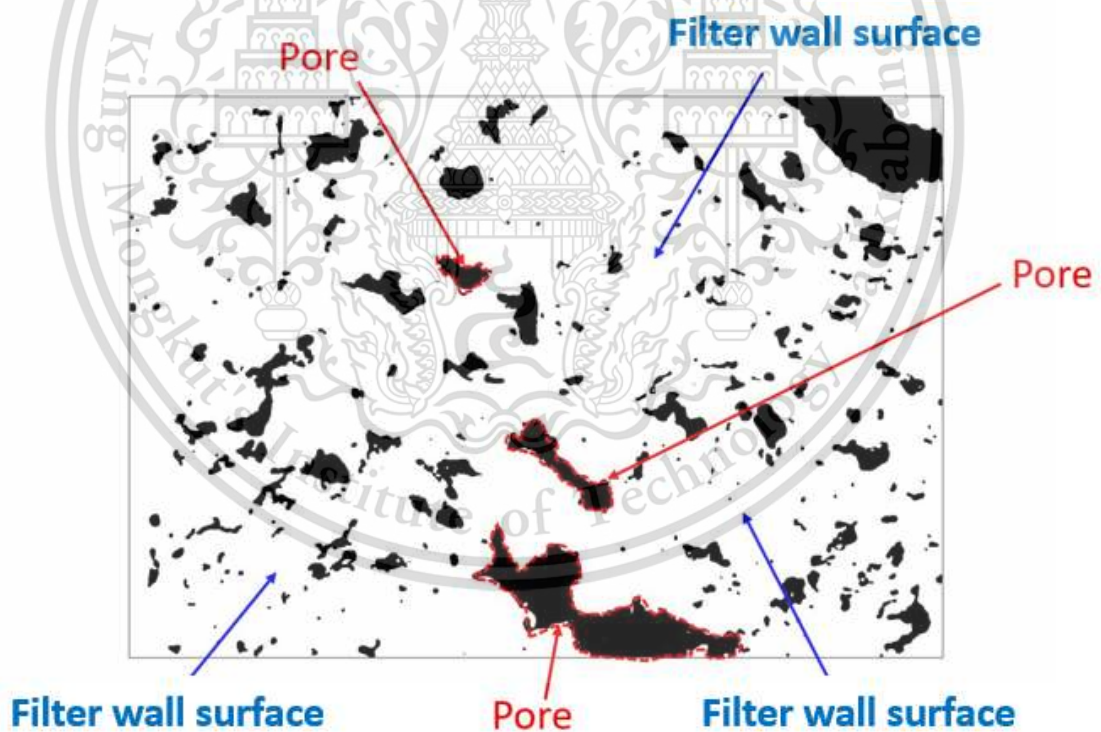


Figure 3.8b Two-color images

3.4 Thermogravimetric analysis

Thermogravimetric Analysis or Thermal Gravimetric Analysis (TGA) is a type of testing that is performed on samples to determine changes in weight in relation to change in temperature. Such analysis relies on a high degree of precision in three measurements: weight, temperature, and temperature change. As many weight loss curves look similar, the weight loss curve may require transformation before results may be interpreted. Derivative of weight loss curve can be used to tell the point at which weight loss is most apparent. Again, interpretation is limited without further modifications and deconvolution of the overlapping peaks may be required. Typically, TGA analysis has 2 types; Isothermal TGA and Non Isothermal TGA. Isothermal TGA works at constant temperature and weight loss is recorded with time, meanwhile Non-isothermal TGA performs on continuous increasing temperature with time. In addition, weight change is recorded. Simultaneous TGA-DTA/DSC measures both heat flow and weight changes (TGA) in a material as a function of temperature or time in a controlled atmosphere. Simultaneous measurement of these two material properties not only improves productivity but also simplifies interpretation of the results. The complementary information obtained allows differentiation between endothermic and exothermic events, which have no associated weight loss and those, which involve a weight loss (e.g. degradation). Figure 3.9 shows schematics of Thermogravimetric Analysis operation.

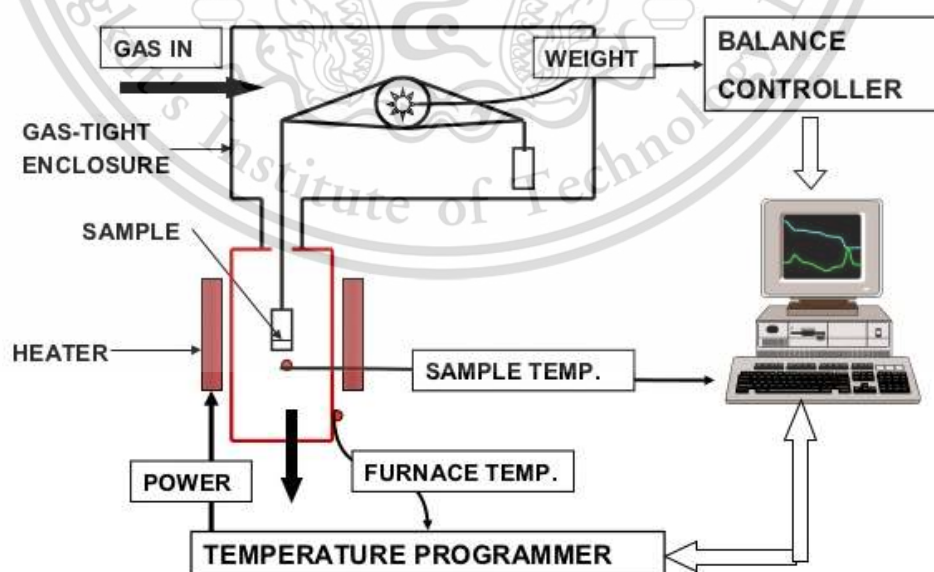


Figure 3.9 Schematics of thermogravimetric analysis operation

The oxidation kinetics behavior of soot was investigated by using TGA method. In this research, soot is assumed to be the 50wt.% of each sintered mullite powder mixed with 50wt.% Carbon black (N-330) as show in figure 3.10.

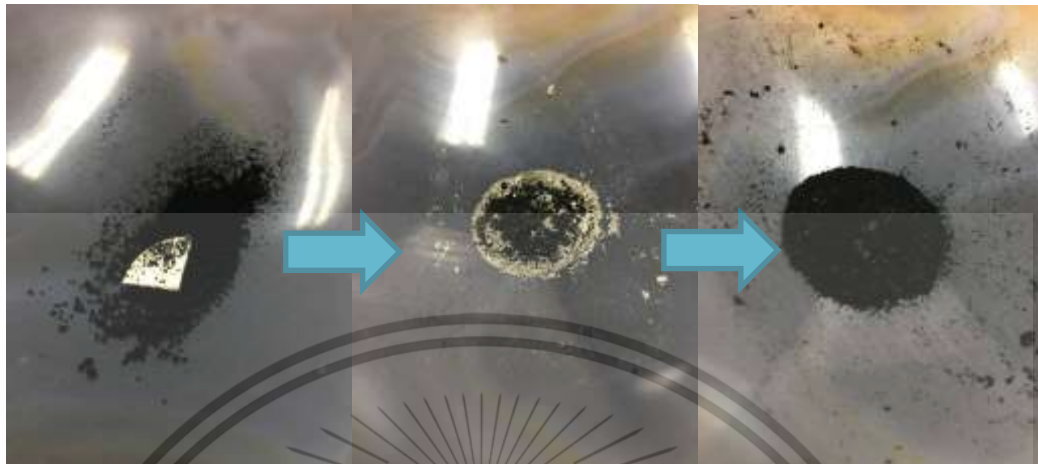


Figure 3.10a Mullite mixed with 50wt.% Carbon black



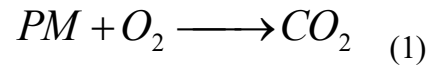
Figure 3.10b Mullite sample for TGA

The oxidation kinetics of Carbon black was studied based on the soot oxidation kinetics as shown in Karin et al. work [3], [5]. Chemical kinetics of Carbon black on mullite and acicular mullite are studied by using mass conversion behavior. The chemical reaction rate can be calculated from the result of mass conversion curve from TGA analysis, as shown in Eq. (1). Mass conversion can be based on the chemical kinetics, as expressed in Eq. (2). Where PM is mass of samples: (1) 50wt.% CB and 50wt.% ML

This material is reserved for educational use only, not allowed for commercial use.

Forbidden to modify the content, and cite the document when use.

and (2) 50wt.% Carbon black and 50wt.% acicular mullite mixture, t is time, n and m are the reaction order of soot and oxygen, respectively.



$$-\frac{d[PM]}{dt} = k[C]^n[O_2]^m \quad (2)$$

3.5 Archimedes method for porosity

The porosity of porous materials can be measured using the Archimedes buoyancy technique with dry weights as show in figure 3.11a, saturated weights as show in figure 3.11b and immersed weights in water as show in figure 3.11c

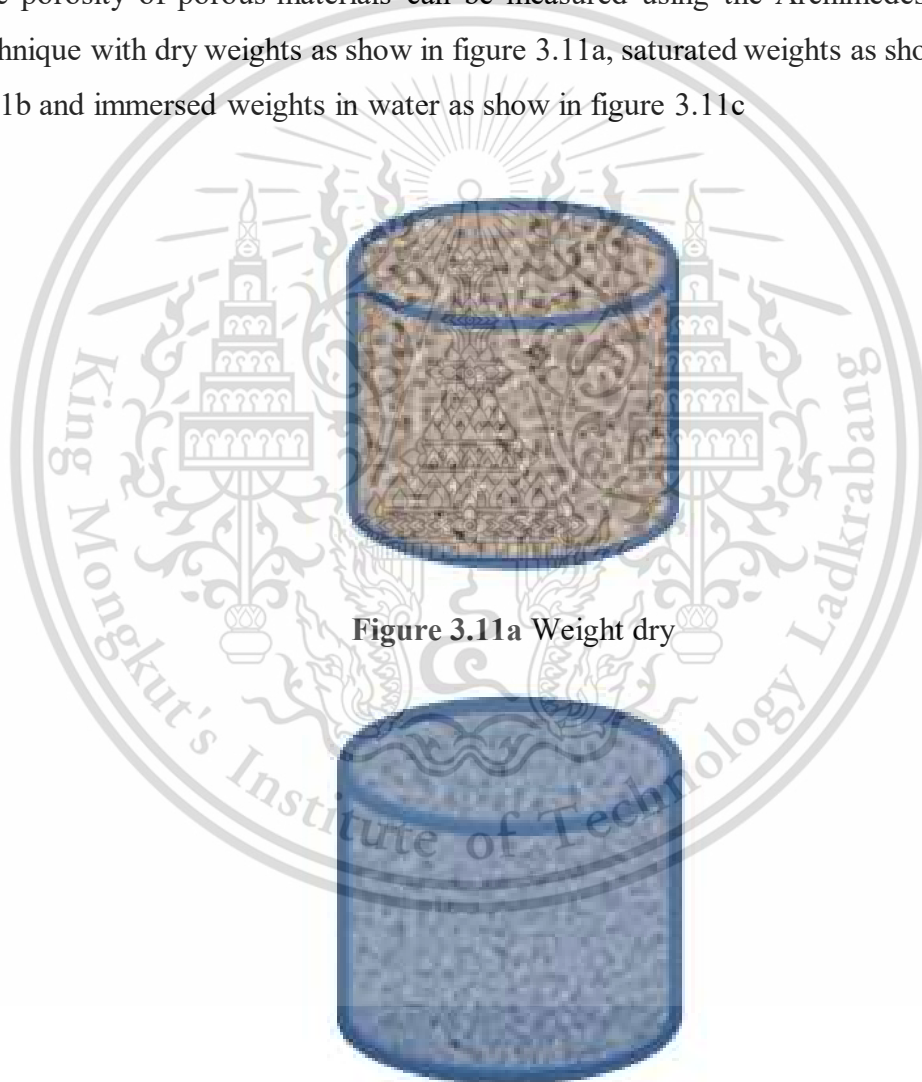


Figure 3.11a Weight dry



Figure 3.11b Weight saturated

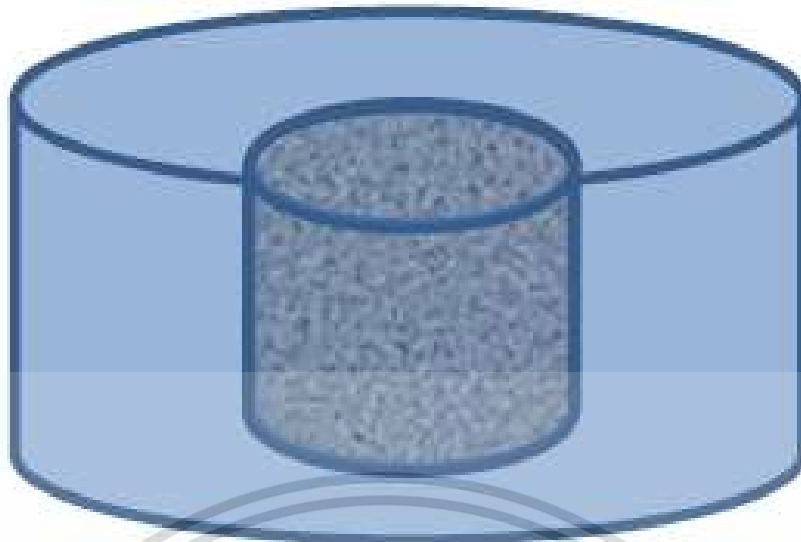


Figure 3.11c Weight immersed

Figure 3.12 shown the mullite sample weight. Then the porosity can be calculated from different weights as use below equation.

Weight of water in pore space

$$W_{\text{wtr}} = W_{\text{sat}} - W_{\text{dry}}$$

Pore volume

$$V_p = W_{\text{wtr}} / \rho_{\text{wtr}}$$

Bulk volume (from previous example)

$$V_b = \pi r^2 h$$

Porosity

$$\Phi = V_p / V_b$$



Figure 3.12a The sample weight dry



Figure 3.12b The sample weight immersed

This material is reserved for educational use only, not allowed for commercial use.
Forbidden to modify the content, and cite the document when use.

3.6 Permeability equipment

This test method covers the measurement of the air permeability--the rate of airflow passing perpendicularly through a known area under a prescribed air pressure differential between the surfaces of a material. It was expressed in liters/min. Air permeability is an important factor in the performance of such textile materials as gas filter, fabrics for air bags, clothing, mosquito netting, parachutes, sails, tentage, and vaccum cleaners. It can also be used to provide an indication of the breathability of weather-resistant and rainproof fabrics. In this research used permeability equipment to evaluated difference pressure of mullite in each case (mullite and acicular).

Figure 3.13 shown the Permeability equipment needed:

- 1) Air tank
- 2) Flow switch to use control air flow rate
- 3) Difference pressure sensor
- 4) Monitoring, Its show data of difference pressure in every second
- 5) Airflow pipe
- 6) Relief valve

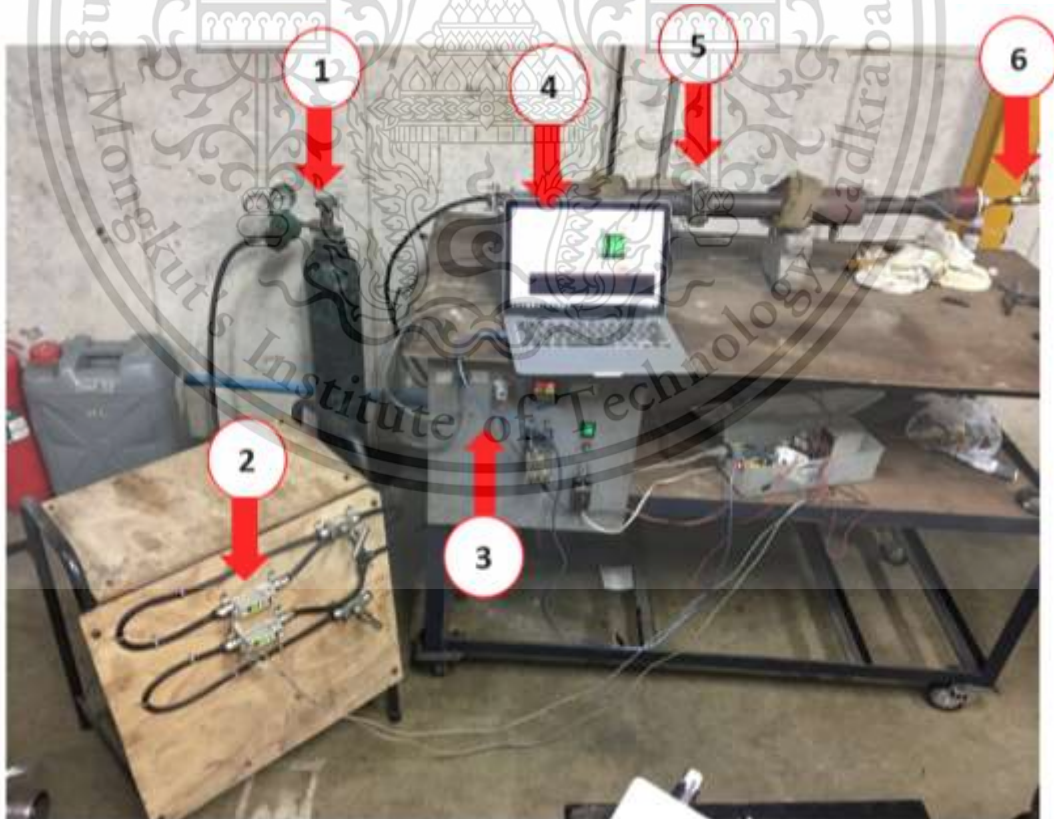


Figure 3.13 Permeability equipment

This material is reserved for educational use only, not allowed for commercial use.

Forbidden to modify the content, and cite the document when use.

How the Test Works:

A circle of mullite sample is clamped into the middle of pipe between coupling as shown in figure 3.14 and through use of a relief valve; the air pressure is made different on one side of the mullite sample. Airflow will occur from the side with higher air pressure, through the mullite sample, to the side with the lower air pressure. From this rate of airflow, the air permeability of the mullite sample is determined in term of difference pressure as show in diagram figure 3.15.

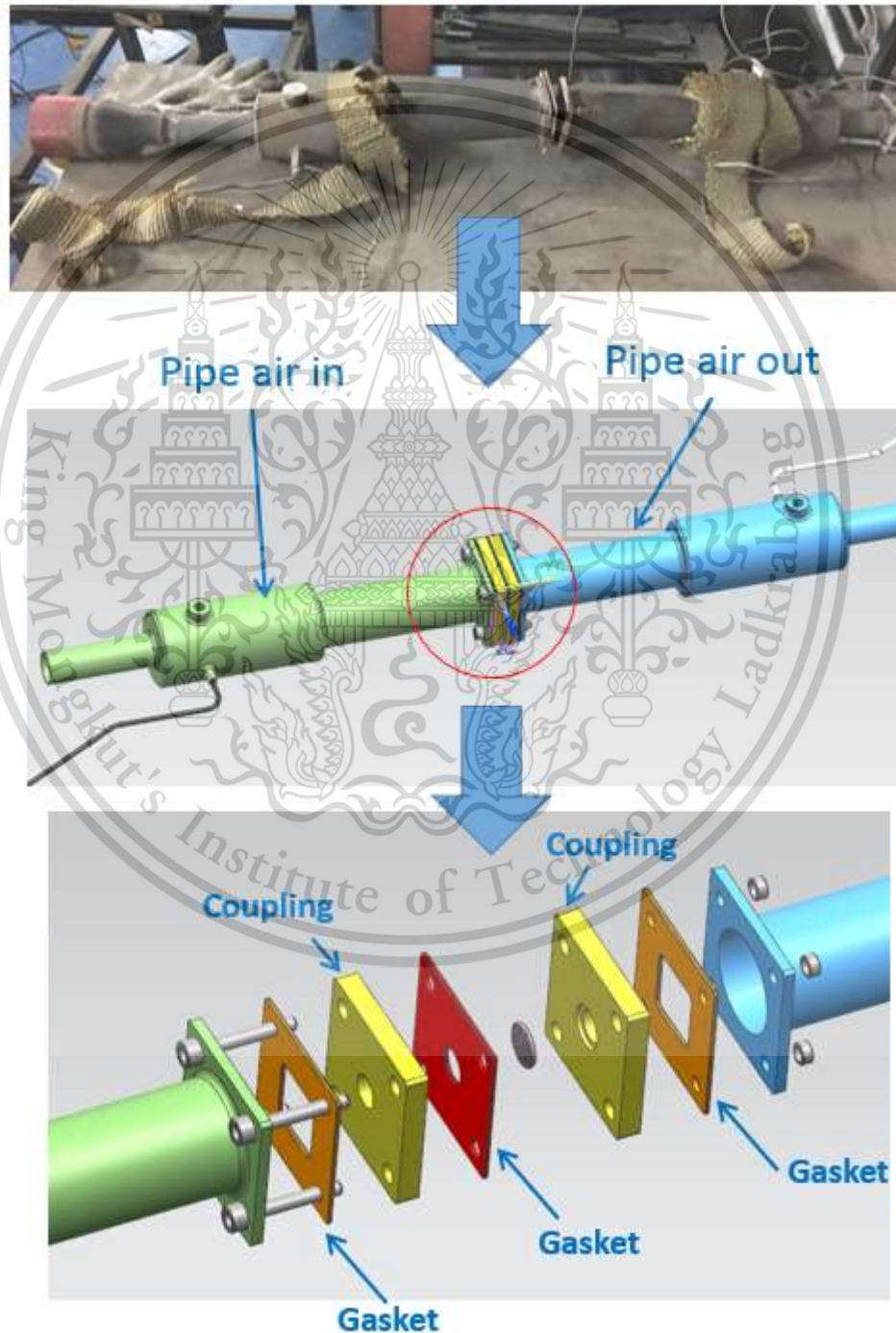


Figure 3.14 Airflow pipe

This material is reserved for educational use only, not allowed for commercial use. Forbidden to modify the content, and cite the document when use.

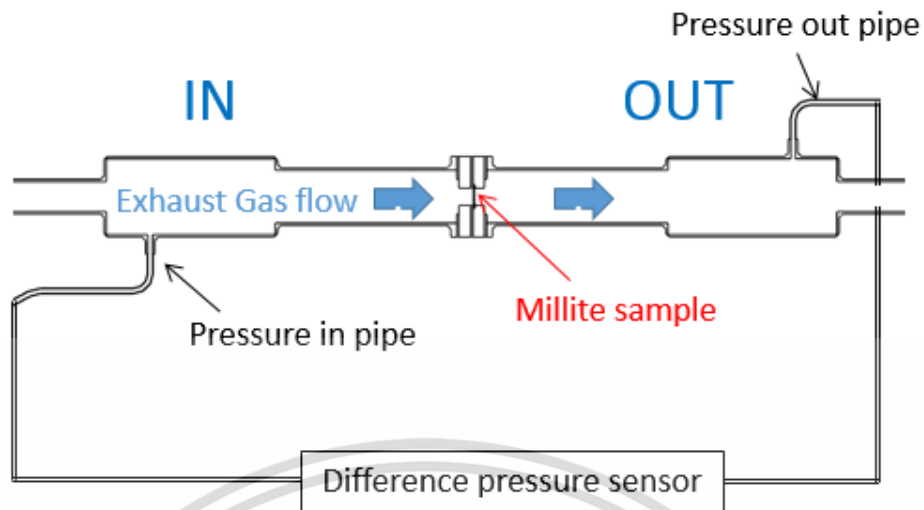


Figure 3.15 Difference pressure diagram

For the pipe, it have to made new design for coupling and gasket to match with the mullite sample. Because cylindrical pellet of the mullite sample have approximately diameter of 25 mm, 2 mm in thickness.

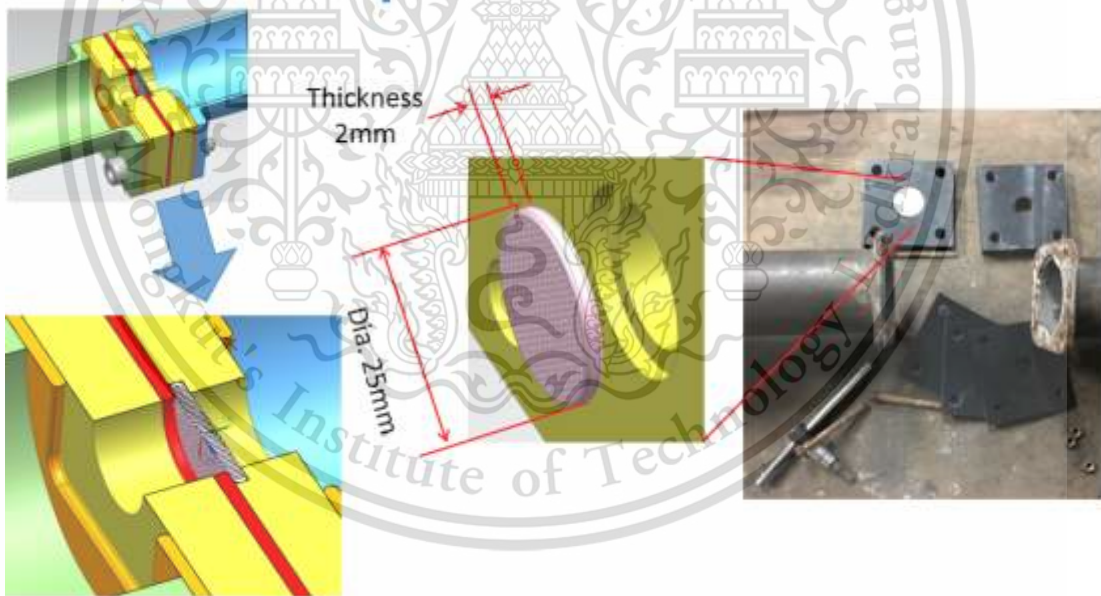


Figure 3.16 New coupling design

CHAPTER 4

RESULTS AND DISCUSSIONS

4.1 Morphologies of Fabricated Porous Mullite

Figure 4.1 show the morphologies of SEM images of the sintered mullite samples. e.g., TiO_2 (10wt.%), AlF_3 (10wt.%) and V_2O_5 (10wt.%) at constant sintering temperature and holding time. The figure shows SEM images with 300X magnification. The mullite sample (1), (2) and (3) are look similar in morphologies and pore size as show in figure 4.1a, 4.1b and 4.1c. There have uniform pore structure same as conventional DPF made by SiC. For the mullite sample (4) and (5) have non-uniform pore structure look like conventional DPF made by cordierite as show in figure 4.1d and 4.1e. Moreover, sample (4) and (5) have pore size larger than sample (1), (2) and (3) because it could be effected from addition V_2O_5

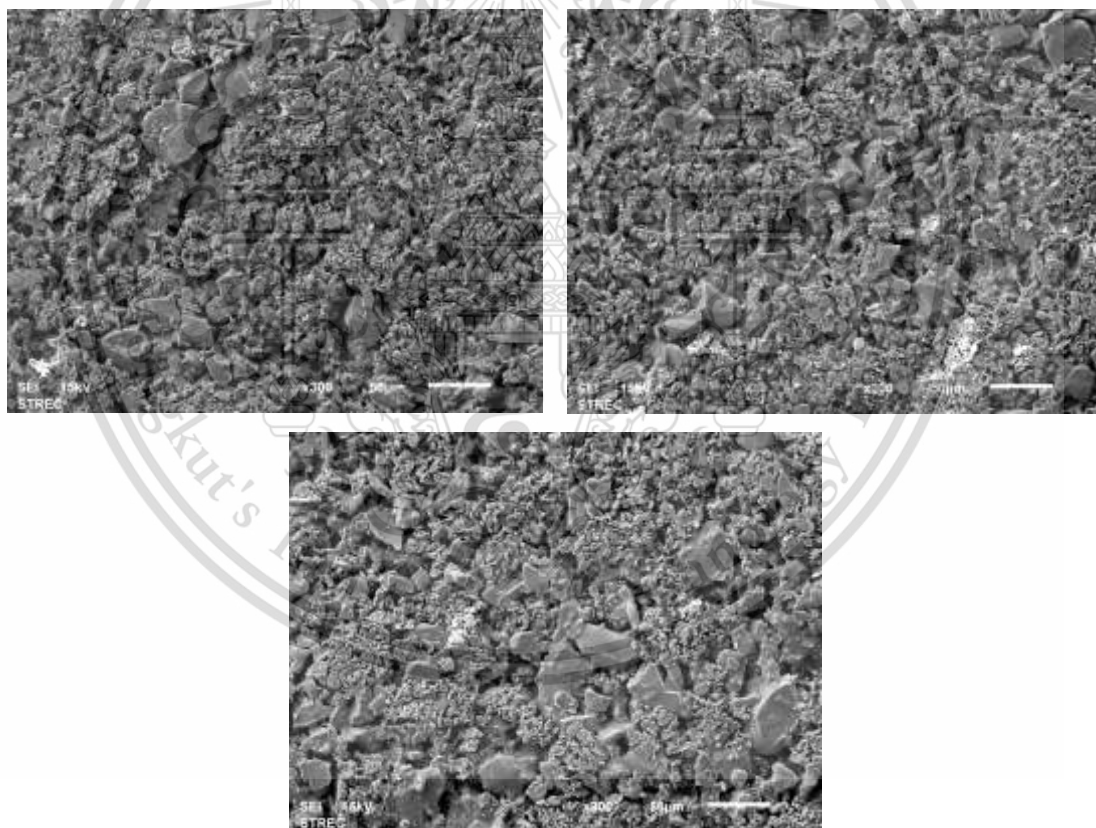


Figure 4.1a SEM images 300X of sintered Mullite

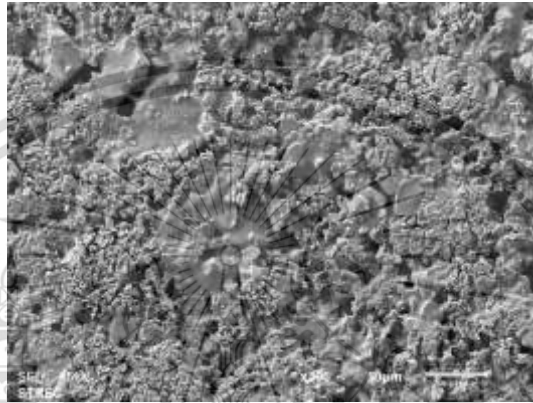
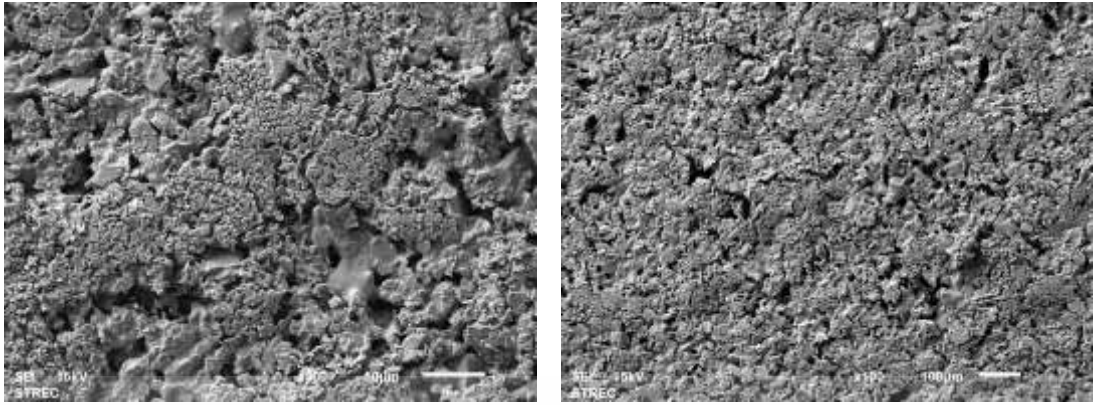


Figure 4.1b SEM images 300X of sintered Mullite + TiO₂

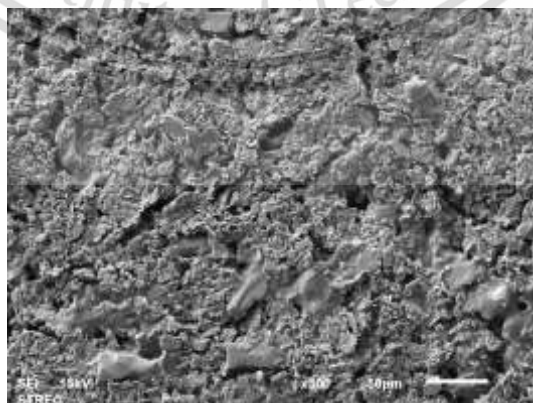
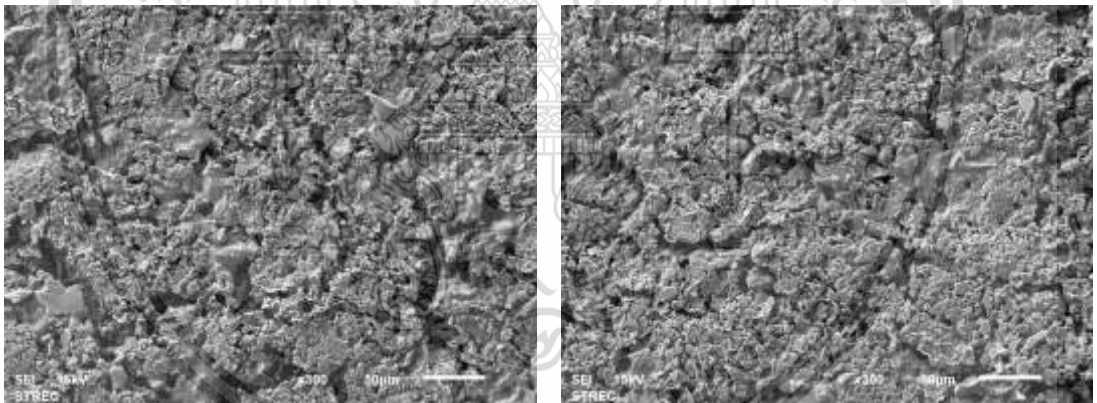


Figure 4.1c SEM images 300X of sintered Mullite + TiO₂ + AlF₃

This material is reserved for educational use only, not allowed for commercial use.
Forbidden to modify the content, and cite the document when use.

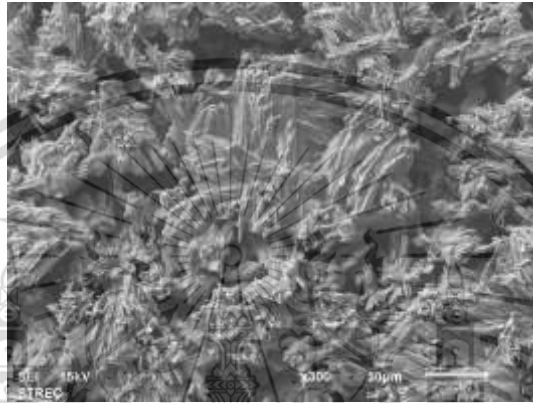
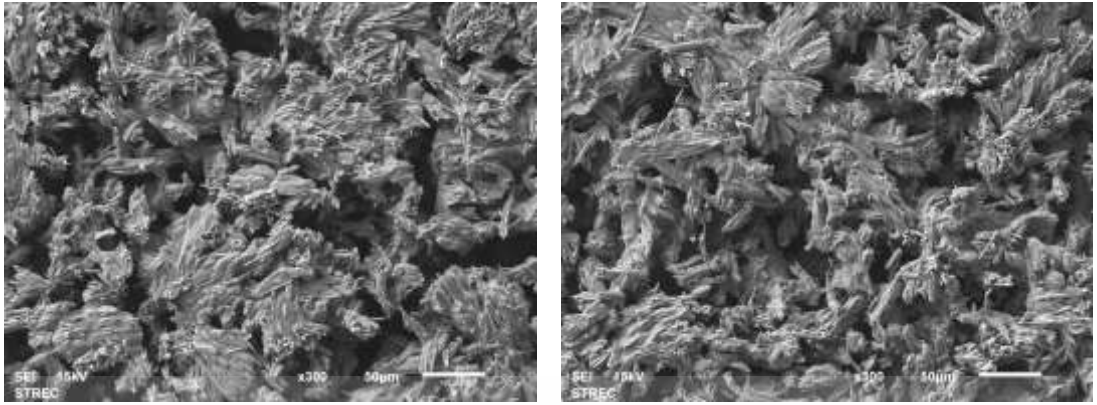


Figure 4.1d SEM images 300X of sintered Mullite + TiO₂ + V₂O₅

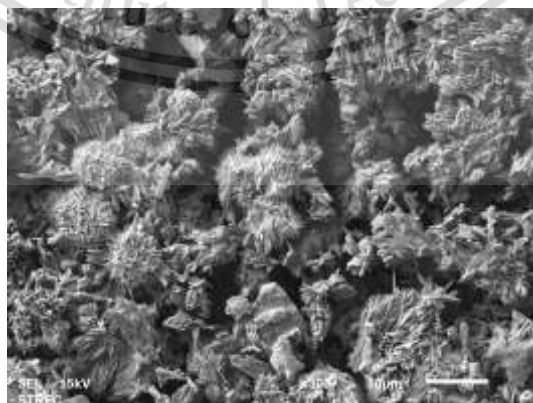
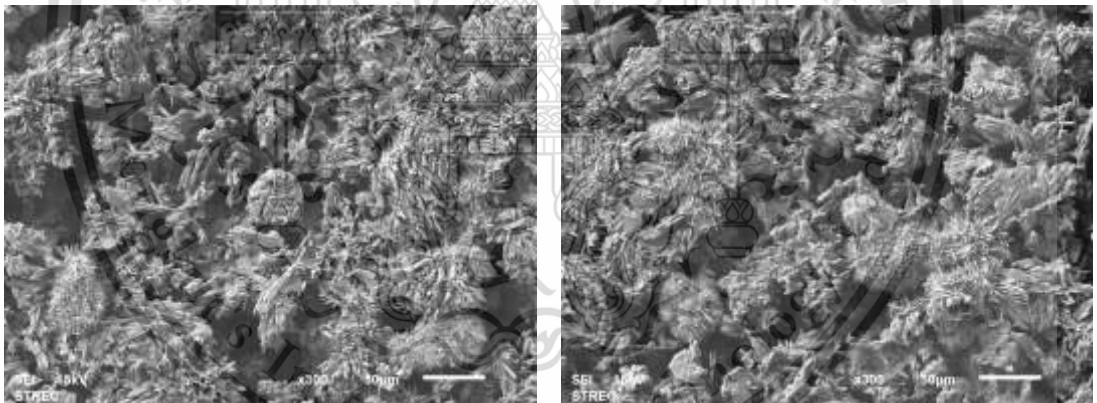


Figure 4.1e SEM images 300X of sintered Mullite + TiO₂ + AlF₃ + V₂O₅

Figure 4.2 show effects of TiO_2 10wt.% AlF_3 10wt.% and V_2O_5 10wt.% contents on morphologies of mullite DPFs with 35wt.% CB at 1300 °C and holding time of 1 h. The left figure shows SEM images with 1000X magnification. The right figure shows 3000X magnification. The mullite DPFs with TiO_2 and AlF_3 content resulted in more rough surface structures as figure 4.2b, 4.2c than pure 100% mullite as figure 4.2a. However, the morphologies structure of the sample (1), (2) and (3) looks like a small and large circle plate combined. In case of sample, (4) and (5) the results showed that the mullite DPFs with V_2O_5 10wt% added clearly observed acicular mullite structure, there are found very small pin shape on the mullite surface as figure 4.2d. In addition for sample (5) have width less than 1micron as figure 4.2e.

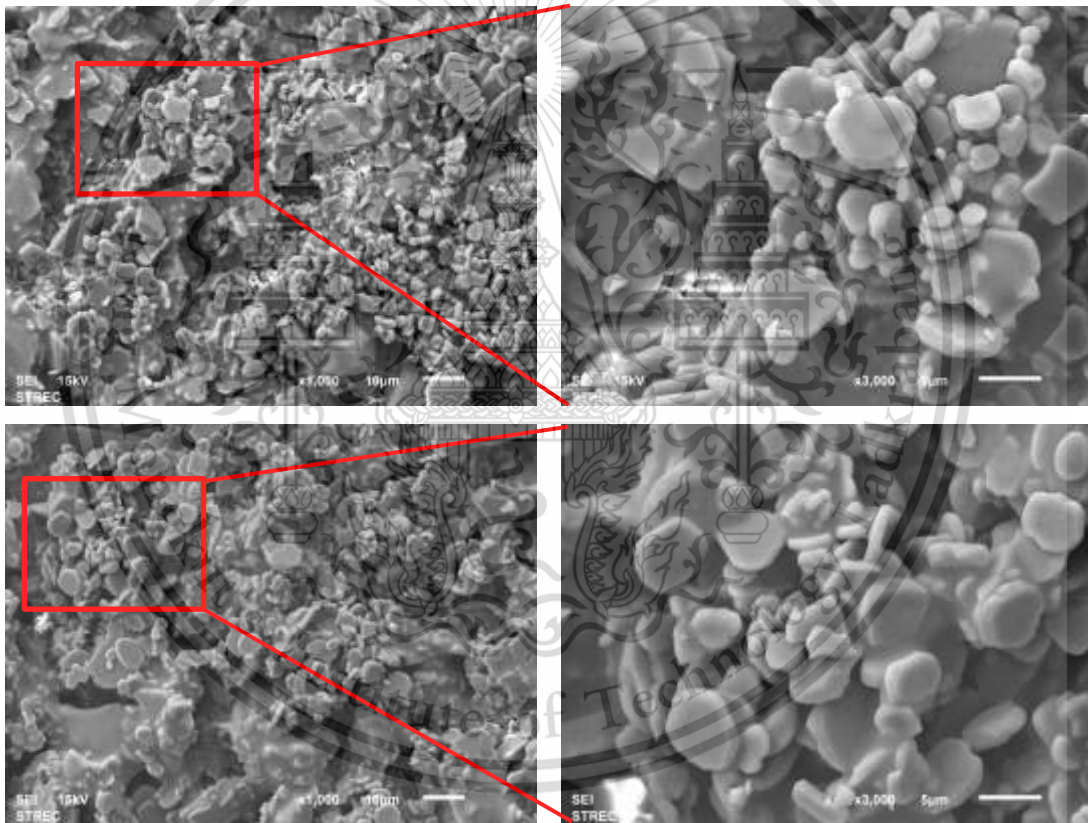


Figure 4.2a SEM images 1000X and 3000X of sintered Mullite

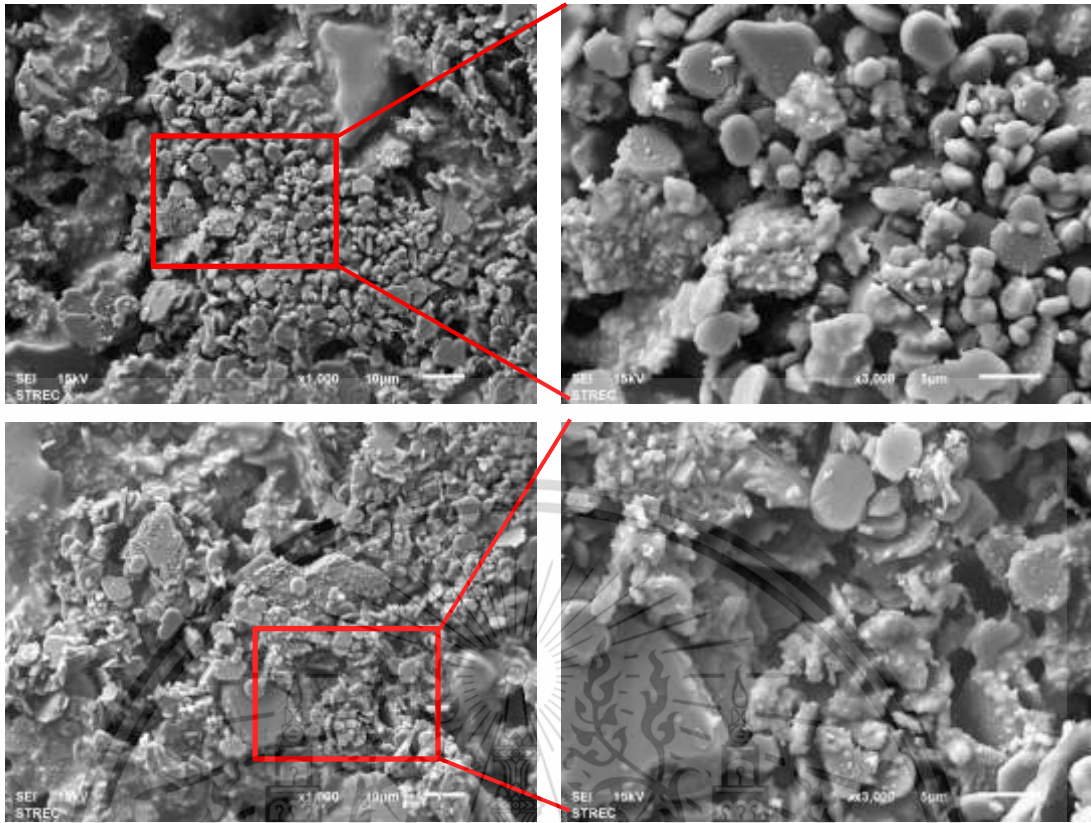


Figure 4.2b SEM images 1000X and 3000X of sintered Mullite + TiO₂

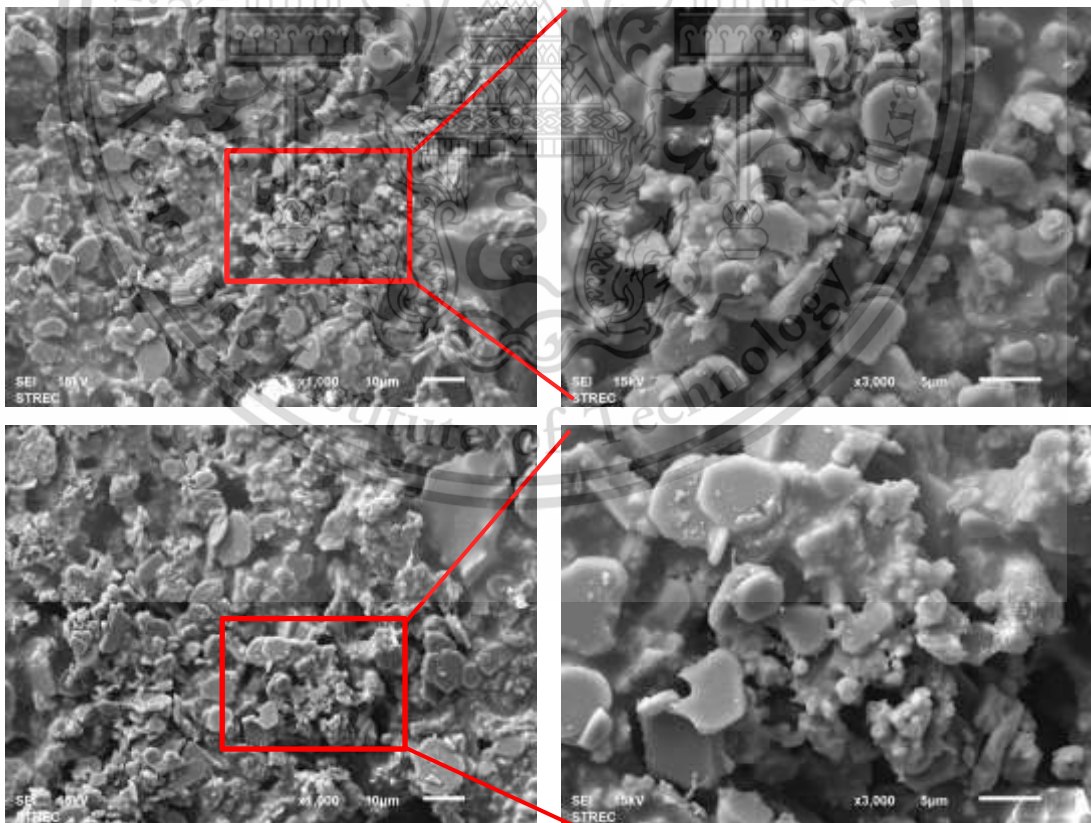


Figure 4.2c SEM images 1000X and 3000X of sintered Mullite + TiO₂ + AlF₃

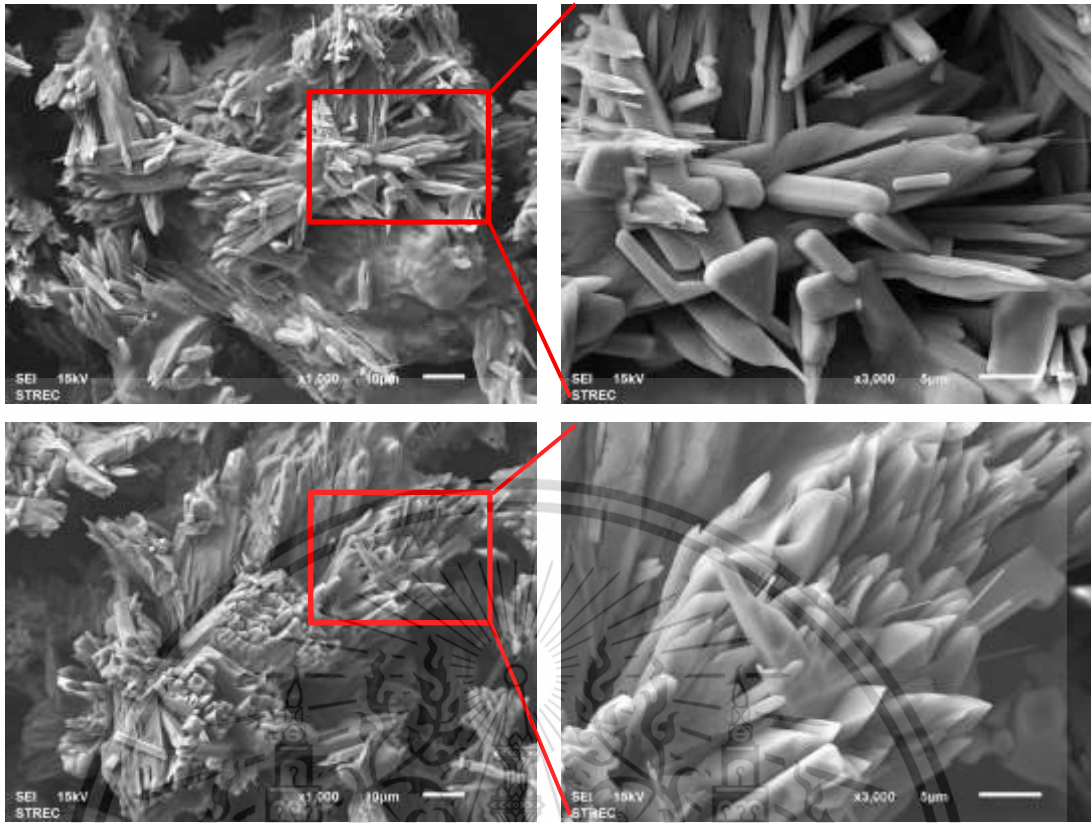


Figure 4.2d SEM images 1000X and 3000X of sintered Mullite + TiO₂ + V₂O₅

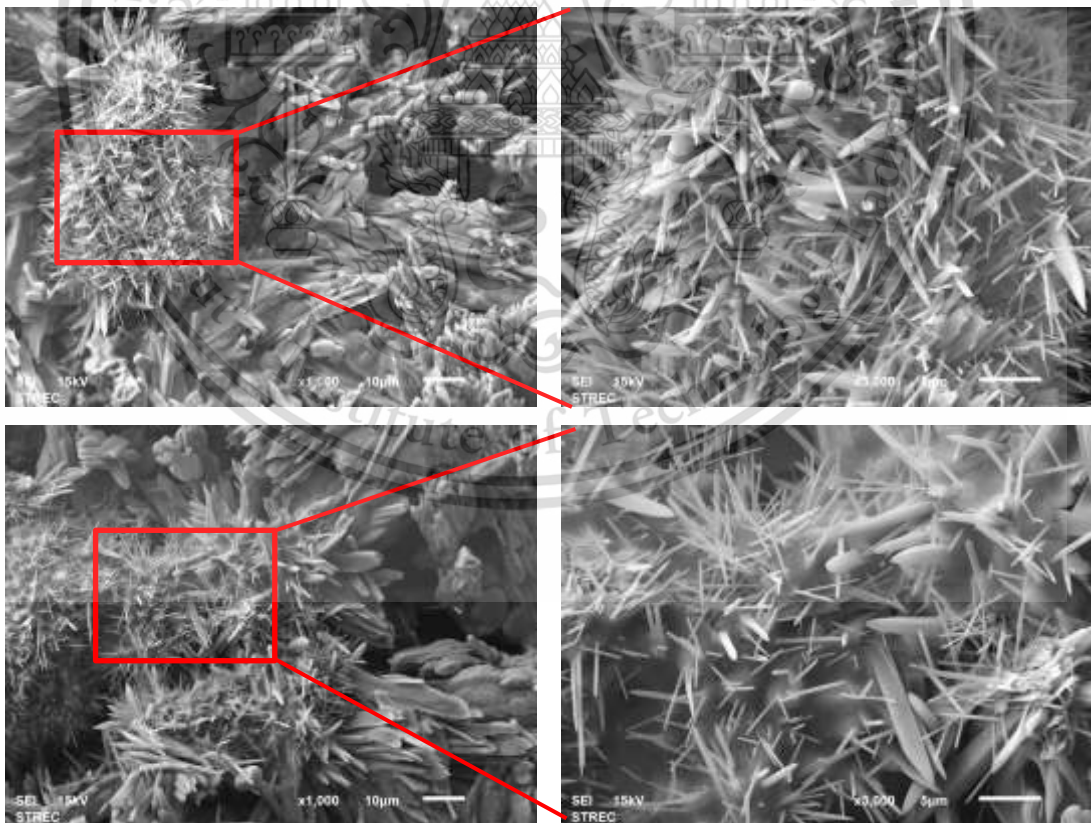


Figure 4.2e SEM images 1000X and 3000X of sintered Mullite + TiO₂ + AlF₃ + V₂O₅

4.2 Images processing for pore size distribution

The left figure 4.3 shows SEM images with 300X magnification. The qualitative SEM images are used to analyze and determine pore size distribution. In the two-color images, the black color indicates the size of pore. It was found that pore size of mullite and mullite with 10wt.% TiO_2 in mullite sample (1), (2) are the same as shown in figure 4.3a and 4.3b. The mullite with 10wt.% TiO_2 and 10wt.% AlF_3 in sample (3) content provides slightly higher number of small pores as shown in figure 4.3c. However, the mullite sample (4) and (5) with 10wt.% V_2O_5 contents as acicular mullite observe large pore size and melted grains in the structure at surface of mullite as shown in figure 4.3d and 4.3e. This result should be in high open porosity. The acicular mullite structure is observed with adding V_2O_5 content. This characteristic contributes to a higher permeability and lower backpressures into DPFs configuration.

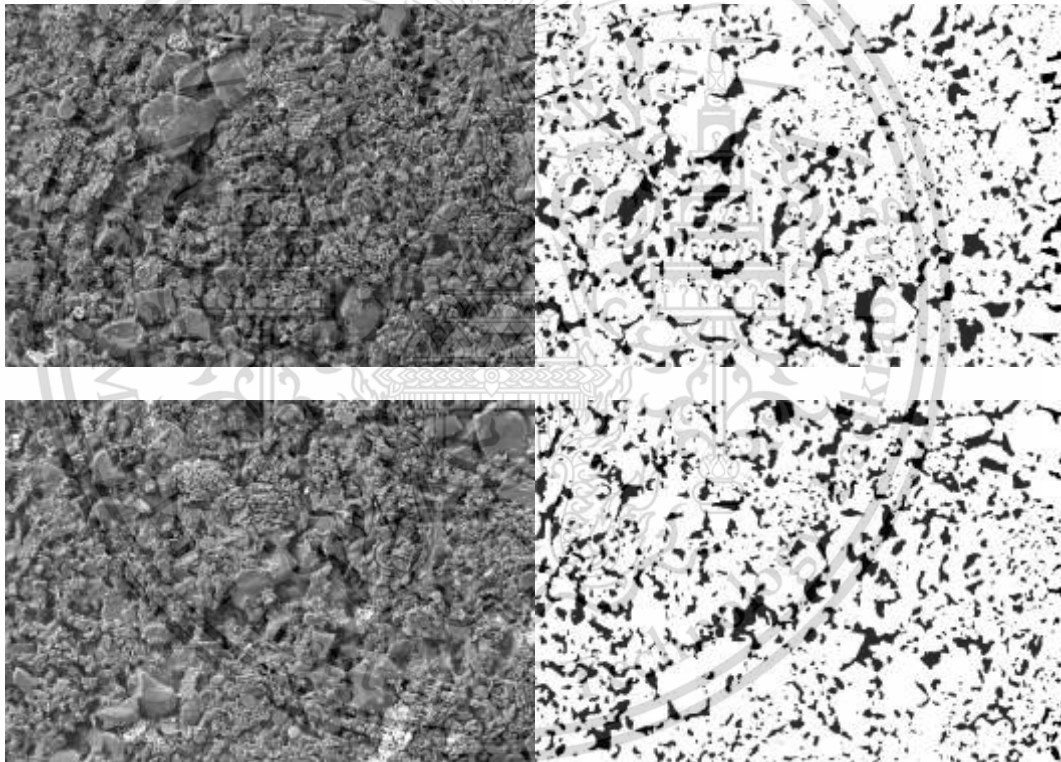


Figure 4.3a SEM and B&W images of sintered Mullite

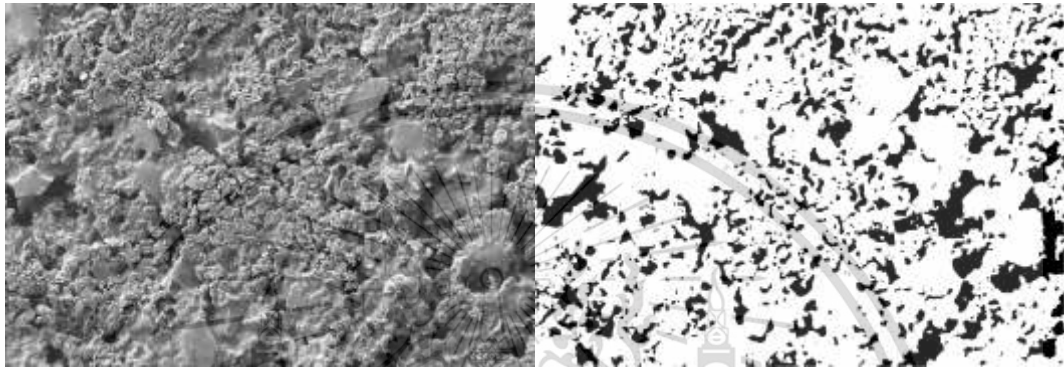
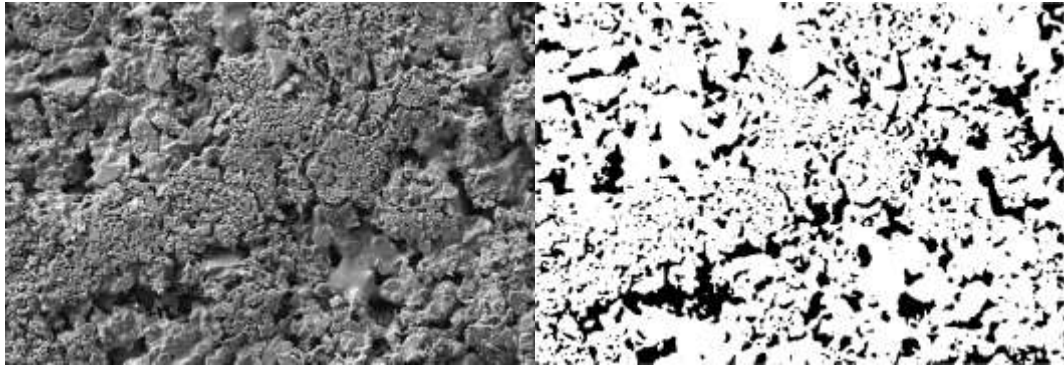


Figure 4.3b SEM and B&W images of sintered Mullite + TiO₂

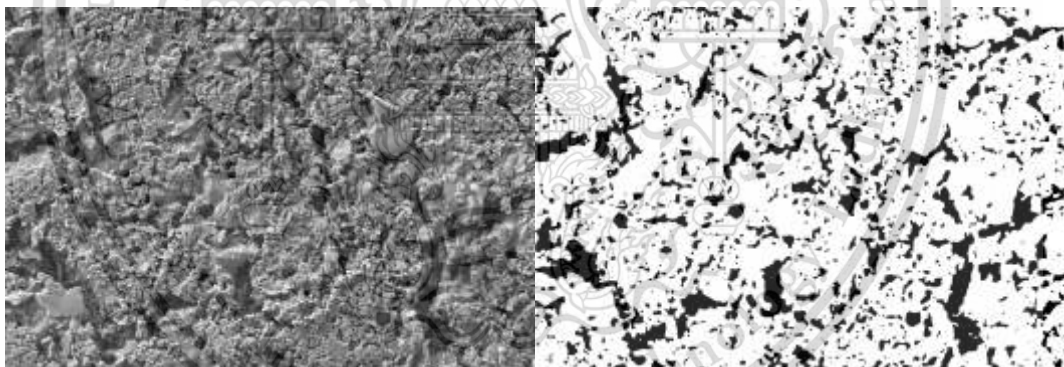


Figure 4.3c SEM and B&W images of sintered Mullite + TiO₂ + AlF₃

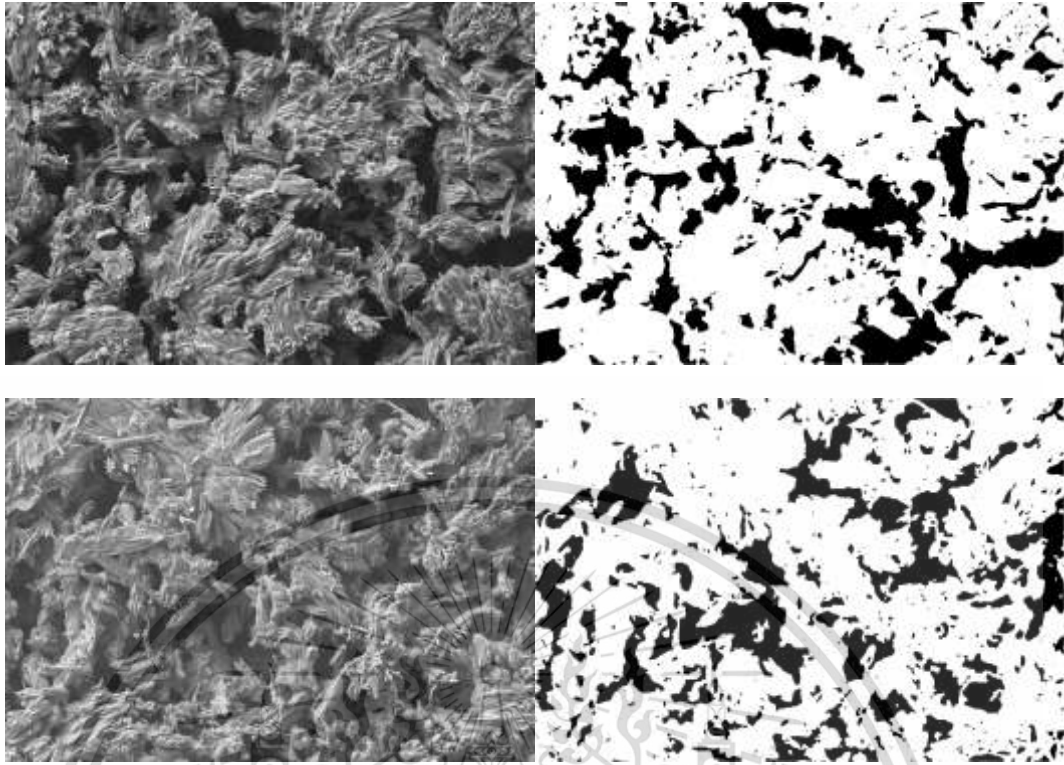


Figure 4.3d SEM and B&W images of sintered Mullite + TiO₂ + V₂O₅

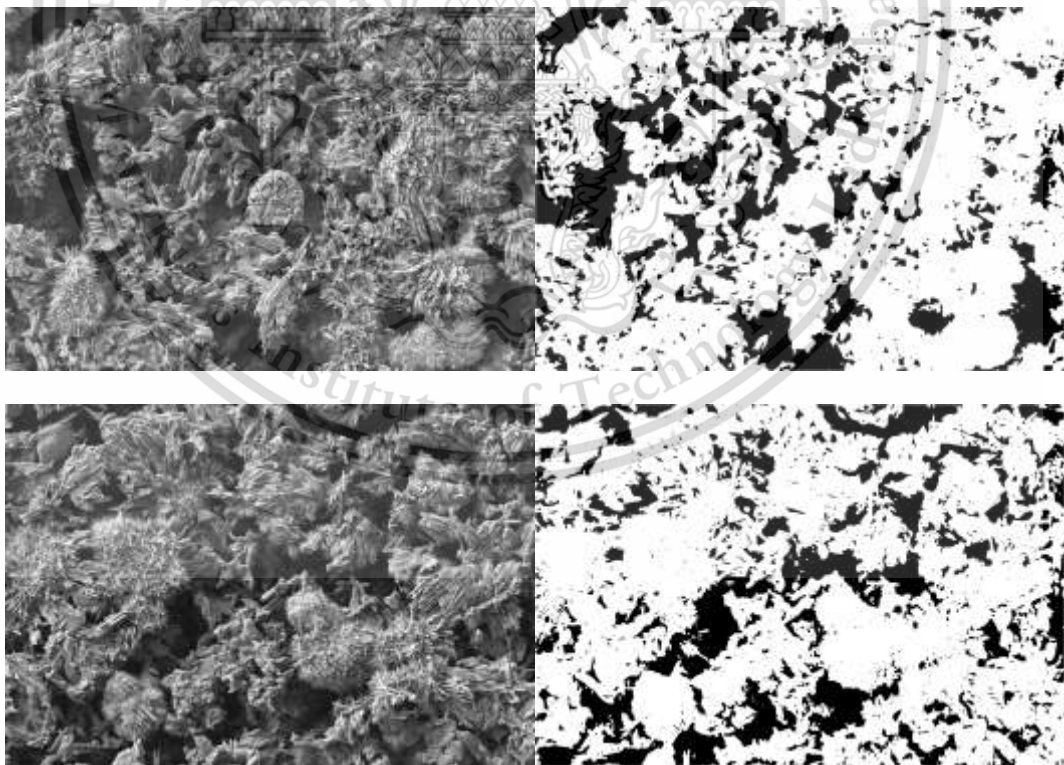


Figure 4.3e SEM and B&W images of sintered Mullite + TiO₂ + AlF₃ + V₂O₅

Figure 4.4 shows pore size distribution of the sintered mullite samples. At range pore diameter 2 μm to 10 μm , the higher amount of small pore is observed. In addition, in this range of the pore number of mullite in sample (1) is slightly higher than mullite with TiO_2 content. However, when it added AlF_3 in mullite sample (3) number of pore in small range was highest. On the other hand, the mullite with adding V_2O_5 in sample (4) and (5) observed the lowest amount of pore. This is due to higher porosity. The mullite with adding V_2O_5 can created larger pore size at 50 μm to 60 μm due to V_2O_5 enhancement. In addition, the mullite with adding V_2O_5 observed largest pore size because V_2O_5 provide more melted grains in the mullite structure.

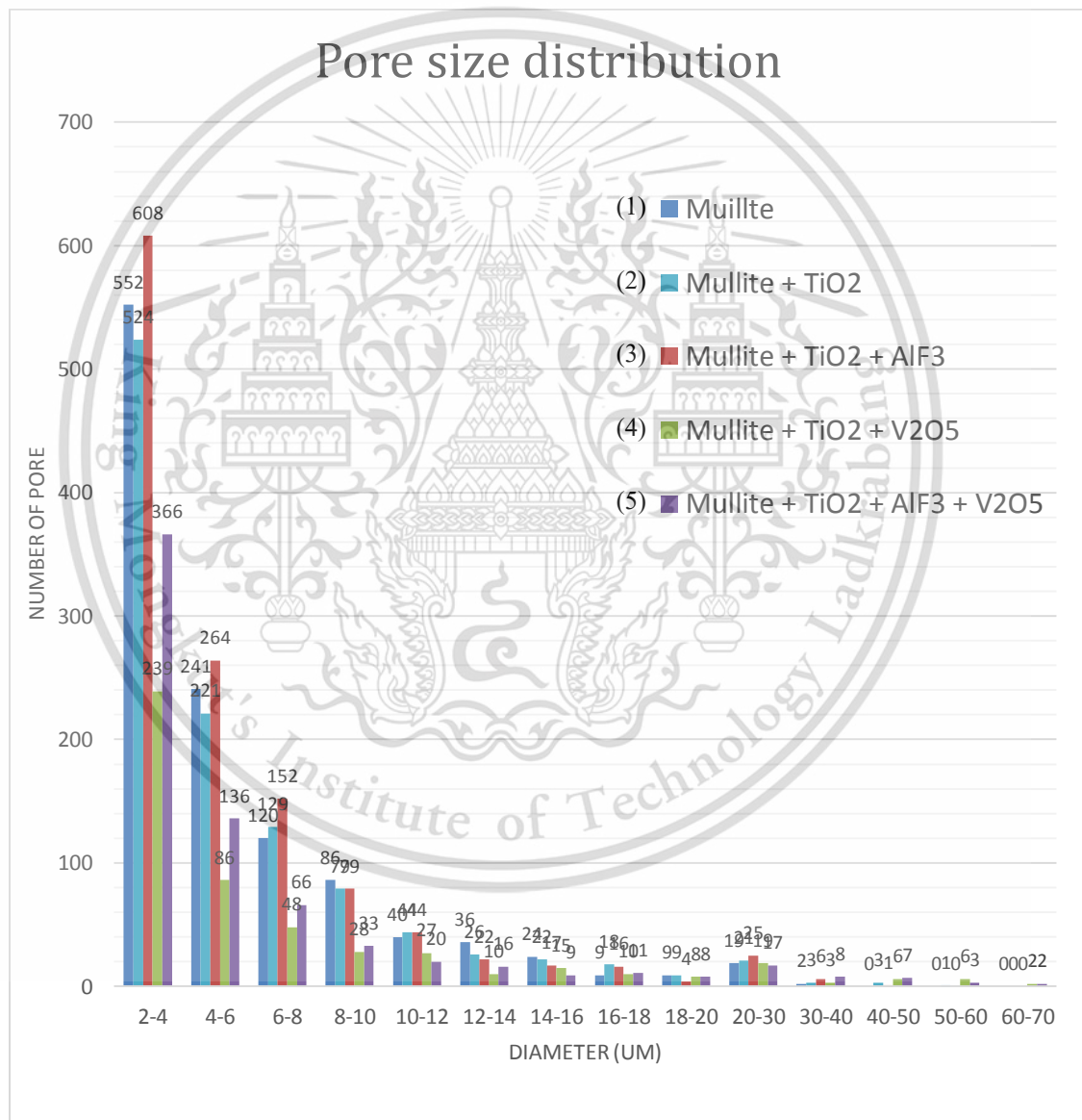


Figure 4.4 Pore size distribution

Table 4.1 shows the amount of pore the sintered mullite samples. The mullite in sample (1), (2) and (3) show high amount of pore. Moreover, I mullite sample (3) with adding AlF_3 shown highest amount of because it observed high amount of small pore. However, when adds V_2O_5 in mullite sample (4) and (5) the amount of pore reduced about two times because V_2O_5 caused melted grains in structure explicitly. Increasing pore quantity also increases the efficiency of filtration. The mullite samples with the addition of AlF_3 into the sample (3) and (5) will notice that the overall number of pores has increased. In fact, that the small pore diameter influences effectively to the filtration efficiency and pressure loop characteristics in DPFs. In addition, the small pore size might contribute to easier to trapped PM but might attribute to obstruct the gas flow.

Samples	Details	Amount of pore
1	Mullite ($Al_2O_3 + SiO_2$)	1138
2	ML + TiO_2	1100
3	ML + $TiO_2 + AlF_3$	1238
4	ML + $TiO_2 + V_2O_5$	507
5	ML + $TiO_2 + AlF_3 + V_2O_5$	702

Table 4.1 Total amount of pore

4.3 Porosity of Mullite

Table 4.2 shows porosity of the sintered mullite samples at constant sintering temperature 1300°C and 1-hour holding time. The porosity percentage is percentage of the empty volume to total volume ratio based on Archimedes' principle of water substitution. In this table, The mullite sample (1) shows 35.69% porosity while mullite with adding 10wt.% TiO₂ in mullite sample (2) increases 4.13% porosity percentage. However, the mullite sample (3) and (4) with addition TiO₂ AlF₃ and TiO₂ + V₂O₅M respectively. The porosity are 38.85% and 39.82% that are not effected to porosity Moreover, the sample of acicular mullite in sample (5) shows 46.08% the highest porosity that are the muullite contain add substance TiO₂, AlF₃, and V₂O₅.

Samples	Details	% Porosity
1	Mullite (Al ₂ O ₃ + SiO ₂)	35.69
2	ML + TiO ₂	39.51
3	ML + TiO ₂ + AlF ₃	38.85
4	ML + TiO ₂ + V ₂ O ₅	39.82
5	ML + TiO ₂ + AlF ₃ + V ₂ O ₅	46.08

Table 4.2 Porosity percentage of Mullite

When compare the porosity with totalnumber of as graph show in figure 4.5. It can be seen that in mullite sample (1), (2) and (3), the porosity will be in the range of 35.69%-39.51% and the number of pore will be in the range 1100-1238, which is likely in the same way. But while the results of the mullite sample (4) and (5) did not show that same way. This sample has a porosity value of 39.82%-46.08 show high porosity, but the number of pore is clearly a small value, which is in the range 507-702. According to the comparison of the graph showing that the amount of pore does not affect the porosity that occurs at all.

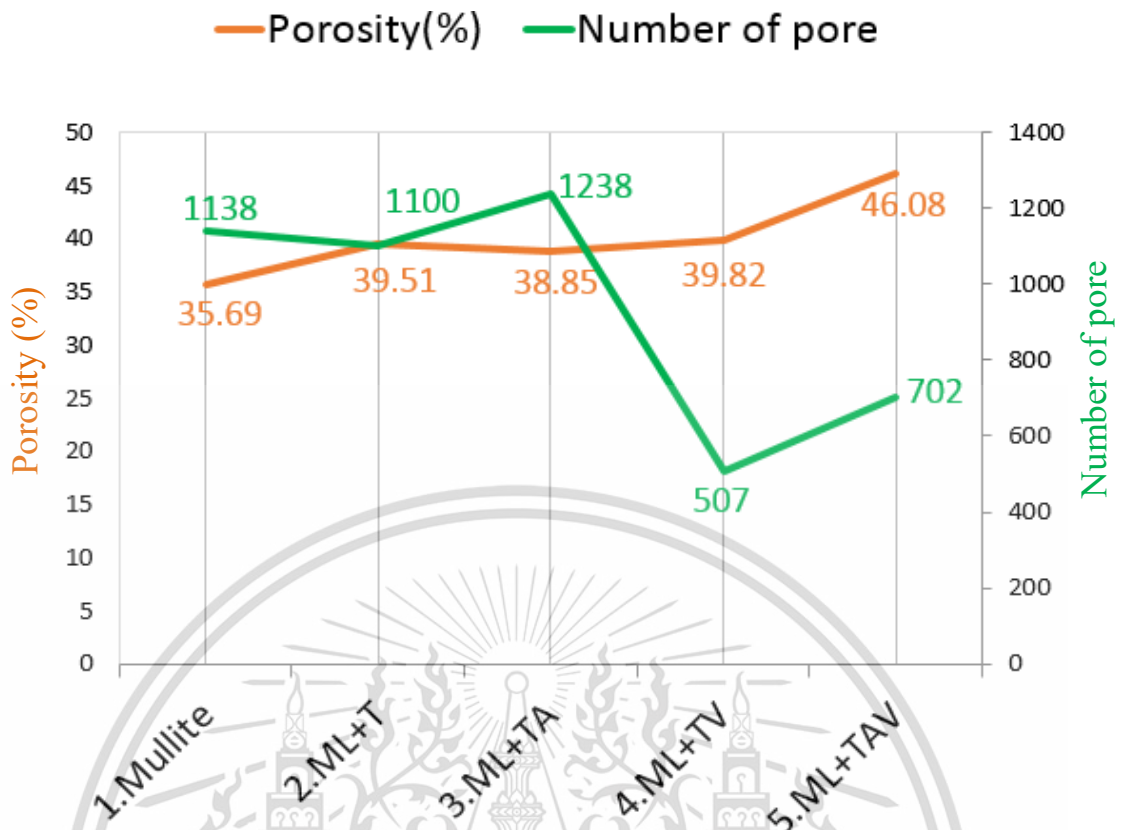


Figure 4.5 Graph porosity compare with number of pore

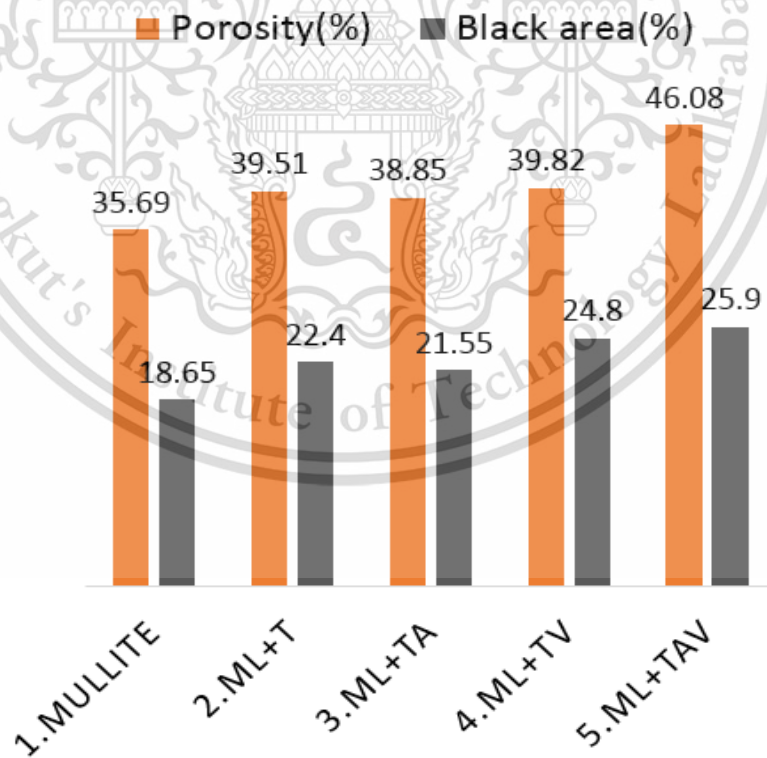


Figure 4.6 Graph porosity compare with black area

This material is reserved for educational use only, not allowed for commercial use.

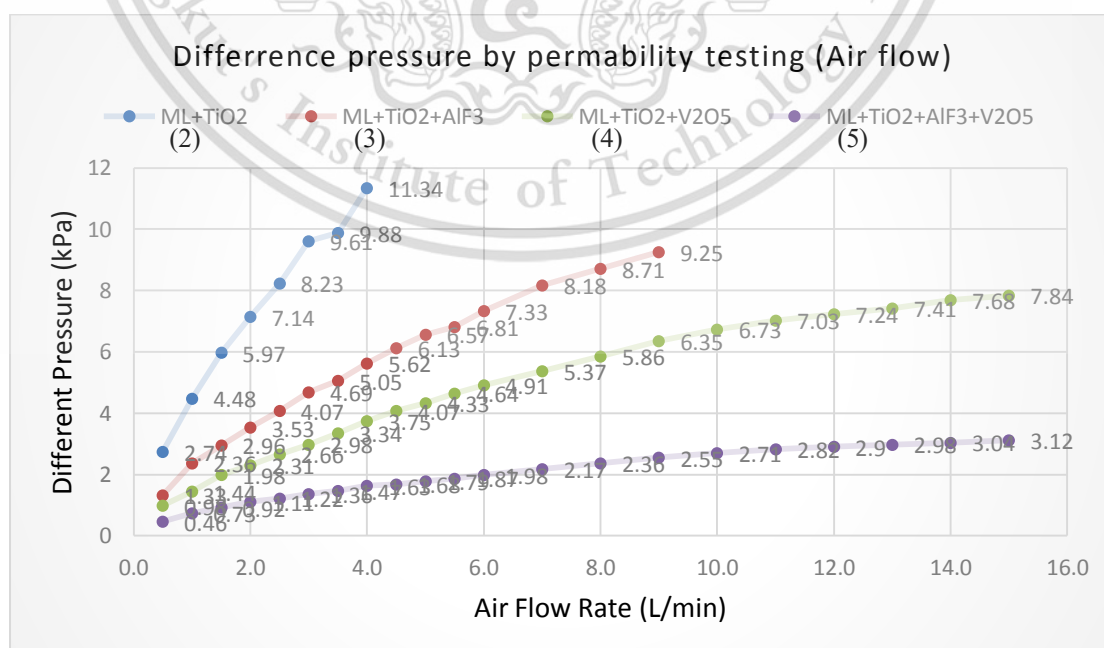
Forbidden to modify the content, and cite the document when use.

4.4 Pressure drop by permeability testing

The permeability testing is a measure of the amount of air that passes through a mullite sample and can vary dramatically from substance to substance and air to air. In this Research experimental the air will be pass through a hole diameter 15mm and mullite sample have thinness 2mm. The condition of airflow will start from 0.5 L/min to 15 L/min. Then the data recorded in term of difference pressure in unit kPa and recorded every one second. Figure 4.7 show the difference pressure results of

1. sample of mullite with addition TiO_2 ,
2. sample of mullite with addition TiO_2 and AlF_3 ,
3. sample of mullite with addition TiO_2 and V_2O_5
4. sample of mullite with TiO_2 , AlF_3 and V_2O_5

The results show that in case of mullite sample (1) have trend of difference pressure graph highest and maximum pressure at 11.34 kPa. The second is mullite sample (2) have maximum pressure at 9.25 kPa. This both sample have high number of small pore, therefore the air is likely to be difficult to flow through, causing back high backpressure. On the other hand, mullite sample (4) and (5) have larger pore size, causing low difference pressure and have maximum pressure at 7.98 kPa and 3.12 kPa respectively. Moreover, mullite sample (5) is the best in low backpressure because it have high porosity as well.



This material is reserved for educational use. **Figure 4.7** Graph pressure drop and for commercial use. Forbidden to modify the content, and cite the document when use.

4.5 Energy Dispersive X-ray Analyzer

EDX is a tool used to analyze the amount of elements that we analyze. By analyze the percentage, can set 2 analysis points:

1. Area Analysis is analyzed as a square micron area.
2. Point Analysis is analyzed as a small analytical point is small to micron level, up to nanometer level.

From Figure 4.8 is a space analysis. The analysis results according to Table 4.3, it can be seen that in the mullite sample (4) and (5), Mullite has a acicular structure. There will be a quantity of vanadium (V) 6.17% and 19.68%, respectively. Notice clearly that the mullite sample (5) has a very high percentage of vanadium (V) and have a lot of the small needle shape. However, besides to the effects of vanadium, the addition of AlF_3 should have an impact on the size and the number of needles significantly.

Conditions	Weight (%)					
	C	O	Al	Si	Ti	V
Mullite ($Al_2O_3 + SiO_2$)	6.54	44.45	27.42	21.24	-	-
ML + TiO_2	6.32	44.19	34.07	4.93	10.5	-
ML + $TiO_2 + AlF_3$	5.9	44.24	32.63	9.21	7.58	
ML + $TiO_2 + V_2O_5$	4.76	46.72	20.31	11	11.04	6.17
ML + $TiO_2 + AlF_3 + V_2O_5$	4.42	44.99	13.17	8.22	9.51	19.68

Table 4.3 Display quantitative results with EDX

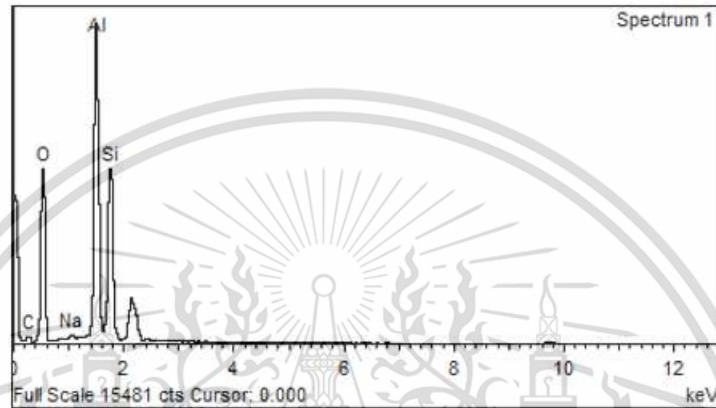
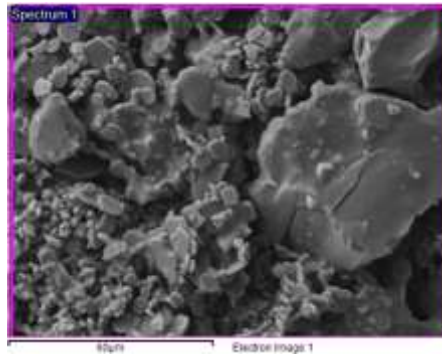


Figure 4.8a EDX of sintered Mullite

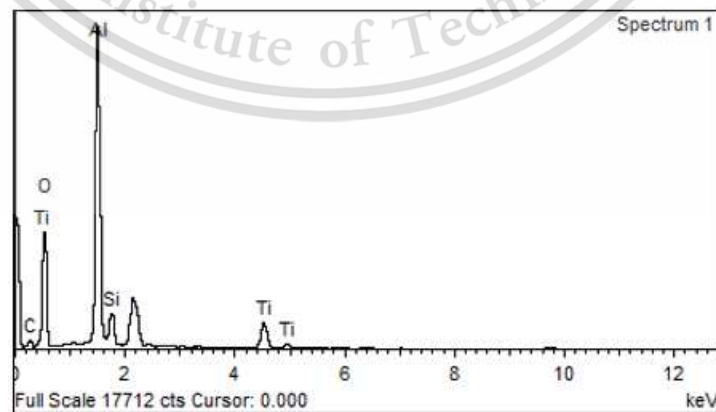
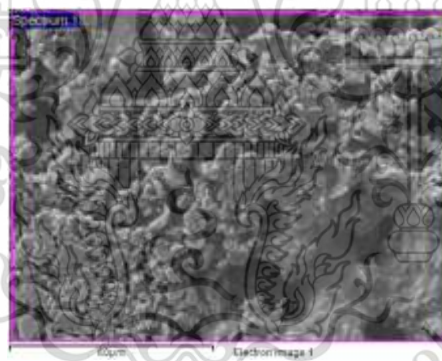


Figure 4.8b EDX of sintered Mullite with TiO₂

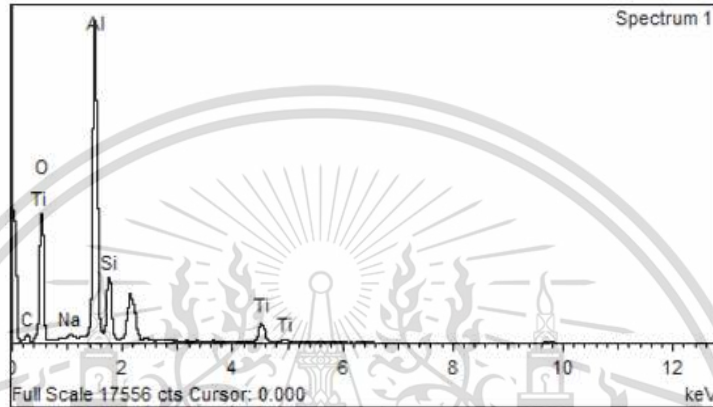
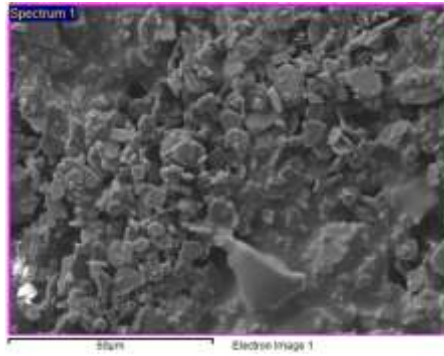


Figure 4.8c EDX of sintered Mullite with TiO₂+AlF₃

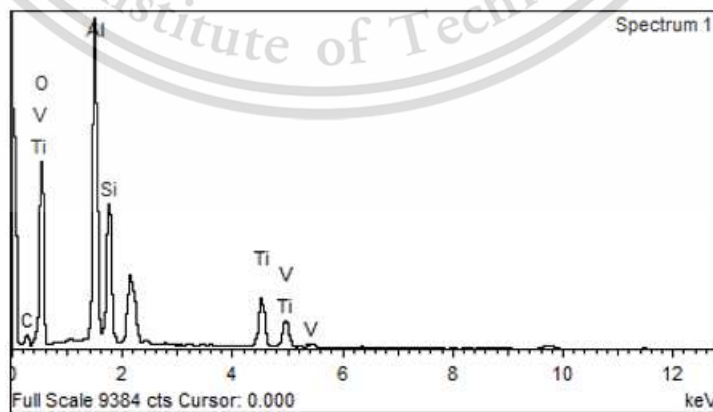
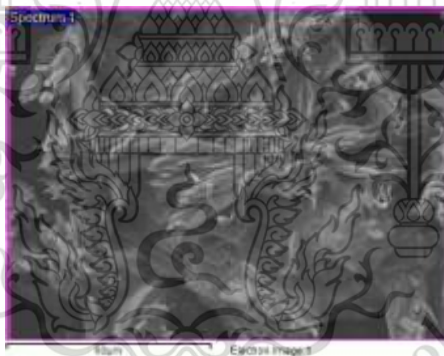


Figure 4.8d EDX of sintered Mullite with TiO₂+V₂O₅

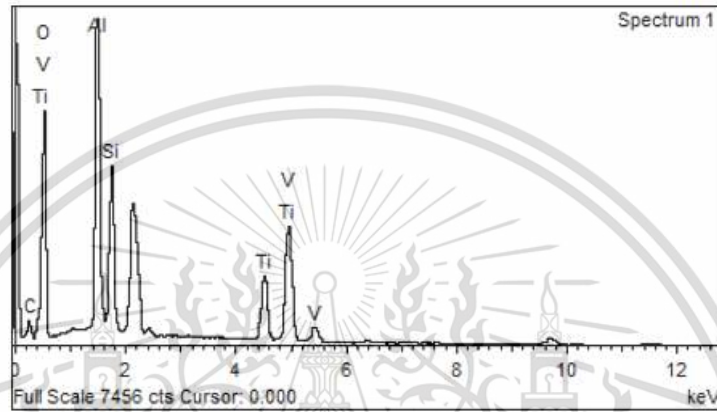
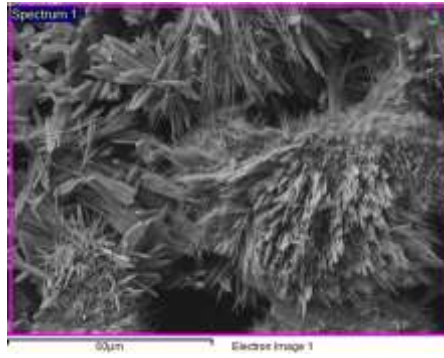


Figure 4.8e EDX of sintered Mullite with TiO₂+AlF₃+V₂O₅

4.6 SEM of carbon black trapping

For the carbon black trapping test, There are conducted a simulation experiment to detect particulate matter by using carbon back instead. The method of experiment is that it starts with preparing two sample types. Is for carbon black Mullite and acicular mullite. In order to compare the efficiency of the trap between needle and without needle. There are two types of testing method as show in figure 4.9.

1. Mixing test – Mixed mullite with carbon black 1:1
2. Sprinkle test – Sprinkle carbon black on mullite surface and blow out.



Figure 4.9 Carbon black trapping test; Mixing(left) Sprinkle(right)

Figure 4.10 show the trapping results of SEM image of mixing test. From the SEM image, it looks like the mullite sample is covered by carbon black with both of mullite and acicular mullite. It mean that carbon black or particulate matter can be attached or trapped to mullite.

Figure 4.11 show the trapping results of SEM image of sprinkle test. From the SEM image, the sample of mullite without needle shape carbon black will be trapped on the surface of mullite wall. On the other hand, in case of acicular mullite that have needle structure on the surface. Almost the carbon black will be trapped at the tip of the needle in both of single and agglomerate.

Therefore, the needle structure in acicular mullite could be more efficiency for trapping particulate matter in both of singer particle and agglomerate particle as show in figure 4.12. However, it need to test on real engine to clarify the trapping performance in case of acicular mullite.

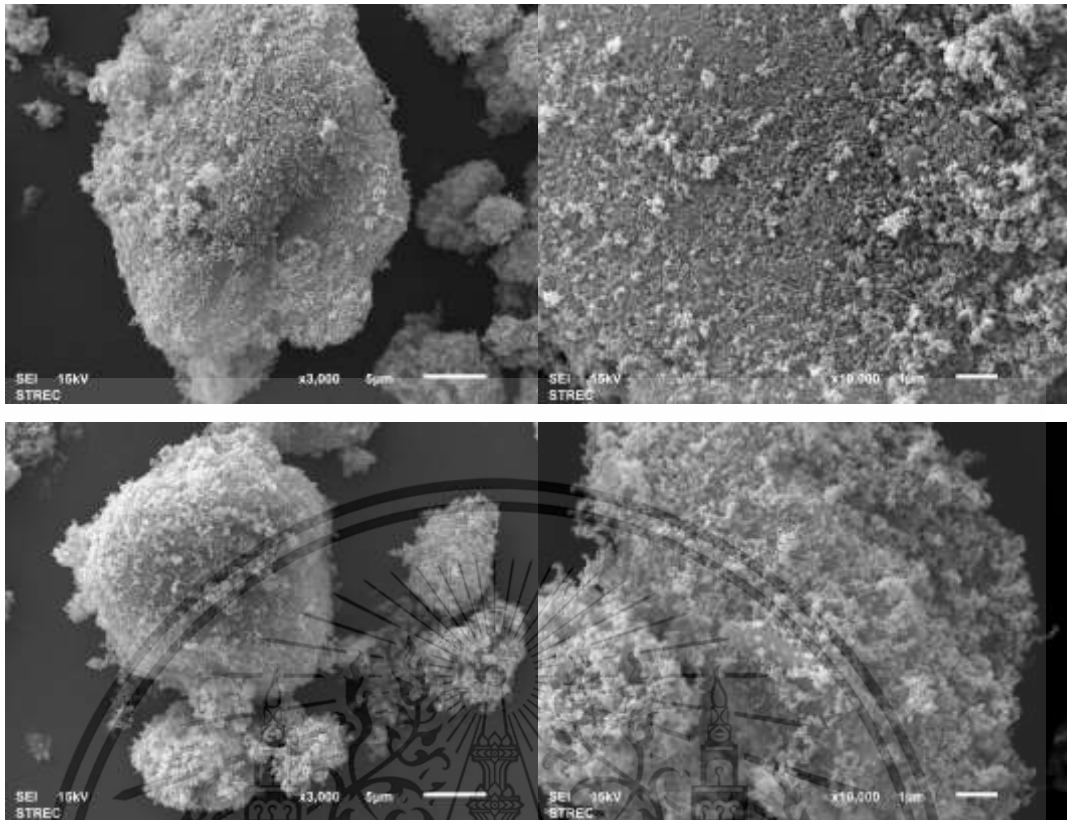


Figure 4.10a SEM of mullite with CB by mixing

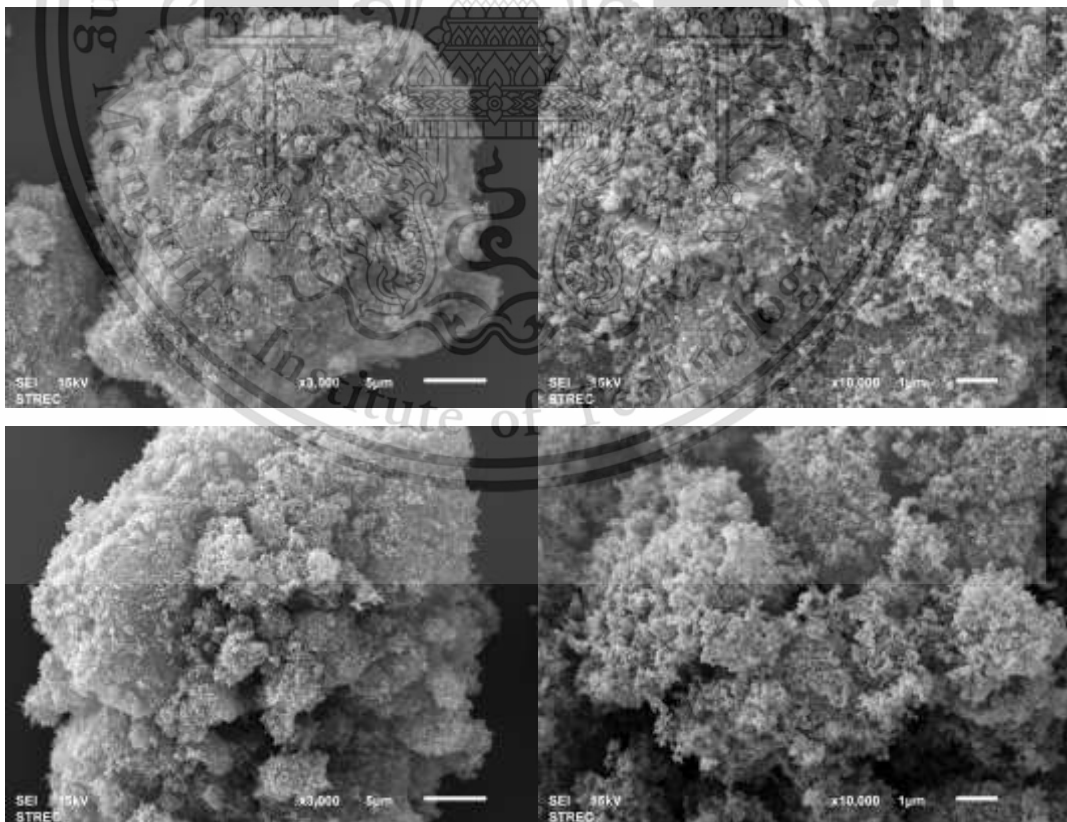


Figure 4.10b EDX of acicular mullite with CB by mixing

This material is reserved for educational use only, not allowed for commercial use.
 Forbidden to modify the content, and cite the document when use.

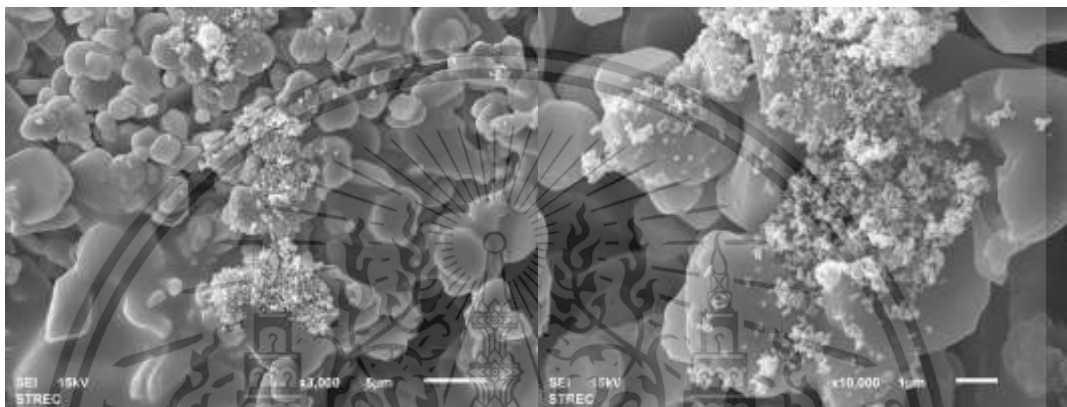
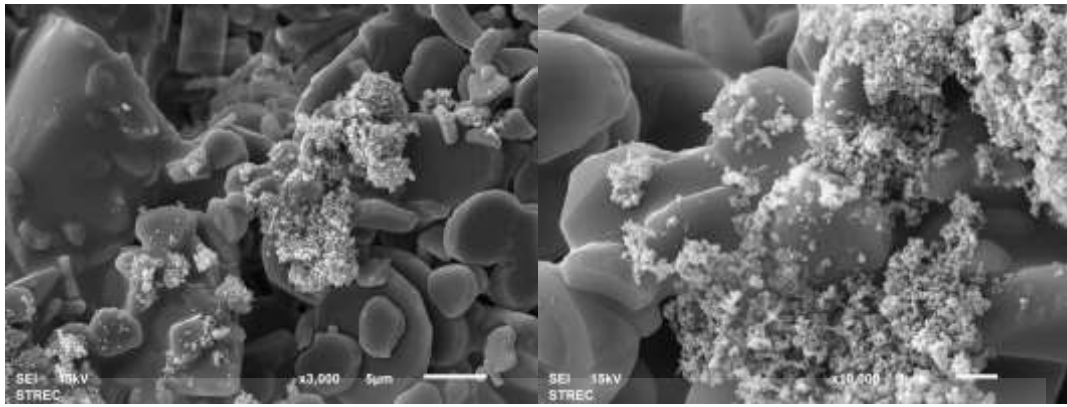


Figure 4.11a SEM of mullite with CB by sprinkle

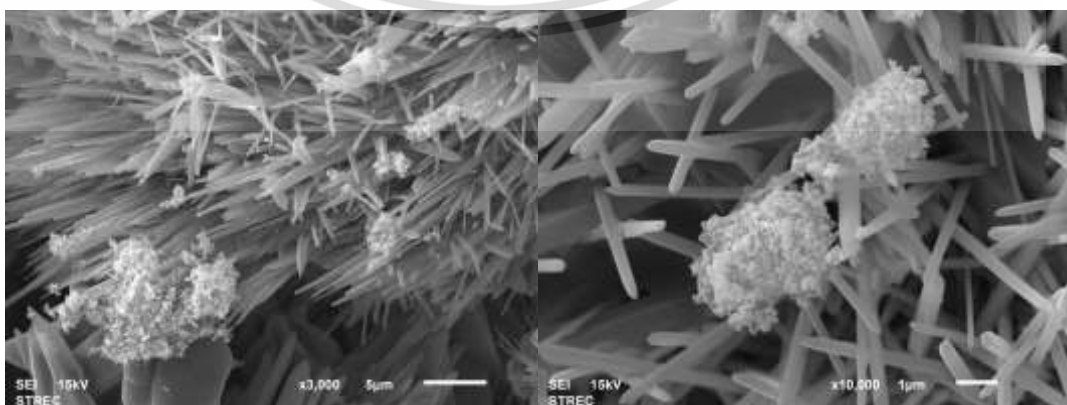
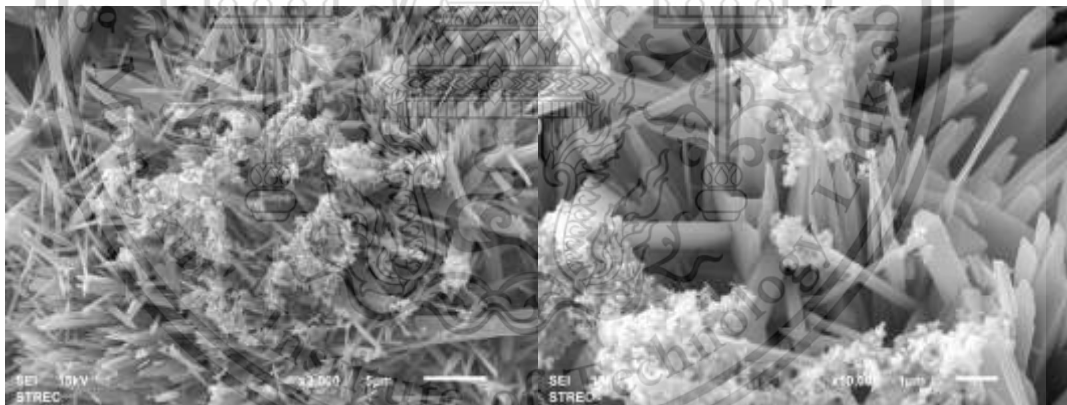


Figure 4.11b EDX of acicular mullite with CB by sprinkle

This material is reserved for educational use only, not allowed for commercial use.

Forbidden to modify the content, and cite the document when use.

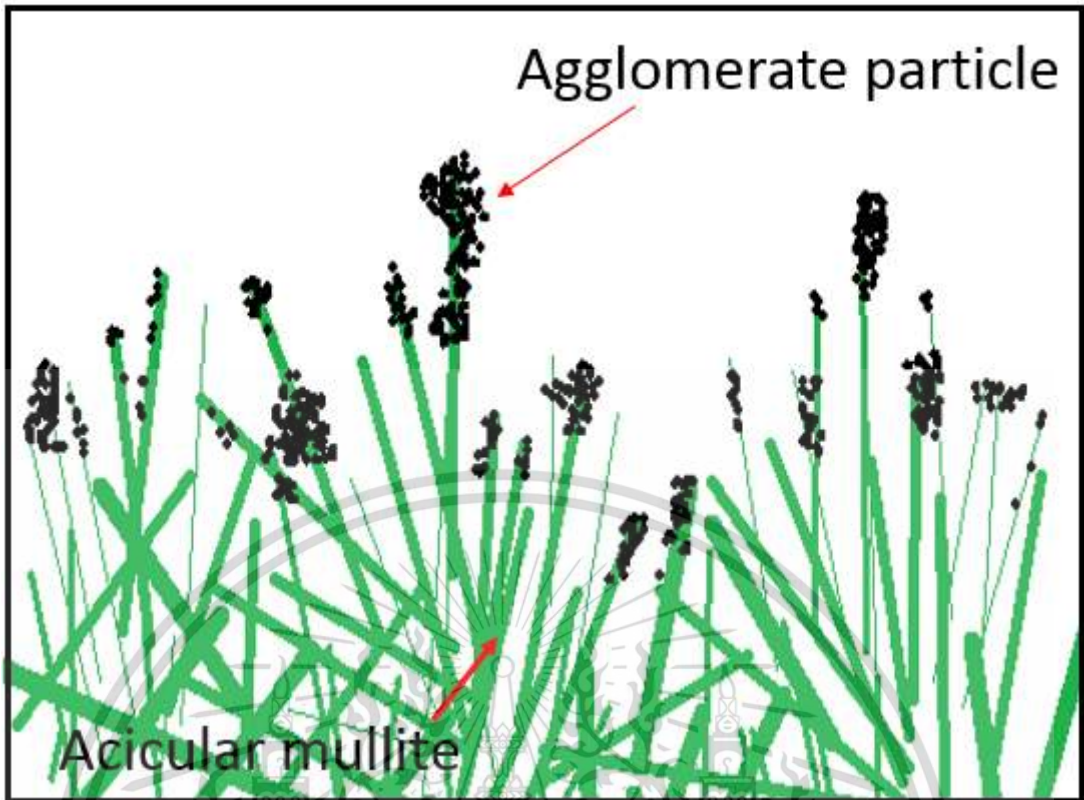


Figure 4.12a Particulate matter trapped on acicular mullite

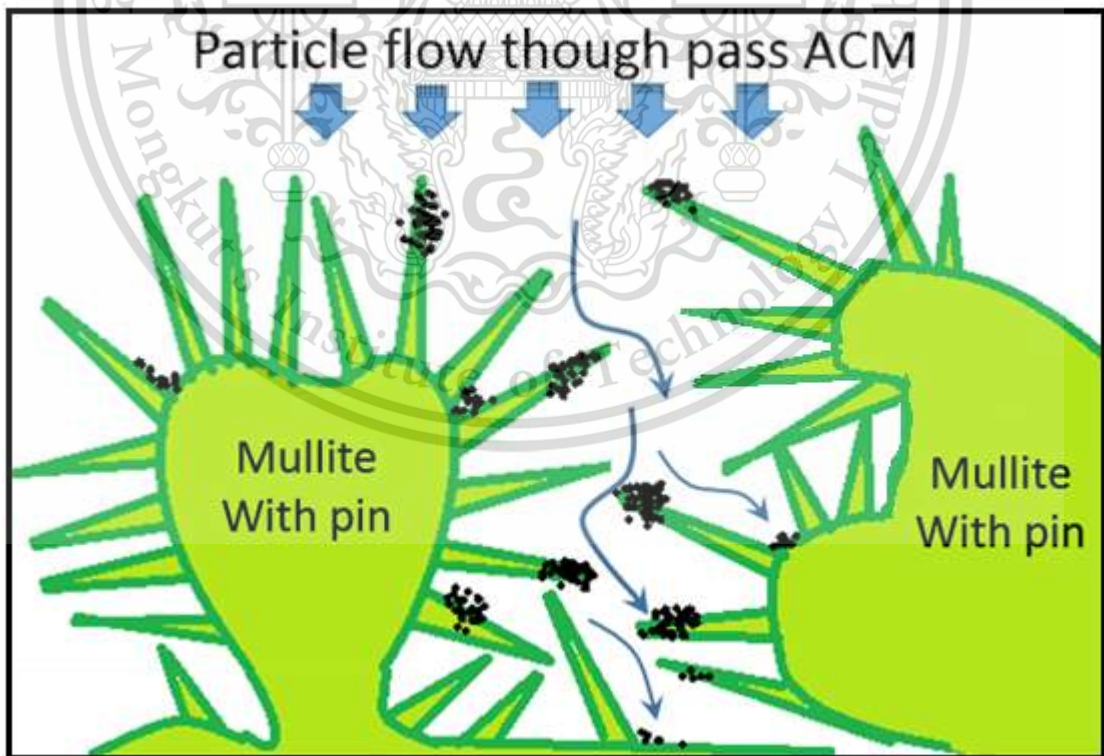


Figure 4.12b Movement of PM into the acicular mullite

4.7 Oxidation kinetics

The oxidation kinetic of mixing mullite with carbon black 1:1 tight contact, impact on only surface of the mullite sample. It was analyzed by isothermal TGA method to investigate oxidation behavior of the particulate matter. The carbon black mass conversion is plotted with respect to time as shown in Figure 4.12. Graph shows mass conversion of soot oxidation on sintered mullite by using isothermal TGA technique at 550°C, 575°C, 600°C and 620°C. Soot oxidation on acicular mullite is faster than that of mullite in all of temperature due to oxygenated chemical structure in V_2O_5 as seen as the mass conversion is dramatically drop. This is contributes to faster oxidation in DPFs. On the other hand, mullite with TiO_2 added made the slowed oxidation compared to mullite.

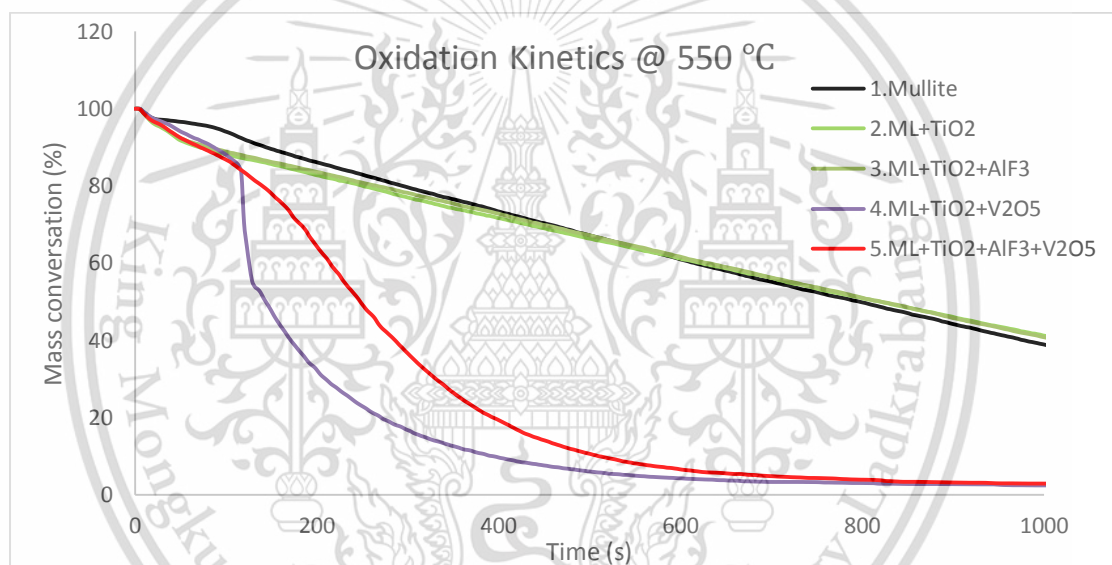


Figure 4.13a Normalized mass conversion of CB with mullite 550°C

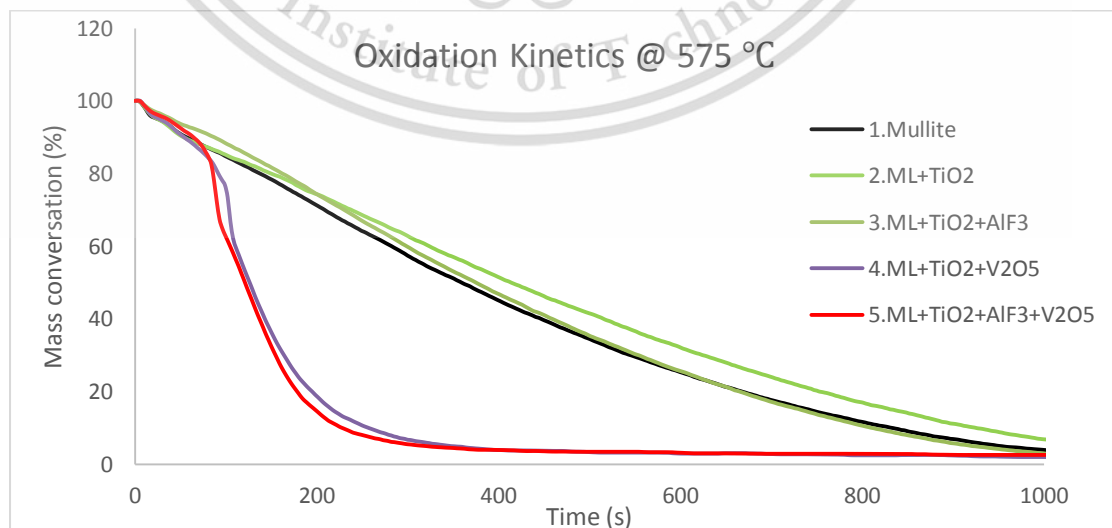


Figure 4.13b Normalized mass conversion of CB with mullite 575°C

This material is reserved for educational use only, not allowed for commercial use.

Forbidden to modify the content, and cite the document when use.

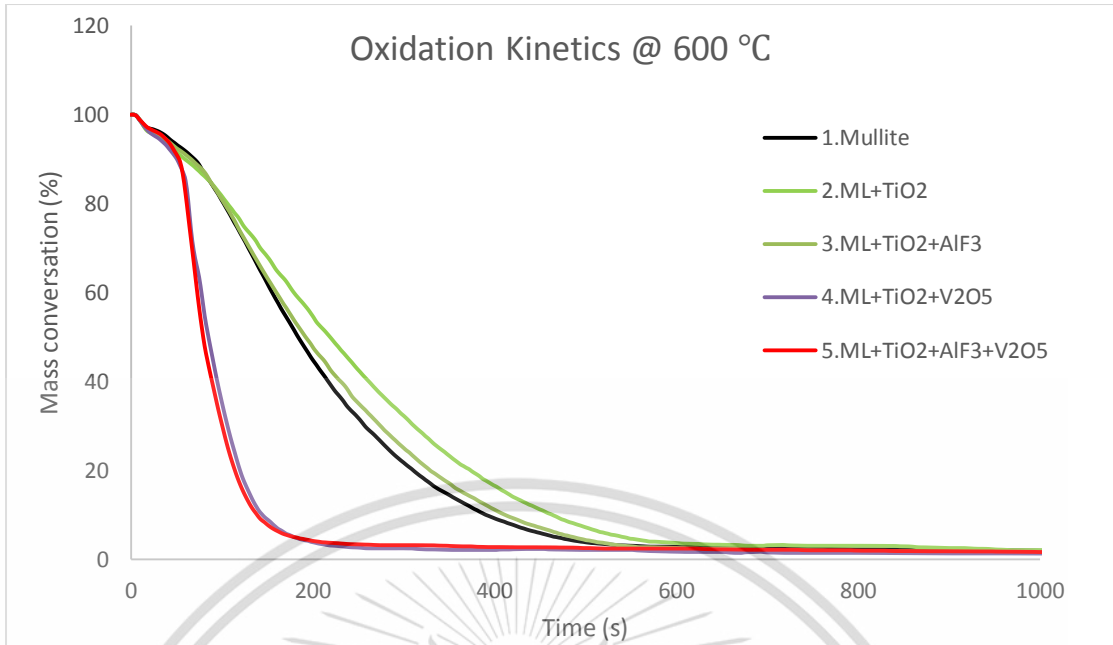


Figure 4.13c Normalized mass conversion of CB with mullite 600°C

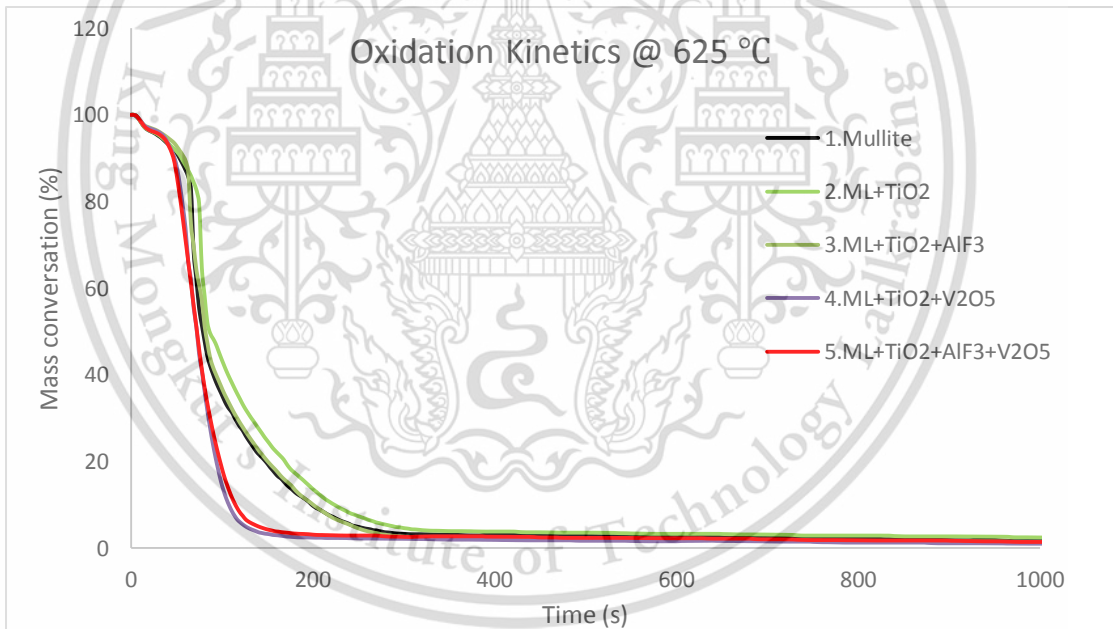


Figure 4.13d Normalized mass conversion of CB with mullite 625°C

Chemical kinetics of TGA is analyzed by a simple relationship as Eqn.4.1



Global chemical reaction rate equation or rate of PM mass conversion is described as relationships as Eqn.4.2

$$\frac{-d[c]}{dt} = kC^n O_2^m \quad (4.2)$$

According to the Arrhenius expression form of Eqn. 2.5, rate constant in this research can be expressed as Eqn.4.3

$$k = A e^{\left(\frac{-E_a}{RT}\right)} \quad (4.3)$$

Modification of Eqn. 4.2 and Eqn. 4.3 yields Arrhenius linear equation form expressed as Eqn. 4.4

$$\ln \left| \frac{-d[c]}{dt} \right| = -\frac{E_a}{RT} + \ln A + n \cdot \ln[C] + m \cdot \ln[O_2] \quad (4.4)$$

where ;

n is order of reaction with respect to $[C]$

$[c]$ is PM concentration which is equivalent to PM % mass

$[O_2]$ is oxygen concentration

m is order of reaction with respect to $[O_2]$

k is rate constant which depend on A, E_a, R, T

A is particle collision frequency factor

E_a is activation energy

R is gas constant

T is reaction temperature (K)

Activation energy (E_a) is the minimum energy which is required to initiate and complete a chemical reaction. The lower activation energy means the better reactivity. From the mass conversion graphs (Figure 4.12), rate of mass conversion was selected within the zone of constant slope for accurate E_a estimation. From the equation form of Eqn. 4.4, it can be simplified as a linear equation form of $Y = m \cdot X + c$. where Y axis is equivalent to $\ln \left| \frac{-d[C]}{dt} \right|$, m is equivalent to $-\frac{E_a}{R}$, X is equivalent to $\frac{1}{T}$, and C- intercept is responsible for the remaining terms; $\ln A + n \cdot \ln[C] + m \cdot \ln[O_2]$. As a result, the data of PM mass conversion rate can be plotted as a graph in Figure 4.13 and activation energy can be calculated as shown in Table 4.4.

- The activation energy needed in acicular mullite condition is lower than mullite.
- The impact of mixing acicular mullite might be acting as catalyst on CB oxidation kinetics.
- The physical impact in acicular mullite is lower than mullite (i.e. LnA)

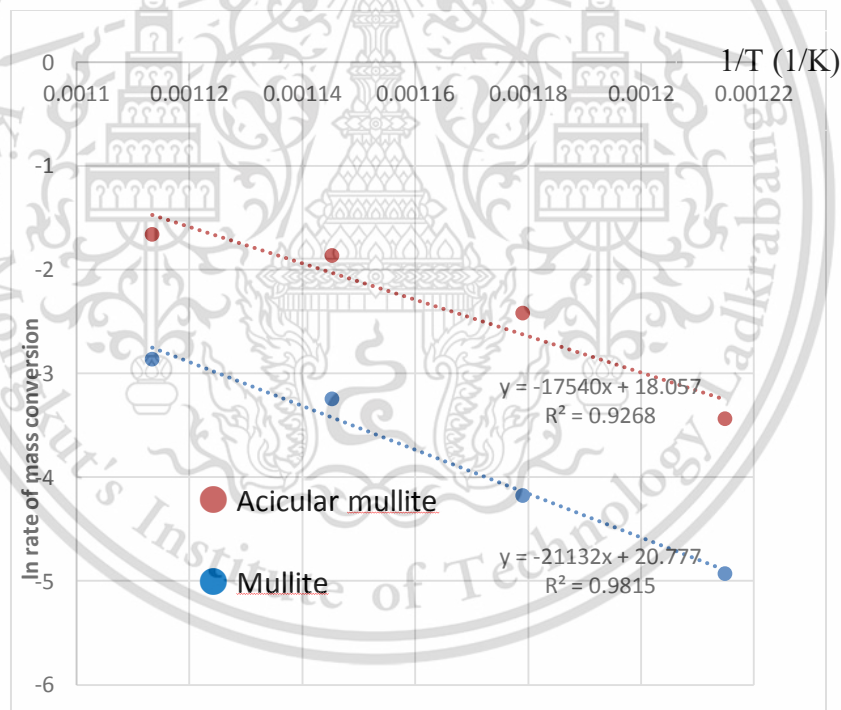


Figure 4.14 Graph for E_a determination

50% Burned soot	Mullite	Acicular mulite
E_a (kJ/mol)	176	146
LnA	21	18

Table 4.4 Calculated activation energy

This material is reserved for educational use only, not allowed for commercial use.

Forbidden to modify the content, and cite the document when use.

CHAPTER 5

CONCLUSIONS AND RECOMMENDATIONS

This research presented the morphologies and microstructure of mullite DPFs by using SEM and image processing. The effects of TiO_2 , AlF_3 and V_2O_5 contents on the mullite structure were investigated. The compositional analysis was done with EDX to analyze the composition of acicular mullite. The image processing was done by Image J program. The oxidation kinetics behavior of soot has been successfully investigated by using TGA.

- The carbon black helped to open the porosity in the Mullite structure that might be useful for DPF operation. The optimal amount of carbon black 35%wt . It can produce porosity is in the range of 35% - 45% based on the sintering temperature 1,300°C.
- The Mullite with the addition of V_2O_5 results in the formation of many small needle structures (Acicular mullite). However, it found large pores around 60-70 μm , therefore increasing V_2O_5 may reduce the mechanical strength of DPFs.
- The Mullite with the addition of AlF_3 results in an increase in the number of pores on the Mullite structure about 10% when compared with Mullite. Which will result in a higher surface area for PM trapping as well.
- Relation of all factors, pore size, porosity, pore number, pin shape, pressure drop can be controlled by adding the amount of TiO_2 , AlF_3 and V_2O_5 into the mullite. We can increase mechanical strength by adding TiO_2 , increase pore number by adding AlF_3 . Finally, we can increase the amount of pin and control pin size by adding V_2O_5 . Therefore, in the near future AlF_3 and V_2O_5 are the key materials to develop pin shape in the next generation of diesel particulate filter.

REFERENCES

1. Energy consumption by sector 2030, https://www.researchgate.net/figure/Energy-Consumption-by-Sector-2030_fig6_299172099
2. BP Energy outlook 2030, <https://www.slideshare.net/MarcellusDN/bp-energy-outlook-2030>
3. 4 stroke diesel engine working, <https://www.youtube.com/watch?v=DACGe2WNd3Q>
4. Soot or particulate matter emitted from Diesel Engine, <http://www.newdmax-club.com/index.php?topic=35443.0>
5. Diesel Particulate Filter (DPF) in the exhaust gas and DPF structure, P. Karin, “Microscopic Visualization and Characterization of Particulate Matter Trapping and Oxidation in Diesel Particulate Filters and Membrane Filters”, PhD. Thesis, Tokyo Institute of Technology, Japan.
6. Acicular Mullite (ACM), https://www.energy.gov/sites/prod/files/2014/03/f9/2005_deer_pyzik.pdf
7. Efficiency of the ideal engine, Klell Manfred-Technical University of Graz, Reduction of CO2 Emissions in Mobility, 2012
8. Composition of particulate matter, https://nptel.ac.in/courses/112104033/lecture12/12_2.htm
9. Maricq, M. M., “Chemical characterization of particulate emissions from diesel engines: A review,” *Journal of Aerosol Science*, 38(11):1079-1118, 2007, doi: 10.1016/j.jaerosci.2007.08.001.
10. Preechar Karin, Park Watanawongskorn, Jiramed Boonsakda , Impact of Biodiesel on Small CI Engine Combustion Behavior and Particle Emission Characteristic , JSAE 20179094 / SAE 2017-32-0094
11. Karin, P., Boonsakda, J., Siricholathum, K., Saenkhumvong, E., Charoenphonphanich, C., and Hanamura, K. “Morphology and oxidation kinetics of CI engine’s biodiesel particulate matters on cordierite Diesel Particulate Filters using TGA,” *International Journal of Automotive Technology*, 18(1):31–40, 2017, doi: 10.1007/s12239-017-0003-y.
12. Preechar Karin, Yutthana Songsaengchan, Songtam Laosuwan, Chinda Charoenphonphanich, Nuwong Chollacoop, Katsunori Hanamura , “Physical Characterization of Biodiesel Particle Emission by Electron Microscopy” , JSAE 20139150 / SAE 2013-32-9150

13. Karin, P., Borhanipour, M., and Songsaengchan, Y., et al, "Oxidation kinetics of small CI engine's biodiesel particulate matter," *International Journal of Automotive Technology*, 16(2):211–219, 2015, doi: 10.1007/s12239-015-0023-4.
14. Diesel Particulate Filter system, www.audi-technology-portal.de
15. Hiroshi Oki, Preechar Karin and Katsunori Hanamura , "Visualization of Oxidation of Soot Nanoparticles Trapped on a Diesel Particulate Membrane Filter" , Tokyo Institute of Technology, Published 04/12/2011
16. Jingjie Cao, Xinfu Dong, Lingling Li, Yingchao Dong, Stuart Hampshire, "Recycling of waste fly ash for production of porous mullite ceramic membrane supports with increased porosity" , *Journal of the European Ceramic Society* 34(2014) 3181-3194
17. Movement mechanism of particle matter, PM of exhaust gas caught by various mechanisms, <http://raet-aircondition.blogspot.com/2009/02/blog-post.html>
18. Eakkawut Saenkhumvong, Preechar Karin, "Microstructure of Diesel Particulate Matters by electronic microscope" , Me-NETT31
19. Choi, S., Myung, C. L., and Park, S., "Review on characterization of nano-particle emissions and PM morphology from internal combustion engines: Part 2", *International Journal of Automotive Technology*, 15(2):219-227, 2014, doi:10.1007/s12239-014-0023-9.
20. Oki, H., Karin, P., and Hanamura, K., "Visualization of Oxidation of Soot Nanoparticles Trapped on a Diesel Particulate Membrane Filter," *SAE International Journal of Engines*. 4(1):515–526, 2011, doi:10.4271/2011-01-0602.
21. Karin, P., Cui, L., Rubio, P., Tsuruta, T., and Hanamura, K., "Microscopic Visualization of PM Trapping and Regeneration in Micro-Structural Pores of a DPF Wall," *SAE International Journal of Fuels and Lubricants*. 2(1):661-669, 2009, doi: 10.4271/2009-01-1476.
22. Eastwood, P., "Particulate Emissions from Vehicles". (Chichester, UK: John Wiley & Sons, Ltd, 2007), doi: 10.1002/9780470986516.
23. ASTM International, "ASTM C20-00, Standard Test Methods for Apparent Porosity, Water Absorption, Apparent Specific Gravity, and Bulk Density of Burned Refractory Brick and Shapes by Boiling Water," West Conshohocken, PA.
24. Cao, J., Dong, X., Li, L., and Dong, Y., et al., "Recycling of waste fly ash for production of porous mullite ceramic membrane supports with increased porosity," *Journal of the European Ceramic Society*, 34(13):3181-3194, 2014, doi: 10.1016/j.jeurceramsoc.2014.04.011.

25. Stewart, M. L., Gallant, T. R., Kim, D. H., Maupin, G. D., and A. Zelenyuk, "Fuel Efficient Diesel Particulate Filter (DPF) Modeling and Development," PNNL-19476, 991593, 2010.
26. Tatsuo T, Akira N, Ryouji N, Katsuhiko S. Approach to High Efficiency Diesel and Gas Engines. Mitsubishi Heavy Ind Ltd. 2008;2008(45):1.
27. Heywood JB. Internal combustion engine fundamentals. New York: McGraw-Hill; 1988. 930 p. (McGraw-Hill series in mechanical engineering).
28. Kittelson DB. Engines and nanoparticles. J Aerosol Sci. 1998 Jun;29(5–6):575–88.
29. Tartakovsky L, Aronov B, Zvirin Y. Modeling of the Regeneration Processes in Diesel Particulate Filters. Energy Power. 2012 Dec 1;2(5):96–106.
30. Schematics of scanning electron microscopy operation [Internet]. Available from:<http://li15594.members.linode.com/myscope/sem/practice/principles/layout.php>
31. Park W, Preechar K, Chinda C, Jiramed B, Katsunori H, Nuwong C. Impact of Diesel Engine Combustion Characteristics on Particulate Matter's Morphology and Nanostructure from Ethanol-blended Biodiesel.
32. Stewart ML, Gallant TR, Kim DH, Maupin GD, Zelenyuk A. Fuel efficient diesel particulate filter (DPF) modeling and development. Pacific Northwest National Laboratory (PNNL), Richland, WA (US), Environmental Molecular Sciences Laboratory (EMSL); 2010.
33. Akiyoshi N, Kentaro I, Osamu Y, Kazuya T, Kousuke U, Tetsuro T, et al. Development of Innovative Diesel Particulate Filters based on Aluminum Titanate: Design and Validation. RD Rep "SUMITOMO KAGAKU." 2011(2).

APPENDIX A :
PUBLICATIONS

SETC

Preliminary Program

NOVEMBER 15-17, 2017
JAKARTA, INDONESIA

23RD SMALL ENGINE TECHNOLOGY CONFERENCE
“SMALL ENGINE TECHNOLOGY -
GENERATING A PROMISING FUTURE”

2017

King Mongkut's Institute of Technology Ladkrabang

SETC
2017 JAKARTA

SAE
Society of Automotive Engineers of Japan, Inc.

SAE
INTERNATIONAL

IATO
SAE - INDONESIA

Impact of Biodiesel on Small CI Engine Combustion Behavior and Particle Emission Characteristic

Preechar Karin, Park Watanawongskorn, Jiramed Boonsakda
Eakkawut Saenkhumvong, Sippakorn Rungsritanapaisan, Settavit Srivarocha
Chinda Charoenphonphanich
King Mongkut's Institute of Technology Ladkrabang

Nuwong Chollacoop
National Science and Technology Development Agency

Katsunori Hanamura
Tokyo Institute of Technology

Copyright © 2017 SAE Japan and Copyright © 2017 SAE International

ABSTRACT

Diesel engines are high thermal efficiency because of high compression ratio but produce high concentration of particulate matter (PM) because of direct injection fuel diffusion combustion. PM must be removed from the exhaust gas to protect human health. This research describes biodiesel engine performance, efficiency and combustion behavior using combustion pressure analyzer. It was clearly observed that PM emitted from CI engines can be reduced by using renewable bio-oxygenated fuels. The morphology and nanostructure of fossil fuel and biofuel PMs were investigated by using a Scanning electron microscopy (SEM) and Transmission electron microscopy (TEM). The morphology of biodiesel and diesel doesn't have much different in the viewpoint of particulate matter trapping using DPF micro surface pores. The agglomerated ultrafine particles and primary nanoparticles sizes of diesel and biodiesel engine's PM are approximately 50-500 nm and 20-50 nm, respectively. The primary particle of biodiesel engine's PM is smaller than that of fossil diesel. The average of diesel and biodiesel PM's carbon platelets is in the range of 0.2-5.2 nm.

INTRODUCTION

Diesel engines are considered as one of the highest thermal efficiency engines among internal combustion engines (ICE) [1]. However, a major disadvantage is particulate matter (PM) emission which is harmful to human body and environment. Biofuels, such as biodiesel or ethanol, have been often discussed as alternatives for diesel fuel replacement since they are obtained from renewable sources and their benefits in emission reduction. Biodiesel consists of alkyl monoesters of fatty acids derived from vegetable oil or animal fats. Due to its similar physical properties to diesel fuel, there is no need to modify the engine when the engine is fueled with the blends [2-4]. In terms of engine performance

and emission, many researchers have investigated effects of biodiesel fuel on diesel engines. M.M. Hasan *et al.* [5] investigated effects of biodiesel by blending with the maximum blend ratio of 30% biodiesel. Operated with a single-cylinder diesel engine, brake thermal efficiency of the blends was similar to diesel base fuel. There was a decrease of nitrogen oxides and smoke emission, while maximum heat release rate and maximum pressure for the blends at higher load were increased. Mohanad *et al.* [6-7] conducted investigations of a 4-cylinder diesel engine powered by rapeseed biodiesel blend. They showed that ignition delay increased for higher cetane number. Sakthivel *et al.* [8] studied performance, emission, and combustion characteristics of a diesel engine, injection timing is a major parameter that sensitively affects the engine performance, emission and durability. The brake thermal efficiency for B20 was higher compared to diesel in the entire load. The ignition delay and combustion duration were shorter for biodiesel than diesel which results in lower heat release rate, peak pressure and rate of pressure rise. Retardation of injection timing caused decrease in emission and combustion parameters like Oxides of Nitrogen (NO_x), Hydrocarbon (HC) and Carbon Monoxide (CO), peak pressure, ignition delay, combustion duration and heat release rate which increased with advancement in injection timing. An according research from Guven *et al.* [9] showed that biodiesel blends caused decrease in maximum pressure and heat release rate and retarded further far away from top dead center.

Diesel particulate matters consist of a solid fraction and a soluble organic fraction (SOF). Primary particles of the PMs, composed of carbon and metallic ash, are coated with SOF and sulfate. The mean diameter of primary particles is usually in the range of 20-80 nm. Agglomerated particles are an assembly of primary particles and surface area does not differ appreciable from the sum of specific surface areas of primary particles. Agglomerated particle size is normally 80-300 nm [10]. Scanning Electron Microscope (SEM) and Transmission Electron Microscope (TEM) observation of PMs have been conducted by several researchers [11]. A

SETC2017

primary soot particle has two distinct parts; an inner core and an outer shell [12-13]. Generally, a primary particle from ICE has only one core with concentric fringe pattern which is hard to be distinguished as inner core or outer shell [14]. Size distributions of diesel engine's PMs have been categorized as PM10, diameter (D) < 10 micron; fine particles, D < 2.5 micron; ultrafine particles, D < 0.1 micron; and nanoparticles, D < 0.05 micron or 50 nm. [15].

METHODOLOGY

Table 1. Engine specification.

Items	Details
Engine type	1-cylinder, Natural aspirated, Direct injection, Compression Ignition Engine
Bore x Stroke	97 mm x 96mm
Displacement	709 cm ³
Compression ratio	18:1
Rated power	9.2 kW @ 2400 rpm
Injection timing	19° CA bTDC
Injection pressure	22 MPa

Table 2. Fuel properties.

Properties	Diesel	Biodiesel
Chemical formula	C _{14.2} H ₂₈	C _{14.9} H _{29.9} O _{1.9}
Carbon (% mass)	85.1	74.5
Hydrogen (% mass)	14.0	12.5
Oxygen (% mass)	0.9	13.0
Auto ignition temp (°C)	288	294
Calorific value (kJ/kg)	46,180	39,525
Heat of vaporization (kJ/kg)	250	300
Viscosity @ 40°C (mm ² /s)	3.0	4.5
Density @ 25°C (kg/m ³)	844.8	875.3
Stoichiometric air fuel ratio	14.7	12.3
Distillation (°C)		
T10	214.3	336.2
T30	250.3	339.7
T50	281.5	341.4
T70	312.5	345.4
T90	352.3	351.2

The experiment was carried out on a 1-cylinder natural aspirated, direct injection, displacement of 709 cm³, compression ratio of 18:1, diesel engine. Fuel injection system was not modified (mechanical fuel injection system). Engine specification was represented in Table 1. The engine was coupled with an eddy-current dynamometer and a control

SETC2017

system to adjust engine speed and engine load. Fuel supply system was set with a weight scale to measure fuel consumption. For parameter analysis in the combustion chamber, pressure versus crank angle data were measured by a piezoelectric sensor (Kistler 6052C31, 250Bar, sensitivity: ±0.5%) and a crank angle encoder (CA-RIE-360, resolution: 360 pulses/rev.). Signals of the cylinder pressure were recorded with one-degree resolution of crank angle. For further statistical analysis, two hundred engine cycles were recorded with three repeats. The pressure signals then were amplified with the data acquisition equipment (DEWESoft SIRIUSI-HS-CA) to obtain heat release rate.

The fuels used in this research include commercial diesel and biodiesel (B100). The commercial diesel contains approximately 5% biodiesel due to the regulation while the biodiesel was produced from palm-olein (B100-TIS2313-2549). Fuels properties are shown in Table 2. Biodiesel is more homogeneous molecules which shown by vaporize temperature. It is very narrow and very high around 610 to 620 Kelvin. This implies that biodiesel has higher heat of vaporization. Engine performance curve, brake specific fuel consumption (BSFC) and brake thermal efficiency (BTE) were measured to see overview effects of biodiesel compared with commercial diesel. In-cylinder pressure, net heat release rate, and accumulative heat release from selected engine operating conditions were then recorded to see combustion characteristics.

PM's quantity was measured by an opacity diesel smoke meter (OKUDA DSM-240, 0-100%, ±3% accuracy) which optically evaluate soot collected on paper filters by light reflection method. PM powder was collected by using an in-house metal-net particle collector to investigate morphology and nanostructures by using scanning electron microscopy (FE-SEM: Hitachi SU5000), and transmission electron microscopy (TEM: JEOL JEM-2100Plus)

RESULTS AND DISCUSSION

Combustion Characteristics

The engine performance curve of diesel and biodiesel is plotted in Fig. 1 (a). Engine load decreases as increasing engine speed for all fuels. Brake specific fuel consumption (BSFC) and Brake thermal efficiency (BTE) are shown in Fig. 1 (b) and (c), respectively. BSFC of the biodiesel are higher than that of diesel at all load conditions due mainly to the lower calorific value. Thus, the amount of fuel supply into the engine must be greater. The trend shows decrease in the BSFC as the engine load increase. It can be explained as; when the engine load increases, combustion temperature which is implied from the rise of Exhaust gas temperature (EGT) as shown in Fig. 1 (d) increases as well. Reactivity of fuel and oxygen activates conversion of combustion heat to mechanical work much more than amount of energy from the fuel input. That is why the BSFC decreases as the engine load increases. BTE plots show that as the engine load increases, the engine produces more thermal efficiency for both fuels. The BTE of biodiesel is higher than diesel at all load condition because the fuel properties such as more oxygen fraction could promote complete combustion which biodiesel could reach optimum BTE at less load compared with diesel.

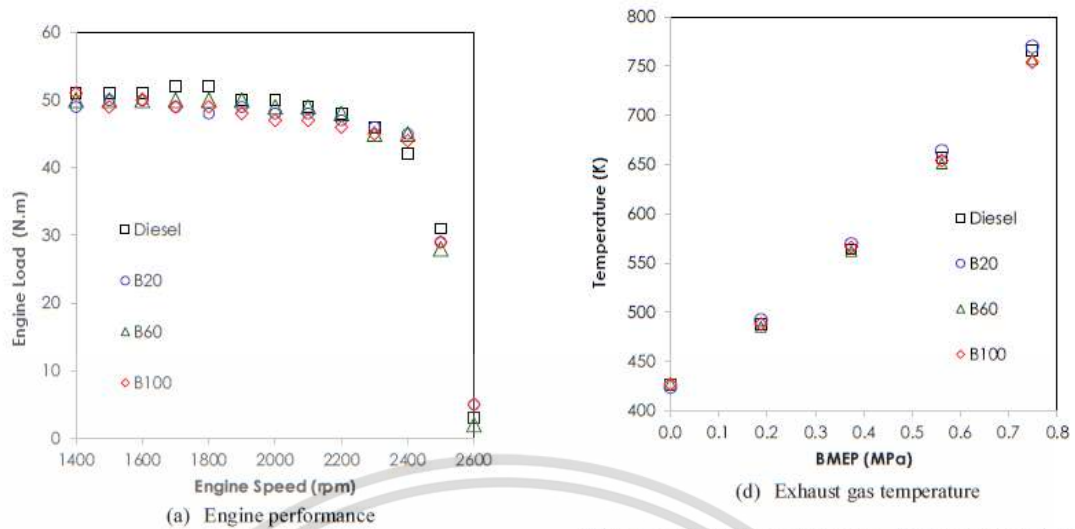
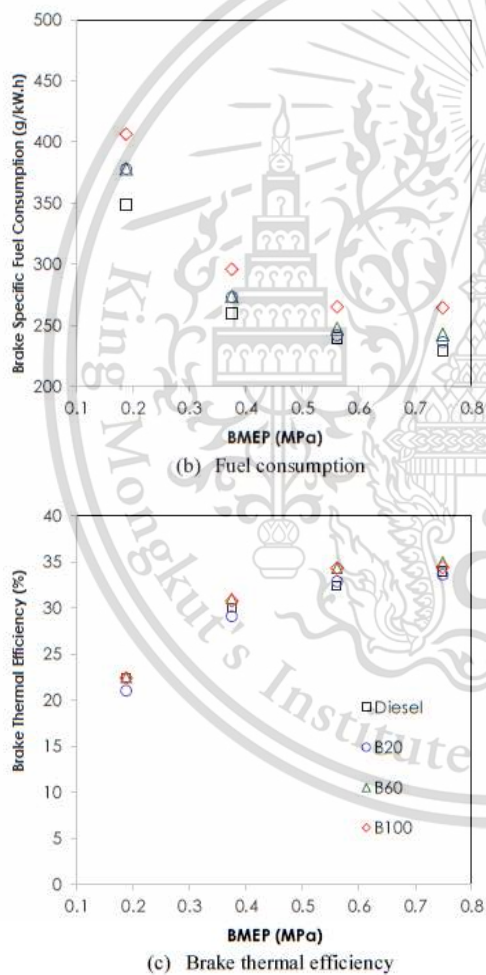
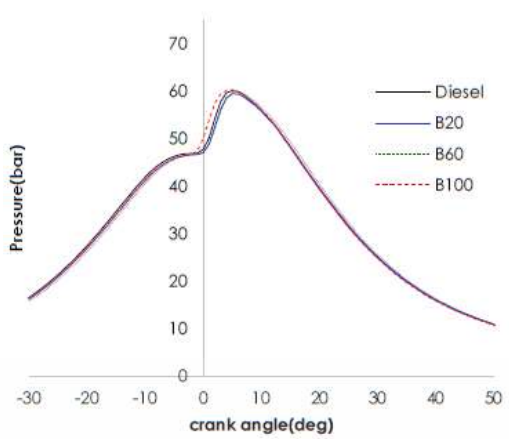


Figure 1. (a) Engine performance, (b) Brake specific fuel consumption (BSFC), (c) Brake thermal efficiency (BTE), and (d) Exhaust gas temperature (EGT) at the engine speed of 2000 rpm.

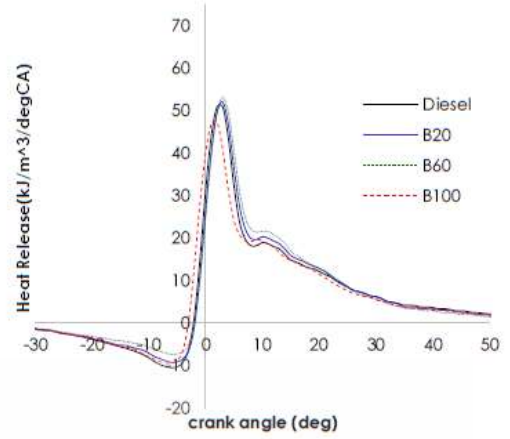


In-cylinder pressure variation with respect to crank angle is shown in Fig. 2, and heat release rate in Fig. 3. The engine load was varied in the range of 0.2 MPa, 0.4 MPa, and 0.6 MPa at constant engine speed of 2400 rpm. Peak pressures of all fuels increase with the increasing engine load. Considering the biodiesel at 0.2 MPa and 0.4 MPa BMEP load, the pressure rises of biodiesel before reaching peak pressure occurs prior to the diesel. This is the effect of higher oxygen fraction in fuel promote faster combustion. At higher engine load, the increase of combustion temperature cause better fuel vaporization for both fuels, so there is no significant in pressure rise with respect to crank angle.

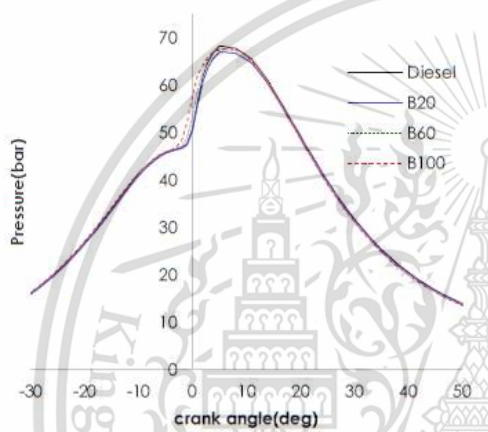
Heat release rate plots show that combustion processes of all fuels start with ignition delay, premixed combustion phase, and followed by diffusion combustion phase. At same start of injection of 19° CA bTDC in the condition of 0.2 MPa and 0.4 MPa BMEP load, biodiesel has shorter ignition delay, while a higher peak of the heat release can be observed on diesel on all load conditions. From fuel properties of biodiesel, density and auto ignition temperature was negative impact with shorter ignition delay, so oxygen fraction is that mainly effects of shorter ignition delay than diesel fuel. The reason is that low temperature in the low load condition with higher oxygen fraction causes the biodiesel start combustion earlier. However, longer ignition delay in diesel causes enough fuel atomization and mixing with oxygen, so it produces higher peaks of heat release rate. In addition, it is also well-known that the high bulk modulus of the biodiesel makes the injection timing earlier in the case of mechanical injection system, which may advance the auto-ignition timing.



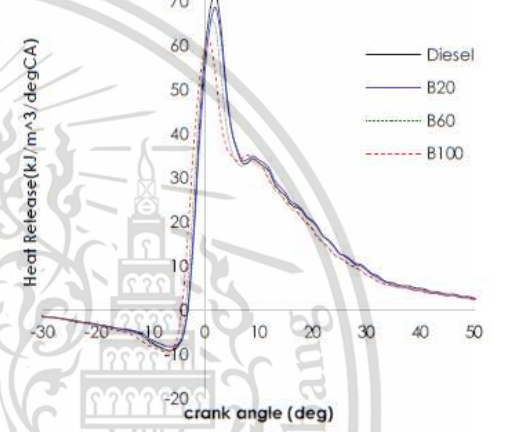
(a) 0.2 MPa BMEP



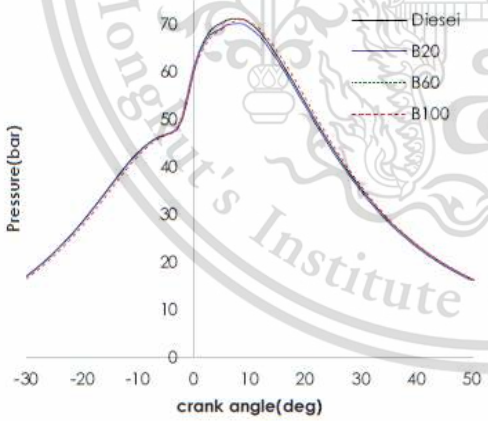
(a) 0.2 MPa BMEP



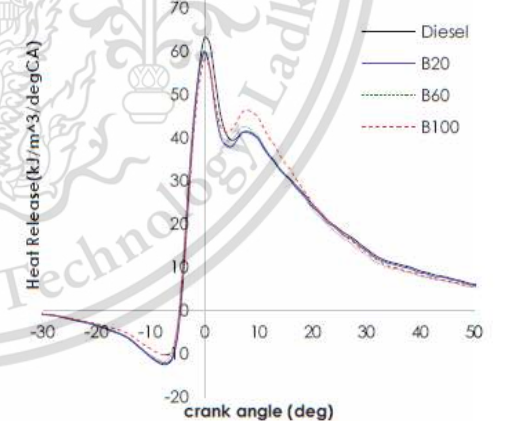
(b) 0.4 MPa BMEP



(b) 0.4 MPa BMEP



(c) 0.6 MPa BMEP

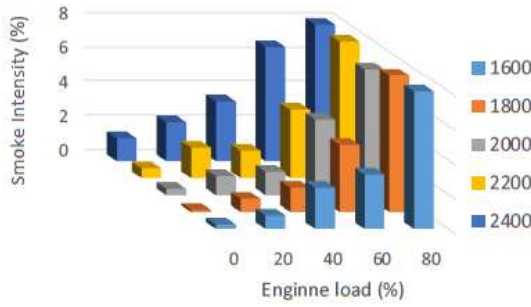


(c) 0.6 MPa BMEP

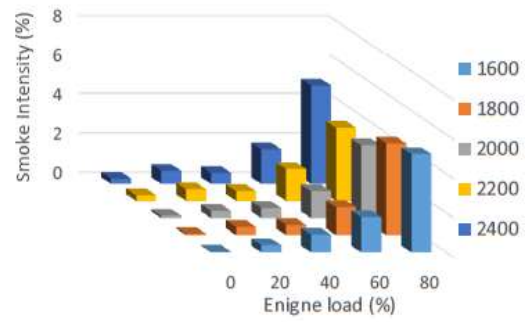
Figure 2. In-cylinder pressure versus crank angle at engine speed of 2400 rpm, (a) 0.2 MPa BMEP, (b) 0.4 MPa BMEP and (c) 0.6 MPa BMEP.

Figure 3. Heat release rate versus crank angle at engine speed of 2400 rpm, (a) 0.2 MPa BMEP, (b) 0.4 MPa BMEP and (c) 0.6 MPa BMEP.

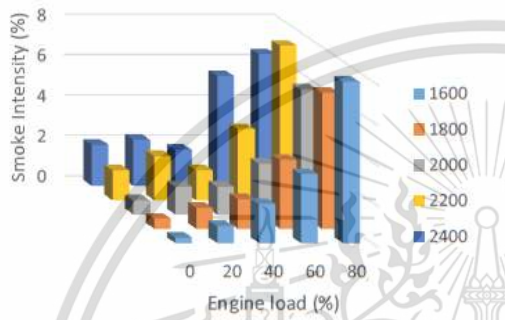
SETC2017



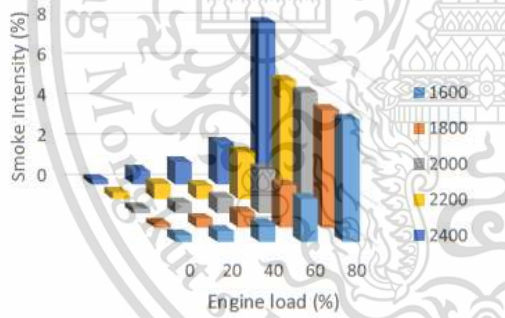
(a) Diesel engine's particulate matter



(d) B100 engine's particulate matter



(b) B20 engine's particulate matter



(c) B60 engine's particulate matter

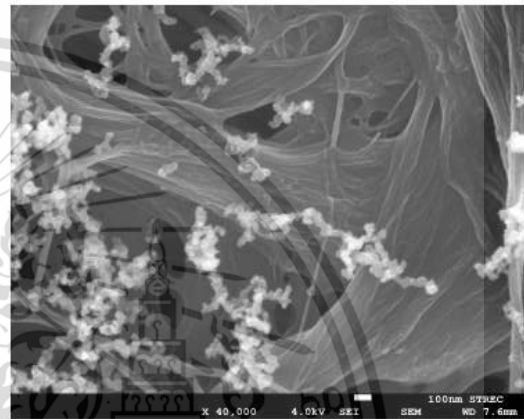


Figure 5. SEM image of diesel engine's fine particle emission in the condition of 80% load engine operation.

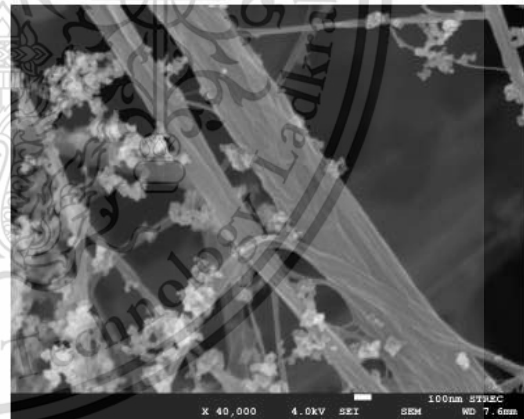


Figure 6. SEM image of B100 engine's fine particle emission in the condition of 80% load engine operation.

Figure 4. Quantity of (a) diesel (b) B20 (c) B60 and (d) B100 engine's PM using opacity smoke meter in each engine load and engine speed operation condition.

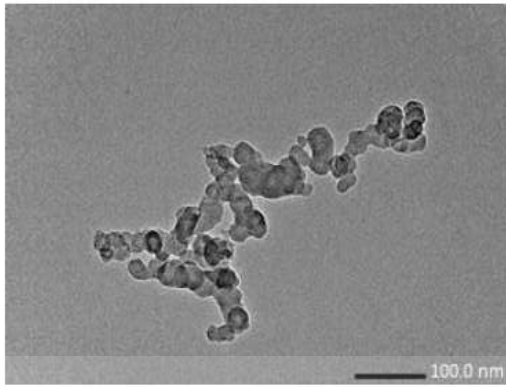


Figure 7. TEM image of diesel ultrafine particle emission in condition 80% load operation.

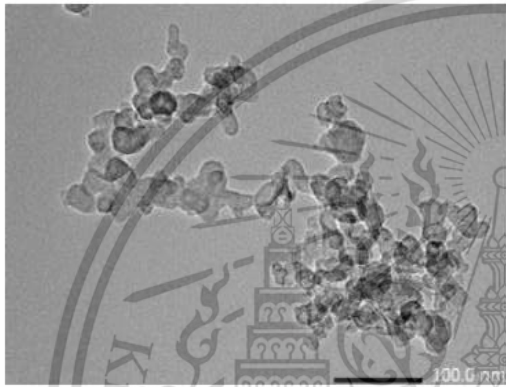


Figure 8. TEM image of B100 ultrafine particle emission in condition 80% load operation.

Particle Emission Characteristics

Figure 4 shows measurement results of smoke intensity which is an indirect method to estimate PM's quantity. The intensity is strongly dependent on the engine load. The more engine load, the greater smoke intensity due to more fuel supply for combustion. In this research, much amount of particle was used to determine the integrity of combustion process. The biodiesel produces less smoke than the diesel at almost all engine operating conditions because oxygenated fuel promote more complete combustion and better fuel-oxygen's reactivity.

Morphology and nanostructure of the PM were investigated by electron microscopy. Some PM's types were found on the paper filters such as fine particles and ultrafine particles. Ultrafine particles of diesel and biodiesel engine's PM consist of many single nanoparticles. Figure 5 and 6 show fine particle of diesel and biodiesel in the condition of 80% (engine torque of 38 Nm) load engine operation, respectively.

Agglomerated ultrafine particles of diesel and biodiesel engine's PM was also clearly observed using TEM as shown in Fig. 7 and 8, respectively. The average agglomerated ultrafine particle diameter size are in the range of 50-500 nm. Primary nanoparticles of diesel and biodiesel

SETC2017

engines was also clearly observed using TEM as shown in Fig. 9 and 10, respectively. The average primary nanoparticle diameter size are in the range of 20-50 nm. Each carbon platelet in the inner core and outer shell of primary nanoparticle was also clearly observed by TEM.

Moreover, TEM image is used for numerate platelet number that aggregate layered in the particle. Each of platelet is consisted properly by carbon atom from incomplete combustion product. Figures 11, 12 and 13 are the images of original 10 nm² focused area, after post processing of two colors and after post processing of skeleton carbon platelet length estimation of diesel fuel. Figures 14, 15 and 16 are the images of original 10 nm² focused area, after post processing of two colors and after post processing of skeleton carbon platelet length estimation of biodiesel, respectively. From the skeleton images, the carbon platelets inside the PM were measured by image processing program. The skeleton carbon platelets, which have 1-unit pixel width for each platelet, were measured for the white area in the image to be a carbon platelet length. The estimated of platelet sizes distribution in each condition are shown in Fig.17 and 18. The average of diesel and B100 PM carbon platelets is in the range of 0.2-5.2 nm.

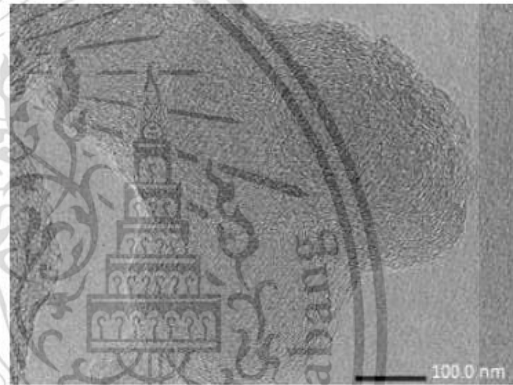


Figure 9. TEM image of diesel primary nanoparticle emission in condition 80% load operation.

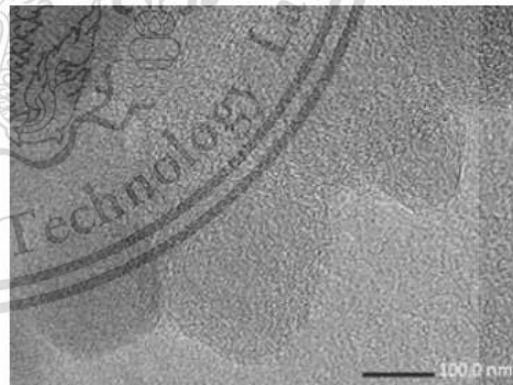


Figure 10. TEM image of B100 primary nanoparticle emission in condition 80% load operation.

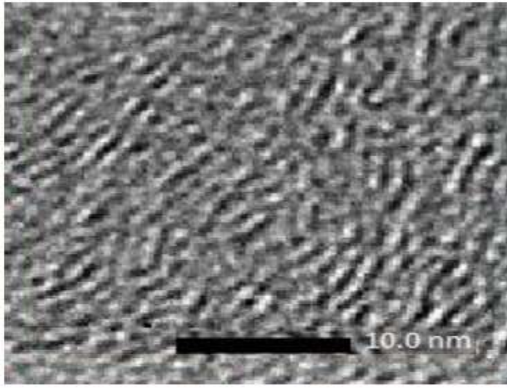


Figure 11. TEM images of engine 80% load operation diesel single PMs.

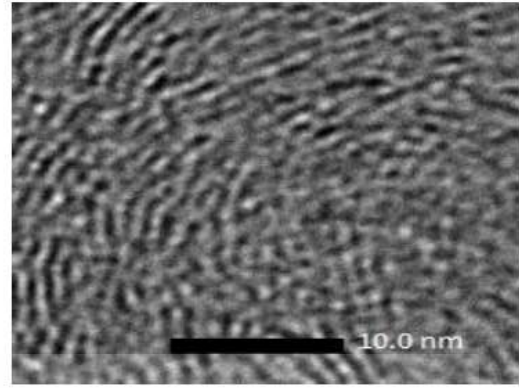


Figure 14. TEM images of engine 80% load operation B100 single PMs.

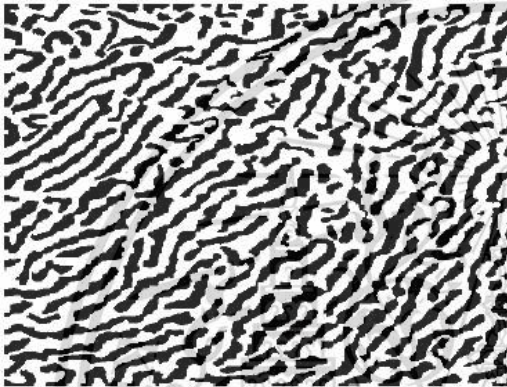


Figure 12. Two colors TEM images post process of engine 80% load operation diesel single PMs 10nm² focused area.

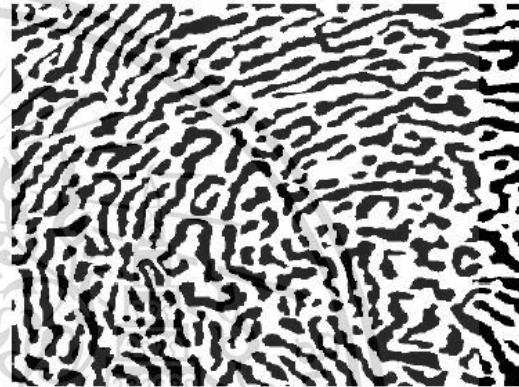


Figure 15. Two colors TEM images post process of engine 80% load operation B100 single PMs 10nm² focused area.

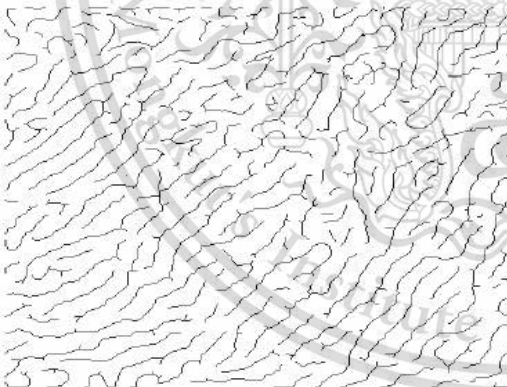


Figure 13. Skeleton TEM images post process of engine 80% load operation diesel single PMs 10nm² focused area.

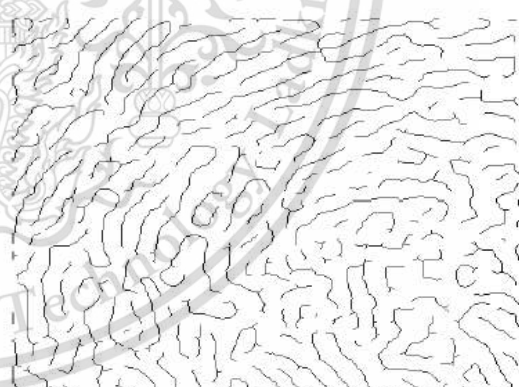


Figure 16. Skeleton TEM images post process of engine 80% load operation B100 single PMs 10nm² focused area.

SETC2017

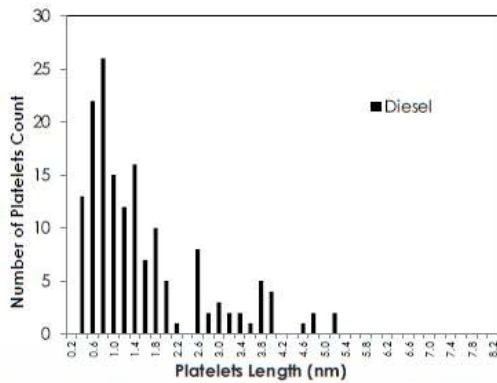


Figure 17. Platelet sizes distribution of diesel PM's carbon platelets.

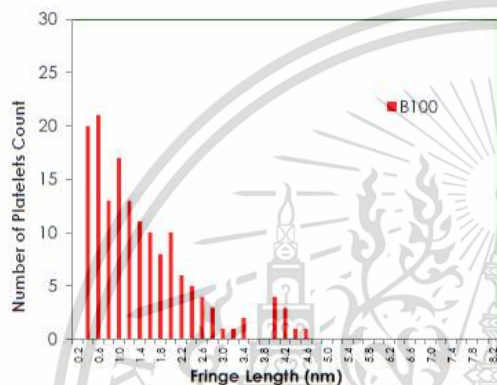


Figure 18. Platelet sizes distribution of B100 PM's carbon platelets.

CONCLUSIONS

The amount of particulate matter emitted from CI engine depend on several variables. The result shows the parameter which has the highest effect on PM quantity is engine load, concentration of biodiesel and engine speed respectively. When increase concentration of biodiesel in fuel, PM reduce because oxygen concentration in fuel increase. Higher concentration of oxygen makes more complete combustion and higher thermal efficiency. The quantities of particulate matter emitted from biodiesel engine are approximately a half of diesel engine's particulate matter. Morphology of CI engine's PM10, PM2.5, ultrafine particle and nanoparticle was characterized using SEM and TEM successfully. The morphology of biodiesel and conventional diesel doesn't have much different in the viewpoint of particulate matter trapping using DPF micro surface pores.

REFERENCES

1. J. B. Heywood, *Internal Combustion Engine Fundamental, McGraw-Hill series in mechanical engineering*, Singapore, (1998).

SETC2017

2. L. Zhu, C. Cheung, W. Zhang, and Z. Huang, Combustion, performance and emission characteristics of a DI diesel engine fueled with ethanol-biodiesel blends. *Fuel*, 90 (5), 1743-1750, (2011).
3. A. S. Ramadhas, S. Jayaraj and C. Muraleedharan, Use of vegetable oils as I.C. engine fuels – a review. *Renew Energy*, 29, 727–42, (2004).
4. M. S. Graboski and R. L. McCormick, Combustion of fat and vegetable oil derived fuels in diesel engines. *Prog Energy Combust Sci*, 24, 125–64, (1998).
5. M.M. Hasan and M.M. Rahman, Performance and emission characteristics of biodiesel–diesel blend and environmental and economic impacts of biodiesel production, *Renewable and Sustainable Energy Reviews*, 74, 938–948, (2017).
6. M. Aldhaidhawi, R. Chiriac and V. Badescu, Ignition delay, combustion and emission characteristics of Diesel engine fueled with rapeseed biodiesel. *Renewable and Sustainable Energy Reviews*, 73, 178-186, (2017).
7. G.K. Prashant, D.B. Lata and P.C. Joshi, Investigations on the effect of ethanol blend on the combustion parameters of dual fuel diesel engine, *Applied Thermal Engineering*. 96, 623–631, (2016).
8. G. Sakthivel and N. Saravanan and M. Ilankumar, Influence of injection timing on performance, emission and combustion characteristics of a DI diesel engine running on fish oil biodiesel, *Energy*, 116, 1218-1229, (2016).
9. G. Gonca and E. Dobrucali, Theoretical and experimental study on the performance of a diesel engine fueled with diesel-biodiesel blends, *Renewable Energy*, 93, 658-666, (2016).
10. P. Karin, H. Oki, K. Hanamura and C. Charoenphonphanich, Nanostructures and Oxidation Kinetics of Diesel Particulate Matters, *Journal of Research and Applications in Mechanical Engineering*, 1(2), 3-8, (2012).
11. P. Karin, M. Borhanipour, Y. Songsaengchan, S. Laosuwan, C. Charoenphonphanich, N. Chollacoop and K. Hanamura, Oxidation kinetics of small CI engine's biodiesel particulate matter. *International Journal of Automotive Technology*, 16(2), 211-219, 2015.
12. P. Karin, J. Boonsakda, K. Siricholathum, E. Saengkhumvong, C. Charoenphonphanich and K. Hanamura, Morphology and oxidation kinetics of CI engine's biodiesel particulate matters on cordierite Diesel Particulate Filters using TGA. *International Journal of Automotive Technology*, 18(1), 31-40, (2017).
13. T. Ishiguro, Y. Takatori and K. Akihama, Microstructure of diesel soot particles probed by electron microscopy: First observation of inner core and outer shell. *Combustion and Flame* 108(1), 231–234, (1997).
14. R. L. Vander Wal, A. Yezerets, N. W. Currier, D. H. Kim and C. H. Wang, HRTEM study of diesel soot collected from diesel particulate filters, *Carbon*, 45(1), 70–77, (2007).
15. D. B. Kittelson, Engines and nanoparticles: A review. *J. Aerosol Science*, 29(5-6), 575–588, (1998).

ACKNOWLEDGMENTS

The authors gratefully acknowledge the support from Bangchak Corporation Public Co., Ltd., FOCUSLAB Ltd., Thailand Research Fund (TRF), KMITL and NSTDA.



May 23 (Wed.)

- | | |
|--|--|
| <p>026 Path Planning Algorithm via General Graph Optimization
Teruya Yamaguchi (DENSO)
Yasuhiko Mukai · Atsushi Baba (DENSO)</p> <p>027 Detection of the Vehicle Speed and Acceleration Recorded in an Aerial Video by using the Polynomial Approximation of Vehicle Position
Tsubasa Imamura (Kyushu University)
Takuma Inoue · Tsuyoshi Yuno · Taketoshi Kawabe (Kyushu University)</p> <p>028 Trajectory Prediction of Surrounding Vehicles Considering Individual Driving Characteristics
Hanwool Wog (The University of Tokyo)
Yunghoon Ji · Yusuke Tamura (The University of Tokyo)
Yasuhide Kuroda · Takashi Sugano · Yasunori Yamamoto (Mazda)
Atsushi Yamashita · Hajime Asama (The University of Tokyo)</p> <p>029 Driving Behavior Analysis of Elderly Driver with Instructor at Merger in Urban Area
Shunya Okuda (Nagoya University)
Takuma Yamaguchi · Yuki Yoshihara · Hirofumi Aoki (Nagoya University)
Misako Yamagishi (Aichi Shukutoku University)
Yoshiki Ninomiya · Eijiro Takeuchi · Hiroyuki Okuda · Tatsuya Suzuki (Nagoya University)</p> | <p>034 Effects of Ambient Pressure on Soot Formation from a Gasoline Surrogate Fuel behind a Reflected Shock Wave
Mariko Tanaka (Yokohama National University)
Yuki Nagata · Kazuhiro Ishii (Yokohama National University)
Yoshimitsu Kobashi (Hokkaido University)</p> <p>035 Study on Soot Formation Model for Gasoline Surrogate Fuel
Kazuhiro Akihama (Nihon University)
Hirohisa Yui · Yuki Namai · Kazuya Iwata · Osamu Imamura (Nihon University)
Kazuhiro Ishii (Yokohama National University)
Jun Hashimoto (Oita University)</p> <p>036 Analysis of PM Formation from Unsteady Pool Combustion using Thermogravimetric Method
Tatsuya Kauri (Tokyo Denki University)
Yoshihiro Kobayashi · Masataka Arai (Tokyo Denki University)</p> |
| [14:10~16:15] | |
| <p>7 Effect of Automobile Emission on Atmospheric Environment and Control Technology of Automobile Emission I
<OS> Hiroyuki Yamada (Tokyo Denki University)</p> | <p>9 Effect of Automobile Emission on Atmospheric Environment and Control Technology of Automobile Emission III
<OS> Shinichiro Okayama (Nissan Motor)</p> |
| 303 (3F) | |
| <p>[9:30~10:45]</p> <p>030 Characterization of Hydro-Treated Vegetable Oil Combustion Behavior and Particle Emission Nanostructure
Sippakorn Rungseritanapaisan (KMITL)
Pop-Paul Ewphun (Tokyo Institute of Technology)
Preechar Karin (KMITL)
Hidenori Kosaka · Susumu Sato (Tokyo Institute of Technology)
Nuwong Chollacoop (NSTDA)</p> <p>031 Impact of TiO₂ on Sintered Mullite Porous Surface Microstructure using Scanning Electron Microscopy and Image Processing
Settavit Sirivarocha (KMITL)
Preechar Karin (KMITL)
Katsumori Hanamura (Tokyo Institute of Technology)
Nuwong Chollacoop (NSTDA)
Eakkawat Saenkhumwong (KMITL)</p> | <p>037 A Study of the Improvement in Measurements of Soot and Particle Emissions from a DI Gasoline Engine
Qian Xiong (Chiba University)
Takuya Takeda (Nihon University)
Tatsuya Kuboyama · Yasuo Moriyoshi (Chiba University)
Kazuhiro Akihama (Nihon University)
Jun Hashimoto (Oita University)
Hisakazu Suzuki (Chiba University)</p> <p>038 Analytical Approach for Identifying Sources of Microparticles Generated in a Gasoline Direct-Injection Engine
Yasuyuki Kiya (SUBARU)
Akira Ogura · Yoichi Saito · Shota Tobe · Yumi Suzuki · Shuhei Kawashima · Kazuhiro Saiki · Toshihiro Maeda · Yu Kanamaru (SUBARU)
Kenji Takeda · Kunio Tabata · Kazuya Tsurumi (Horiba)</p> <p>039 Development of Sheet Metal Turbine Housing for Diesel Engine
Satoru Yokoshima (Calsonic Kansei)
Shunichi Mitsubishi · Hiroyuki Okamoto (Calsonic Kansei)</p> <p>040 Development of a Method for Visualization and Simulation of Refueling in a Vehicle
Takumi Hasegawa (SUBARU)
Tetsuya Kaneko · Yusuke Yamaguchi (SUBARU)
Tien Vu Dinh (SUBARU TECHNO)</p> |

Impact of TiO₂ on Sintered Mullite Porous Surface Microstructure using Scanning Electron Microscopy and Image Processing

Settavit Sirivaracha ¹⁾ Preechar Karin ¹⁾ Eakkawut Saenkhumvong ²⁾

Nuwong Chollacoop ³⁾ and Katsunori Hanamura ⁴⁾

1) International College, King Mongkut's Institute of Technology Ladkrabang
Ladkrabang, Bangkok, 10520, Thailand

2) Faculty of Engineering, King Mongkut's Institute of Technology Ladkrabang
Ladkrabang, Bangkok, 10520, Thailand

3) National Metal and Materials Technology Center (MTEC), National Science and Technology Development Agency (NSTDA),
Klong Luang, Pathumthani, 12120, Thailand

4) Department of Mechanical Engineering, Tokyo Institute of Technology
1-44-18 Haya-miya, Netsumi-ku, Tokyo, 179-0085, Japan

ABSTRACT: Diesel combustion exhaust is source of particulate matter emitted to the atmosphere, which is component of air pollution that implicated in human health. Particulate matter should be removing from the exhaust gas before emitted to the atmosphere. This study is investigating particulate matter morphology and nanostructure by using electron microscope. Study primary size and agglomerate size of particulate matter by using image processing. The results can be used for basic information to develop the fabrication process of acicular mullite filter in order to study particulate matters trapping and oxidation mechanisms of combustion ignition engine.

KEY WORDS: heat engine, diesel particulate matter, particulate matter, morphology and nanostructure, acicular porous media.

(A1)

1. INTRODUCTION

Among compression ignition engines, diesel engines have high thermal efficiency than spark ignition engines when consider at the same engine loads. This is due to its higher compression ratio and inherent lean combustion¹⁾. However, diesel engines emitted much exhaust gas emissions, especially NO_x and particulate matter (PM). PM is one of important emission that affects to atmosphere and human health²⁾. This must be removed from exhaust gas emissions ahead of releasing a global environment. From this reason, diesel particulate filters (DPF) plays an importance in a role of diesel aftertreatment system in order to suppress the kind of PM³⁾.

DPF is generally made of ceramic materials such as SiC and cordierite, mullite and metal. Recently, using the lattice Boltzmann method, particulate trapping and chemical reaction were evaluated the DPF structure, the results of SEM images of trapped particulates, provide sufficient information to design and develop DPF, and the concept of low backpressure filtration⁴⁻⁶⁾. In order to approach the DPF design and trapping mechanism, it is necessary to understand the particulate trapping behavior of filtration surface and performance.

From previous researches through microscopic visualization experiments were studied, using diesel particulate membrane filter (DPMF) as the nanoparticle membrane sintered on the DPF wall surface instead of the soot cake⁷⁾. This can improve filtration performance and efficiency at the beginning of trapping process and reduce energy consumption during the regeneration process⁸⁾.

From previous researches showed that the DPMF has a membrane composed of SiC nanoparticles with mixed sizes of 80 and 500 nm, sintered on the conventional DPF at 1700 °C. The membrane has a wall thickness of 20 μm and porosity of 60%. Moreover, in the case of the DPMF, the diesel particulates are trapped by fine surface pores. The soot cake of DPMF is developed faster than in the case of conventional DPF with porosities of 42%, due to the very fine and very shallow surface pores⁹⁾. The particulates trapped inside the fine surface pores of the membrane and large surface pores of the conventional DPF decrease gradually with time along the contours of the pores.

Even though several researches reported on DPF filter with various types of material filter, but there is currently insufficient evidence to support the filter with additive TiO₂ is appropriately for DPF system, and further research is needed to investigate the operation of mullite porous surface. Especially, the design of the

mullite porous media by addition of TiO_2 . The additive TiO_2 is helpful to increasing porosity for trapping mechanism design in the DPF surface.

Therefore, this paper aimed to investigate the porosity and pore size distribution of acicular porous mullite. The sintering process at various sintering times and temperatures were implemented. The images of filtration surface were practically investigated using scanning electron microscopy (SEM) with a constant amount of TiO_2 . Moreover, various amounts of carbon black were used to study whatever affecting the porosity. The image processing of two-color image was done by "Image J" program.

2. METHODOLOGY

2.1. Particulate matter morphology and nanostructure

Particulate matter (PM) consists of microscopic solids or liquid droplets which are so small size that can cause serious health problems. Particulate matter is the most important characteristics of diesel emissions which is responsible for black smoke traditionally associated with diesel powered vehicles. Diesel particulate matter emission is usually abbreviated as PM or DPM. Size of PM particles can be classified into various types. Particles normally found in the atmosphere can be derived into four types: PM_{10} , fine particles, ultrafine particles and nanoparticles³². The particle size is an important factor as considerable as PM smaller than $2.5 \mu\text{m}$. The particles smaller than $2.5 \mu\text{m}$ constitute more than 90% by mass of the total PM in the diesel exhaust. Composition of PM collected on a filter. The various components adsorbed on the surface of spherical soot particles³³. From this reason, PM particles must be removed before releasing to the environment. One of technique for removing PM is to develop the trapping mechanism process by enhancement of DPF filter^{33,34}.

2.2. Study and design the filtration to Acicular porous media for using the diesel particulate matter

Figure 1 shows the schematic diagram for designing the filtration. This paper used two main substance to study the filtration; Aluminium oxide (Al_2O_3) and Silicon dioxide (SiO_2). These are mainly in the conventional DPF. The variable substance is Titanium dioxide (TiO_2) which added to investigate the filtration. The carbon black was used to open the porosity of DPF. The substance was weighed in order to ensure the chemical proportion. All substances were ground and mixed together. The mixing substances were pressed pellet. Then, the pellet was sintered in the ceramic sintering furnace under $1200 - 1600 \text{ }^\circ\text{C}$,

holding time 1-3 hr. In addition, the filtration of this paper was the cordierite type with non-catalyst.

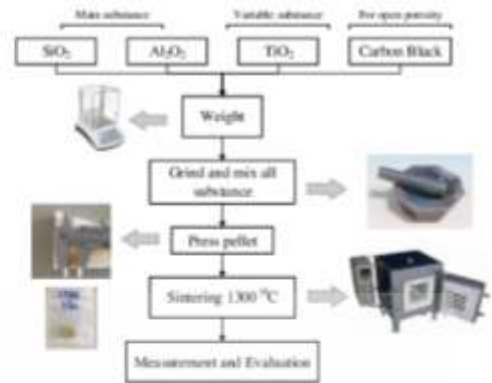


Fig. 1 Schematics diagram for designing the filtration

2.3 Scanning electron microscopy (SEM) and image processing

2.3.1 Scanning electron microscopy (SEM)

The SEM uses a focused beam of electrons to generate a variety of signals at the surface of sample. The signals that derive from electron-sample interactions reveal sufficient information about the sample including morphology, composition, and structure and orientation of materials dressing up the sample. The position of the electron beam on the sample is controlled by scan coils situated above the objective lens. These coils allow the beam to be scanned over the surface of the sample. This beam scanning exhibits the information about area definition on the sample to be collected. As a result of the Electron-sample interaction, a number of signals are built. These signals are then detected by appropriate detectors³⁵.

2.4. Image processing

Figure 3 (a) shows the raw image from SEM. In this paper, the SEM of model JSM-6400 is tungsten filament source, 3.5 nm resolution at 30 kV, magnification of 10-30000, SE and BE detector. The image has 1260×870 pixels. This image was analyzed to find the porosity of filtration surface. Figure 3 (b) shows two-color image. The images were analyzed by image processing with software called "Image J" to measure quantitative data of the porosity size and pore size distribution. The threshold of is set 20-30% of background. The determination of porosity size was evaluated as same as the determination of PM by using SEM³⁶. In this paper, the each point of black color is used to calculate the porosity and pore dimension.

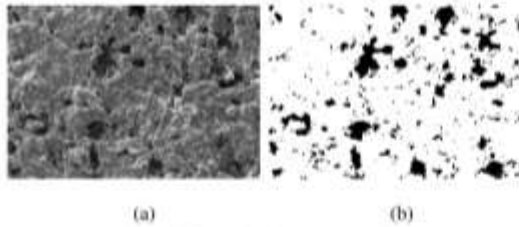


Fig. 3 Two color image processing
(a) Raw image; (b) Black-white image

2.6. Experimental condition

Table 1 shows experimental condition. Four types were implemented; (1) conventional DPF, (2) $\text{Al}_2\text{O}_3 + \text{SiO}_2 + 40\% \text{TiO}_2 + 30\% \text{Carbon black (CB)}$, (3) $\text{Al}_2\text{O}_3 + \text{SiO}_2 + 40\% \text{TiO}_2 + 40\% \text{CB}$ and (4) $\text{Al}_2\text{O}_3 + \text{SiO}_2 + 40\% \text{TiO}_2 + 50\% \text{CB}$. The TiO_2 was applied to study the pore size distribution at a constant amount. The carbon black was varied to study the porosity dimension. The pellet of mixing substance was sintered at various sintering time 1, 2 and 3 hr. The sintering temperatures were varied at 1200-1600 °C to study effects of sintering temperatures on the surface filter.

Sample	Parameters	TiO_2	Carbon black (CB)
(1)	Conventional DPF	-	-
(2)	$\text{Al}_2\text{O}_3 + \text{SiO}_2$	4%wt	30%wt
(3)	$\text{Al}_2\text{O}_3 + \text{SiO}_2$	4%wt	40%wt
(4)	$\text{Al}_2\text{O}_3 + \text{SiO}_2$	4%wt	50%wt

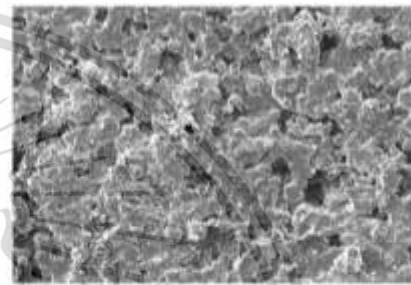
3. RESULTS AND DISCUSSION

This paper aimed to investigate the porosity and pore size distribution of acicular porous mullite. The sintering process at various sintering times and temperatures were tested. The images of filtration surface were practically investigated using scanning electron microscopy (SEM) with a constant amount of TiO_2 . Moreover, various amounts of carbon black were used to study whatever affecting to the porosity. The image processing of two-color image was done by 'Image J' program. The results of an investigation on the sintered mullite porous surface microstructure using scanning electron microscopy (SEM) and image processing were presented in the term of SEM images, two color image, porosity size and pore size distribution.

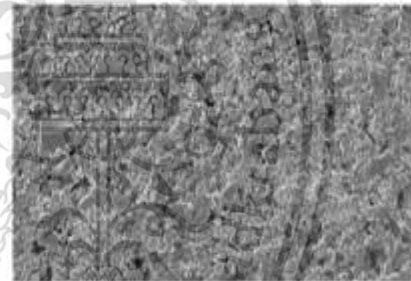
3.1 SEM image

Figure 4 show SEM images of 1300 °C and 1 hr as representative. The images were presented the filtration surface at each sample. It is found that conventional DPF is observed large

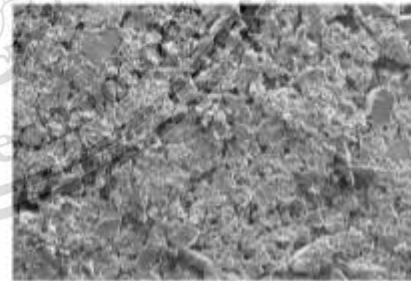
porosity while the addition of TiO_2 with 30%CB is observed much more fine porosity. The addition of TiO_2 with 40%CB and 50% are observed porosity the same as 30%CB. The addition of TiO_2 attributes to increase of porosity quantity as displayed by more narrow porosity compared to conventional DPF. This characteristic contributes to a higher permeability and lower backpressures into DPF^[10]. The addition of TiO_2 has influenced to increase of the fine porosity. The increase of carbon black (CB) has influence to increase of porosity size and dimension. The addition of TiO_2 with 50%CB is observed slightly large porosity size compared to conventional DPF and 40%CB due to carbon black improvement. Consequently, increasing carbon black increases porosity size of the filter. Meanwhile, the additive could improve porosity quantity.



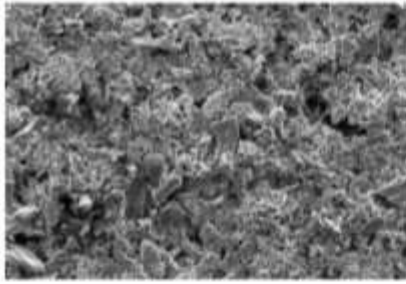
(a) Conventional DPF



(b) $\text{Al}_2\text{O}_3 + \text{SiO}_2 + \text{TiO}_2 + 30\% \text{CB}$



(c) $\text{Al}_2\text{O}_3 + \text{SiO}_2 + \text{TiO}_2 + 40\% \text{CB}$



(d) $\text{Al}_2\text{O}_3 + \text{SiO}_2 + \text{TiO}_2 + 50\% \text{CB}$

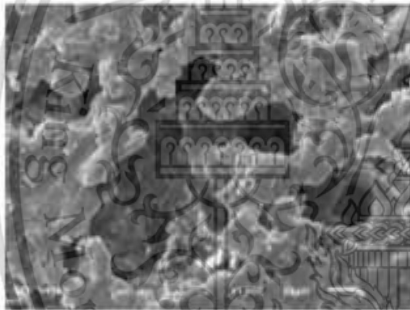
Fig. 4 SEM images of (a) Conventional DPF;

(b) $\text{Al}_2\text{O}_3 + \text{SiO}_2 + \text{TiO}_2 + 30\% \text{CB}$;

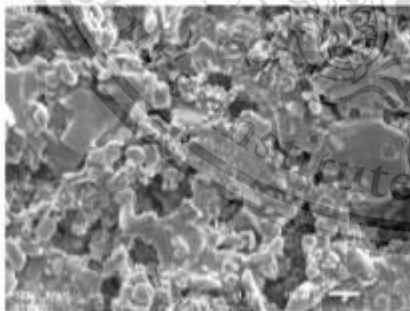
(c) $\text{Al}_2\text{O}_3 + \text{SiO}_2 + \text{TiO}_2 + 40\% \text{CB}$;

(d) $\text{Al}_2\text{O}_3 + \text{SiO}_2 + \text{TiO}_2 + 50\% \text{CB}$

Figure 5 show SEM images of 1300 °C and 1 hr magnification of 1000X as representative. It is found that the size of porosity of conventional DPF is wider compared to among addition of TiO_2 . Moreover, the conventional DPF shows the cube shape at the surface while the addition of TiO_2 is observed the flake shape. This is due to the addition of TiO_2 has influenced to more fine porosity.



(a) Conventional DPF



(b) $\text{Al}_2\text{O}_3 + \text{SiO}_2 + \text{TiO}_2 + 40\% \text{CB}$

Fig. 5 SEM images (1000X) of (a) Conventional DPF;

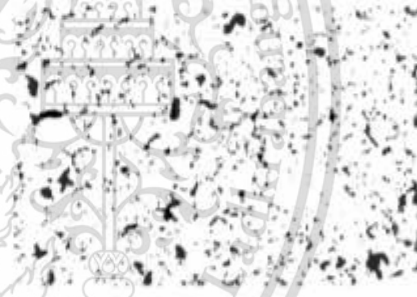
(b) $\text{Al}_2\text{O}_3 + \text{SiO}_2 + \text{TiO}_2 + 40\% \text{CB}$;

3.2 Two color image

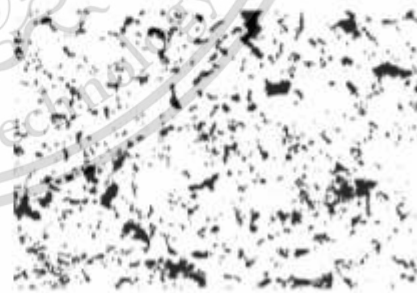
Figure 6 show two color images of 1300 °C and 1 hr as representative. Two color images as black-white images were analyzed by Image J program. The porosity is calculated by the black area of an image. The conventional DPF exhibits explicitly the porosity compared to among additive TiO_2 . Meanwhile, the pore size distribution or black area of among added TiO_2 is higher than conventional DPF. The porosity of additive TiO_2 with 30%CB gives narrower than conventional DPF, 40%CB and 50%CB. Increasing carbon black percentage gives more black area to the images, which also increases the porosity.



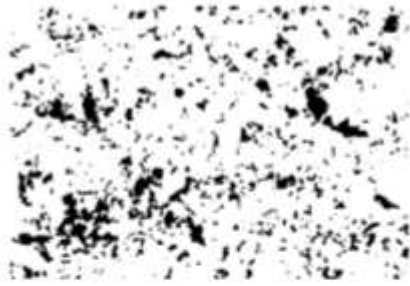
(a) Conventional DPF



(b) $\text{Al}_2\text{O}_3 + \text{SiO}_2 + \text{TiO}_2 + 30\% \text{CB}$



(c) $\text{Al}_2\text{O}_3 + \text{SiO}_2 + \text{TiO}_2 + 40\% \text{CB}$



(d) $\text{Al}_2\text{O}_3 + \text{SiO}_2 + \text{TiO}_2 + 50\%\text{CB}$

g. 6 SEM images (300X) of (a) Conventional DPF;

(b) $\text{Al}_2\text{O}_3 + \text{SiO}_2 + \text{TiO}_2 + 30\%\text{CB}$;

(c) $\text{Al}_2\text{O}_3 + \text{SiO}_2 + \text{TiO}_2 + 40\%\text{CB}$;

(d) $\text{Al}_2\text{O}_3 + \text{SiO}_2 + \text{TiO}_2 + 50\%\text{CB}$

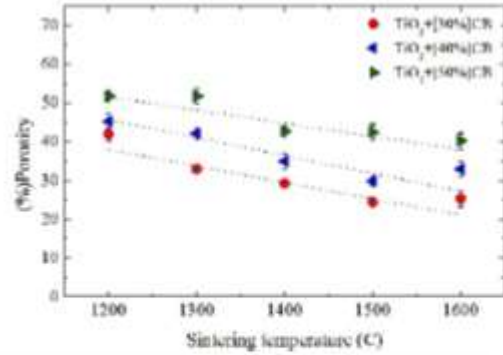


Fig. 7 Effects of sintering temperatures on the porosity

3.3 Porosity

Figure 7 shows effects of sintering temperatures on the porosity. It is found that increasing temperature decreases linearly the porosity because the temperatures obstructed the growth of the pore. Increasing temperature from 1200 to 1600 °C decreases 50.82% in conventional DPF, 33.38% in 30%CB, 22.71% in 40%CB and 14.44% in 50%CB, respectively. On the contrary, increasing carbon black percentage leads to increase the porosity. Increasing carbon black percentage leads to increase 49.03% at 1200 °C, 51.55% at 1300 °C, 69.00% at 1400 °C, 81.05% at 1500 °C and 69.27% at 1600 °C, respectively. Increasing carbon black percentage is not only increased the porosity but also increase pore diameter. This also reduces the mechanical strength of the porosity of the filter.

Figure 8 shows effects of sintering time on the porosity. The sintering times insignificant affect to the porosity. Even though increasing carbon black percentage also insignificant affect to the porosity as high as the addition of TiO_2 . From this reason, this paper focused on the addition of TiO_2 with different carbon black percentage.

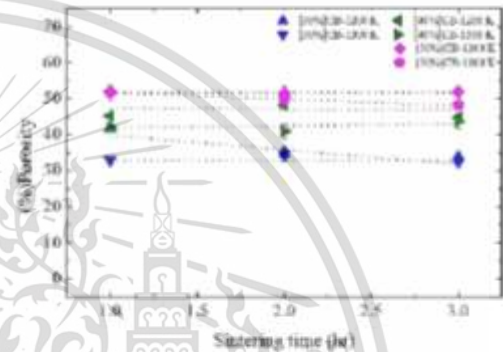


Fig. 8 Effects of sintering times on the porosity

3.4 Pore size distribution

Figure 9 illustrates the average pore size distribution of the sample under 1300 °C and 4 hr as representative. The pore size distribution of conventional DPF and among additive TiO_2 were compared and calculated from average diameter of black area. From this figure, it is found that almost pore size distribution was observed between 2-10 μm . The diameter of 2-10 μm shows the highest count number of pore size distribution. The pore size

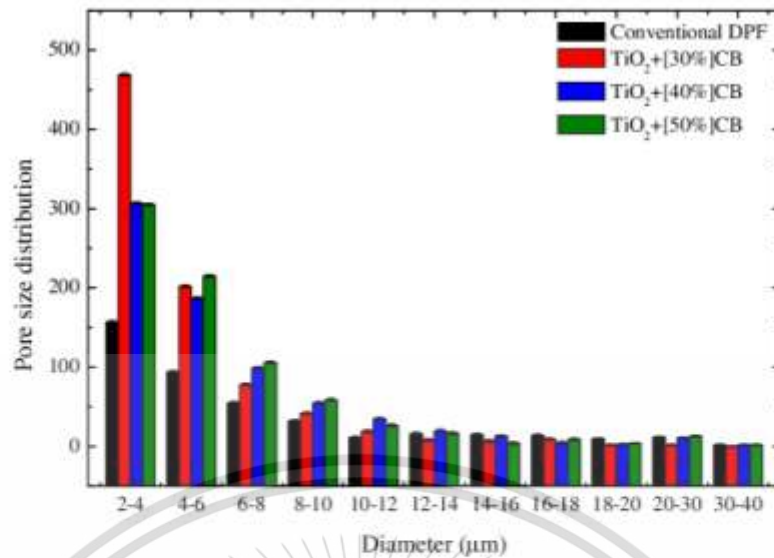


Fig. 9 Pore size distribution at 1300 °C and 1 hr

distribution is hardly to find the count number at the large diameter. Moreover, the porosity of among addition of TiO₂ have higher than conventional DPF around 2 times in the case of 2-4 µm diameter due to the formation and growth of stiff skeleton needle-like mullite crystals. Increasing pore quantity also increases the efficiency of filtration. In fact that the small pore diameter affects effectively to the filtration efficiency and pressure drop characteristics in DPF^[14]. Increasing carbon black percentage lead to increasing pore size distribution in the surface filter. The pore diameter of additive TiO₂ with 30%, 40% and 50% have higher 66.52%, 48.86% and 48.52% compared to conventional DPF. In addition, the small pore size might contribute to easier to trapped PM but might attribute to obstruct the gas flow.

4. CONCLUSION

This paper investigated porosity and pore size distribution of acicular mullite. The conventional DPF and mullite added TiO₂ were investigated using scanning electron microscopy (SEM) and image processing. The effects of sintering times and temperatures were investigated. The image processing was done by using Image J program. The conclusion can be expressed as follows:

(1) The sintering temperatures have largely affected to decreasing the porosity as much as increasing sintering temperatures. However, the sintering times insignificant affect to the porosity.

(2) The addition of TiO₂ provided fine porosity, and higher porosity quantity into the filtration compared to the conventional DPF. In addition, among TiO₂ also can increase pore quantity. This also increases the filtration efficiency.

(3) The carbon black helped to open the porosity size in the filtration surface that might useful for DPF operation. But increasing carbon black reduced mechanical strength of the filter. So that the optimization of TiO₂ with carbon black composition is needed for further DPF design.

5. ACKNOWLEDGEMENT

The authors would like to thank Thailand Advance Institute of Technology, Tokyo Institute of Technology (TAIST-Tokyo Tech), National Metal and Materials Technology Center (MTEC), National Science Development Agency (NSTDA), Science Technology-Engineering Mathematics, (STEM No. SCA-CO-2560-5106-TH) for providing scholarship, Thailand Research Fund (TRF) for research funding.

REFERENCE

1. Tatsuo T, Akira N, Ryouji N, Katsuhiko S. Approach to High Efficiency Diesel and Gas Engines. Mitsubishi Heavy Ind Ltd. 2008;2008(45):1.
2. Heywood JB. Internal combustion engine fundamentals. New York: McGraw-Hill; 1988. 930 p. (McGraw-Hill series in mechanical engineering).

3. Karin P, Cui L, Rubio P, Tsuruta T, Hanamura K. Microscopic visualization of PM trapping and regeneration in micro-structural pores of a DPF wall. *SAE Int J Fuels Lubr.* 2009;2(2009-01-1476):661-669.
4. Oki H, Karin P, Hanamura K. Visualization of Oxidation of Soot Nanoparticles Trapped on a Diesel Particulate Membrane Filter. *SAE Int J Engines.* 2011 Apr 12;4(1):515-26.
5. Karin P, Hanamura K. Particulate matter trapping and oxidation on a catalyst membrane. *SAE Int J Fuels Lubr.* 2010;3(2010-1-808):368-379.
6. Kittelson DB. Engines and nanoparticles. *J Aerosol Sci.* 1998 Jun;29(5-6):575-88.
7. Tartakovsky L, Aronov B, Zvirin Y. Modeling of the Regeneration Processes in Diesel Particulate Filters. *Energy Power.* 2012 Dec 1;2(5):96-106.
8. Schematics of scanning electron microscopy operation [Internet]. Available from: <http://i155-94.members.linode.com/myscope/sem/practice/principles/layout.php>
9. Park W, Preechar K, Chinda C, Jiramed B, Katsunori H, Nuwong C. Impact of Diesel Engine Combustion Characteristics on Particulate Matter's Morphology and Nanostructure from Ethanol-blended Biodiesel.
10. Stewart ML, Gallant JR, Kim DH, Manpat GD, Zelenyuk A. Fuel efficient diesel particulate filter (DPF) modeling and development. Pacific Northwest National Laboratory (PNNL), Richland, WA, (US); Environmental Molecular Sciences Laboratory (EMSL); 2010.
11. Akiyoshi N, Kenichi I, Osamu Y, Kazuya T, Kouzou U, Tetsuro T, et al. Development of Innovative Diesel Particulate Filters based on Aluminum Titanate. Design and Validation. RD Rep "SUMITOMO KAGAKU" 2011(2).

CALL FOR PAPERS

TSAE to host Asia-Pacific Automotive Engineering Conference in Bangkok
Society of Automotive Engineers - Thailand (TSAE), is proud to host the biennial 20th Asia-Pacific Automotive Engineering Conference (APAC-20), a conference of *Next Revolution in Automotive Industry* from 1-4 April, 2019 in Bangkok, Thailand.
This biennial conference will congregate experts on these subjects, provide ideal platform for exchanging ideas as well as opportunity to broaden network in an environment where west and east auto industry meet and prosper. The conference will be held in conjunction with 40th Bangkok International Motor Show and exhibition for local as well as international automotive engineering and testing companies.

Important Dates

Abstract submission:
September 15, 2018
Acceptance Notification:
September 30, 2018
Manuscripts Submission:
December 4, 2018
Final manuscripts acceptance notification:
January 25, 2019
Paper Presented:
April 1-3, 2019

Technical Topics

1. BEV/HEV/PHEV/FCEV Technologies
2. ADAS/Autonomous /ITS /Connected Vehicles Technologies
3. Internal Combustion Engine Technology
4. Advanced Transmission System and Drive line/Chassis Systems and Integration
5. Vehicle Design, Development and Testing
6. Vehicle Safety Technologies
7. Advance Vehicle Manufacturing, New Materials and Lightweight Technologies



Asia-Pacific Automotive Engineering Conference

BEST PAPER AWARD

Presented to

Settavit Sirivarocha

for the paper entitled

Impact of TiO₂ and V₂O₅ on Sintered Mullite Porous Microstructure and Soot Oxidation Kinetics Using SEM and TGA

Thiboodee Harnprasert
TSAE President

Given at Bangkok Thailand
April 3, 2019

Impact of TiO_2 and V_2O_5 on Sintered Mullite Porous Microstructure and Soot Oxidation Kinetics using SEM and TGA

Settavit Sirivaracha, Preechar Karin, Eakkawut Saenkhumvong
King Mongkut's Institute of Technology Ladkrabang, Thailand

Nuwong Chollacoop
National Science and Technology Development Agency (NSTDA), Thailand

Katsunori Hanamura
Tokyo Institute of Technology, Japan

Copyright © 2019 SAE International

Abstract

The exhaust emissions from diesel combustion are the sources of particulate matter emitted to the atmosphere, which are components of air pollution that implicated in human health such as lung cancer. At present the diesel particulate filter can remove PM from the exhaust gas before emitted to the atmosphere. This research is investigating morphology and structure of acicular mullite to develop the fabrication process filter in order to study particulate matters trapping and oxidation mechanisms.

This paper used two main substances to study the structure of diesel particulate filter (DPFs): Aluminum oxide (Al_2O_3) and Silicon dioxide (SiO_2). These are mainly in the conventional DPFs. The variable substances are Titanium dioxide (TiO_2) and Vanadium oxide (V_2O_5), which added to investigate and produce the acicular mullite DPFs structure. The mullite samples were sintered at 1300°C with holding time of 1 h. Moreover, a constant amount of carbon black (CB) were used to open the porosity of mullite DPFs. The images of mullite porous microstructure surface were practically investigated using Scanning Electron Microscopy (SEM). The image processing of two-color image was done by using Image J processing program to obtain pore size distribution. In addition, the oxidation kinetics behavior of soot was investigated by using isothermal Thermo-gravimetric analysis (TGA) method.

The results of this paper provided useful information about impact of Titanium dioxide (TiO_2) and Vanadium oxide (V_2O_5) on mullite DPFs. Therefore, the results can be used for the DPFs development of advanced academic and the practical in industry.

Introduction

Particulate matters (PMs) are the significant emissions and contributor to environmental degradation and a drawback of using Compression Ignition (CI) engines. A review of physical and chemical of PMs characterization method have been reported by several researchers [1, 2]. The method to removing typically PMs have been introduced by many researchers. One of suitable technique to restrain PMs from the engines is using Diesel particulate filters (DPFs), which plays an importance in the role of PM trapping and oxidation [3, 4]. DPFs is the after-treatment system which is typically waff-flow

structure, consisting of many rectangular channels with alternate channels blocked using cement at each end. when the exhaust gas passed through the channel of DPFs, the microscale pores will trap the particle emissions as well as technology of DPFs [5]. PM trapping and oxidation processes in the DPFs have been investigated various engine operating condition [2]. PMs must be oxidized to regenerate the DPFs and reduced the back pressure. DPFs can be made by several type of ceramic materials such as cordierite and silicon carbide (SiC). However, researcher try to develop DPFs materials.

Researches have been employed the ceramic mullite and concluded an advantages such as increased porosity and high mechanical strength. The results showed that microstructure of mullite (ML) DPFs is improved by using 4 wt. % Al_2O_3 and 3 wt. % V_2O_5 contents at sintering temperature of 1300°C . The porosity is increased up to 50% [5]. H. Tan [6] showed mullite sintered at 1000°C with 3 h holding time. This study reported that the mullite exhibited acicular mullite (ACM) with 0.06-0.3 μm in acicular diameter.

Previous research has shown that the ML structures have high opened porosity and mechanical strength. However, the investigation on the morphologies, microstructures and mechanical properties of ACM have insufficient data. Further research is needed to provide more evidence to support ACM design throughout the operation and trapping mechanism of DPFs.

The objective of this paper is to investigate the porosity and pore size distribution of mullite with TiO_2 and V_2O_5 additions by using SEM and image processing and to develop the fabrication process of ACM in order to study DPFs structure and oxidation mechanisms. The samples of ML were sintered at constant temperature of 1300°C with a holding time of 1 h. The image processing was done by using the Image J processing program. The compositional analysis of ACM structures was done using SEM combined with an energy dispersive X-ray analyzer (EDX). In addition, Thermo-Gravimetric Analysis (TGA) has been performed to study chemical kinetics of soot oxidation kinetics. The results were presented in terms of morphologies of SEM and two-color image, porosity, pore size distribution, amount of pore percentage of mass conversion and rate of mass change of soot oxidation kinetics.

Page 1 of 8

01/23/2019

Methodology

Materials Fabrication Process

The fabrication process and characterization of ML membrane supports have been investigated in this paper. The structure of mullite is consists of 72wt.% Al_2O_3 and 28wt.% SiO_2 . The Al_2O_3 and SiO_2 are main substances to prepare the chemical structure of ML membrane supports. The TiO_2 and V_2O_5 as additives were used to mix with ML DFFs to prepare ACM structure. Moreover, the TiO_2 and V_2O_5 additions were applied at a constant amount of 10wt.%. This was precisely measured and evaluated for each step of mixing substance by digital weight scale. In addition, carbon black (CB) was also applied to ML DFFs for open porosity at constant amount of 35wt.%.

The schematic diagram of ML fabrication process is shown in Fig. 1. The ML substances of TiO_2 , V_2O_5 and CB were measured to ensure the chemical proportion. The substances were ground and mixed with 5wt.% organic binder PVA-1750 in the manually alumina mortar. The hydraulic press machine at constant pressure of 500 psi was used to press the mixture into cylindrical pellet with approximately diameter of 25 mm, 2 mm in thickness by following experimental conditions, as presented in Fig. 2(a). Then, the cylindrical pellet is ready to sinter at constant heating rate $5^\circ C/min$ by an electrically heated furnace. The ML membrane support was kept at a constant temperature of $500^\circ C$ with holding time of 2 h to eliminate the organic binder PVA-1750. Then, the mullite sample was again heated at heating rate $5^\circ C/min$ with holding time of 1 h until reaching the final sintering temperatures of $1300^\circ C$ as presented in Fig. 2(b).

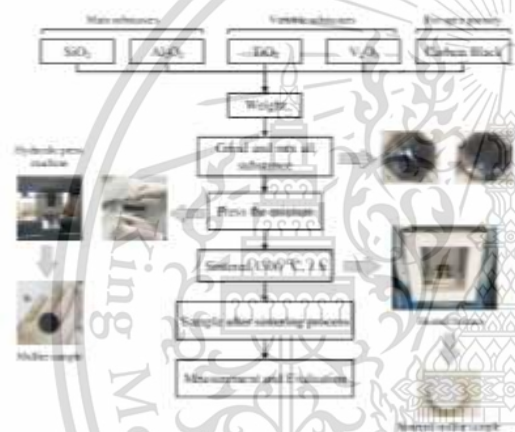


Figure 1. Schematic diagram of mullite fabrication process.



Figure 2. (a) Mullite samples, (b) Sintered mullite samples.

Scanning Electron Microscopy Image Analysis

Scanning Electron Microscopy (SEM, JSM-6400 model) is tungsten filament source, 3.5 nm resolution at 30 kV, magnification of 10-30000, SE and BE detector, was used to observe the ML and ACM structure. Fig. 3 show SEM images (1260 x 870 pixels, 300X) of ML that used to analyze experimental data by image processing analysis using the Image J processing program. Fig. 3a shows the raw image of sintered ML surface. The analytical image was used to measure quantitative data of the porosity and pore size distribution. The threshold of image is defined and setup 20-30% of background. The determination of porosity was evaluated as same as the determination of particle number by using SEM [2]. In this paper, each point of black color is used to fine pore size as illustrated in Fig. 3b.

The analytical data were presented in the term of morphologies of SEM images, porosity and pore size distribution. The porosity percentage is percentage of the black volume to total volume ratio based on Archimedes' principle of water substitution [7]. In addition, the energy dispersive X-ray analyzer (EDX) technique was applied to study and characterize the chemical composition of the ML membrane supports by using SEM after sintered ML membrane supports.

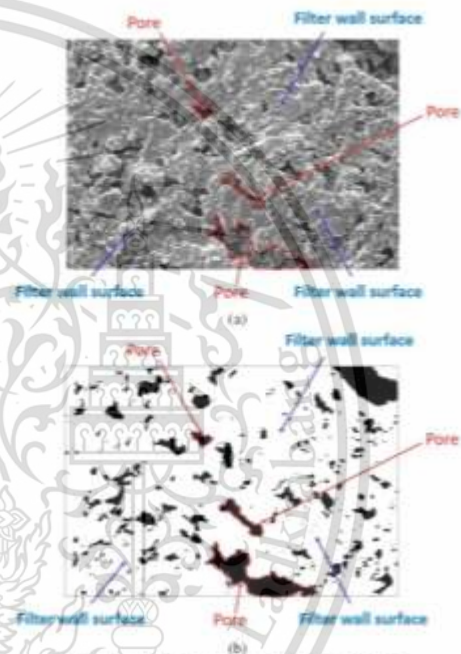


Figure 3. (a) Raw SEM images, (b) Two-color image.

Soot Oxidation Kinetics

The oxidation kinetics behavior of soot was investigated by using TGA method. In this paper, soot is assumed to be the 50wt.% of each sintered ML powder mixed with 50wt.% CB (N-330). The oxidation kinetics of CB was studied based on the soot oxidation kinetics as shown in Karim et al. work [2], [8]. Chemical kinetics of CB on ML

and ACM are studied by using mass conversion behavior. The chemical reaction rate can be calculated from the result of mass conversion curve from TGA analysis, as shown in Eq. (1). Mass conversion can be based on the chemical kinetics, as expressed in Eq. (2). Where PM is mass of samples: (1) 50wt.% CB and 50wt.% ML and (2) 50wt.% CB and 50wt.% ACM mixture, t is time, n and m are the reaction order of soot and oxygen, respectively.



$$-\frac{d[PM]}{dt} = k[C]^n [O_2]^m \quad (2)$$

Experimental Condition

Table 1 shows the experimental condition of this paper. The three different samples were tested and sintered at constant temperature and holding time. TiO_2 , V_2O_5 as additives were used to employ higher porosity and pore number. In addition, the constant amount of carbon black (CB) is used to open porosity of the sample. The samples were (1) Mullite, (2) Mullite with TiO_2 content and (3) Mullite with TiO_2 and V_2O_5 contents as considered as ACM.

Table 1. Experimental condition for sintered mullite membrane supports.

Samples	Substances			
	Mullite	TiO_2	V_2O_5	CB
1	65wt.%	-	-	35wt.%
2	55wt.%	10wt.%	-	35wt.%
3	45wt.%	10wt.%	10wt.%	35wt.%

Results and Discussion

This paper investigated the porosity and pore size distribution of mullite with TiO_2 and V_2O_5 additions by using SEM and image processing and to develop the fabrication process of acicular mullite filter in order to study DPFs structure and oxidation mechanisms. The samples of mullite were successfully sintered at constant temperature of 1300°C with a holding time of 1 h. The image processing was done by using the Image J processing program. The compositional analysis of acicular mullite structures was done using SEM combined with an energy dispersive X-ray analyzer (EDX). Moreover, Thermo-Gravimetric Analysis (TGA) has been individually performed to study oxidation kinetics behavior of soot. Consequently, the results were presented in terms of morphologies of SEM images, porosity, pore size distribution, amount of pore percentage of mass conversion and rate of mass change of soot oxidation kinetics.

Morphologies of Fabricated Porous Mullite

Fig. 4 show the morphologies of SEM images of the sintered ML samples, e.g., TiO_2 (10wt.%) and V_2O_5 (10wt.%) at constant sintering temperature and holding time. The left figure shows SEM images with 300X magnification. The qualitative SEM images is used to analyzed and determined pore size distribution. In the two-color images, the black color indicates the size of pore. It was found that pore size of ML and ML with 10wt.% TiO_2 are the same. The ML with TiO_2 content provides slightly lower number of small pores. However, the ML with 10wt.% TiO_2 and 10wt.% V_2O_5 contents as ACM

observes large pore size and melted grains in the structure [9]. This resulted in high open porosity. The ACM structure is observed with adding V_2O_5 content. This characteristic contributes to a higher permeability and lower backpressures into DPFs configuration [10].

Fig. 5 show effects of TiO_2 (10wt.%) and V_2O_5 (10wt.%) contents on morphologies of mullite DPFs with 35wt.% CB at 1300°C and holding time of 1 h. The left figure shows SEM images with 1000X magnification. The right figure shows 3000X magnification. The mullite DPFs with TiO_2 10wt.% content resulted in more rough surface structures. The results showed that the mullite DPFs with V_2O_5 10wt.% added clearly observed ACM structure, and more ACM quantity.

Porosity

Table 2 shows porosity of the sintered ML samples at constant sintering temperature and holding time. The porosity percentage is percentage of the black volume to total volume ratio based on Archimedes' principle of water substitution [7]. In this figure, ML shows 35.69% porosity while ML with adding 10wt.% TiO_2 increases 4.13% porosity percentage. Moreover, ACM shows 39.82% the highest porosity.

Table 2. Porosity of sintered ML samples.

Samples	Porosity (%)
Mullite (ML)	35.69
ML + 10wt.% TiO_2	39.51
ML + 10wt.% TiO_2 + 10wt.% V_2O_5	39.82

Table 3. Amount of pore of sintered samples.

Samples	Amount of pore
Mullite (ML)	1138
ML + 10wt.% TiO_2	1100
ML + 10wt.% TiO_2 + 10wt.% V_2O_5	507

Table 4. EDX analysis of sintered ML samples.

Condition	Weight (%)						
	C	O	Al	Si	Ti	Na	V
Mullite (ML)	6.54	44.45	27.42	21.24	-	0.35	-
ML + 10wt.% TiO_2	6.32	44.19	34.07	4.93	10.50	-	-
ML + 10wt.% TiO_2 + 10wt.% V_2O_5	4.76	46.72	20.31	11.00	11.04	-	6.17

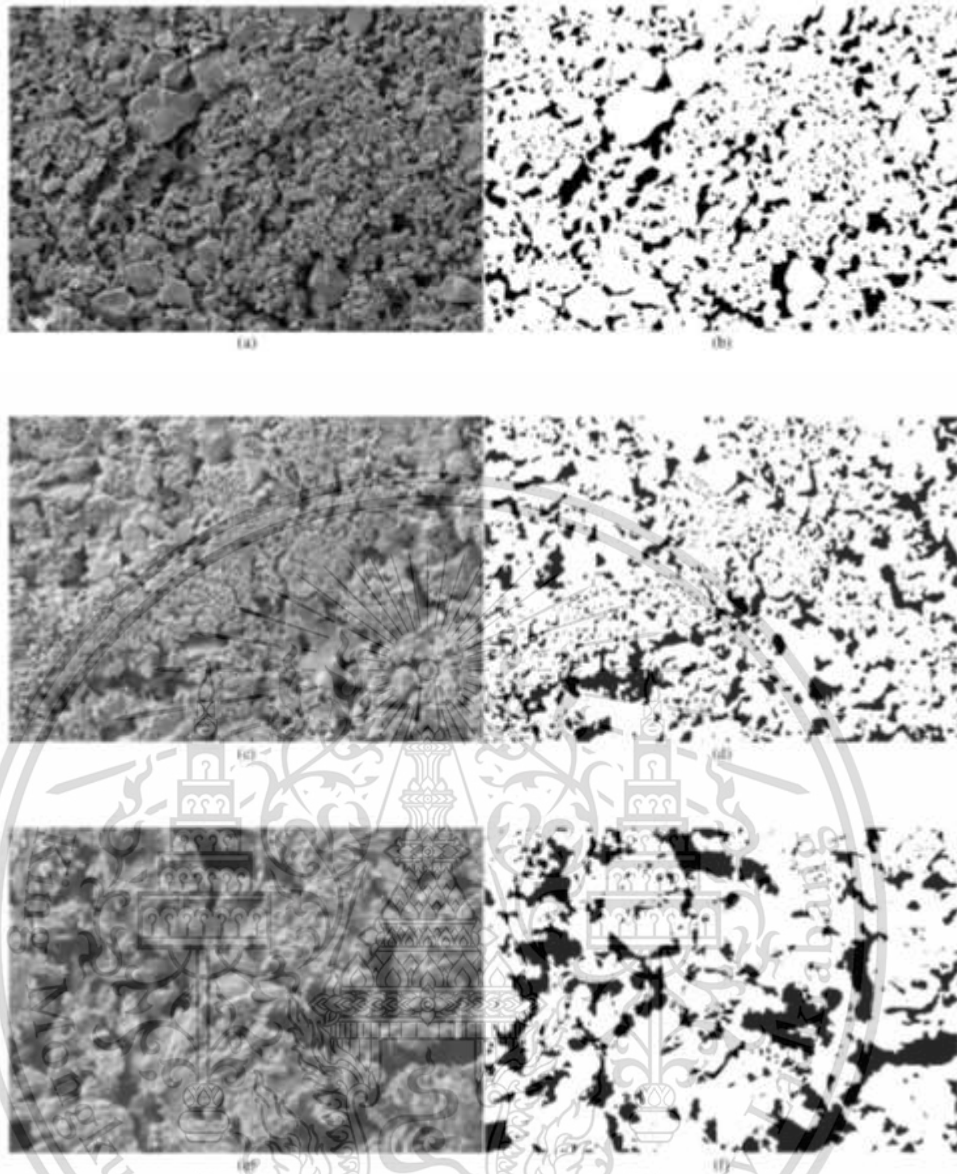


Figure 4. The morphologies of SEM images of the sintered ML samples. (a), (b) ML; (c), (d) ML+10wt% TiO_2 ; (e), (f) ML+10wt% TiO_2 +10wt% V_2O_5 .

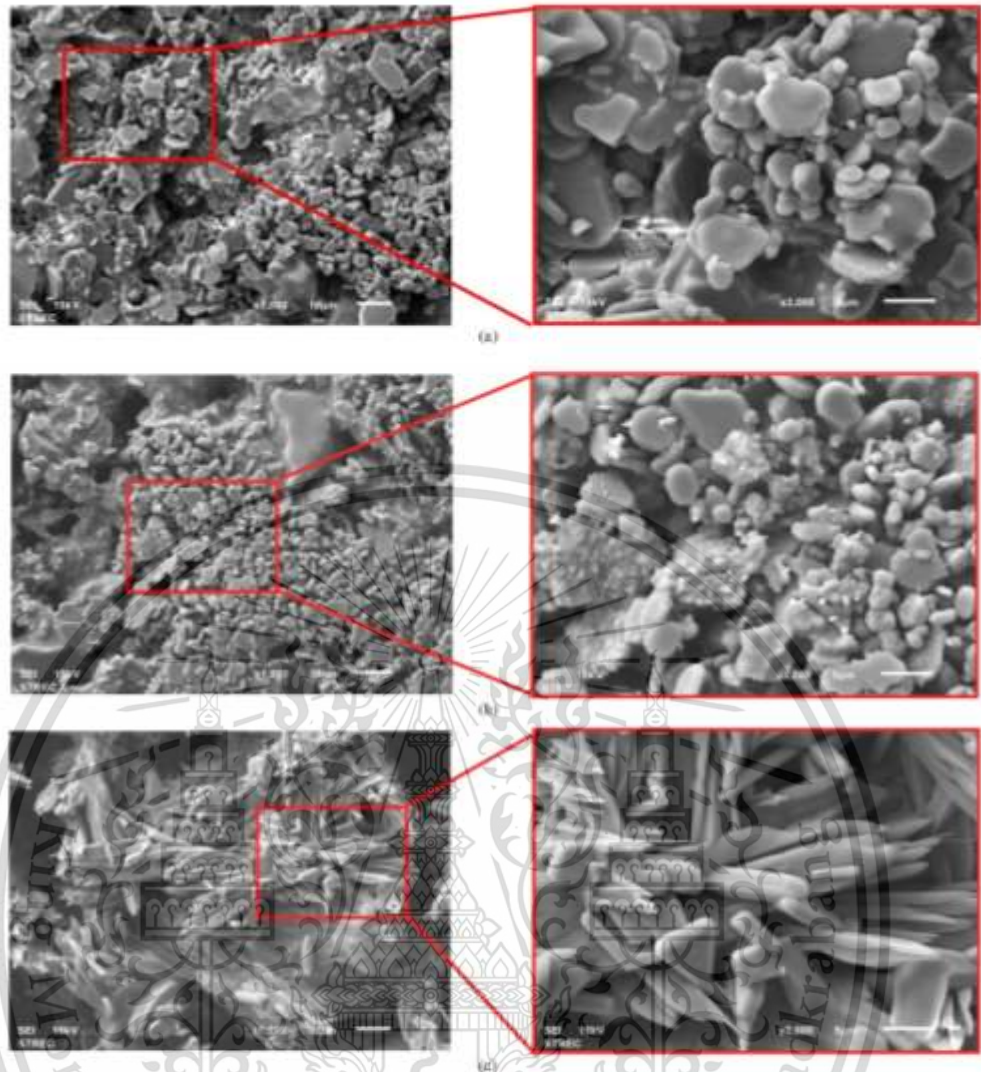
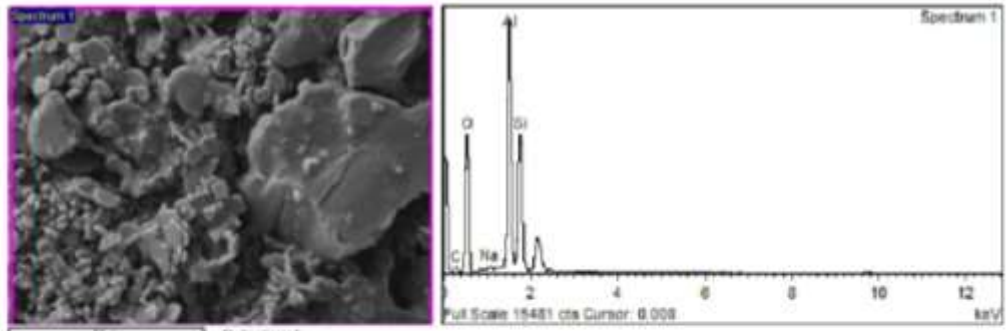
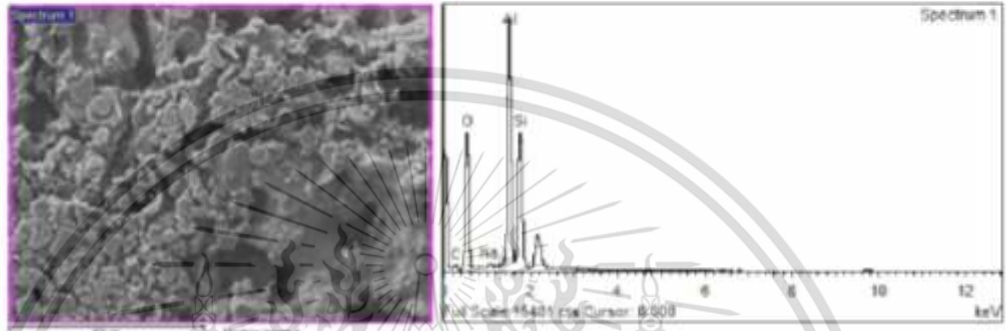


Fig. 5. Morphologies of sintered ML samples at 1300 °C (a) ML, (b) ML+10wt% TiO₂, (c) ML+10wt% TiO₂+10wt% V₂O₅.



(a) Mullite.



(b) Mullite + 10wt.% TiO₂.



(c) Mullite + 10wt.% TiO₂ + 10wt.% V₂O₅.

Figure 6. EDS analysis of (a) Mullite, (b) Mullite + 10wt.% TiO₂, (c) Mullite + 10wt.% TiO₂ + 10wt.% V₂O₅.

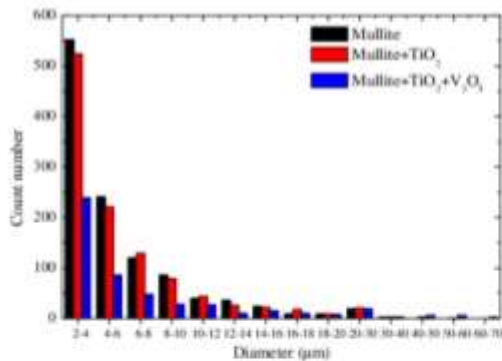


Figure 7. Pore size distribution of fabricated porous mullite.

Energy Dispersive X-ray Analyzer

Table 4 and Fig. 6 show the SEM images combined with EDX analysis of sintered ML sample. The SEM images combined with EDX used to characterize the compositional structure of ACM and to understand the sintered ML samples. The EDX measurement specified as spectrum 1, as shown in Fig. 6. Mostly, the sintered ML samples exhibit O, Al and Si because it is main substance of ML. Moreover, the ACM exhibits 6.17wt.% V.

Pore Size Distribution

Fig. 7 shows pore size distribution of the sintered ML samples. At 2 µm to 10 µm, the higher amount of small pore is observed. In addition, in this range of the pore of ML is slightly higher than ML with TiO₂ content. On the other hand, the ML with adding V₂O₅ observed the lowest amount of pore. This is due to higher porosity. The ML with adding V₂O₅ can created larger pore size at 80 µm to 60 µm due to V₂O₅ enhancement. In addition, the ML with adding V₂O₅ observed largest pore was because V₂O₅ provide more melted grains in the ML structure.

Table 3 shows the amount of pore the sintered ML samples. The ML show highest amount of pore because it observed high amount of small pore. However, when add V₂O₅ the amount of pore reduced about two (µm) because V₂O₅ caused melted grains in structure explicitly. Increasing pore quantity also increases the efficiency of filtration. In fact, that the small pore diameter influences effectively to the filtration efficiency and pressure loss characteristics in DPFs. In addition, the small pore size might contribute to easier to trapped PM but might attribute to obstruct the gas flow.

Soot Oxidation Kinetics

Fig. 8 shows mass conversion of soot oxidation on sintered mullite by using isothermal TGA technique at 600 °C. Soot oxidation on ACM is faster than that of ML due to oxygenated chemical structure in V₂O₅ as seen as the mass conversion is dramatically drop. This is contributes to faster oxidation in DPFs. On the other hand, ML with TiO₂ added made the slowed oxidation compared to ML.

Fig. 9 shows rate of soot mass conversion on sintered ML samples. The results show that the ML with TiO₂ and V₂O₅ as acicular ML show highest rate of soot mass change. This is corresponds to mass conversion results that ACM oxidation is faster than that of ML.

Page 7 of 8

01/23/2019

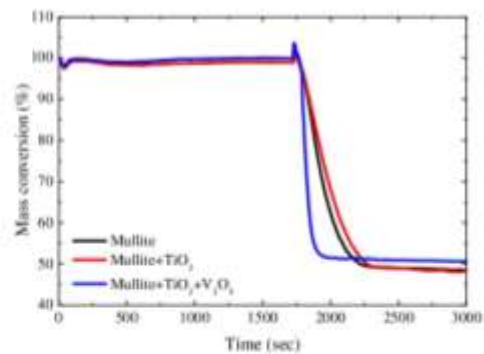


Figure 8. Mass conversion of soot oxidation on sintered ML samples.

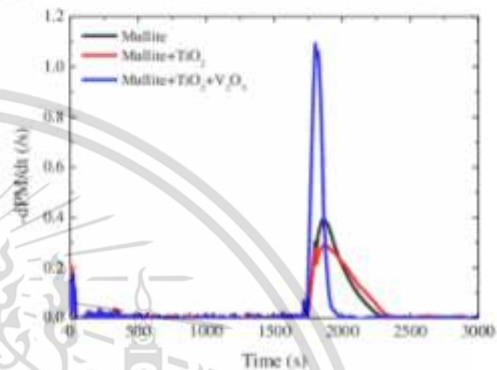


Figure 9. Rate of soot mass conversion on sintered ML samples.

Summary

This paper presented the morphologies and microstructure of mullite DPFs by using SEM and image processing. The effects of TiO₂ and V₂O₅ contents on the mullite structure were investigated. The compositional analysis was done with EDX to analyze the composition of acicular mullite. The image processing was done by Image J program. The oxidation kinetics behavior of soot has been successfully investigated by using TGA.

CB composition required for DPFs configuration design. The 35wt.%CB helps to open the porosity in the mullite microstructure at 1300 °C of sintering temperature. This can be obtained 35%–40% of porosity. The mullite with V₂O₅ content resulted in higher porosity, acicular shape structure and large trapping area. However, the pore size is increase up to 60–70 µm, so that V₂O₅ addition might reduce mechanical strength of the DPFs. In case of acicular mullite, the oxidation of soot is faster than that of non-acicular mullite because acicular shape increasing active site of soot oxidation. Moreover, V₂O₅ on acicular mullite is also play an important role in soot oxidation as catalyst.

Acknowledgments

The authors would like to thank Thailand Advance Institute of Science and Technology, Tokyo Institute of Technology (TAIST-Tokyo Tech).

National Metal and Materials Technology Center (MTEC), National Science Development Agency (NSTDA), Science Technology Engineering Mathematics, (STEM No. SCA-CO2560-5106-TH) for providing scholarship, DEWESOFT (Thailand) Co., LTD. for research supporting. Thailand Research Fund (TRF) for research funding.

Ceramic Society, 34(13):3181-3194, 2014, doi: 10.1016/j.jeurceramsoc.2014.04.011.

10. Stewart, M. L., Gallant, T. R., Kim, D. H., Maupin, G. D., and A. Zelenyuk, "Fuel Efficient Diesel Particulate Filter (DPF) Modeling and Development," PNNL-19476, 991593, 2010.

References

1. Choi, S., Myung, C. L., and Park, S., "Review on characterization of nano-particle emissions and PM morphology from internal combustion engines: Part 2", *International Journal of Automotive Technology*, 15(2):219-227, 2014, doi:10.1007/s12239-014-0023-9.
2. Karin, P., Boonsakda, J., Siricholathum, K., Saenkhumvong, E., Charoenphonphanich, C., and Hanamura, K., "Morphology and oxidation kinetics of CI engine's biodiesel particulate matters on cordierite Diesel Particulate Filters using TGA," *International Journal of Automotive Technology*, 18(1):31-40, 2017, doi: 10.1007/s12239-017-0003-y.
3. Maricq, M. M., "Chemical characterization of particulate emissions from diesel engines: A review," *Journal of Aerosol Science*, 38(11):1079-1118, 2007, doi: 10.1016/j.jaerosci.2007.08.001.
4. Oki, H., Karin, P., and Hanamura, K., "Visualization of Oxidation of Soot Nanoparticles Trapped on a Diesel Particulate Membrane Filter," *SAE International Journal of Engines*, 4(1):515-526, 2011, doi:10.4271/2011-01-0602.
5. Karin, P., Chu, L., Rubio, P., Tsuruta, T., and Hanamura, K., "Microscopic Visualization of PM Trapping and Regeneration in Micro-Structural Pores of a DPF Wall," *SAE International Journal of Fuels and Lubricants*, 2(T):661-669, 2009, doi: 10.4271/2009-01-1476.
6. Eastwood, P., "Particulate Emissions from Vehicles" (Chichester, UK: John Wiley & Sons, Ltd, 2007), doi: 10.1002/9780470986516.
7. ASTM International, "ASTM C29-00, Standard Test Methods for Apparent Porosity, Water Absorption, Apparent Specific Gravity, and Bulk Density of Burned Refractory Brick and Shapes by Boiling Water," West Conshohocken, PA.
8. Karin, P., Borhanipour, M., and Songsaengchun, Y., et al., "Oxidation Kinetics of small CI engine's biodiesel particulate matter," *International Journal of Automotive Technology*, 16(2):211-219, 2015, doi: 10.1007/s12239-015-0025-4.
9. Cao, J., Dong, X., Li, L., and Dong, Y., et al., "Recycling of waste fly ash for production of porous mullite ceramic membrane supports with increased porosity," *Journal of the European*

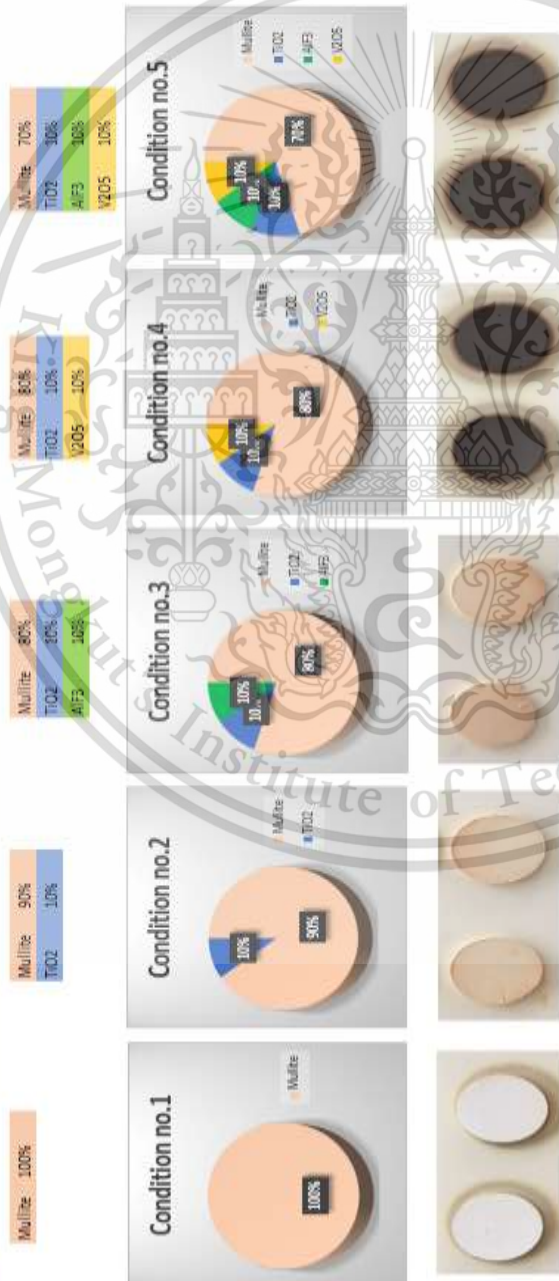
Contact Information

Corresponding Author
Preechar Karin, D.Eng.
Automotive Engineering Program,
King Mongkut's Institute of Technology Ladkrabang, Bangkok, 10520
Thailand.
Email: kkpreech@staff.kmitl.ac.th, Preechar.ka@kmitl.ac.th

APPENDIX B :

DATA RECORDED OF MULLITE

Record data : Mullite sample conditions of Mullite with additive



Product weight 1.05 g Diameter 25mm. Thickness 2mm.

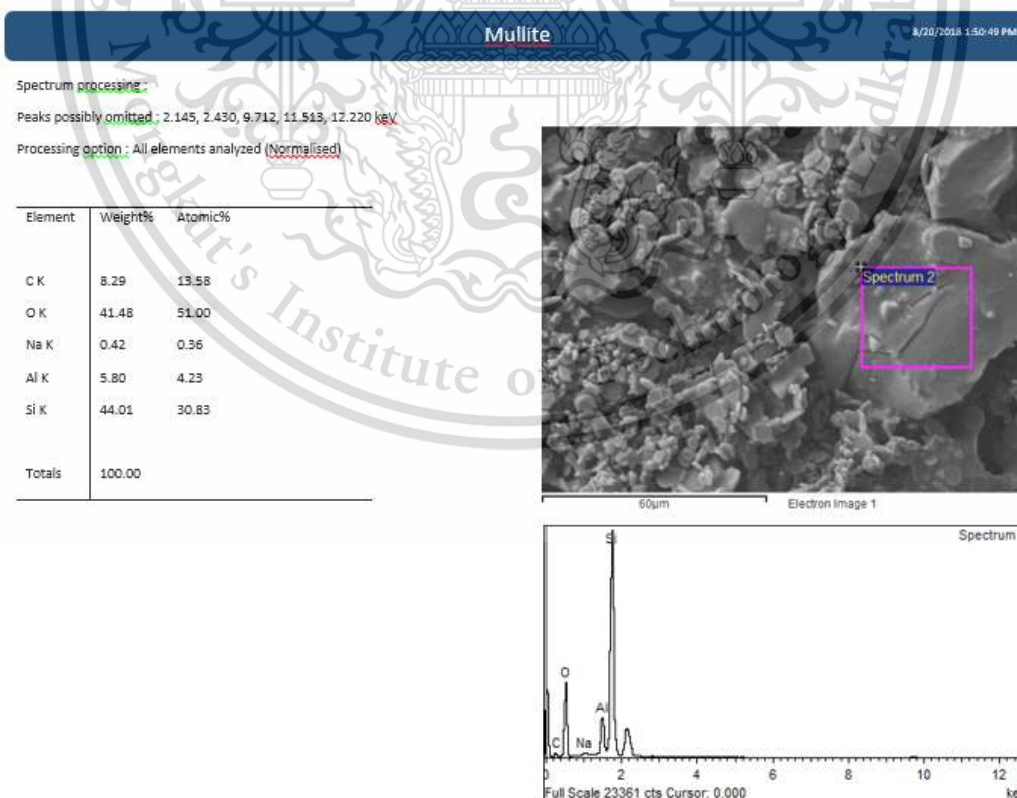
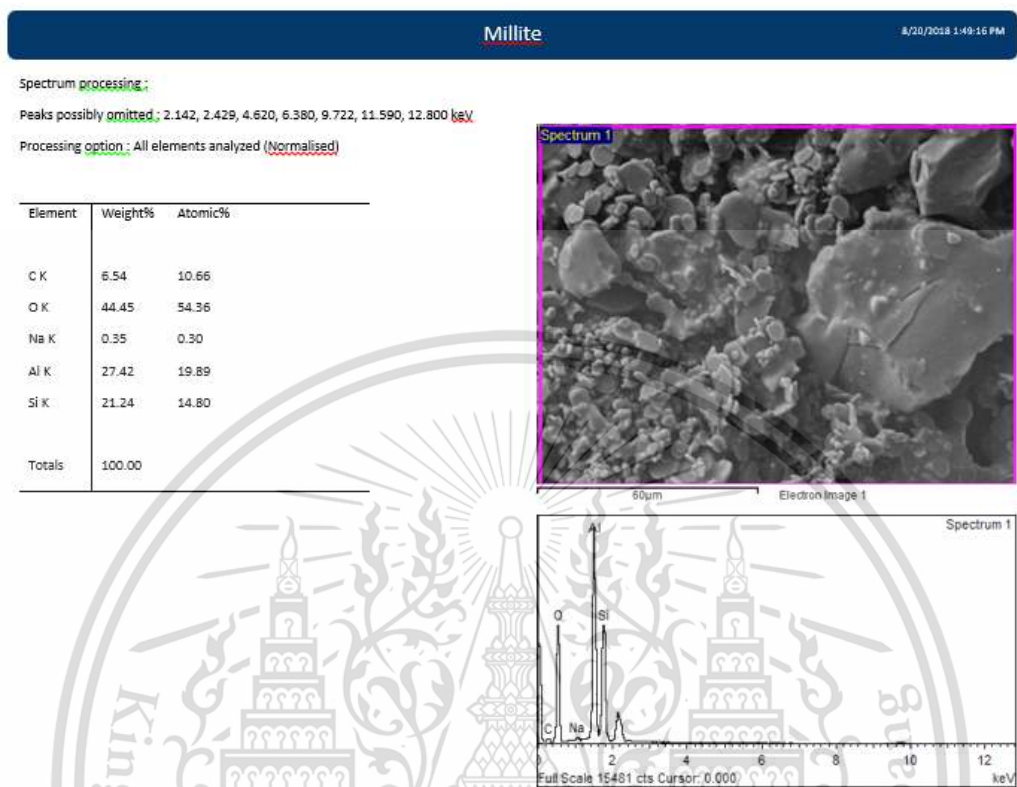
No.	Mullite (Al2O3 72% + SiO2 28%)				TiO2 (10%)				AlF3 (10%)				Al2O3 (10%)				Al2O3 (10%)				Real WT (g)	After Sic	WT loss	Diameter (mm)	Thickness (mm)	Pressure (psi)	Real WT (g)	Thickness (mm)	V of Water (mm3)	V of ML (mm3)	Porosity (%)
	%ratio	Al2O3 (g)	SiO2 (g)	%ratio	Weight (g)	%ratio	Weight (g)	%ratio	Weight (g)	%ratio	Weight (g)	%ratio	Weight (g)	%ratio	Weight (g)	%ratio	Weight (g)	%ratio	Weight (g)	Before Sic											
1.1	100%	0.756	0.294	0%	0	0%	0	0%	0	0%	0	0%	0	0%	0	0%	0	0%	0	1.0195	1.0195	2	1.3697	2	1.3697	350.2	981.25	35.69			
1.2	100%	0.756	0.294	0%	0	0%	0	0%	0	0%	0	0%	0	0%	0	0%	0	0%	0	1.0195	1.0195	2	1.3697	2	1.3697	350.2	981.25	35.69			
2.1	90%	0.680	0.365	10%	0.105	0%	0	0%	0	0%	0	0%	0	0%	0	0%	0	0%	0	1.0195	1.0195	2	1.3697	2	1.3697	350.2	981.25	35.69			
2.2	90%	0.680	0.365	10%	0.105	0%	0	0%	0	0%	0	0%	0	0%	0	0%	0	0%	0	1.0195	1.0195	2	1.3697	2	1.3697	350.2	981.25	35.69			
3.1	80%	0.605	0.435	10%	0.105	10%	0.105	0%	0	0%	0	0%	0	0%	0	0%	0	0%	0	1.0195	1.0195	2	1.3697	2	1.3697	350.2	981.25	35.69			
3.2	80%	0.605	0.435	10%	0.105	10%	0.105	0%	0	0%	0	0%	0	0%	0	0%	0	0%	0	1.0195	1.0195	2	1.3697	2	1.3697	350.2	981.25	35.69			
4.1	80%	0.605	0.435	10%	0.105	0%	0	10%	0.105	0%	0	0%	0	0%	0	0%	0	0%	0	1.0195	1.0195	2	1.3697	2	1.3697	350.2	981.25	35.69			
4.2	80%	0.605	0.435	10%	0.105	0%	0	10%	0.105	0%	0	0%	0	0%	0	0%	0	0%	0	1.0195	1.0195	2	1.3697	2	1.3697	350.2	981.25	35.69			
5.1	70%	0.529	0.506	10%	0.105	10%	0.105	10%	0.105	10%	0.105	0%	0	0%	0	0%	0	0%	0	1.0195	1.0195	2	1.3697	2	1.3697	350.2	981.25	35.69			
5.2	70%	0.529	0.506	10%	0.105	10%	0.105	10%	0.105	10%	0.105	0%	0	0%	0	0%	0	0%	0	1.0195	1.0195	2	1.3697	2	1.3697	350.2	981.25	35.69			

24-Sep-18

7-Aug-18 9:46:18

APPENDIX C :

EDX SHEETS

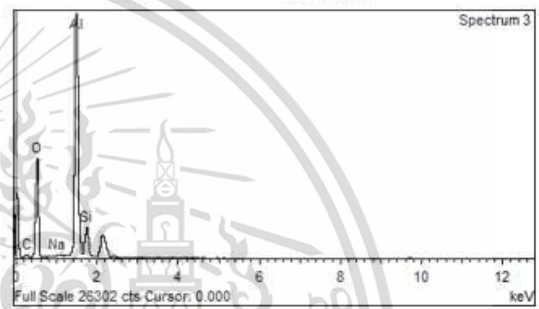
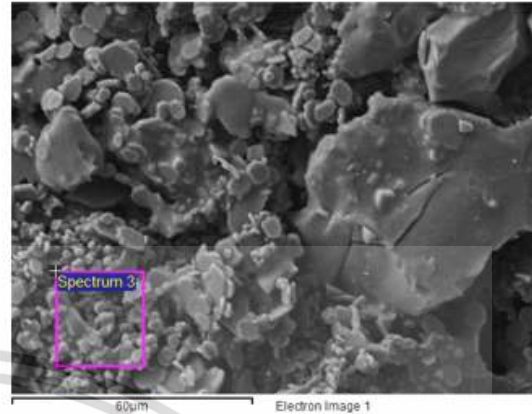


Spectrum processing :

Peaks possibly omitted : 2.143, 2.422, 9.713, 11.556 keV

Processing option : All elements analyzed (Normalised)

Element	Weight%	Atomic%
C K	6.67	10.76
O K	45.38	54.98
Na K	0.24	0.20
Al K	40.19	28.87
Si K	7.52	5.19
Totals	100.00	

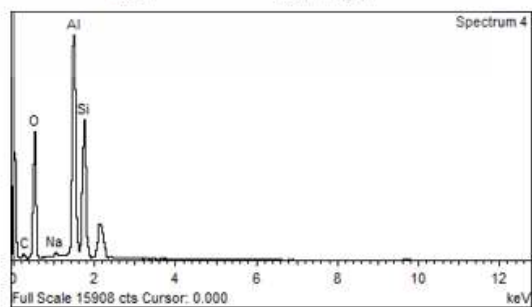
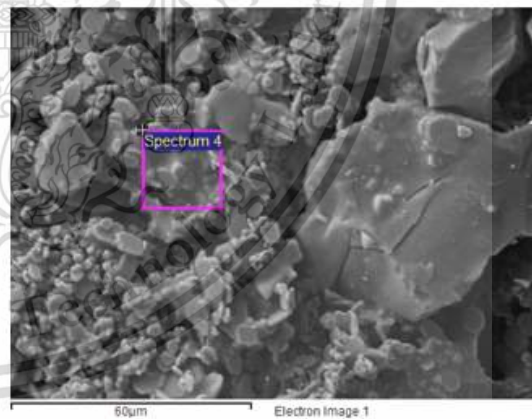


Spectrum processing :

Peaks possibly omitted : 2.143, 2.422, 3.700, 9.711, 11.511 keV

Processing option : All elements analyzed (Normalised)

Element	Weight%	Atomic%
C K	7.08	11.49
O K	44.13	53.81
Na K	0.49	0.41
Al K	25.70	18.58
Si K	22.61	15.71
Totals	100.00	

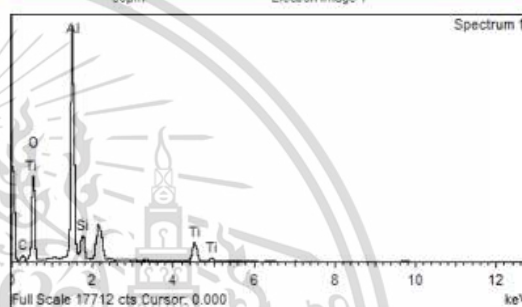
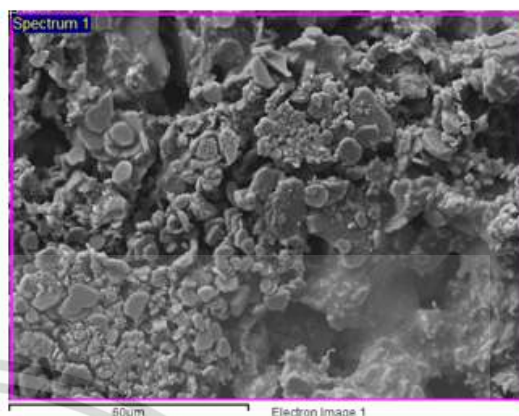


Spectrum processing :

Peaks possibly omitted : 2.147, 2.427, 9.718, 11.560 keV

Processing option : All elements analyzed (Normalised)

Element	Weight%	Atomic%
C K	6.32	10.63
O K	44.19	55.85
Al K	34.07	25.53
Si K	4.93	3.55
Ti K	10.50	4.43
Totals	100.00	

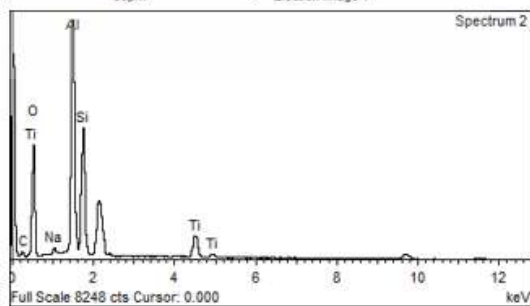
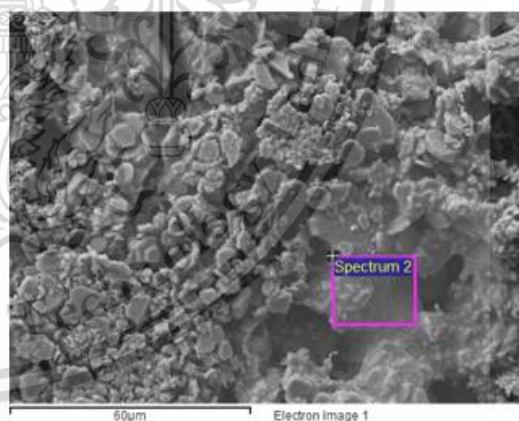


Spectrum processing :

Peaks possibly omitted : 2.142, 2.420, 9.712, 11.480 keV

Processing option : All elements analyzed (Normalised)

Element	Weight%	Atomic%
C K	6.34	10.76
O K	42.20	53.79
Na K	0.74	0.66
Al K	23.95	18.10
Si K	17.61	12.79
Ti K	9.15	3.89
Totals	100.00	

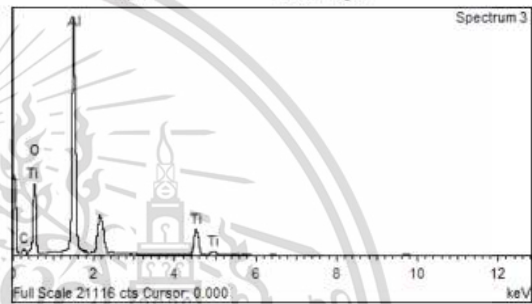
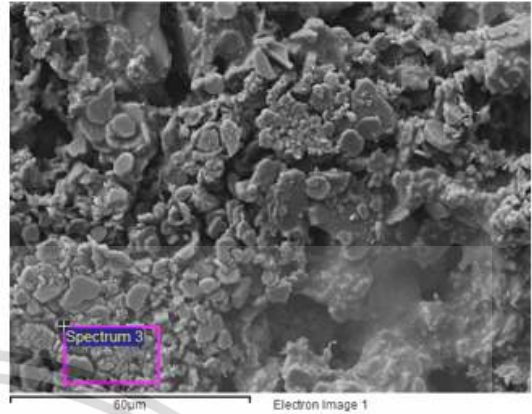


Spectrum processing :

Peaks possibly omitted : 2.145, 2.429, 2.760, 6.413, 9.711, 11.578 keV

Processing option : All elements analyzed (Normalised)

Element	Weight%	Atomic%
C K	5.79	10.01
O K	42.56	55.23
Al K	36.85	28.36
Ti K	14.79	6.41
Totals	100.00	

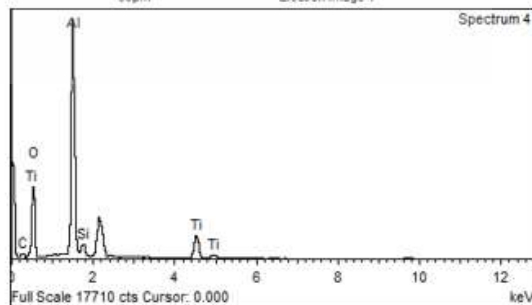
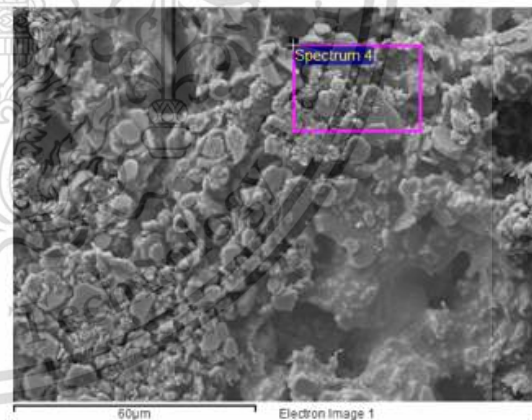


Spectrum processing :

Peaks possibly omitted : 2.143, 2.424, 6.381, 9.709, 11.532 keV

Processing option : All elements analyzed (Normalised)

Element	Weight%	Atomic%
C K	5.41	9.38
O K	41.88	54.54
Al K	36.69	28.33
Si K	2.55	1.69
Ti K	13.47	5.86
Totals	100.00	

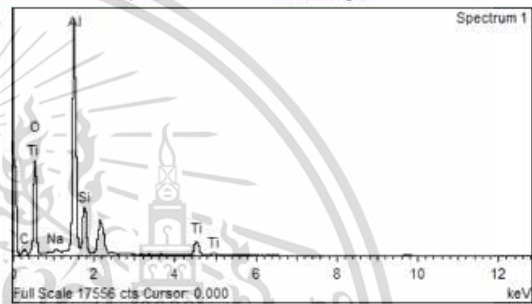
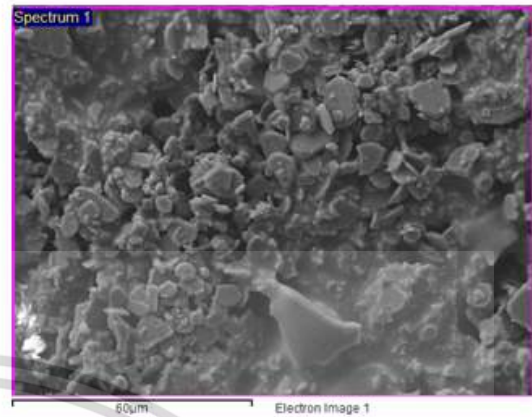


Spectrum processing :

Peaks possibly omitted : 2.144, 2.430, 6.402, 9.720, 11.549 keV

Processing option : All elements analyzed (Normalised)

Element	Weight%	Atomic%
C K	5.90	9.88
O K	44.24	55.62
Na K	0.45	0.40
Al K	32.63	24.33
Si K	9.21	6.60
Ti K	7.58	3.18
Totals	100.00	

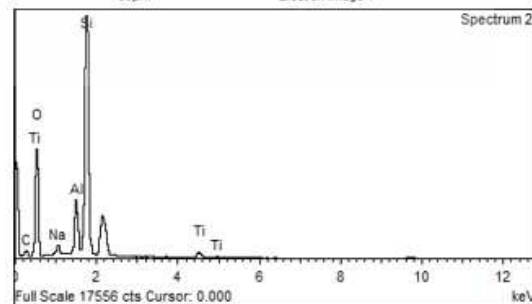
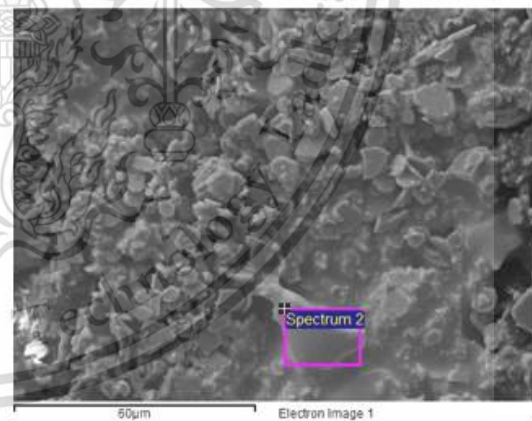


Spectrum processing :

Peaks possibly omitted : 2.143, 2.421, 9.710, 11.558 keV

Processing option : All elements analyzed (Normalised)

Element	Weight%	Atomic%
C K	9.17	14.70
O K	45.09	54.26
Na K	1.41	1.18
Al K	6.58	4.69
Si K	35.25	24.16
Ti K	2.51	1.01
Totals	100.00	

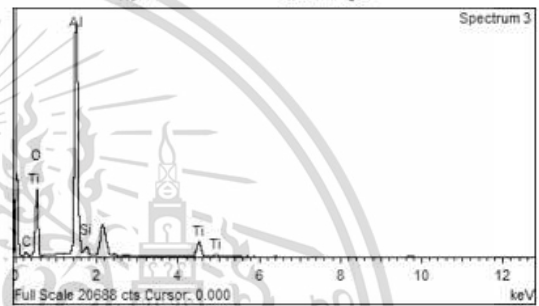
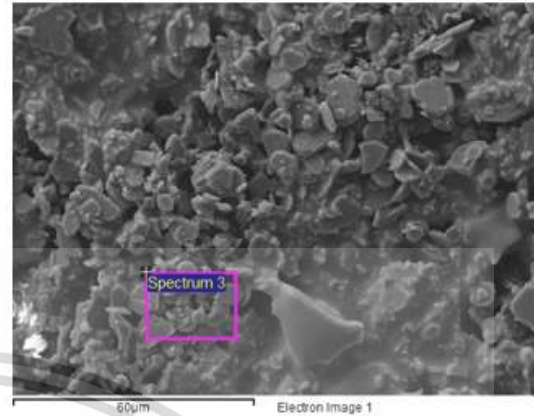


Spectrum processing :

Peaks possibly omitted : 2.145, 2.424, 6.379, 7.520, 9.721, 11.535 keV

Processing option : All elements analyzed (Normalised)

Element	Weight%	Atomic%
C K	6.73	11.39
O K	41.78	53.03
Al K	40.01	30.11
Si K	2.01	1.45
Ti K	9.47	4.01
Totals	100.00	

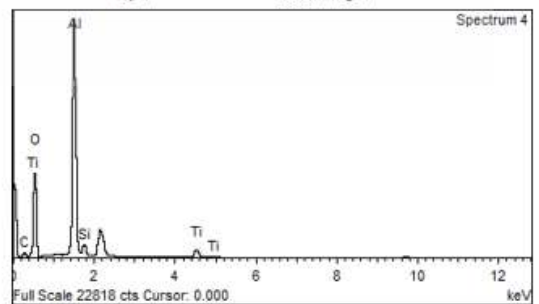
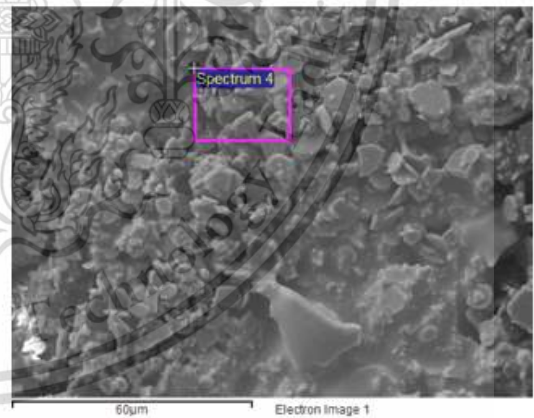


Spectrum processing :

Peaks possibly omitted : 2.145, 2.432, 6.402, 9.710, 11.516 keV

Processing option : All elements analyzed (Normalised)

Element	Weight%	Atomic%
C K	6.67	11.24
O K	44.93	55.24
Al K	40.53	29.55
Si K	2.85	1.99
Ti K	4.83	1.98
Totals	100.00	

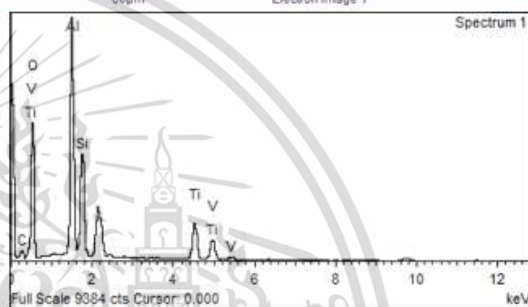
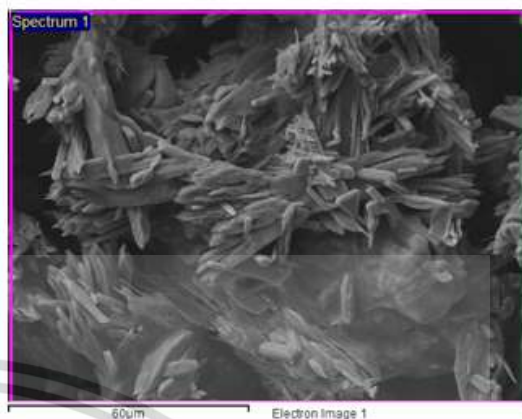


Spectrum processing :

Peaks possibly omitted : 2.143, 2.429, 6.400, 9.712, 11.539 keV

Processing option : All elements analyzed (Normalised)

Element	Weight%	Atomic%
C K	4.76	8.24
O K	46.72	60.68
Al K	20.31	15.64
Si K	11.00	8.14
Ti K	11.04	4.79
V K	6.17	2.52
Totals	100.00	

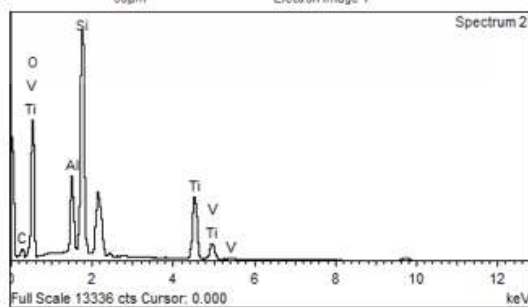
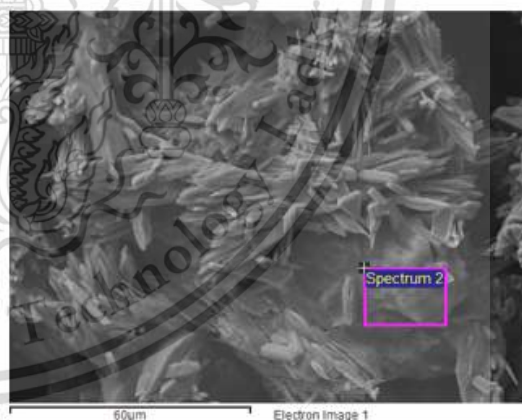


Spectrum processing :

Peaks possibly omitted : 2.141, 2.424, 9.718, 11.541 keV

Processing option : All elements analyzed (Normalised)

Element	Weight%	Atomic%
C K	5.04	8.78
O K	47.73	62.43
Al K	6.08	4.71
Si K	20.03	14.92
Ti K	18.15	7.93
V K	2.97	1.22
Totals	100.00	

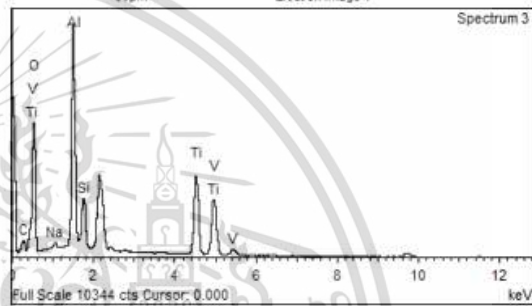
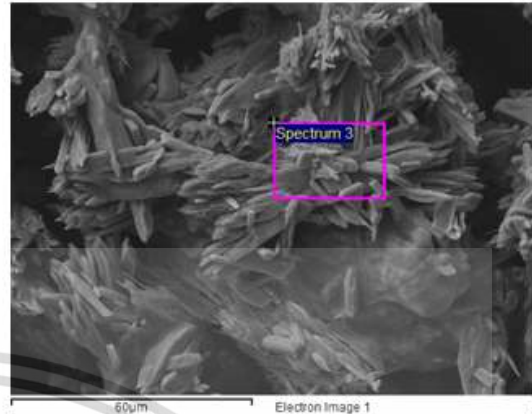


Spectrum processing :

Peaks possibly omitted : 2.145, 2.425, 2.779, 6.398, 9.717, 11.542 keV

Processing option : All elements analyzed (Normalised)

Element	Weight%	Atomic%
C K	4.81	8.97
O K	42.74	59.75
Na K	0.53	0.51
Al K	15.57	12.91
Si K	3.84	3.06
Ti K	18.70	8.74
V K	13.81	6.06
Totals	100.00	

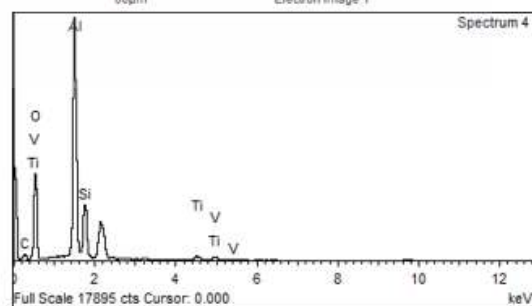
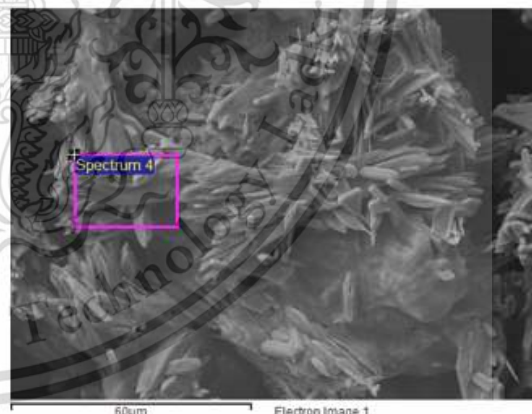


Spectrum processing :

Peaks possibly omitted : 2.144, 2.422, 8.460, 9.715, 11.505 keV

Processing option : All elements analyzed (Normalised)

Element	Weight%	Atomic%
C K	7.30	12.10
O K	41.91	52.12
Al K	35.25	26.00
Si K	11.50	8.15
Ti K	2.23	0.93
V K	1.81	0.71
Totals	100.00	

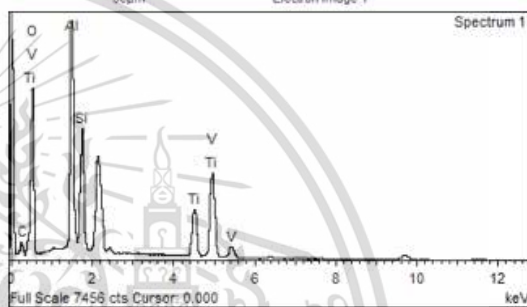
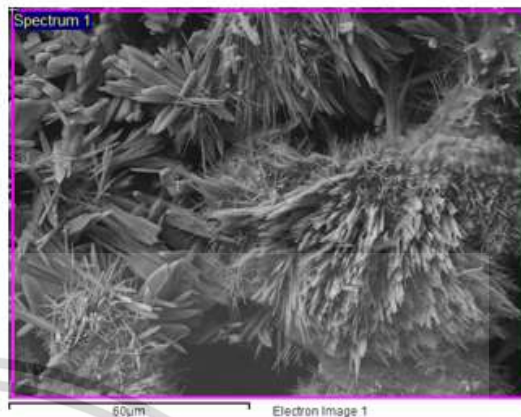


Spectrum processing :

Peaks possibly omitted : 1.040, 2.144, 2.428, 6.399, 9.711 keV

Processing option : All elements analyzed (Normalised)

Element	Weight%	Atomic%
C K	4.42	8.10
O K	44.99	61.85
Al K	13.17	10.74
Si K	8.22	6.44
Ti K	9.51	4.37
V K	19.68	8.50
Totals	100.00	

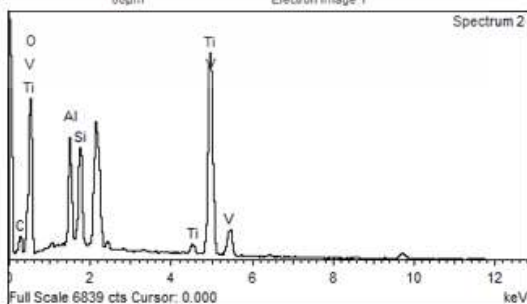
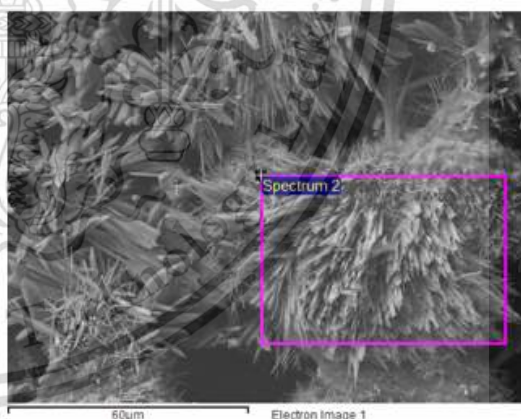


Spectrum processing :

Peaks possibly omitted : 1.040, 2.144, 2.427, 6.418, 8.560, 9.704, 11.512 keV

Processing option : All elements analyzed (Normalised)

Element	Weight%	Atomic%
C K	4.06	8.17
O K	40.40	60.99
Al K	5.74	5.14
Si K	5.28	4.54
Ti K	1.72	0.87
V K	42.80	20.29
Totals	100.00	

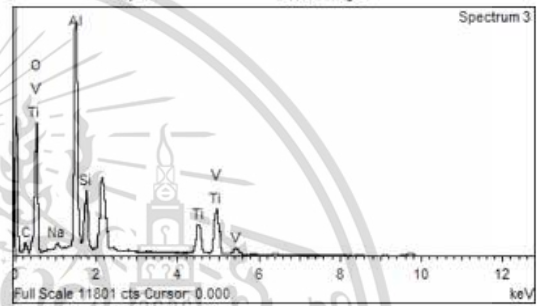
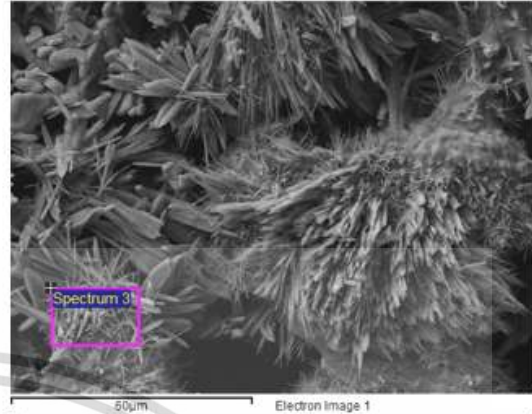


Spectrum processing :

Peaks possibly omitted : 2.144, 2.429, 6.406, 9.720 keV

Processing option : All elements analyzed (Normalised)

Element	Weight%	Atomic%
C K	5.68	10.02
O K	45.58	60.35
Na K	0.62	0.57
Al K	18.67	14.66
Si K	5.70	4.30
Ti K	8.55	3.78
V K	15.20	6.32
Totals	100.00	

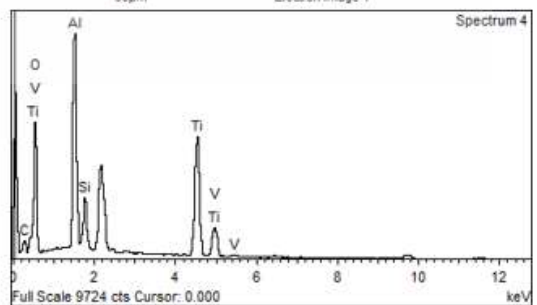
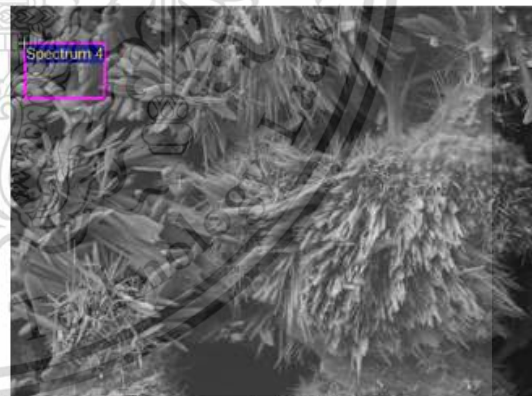


Spectrum processing :

Peaks possibly omitted : 2.143, 2.429, 6.407, 9.718, 11.599 keV

Processing option : All elements analyzed (Normalised)

Element	Weight%	Atomic%
C K	4.77	3.82
O K	44.11	61.18
Al K	14.54	11.96
Si K	3.80	3.00
Ti K	28.13	13.03
V K	4.64	2.02
Totals	100.00	

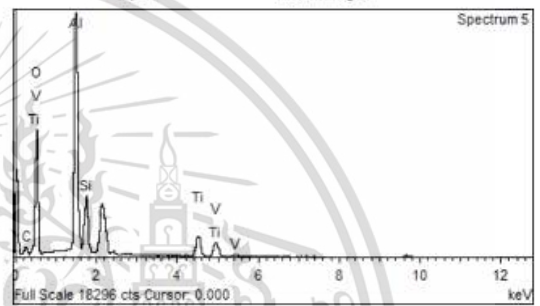
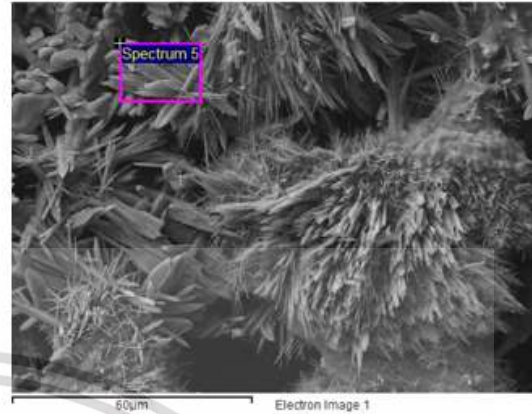


Spectrum processing:

Peaks possibly omitted: 2.143, 2.428, 6.429, 9.709, 11.535 keV

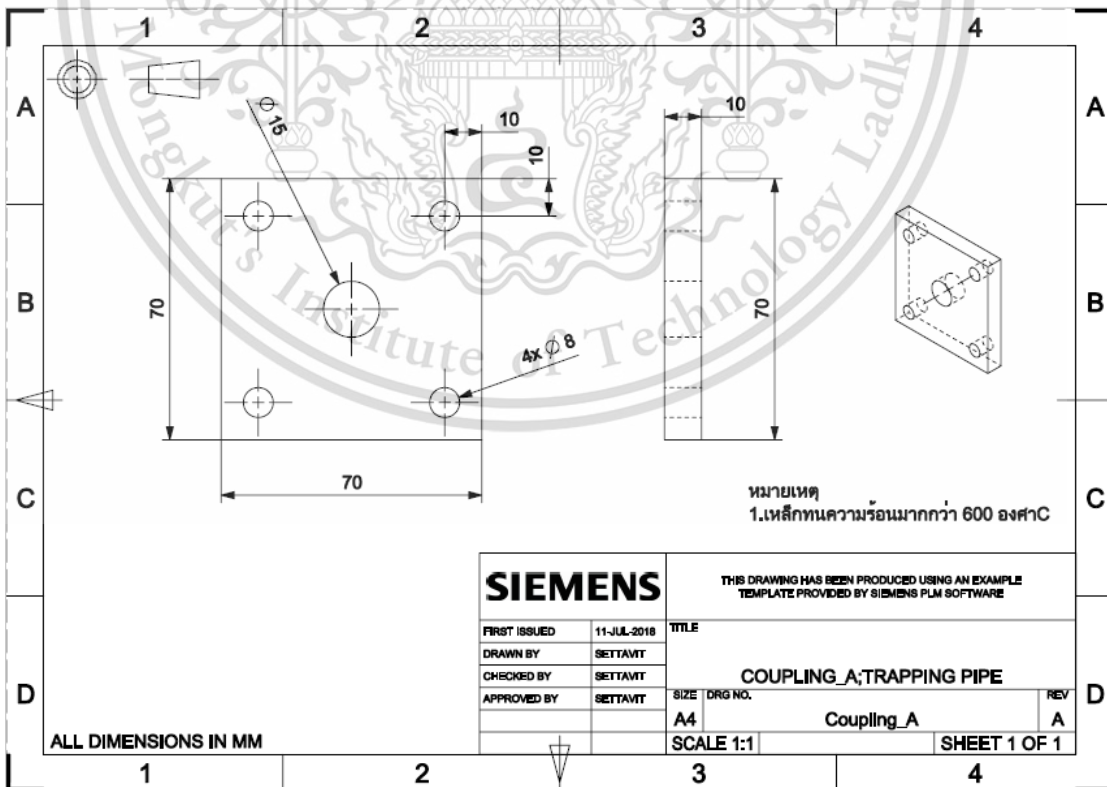
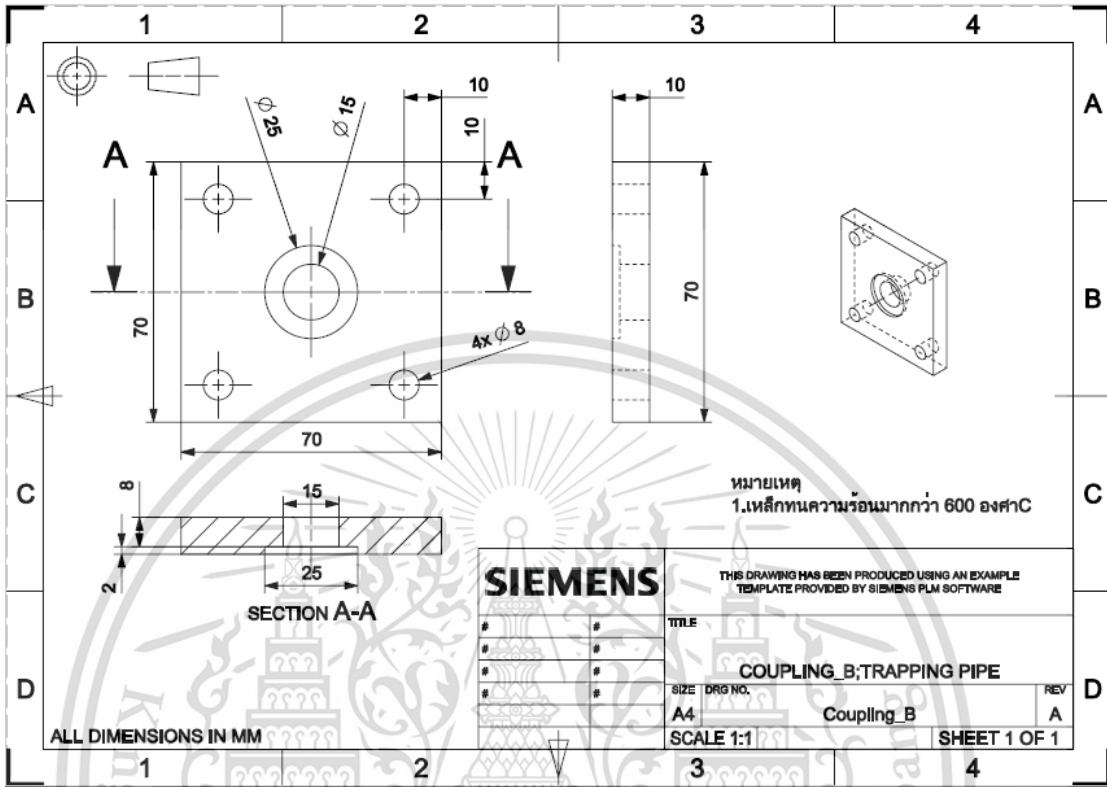
Processing option: All elements analyzed (Normalised)

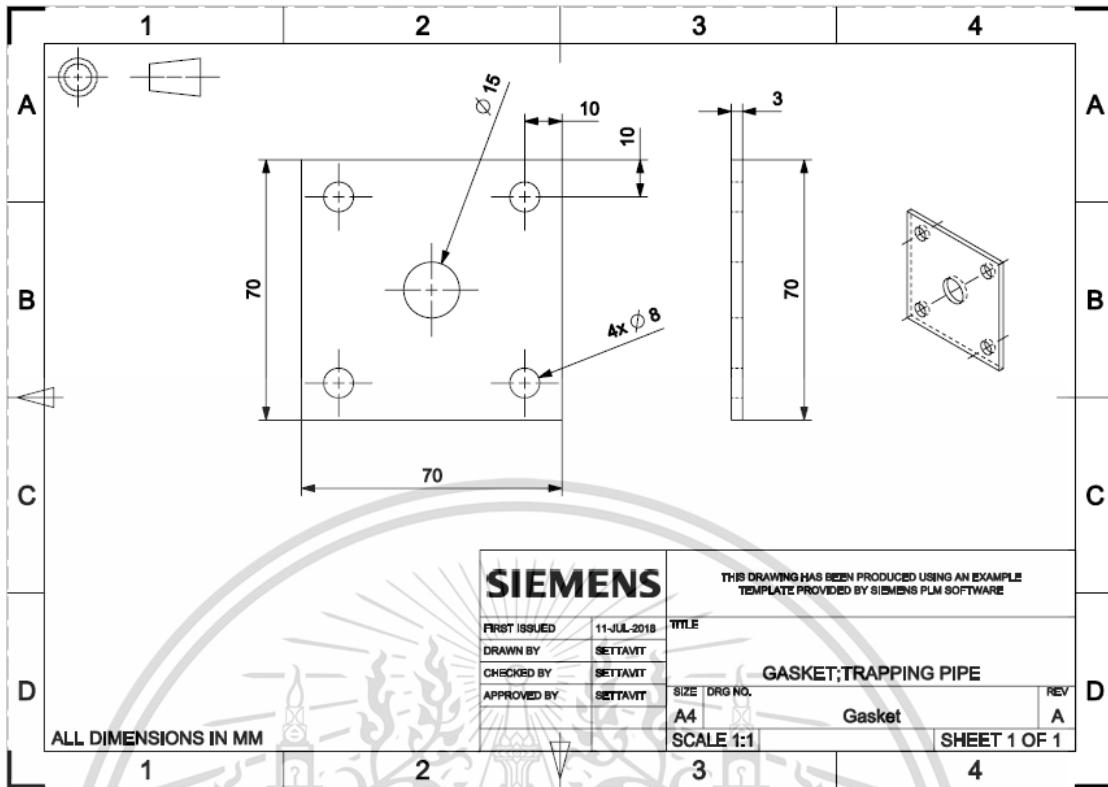
Element	Weight%	Atomic%
C K	6.71	11.19
O K	47.45	59.38
Al K	25.10	18.63
Si K	7.68	5.47
Ti K	7.62	3.27
V K	5.24	2.06
Totals	100.00	



APPENDIX D :

DRAWINGS





APPENDIX E :

COMMENT AND QUESTION FROM THESIS DEFENSE

Q1: Why you have to use TiO_2 for all? Moreover, why you have to added AlF_3 and V_2O_5 ?

Regarding to prewise studied TiO_2 is usually used as a sintering aid to lower the sintering temperature of porous alumina membrane support. Two ways of the addition of TiO_2 are chosen: in-situ precipitation and in-situ hydrolysis. The results show that the distribution status of TiO_2 has an important effect on the property of porous alumina membrane support. In in-situ hydrolysis method, the nano-meter scale TiO_2 distributes evenly on the alumina particles' surface. The bending strength of the support increases sharply and the pore size distribution changes more sharply along with the content of TiO_2 which slightly increases percent weight. Currently, the mechanical properties of the alumina supports are improved by increasing the sintering temperature, prolonging sintering time, or using sintering aids and so on. Under the view of engineering, it has been proved that adding a sintering aid is a simple and feasible way which could balance the bending strength and the porosity. TiO_2 is chosen because TiO_2 has similar lattice parameters to Al_2O_3 . The solid solution can be easily formed during the sintering process. At the same time, the lattice defects are generated in the solid solution due to the valence difference, which promotes the mass transport and reduces the sintering process.

For the addition of AlF_3 and V_2O_5 , I found prewise research mention about low-cost porous mullite ceramic membrane supports were fabricated from recycling coal fly ash with addition of natural bauxite. V_2O_5 and AlF_3 were used as additives to cause the growth of mullite crystals with various morphologies. Dynamic sintering micro structure and phase evolution of the membrane supports were characterized in detail and open porosity, pore size, were determined. It showed an interlocking microstructure composed of an isotropically grown mullite whiskers. Addition of more V_2O_5 lowered the secondary mullitization temperature, resulting in more mullite formation at lower temperatures. The fabricated membrane supports feature high porosity without mechanical strength degradation, possible strengthening mechanism of the mullite whiskers was further discussed.

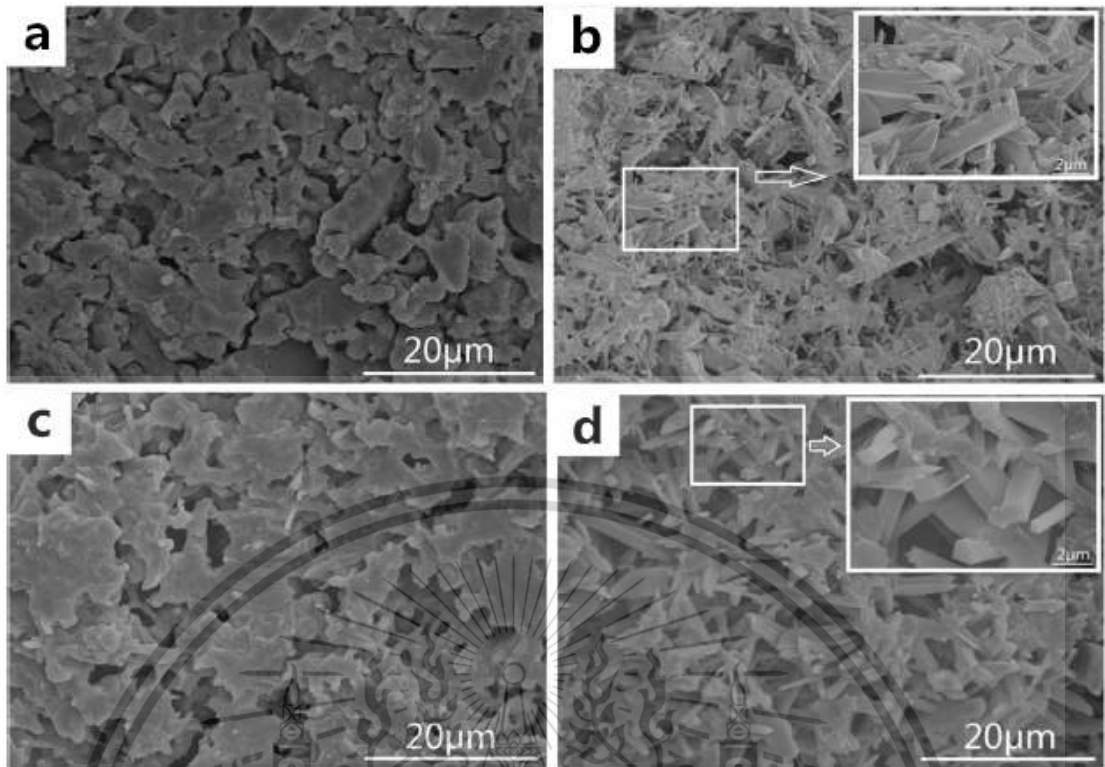
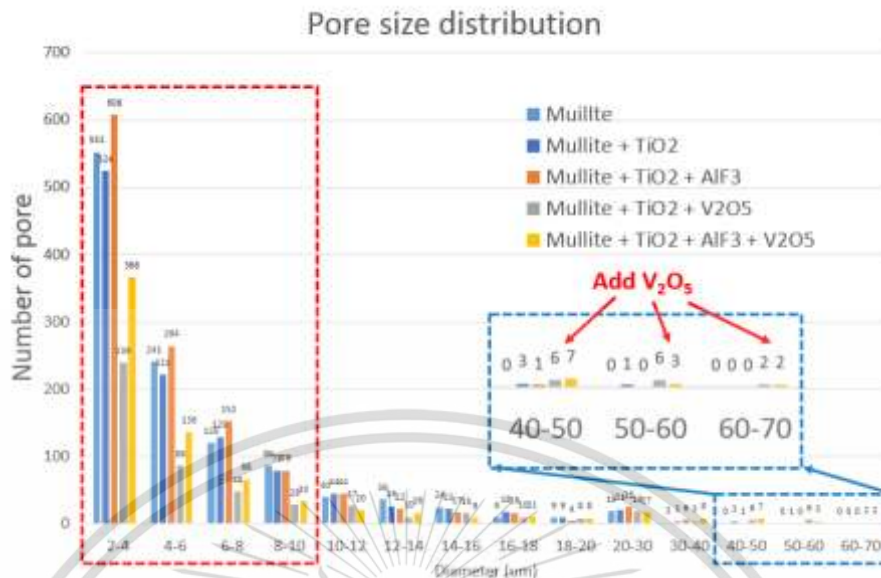


Figure A Fresh fracture surface SEM images of A0V0 and A4V3 membrane supports sintered at different temperatures after biaxial flexural strength tests: (a) A0V0-1300 (sintered at 1300°C), (b) A4V3-1300 (sintered at 1300°C), (c) A0V0-1400 (sintered at 1400°C), (d) A4V3-1400 (sintered at 1400°C).

Fig. A shows the fresh fracture surface SEM images after biaxial flexural strength tests of A0V0 and A4V3 membrane supports sintered at different temperatures. For A0V0-1300 and A0V0-1400 (Fig. A a and c), most of the fractures upon failure occurred from larger glassy phase regions between partially-sintered mullite crystals, which absorb lower fracture energy during strength testing because of lower intrinsic strength of glass. No fractured mullite crystals were observed even after etching with HF solution suggesting that fracture is completely intergranular. Due to the addition of V₂O₅ and AlF₃, though open porosity is greater, there is a significant change in the microstructure of the fabricated mullite membrane supports, which are entirely composed of interlocked mullite whiskers with increased aspect ratio without any appearance of the presence of glassy phase (see Fig. 9b and d). Fresh fracture surfaces of these mullite whiskers were identified by SEM (see the inserted SEM images in Fig. A b and d).

Q2: Page 28 as the graph of pore size distribution. What is the criterial of pore size?



I used the raw image from SEM. In this paper, the SEM of model JSM-6400 is tungsten filament source, 3.5 nm resolution at 30 kV, magnification of 300. Figure B shows two color image. The images were analyzed by image processing with software called “Image J” to measure quantitative data of the porosity size and pore size distribution. The determination of porosity size was evaluated as same as the determination of PM by using SEM. In this research, the each point of black color is used to calculate the pore dimension. Finally summarized to pore size distribution.

Image-J criteria:

- Image size 1270 x 870 pixels
- Threshold 20%-30%
- Remove outliers Bright 5pixels
- Remove outliers Dark 3pixels
- Analyze particle size 3.3um² for average diameter not less than 2um

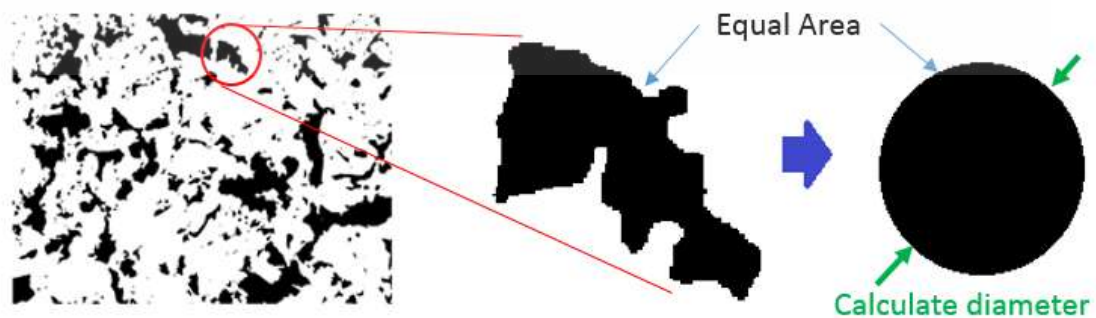
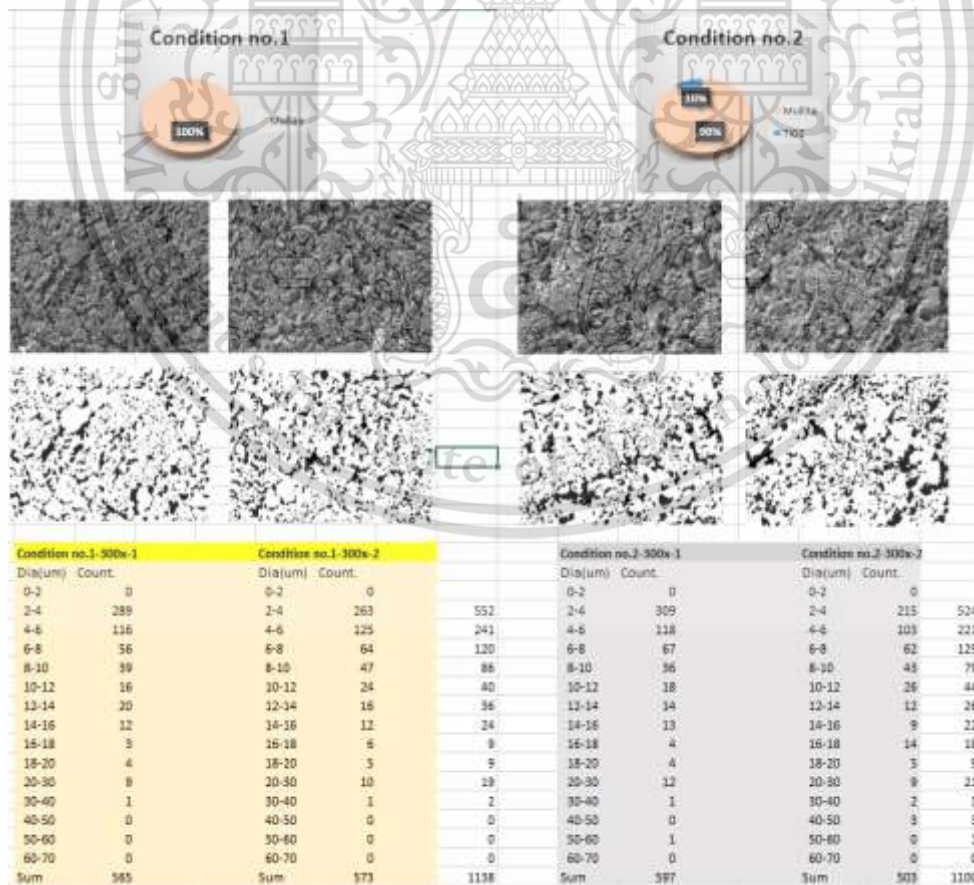
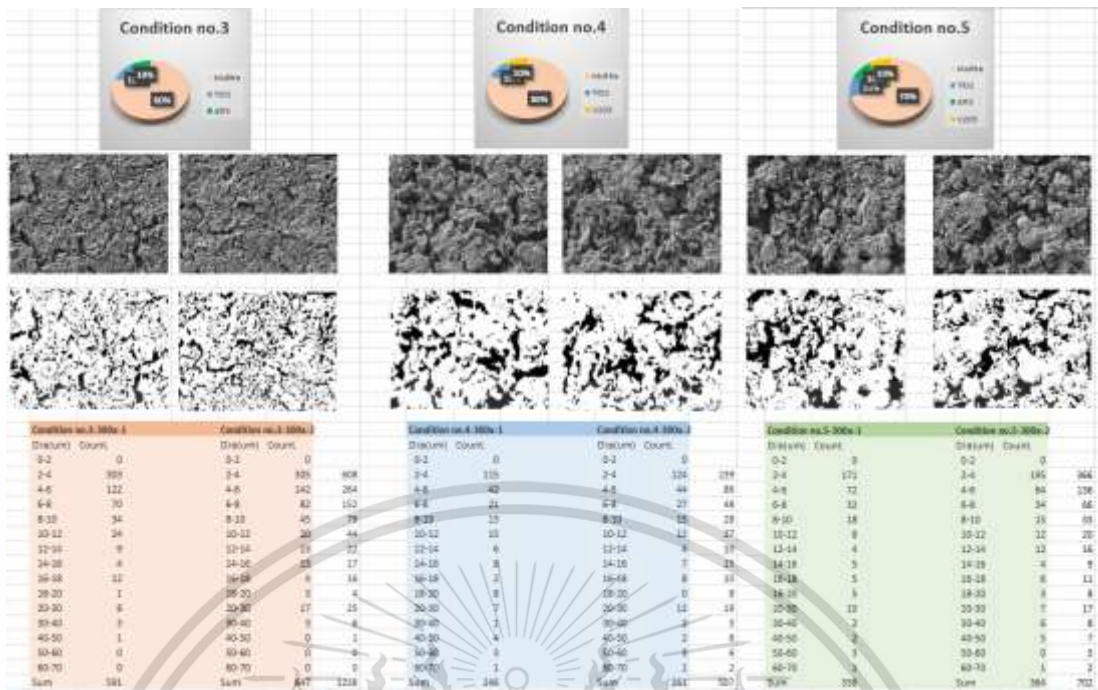


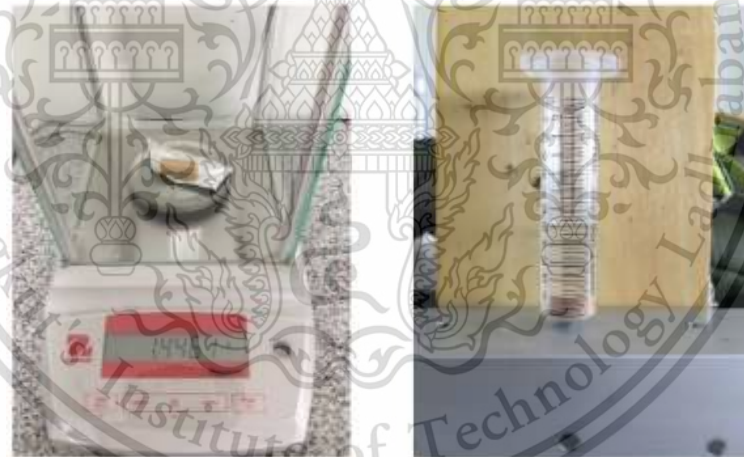
Figure B calculation of pore diameter

	Area	Mean	Min	Max		Diameter(um)		
1	40.066	255	255	255		7.144193		
2	3.311	255	255	255		2.053737	Dia(um)	Count.
3	28.697	255	255	255		6.046213	0-2	0
4	75.937	255	255	255		9.835397	2-4	289
5	53.421	255	255	255		8.249378	4-6	116
6	11.589	255	255	255		3.842272	6-8	56
7	4.305	255	255	255		2.341811	8-10	39
8	138.188	255	255	255		13.26784	10-12	16
9	21.412	255	255	255		5.222684	12-14	20
10	10.265	255	255	255		3.616135	14-16	12
11	5.85	255	255	255		2.729877	16-18	3
12	114.678	255	255	255		12.08663	18-20	4
13	4.525	255	255	255		2.400902	20-30	9
14	3.311	255	255	255		2.053737	30-40	1
15	141.83	255	255	255		13.44155	40-50	0
16	16.004	255	255	255		4.515225	50-60	0
17	11.7	255	255	255		3.860629	60-70	0
18	6.402	255	255	255		2.855769	Sum	565
19	7.505	255	255	255		3.092007		
20	5.077	255	255	255		2.543131		
21	17.881	255	255	255		4.772666		
22	3.532	255	255	255		2.12117		
23	29.359	255	255	255		6.115554		
24	166.774	255	255	255		14.5757		





Q3: About Archimedes method still have some bubble inside sample. Do you have any reference?



The open porosity percentage was considered as the ratio of blank volume to total volume which presents in the range of 0-100%. The open porosity was analyzed using Archimedes' principle of water substitution. The open porosity increases with addition the carbon black 35% by weight. It can produce porosity is in the range of 35% - 45% base on the sintering temperature 1,300°C. About experiment of wet condition, it should be confirmed that the bubble is not in the mullite. Therefore, I tested by dipping the water for 10 minutes and then shaking it to chase the bubble with all of sample conditions.

Then the porosity can be calculated from different weights as use below equation.

Weight of water in pore space

$$W_{wtr} = W_{sat} - W_{dry}$$

Pore volume

$$V_p = W_{wtr} / \rho_{wtr}$$

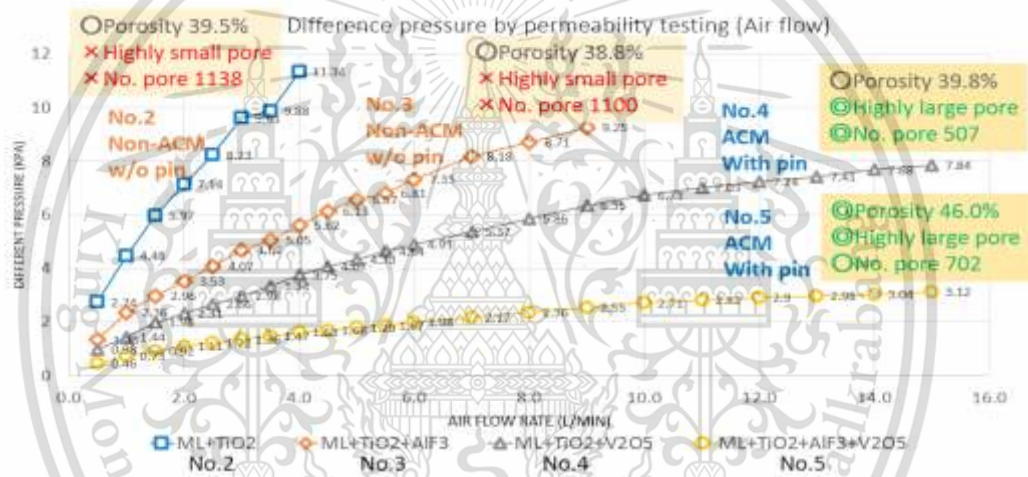
Bulk volume (from previous example)

$$V_b = \pi r^2 h$$

Porosity

$$\Phi = V_p / V_b$$

Q4: Page 30 the pressure drop should be test at low velocity. In addition, the graph should be linear. Why it is not strength line?

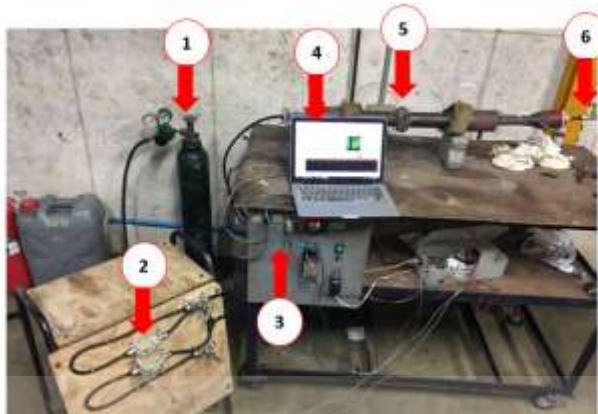


The relationship of pore size, pore number, porosity, permeability and pressure drop.

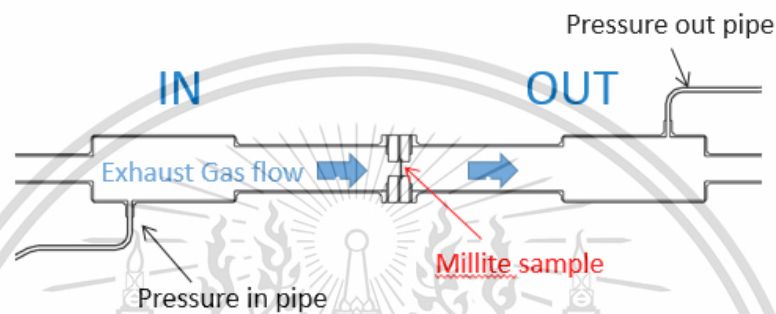
Summary as result of pressure drop.

- High porosity filter offers lower pressure drop increase during filtration.
- When the pore size in downstream region is smaller, the flow is difficult to pass through, resulting in the higher pressure drop.
- On the other hand, the pressure change is smaller in the downstream region where the pore size is larger.

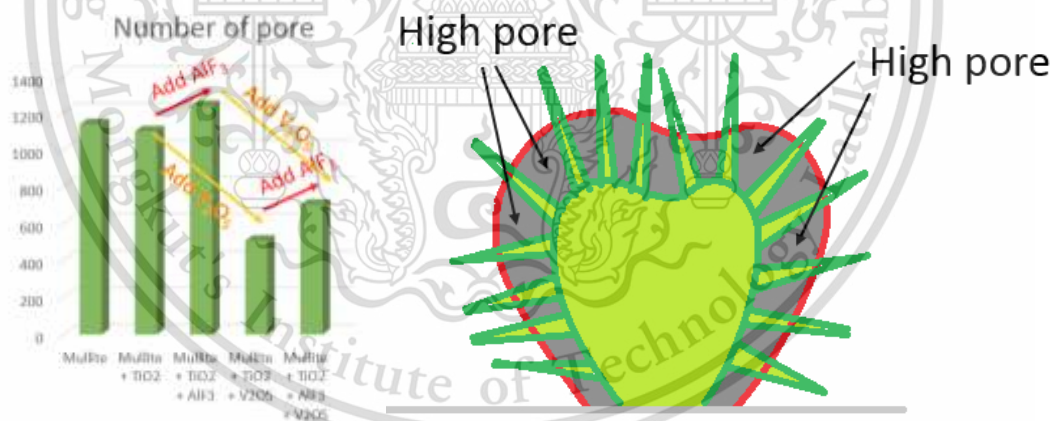
About the question why graph of pressure drop is not strength line. I think in my permeability equipment have setup the relief valve at the end of pipe. Moreover, it had control by fix only one condition. Then, if the airflow are increasing too much, the air cannot flow out at relief valve. Therefore, the graph of pressure drop at high flow rate will be decreasing continuously.



No.	Items name
1	Air Tank
2	Flow switch
3	Diff. Pressure Sensor
4	Monitoring
5	Airflow Pipe
6	Relief Valve



Q5: Page 28 as the graph the number of pore. Why AlF_3 and V_2O_5 effected to the number of pore?



Regarding to SEM image of the sample with addition of AlF_3 and V_2O_5 . We can find acicular or pin structure in the mullite sample. For AlF_3 can perform pin size around $5\mu\text{m}$. So I think the area between pin can increase pore number. For the condition no4 and no5 with added V_2O_5 appeared big pore around $50\text{-}70\mu\text{m}$. I think V_2O_5 have effect to melting point of mullite. That why the number of pore of condition no4 and no5 are decreasing.

AUTHOR BIOGRAPHY

Author: Mr. Settavit Sirivarocha
Degree: Master of Engineering
Date of Graduation: 29th August 2019
Date of Birth: 18th May 1982
Place of Birth: Bangkok, Thailand

Undergraduate and Graduate Education:

Master of Engineering in Automotive Engineering,
King Mongkut's Institute of Technology Ladkrabang, Bangkok

Bachelor degree in Naval Architecture and Marine Engineering,
Kasetsart University Sriracha Campus, Chonburi

Major: Automotive Engineering

Presentations and Publications:

- [1] Preechar Karin, Park Watanawongskorn, Jiramed Boonsakda, Eakkawut Saenkhumvong, Sippakorn Rungsratanapaisan, Settavit Srivarocha, Chinda Charoenphonphanich, Nuwong Chollacoop, and Katsunori Hanamura "Impact of Biodiesel on Small CI Engine Combustion Behavior and Particle Emission Characteristics", The 21st Small Engine Technology Conference (SETC), November 17-19, 2017, Jakarta, Indonesia.
- [2] Settavit Sirivaracha, Preechar Karin, Eakkawut Saenkhumvong, Nuwong Chollacoop, and Katsunori Hanamura "Impact of TiO₂ on Sintered Mullite Porous Surface Microstructure using Scanning Electron Microscopy and Image Processing", Technical Paper, 2018, JSAE Annual Congress (Spring), 23-25 May, 2018, Yokohama Japan.
- [3] Settavit Sirivaracha, Preechar Karin, Eakkawut Saenkhumvong, Nuwong Chollacoop, and Katsunori Hanamura "Impact of TiO₂ and V₂O₅ on Sintered Mullite Porous Microstructure and Soot Oxidation Kinetics using SEM and TGA", Technical Paper, 20th Asia-Pacific Automotive Engineering Conference, 1-4 April 2019, Bangkok Thailand.